INSTITUT POLYTECHNIQUE DE PARIS

TELECOM Paris

IP PARIS

NNT : 2021IPPAT010

Thèse de doctorat

Design of Ultra Dense Passive Optical Network to Support High Number of End Users

Thèse de doctorat de l'Institut Polytechnique de Paris
préparée à Télécom Paris

Ecole doctorale de l'Institut Polytechnique de Paris, n°626 (ED IP Paris)
Spécialité de doctorat: Électronique et optoélectronique

Thèse présentée et soutenue à Ville de soutenance, le 06/05/2021, par

KEBEDE TESEMA ATRA

Composition du Jury :

Delphine MARRIS-MORINI Professeur, Université Paris-Saclay (– C2N)	Président
Hélène CARRERE Maître de conférences, INSA Toulouse	Rapporteur
Josep PRAT Professeur, Universitat Politecnica De Catalunya	Rapporteur
Nikos PLEROS Maître de conférences, Aristotle University of Thessaloniki	Examinateur
Didier ERASME Professeur, Télécom Paris	Directeur de thèse
Cédric WARE Maître de conférences, Télécom Paris	Co-Directeur de thèse
Giancarlo CERULO Ingénieur de recherche, III-V Lab	Encadrant industriel
Fabienne SALIOU Ingénieur de recherche, Orange Labs	Invité

Design of Ultra Dense Passive Optical Network to Support High Number of End Users

In memory of my sister Bethlehem Tesema (*Asnakech*)

Résumé

Les nouveaux réseaux cellulaires de cinquième génération (5G) adoptent une architecture de réseau centralisée, tout en utilisant des technologies à ondes millimétriques pour la transmission sans fil. Une telle architecture nécessite une large bande passante optique ainsi que l'installation d'un grand nombre de transmetteurs-récepteurs optiques. Afin de rendre la prochaine génération de réseaux résidentiels et mobiles abordables pour l'utilisateur final, il est essentiel de transmettre le trafic des utilisateurs sur une liaison en fibre optique partagée de manière rentable. Pour cette raison, des réseaux optiques passifs (PONs), avec des configurations point-multipoint et le multiplexage en longueur d'onde (WDM), sont adoptés par la plupart des opérateurs de réseau d'accès, comme une solution de transport rentable. En outre, il est nécessaire de minimiser la consommation d'énergie par bit et de réduire le coût du transmetteur-récepteur, en fournissant des composants optiques à faible coût et à haut-débit qui peuvent fonctionner à différentes longueurs d'onde dans un système WDM.

Dans ce programme de recherche, nous avons étudié des modulateurs à électro-absorption réfléchissants (REAM) intégrés, de manière monolithique, avec des amplificateurs optiques à semi-conducteurs (SOA) pour réaliser des transmetteurs à faible coût et à haut-débit, pour applications dans les nouvelles générations des réseaux d'accès. Le principal avantage technique d'un EAM-SOA réfléchissant (REAM-SOA) est qu'il peut être utilisé pour réaliser des transmetteurs, indépendants de la longueur d'onde (achromatiques), sur une large gamme de spectre, avec des exigences de contrôle minimales, directement compatibles avec la réallocation des canaux de transmission. Ces caractéristiques permettent de réduire le niveau de planification du réseau (assignation de la longueur d'onde) requise par les opérateurs et ont, donc, un impact significatif sur la réduction du coût global du système.

Dans la première partie de cette thèse, nous présentons la conception des composants, en discutant leurs propriétés physiques de base : le système de matériaux utilisés, l'ingénierie de la structure de bande des régions actives MQW et les guides d'ondes optiques SI-BH. La technologie de fabrication est également décrite, en introduisant les étapes clés du procédé PIC-SIBH. Nous étudions des composants basés sur différentes configurations, pour des modulateurs de longueurs différentes (80, 100 et 150 micromètres). Nous analysons l'optimisation des EAM, en étudiant les caractéristiques de base, comme la bande passante électro-optique (E/O), l'efficacité de modulation et les effets de 'chirp'. Dans la deuxième partie, nous discutons de la caractérisation des propriétés statiques et dynamiques de nos composants. Dans la troisième partie de cette thèse, nous montrons les performances de nos composants pour des transmissions numériques et analogiques. Dans le domaine numérique, nous avons obtenu une transmission indépendante de la longueur d'onde, jusqu'à 25 Gb/s en utilisant le format de modulation 'non-return-to-zero (NRZ)'. Avec des EAM de 100 μm, nous avons également démontré une transmission jusqu'à 50 Gb/s. Dans le domaine numérique, nous avons démontré une transmission radio sur fibre jusqu'à 3 km, à 10 Gb/s, en accord avec les exigences du fronthaul 5G.

Summary

Emerging cellular networks such as the fifth generation (5G) adopt centralized network architecture while using millimeter wave technologies for wireless transmission. Such an architecture requires large optical bandwidth as well as installing a large number of optical transceivers. In order to make the next generation of residential and mobile networks affordable to the end user, it is crucial to transmit the user traffic over a fiber optic link cost-effectively. For that reason, passive optical network (PON) based on wavelength division multiplexing (WDM) is adopted by most access network operators as a cost-effective transport solution. Furthermore, it is also necessary to minimize energy consumption per bit and reduce the transceiver cost by providing low-cost and high-speed optical components that can operate at different wavelengths in a WDM system.

In this thesis, we study reflective electroabsorption modulators (EAMs) monolithically integrated with semiconductor optical amplifiers (SOAs) to realize low-cost and high-speed transmitters for access network applications. The main technical advantage of a reflective EAM-SOA (REAM-SOA) is that it can be used as a wavelength-independent (colorless) transmitter over a wide range of spectrum with minimal control requirements, enabling interchangeable network equipment, which reduces the amount of network (wavelength) planning required by network operators and thus have a significant impact on reducing the overall system cost.

We start with the device design and provide an overview of the material system, device physics, technological aspects, mask layout and structure of the integrated circuit. We also use numerical simulations to study the optical as well as quantum characteristics of the devices. We study different device configurations based on three modulator lengths (80, 100, and 150 micrometers) in order to study different design tradeoffs such as electro-optic (E/O) bandwidth, modulation strength, and modulator-induced chirp. Then, we fully characterize our components in both static and dynamic modes. In digital domain, we achieve up to 16 km wavelength-independent transmission at 25 Gb/s using non-return-to-zero (NRZ) modulation format. With the 100-μm long EAM, we demonstrate transmissions up to 50 Gb/s NRZ. In analog domain, we demonstrate up to 3 km radio-over-fiber transmission at 10 Gb/s, satisfying the requirements of 5G fronthauling.

Table of Contents

1. Introduction 1
   1.1. Mobile Fronthauling Based on Passive Optical Network 3
   1.2. Challenges Associated with Tunable Lasers 7
   1.3. Proposed Network Architecture 10
   1.4. State-of-the-Art Reflective Devices 12
   1.5. Context of the PhD 13
2. Device Design and Technology 18
   2.1. Material System 18
   2.2. Vertical Device Design 23
   2.3. Multiple Quantum Wells 25
      2.3.1. Quantization of Energy 29
      2.3.2. Density of States 32
      2.3.3. Strained Quantum Wells 34
      2.3.4. Effect of Strain on Electronic Band Profiles 36
   2.4. Electronic Band Structures of Compressive Strained MQWs 37
   2.5. Absorption Coefficient 38
      2.5.1. Optical Confinement Factor 41
   2.6. Polarization Sensitivity 43
   2.7. Electroabsorption Effects 45
      2.7.1. Quantum Confined Stark Effect 48
      2.7.2. Carrier Sweepout Time and Saturation Characteristics 54
   2.8. Amplifier Gain and Noise Figure 56
   2.9. Fabrication and Epitaxial Growth Process Flow 60
   2.10. Semi-Insulating Buried Heterostructure 63
   2.11. Device Structure and Schematics 68
   2.12. Optical Mask Layout 70
   2.13. Summary and Discussion 72
3. Performance Analysis of Basic Building Blocks 74
   3.1. Optimization of Spot-Size Converter 75
      3.1.1. Simulation of Waveguide Structures 79

3.1.2. Far-Field Measurement 84
3.2. Insertion Loss 86
3.2.1. Insertion Loss Estimation 86
3.2.2. Insertion Loss Spectrum 90
3.3. Amplifier Gain 92
3.3.1. Experimental Setup 92
3.3.2. Amplified Spontaneous Emission Spectrum 93
3.3.3. Current-Dependent Small-Signal Gain 96
3.3.4. Gain Spectrum 97
3.3.5. Gain Saturation 100
3.4. Amplifier Noise Figure 103
3.5. Modulator Static Extinction Ratio 107
3.6. Dynamic Characteristics 113
3.6.1. Small-Signal Frequency Response 113
3.6.2. Modulator Induced Chirp 124
3.7. Summary and Discussion 137
4. System-Level Demonstrations 141
4.1. Digital Transmissions in the C-Band at 25 Gb/s 142
4.1.1. Experimental Setup 142
4.2. Digital Transmission in the O-Band at 25 Gb/s 150
4.3. Beyond 50G Digital Transmission in the O-Band 152
4.4. Analog Radio-over-Fiber Transmission 158
4.5. Summary and Discussion 164
5. Conclusion and Perspectives 166
5.1. Summary and Conclusion 166
5.2. Perspectives 168
List of Abbreviations 170
References 172
Curriculum Vitae 177
List of Publications 178
Acknowledgments 179

Chapter 1

1. Introduction

In a telecommunication system, the access network is the one that connects end users to the rest of the network, namely metro and core networks. Depending on the type of service provided, the user can be reached directly using a fiber optic cable (e.g., in fiber-to-the-home, FTTH) or via a wireless link (e.g., mobile communication systems). In the latter case, the user equipment (UE) connects to the radio unit (RU) at the cell site, which then relays the radio information to the digital unit (DU) for baseband processing, using radio-over-fiber (RoF) technology. The fiber link between the DU and the RU is known as the fronthaul network [1]−[3]. Most of the discussions in this chapter apply to both residential as well as mobile networks, but we focus on mobile fronthauling that applies to emerging cellular technologies such as 5G and beyond.

One of the advantages of RoF transmission is that the optical link is transparent to the type of radio signal being transmitted. The modulation scheme in the optical domain can be digital RoF (DRoF) or analog RoF (ARoF), where the former is simple but spectrally inefficient whereas the latter is spectrally efficient but prone to nonlinear effects, which can have a significant impact on the transmission error rate [3]. Concerning the protocol interfacing the DU and the RU, the most widely used type is the common public radio interface (CPRI) protocol, an industry specification that introduces functional splits in radio base stations into the radio equipment (RE), which is the RU in this discussion, and the radio equipment controller (REC), which is the DU [4].

Low loss of fiber optic cables provides a great flexibility in choosing a convenient location for installing the DU with respect to the RU. As such, the DU and the RU are separated by a few kilometers (e.g., in 3G and 4G) to a few tens of kilometers (e.g., in 5G and beyond), leading to a centralized radio access network (C-RAN) architecture [1][2].

The main advantage of a C-RAN architecture is that it allows sharing radio resources (e.g., sharing a pool of DUs by several RUs) and facilitates a centralized network management and processing capabilities. However, it also brings two important technical challenges in relation to: (i) the large

amount of data traffic to be carried by the fronthaul network (the optical link), which requires expensive high-speed optical transceivers, and (ii) the latency requirement of the system in order to support time-critical services that are envisioned to be supported by 5G+ networks (e.g., autonomous vehicles, remote surgery, and collaborative robots) [1].

The first challenge arises from the bandwidth inefficiency of the CPRI protocol in CPRI-based DRoF transmissions, which is the most widely used type of interface in existing networks, whereas the second challenge is mainly due to the propagation delay inside a fiber optic cable when the DU and the RU are separated by several kilometers. Several alternative solutions are studied to achieve lower data rate interfaces without compromising the end-to-end delay [2], mainly focusing on functional splits, where some of the functionalities of the DU can be moved to the RU so that the required bandwidth in the optical link can be reduced by performing baseband processing partly at the RU, e.g., by introducing eCPRI [4] and Ethernet-based fronthauling [5], both of which are based on higher layer splitting (instead of the physical layer where CPRI's splitting occurs).

Therefore, with these advancements, the access network is feeling the pressure not only of data traffic growth but also new requirements for mobile fronthauling such as ultra-low latency, high reliability, high availability, and supporting large number of connected users [6][7]. Most of these requirements arise from the evolution of cellular networks to a C-RAN architecture as it is the case for 5G networks, where the DU and the RU can now be separated by a fiber length of 10−20 kms [8], with the DU being located in the central office (CO) and the RU at the remote office (RO), also known as the cell site [1][2].

In the wireless part, millimeter wave (mmWave) technologies, for example in the 60-GHz range (V-band), are being widely studied, exploited, and licensed to take advantage of their inherently large spectral bandwidth [3]. Since the wireless transmission distance at such high frequencies is limited by high propagation loss (e.g., atmospheric and free space losses), network densification (i.e., installing a large number of small cells) is considered as a key deployment strategy in 5G in order to enhance the network capacity [5]. To cope with the challenges associated with mmWaves (e.g., link budget, complexity, and line-of-sight transmission), the small cells integrate beamforming (focusing wireless signals to a specific receiver) as well as beam steering (changing the direction of the radiation pattern) capabilities for 360° coverage, together with massive multiple input multiple output (MIMO) antenna configurations to maximize the user data rate [9].

Nevertheless, network densification being a key deployment strategy in 5G and mmWaves that transmit only up to a few hundred meters taking over the wireless part, the number of high-speed optical transceivers required in the fronthaul network increases tremendously, raising a serious concern on component cost, energy consumption per bit, and equipment footprint. As a result, it is necessary to introduce cost-effective optical transceivers in order to make the next generation of cellular networks affordable to the end user. This work focuses on the realization of low-cost and high-speed optical transmitters with wavelength-independent (colorless) operational capabilities for access network applications.

To transmit radio signals between the RU and the DU using RoF technologies, most access network operators adopted passive optical network (PON) based on wavelength division multiplexing (WDM) as a low-cost transport solution. A key feature of a PON system is that the optical distribution network (ODN) is passive, meaning that only passive components constitute the ODN (the physical fiber and optical devices in the field) while active devices are installed only at the two end offices (the CO and the RO) [8].

1.1. Mobile Fronthauling Based on Passive Optical Network

In order to increase the capacity of the access network, the international telecommunication union (ITU) introduced WDM technology to the access network in its next-generation passive optical network 2 (NG-PON2) standard [8]. The standard defined four 100-GHz-spaced wavelength channels, each carrying a maximum of 10 Gb/s traffic so that the aggregate downlink capacity increases to 40 Gb/s (from the CO to the RO). In this configuration, a single optical line terminal (OLT) located in the CO (close to the DU) connects to multiple optical network units (ONUs) at the RO (close to the RU) either in a point-to-multipoint (PtMP) or a point-to-point (PtP) connectivity. The standard also defined another set of 8×50-GHz-spaced wavelength channels for overlay PtP connectivity [8]. In the upstream direction (ONU to OLT), each ONU transmits at a maximum data rate of 10 Gb/s (in the case of symmetric transmission). In the PtMP connectivity, the number of ONUs per OLT typically exceeds the number of available wavelength channels. As a result, a single wavelength channel is shared by multiple ONUs, and the standard recommends implementing a hybrid time and wavelength division multiplexing (TWDM) scheme for wavelength sharing [8]. For that reason, the standard is commonly referred to as TWDM-PON.

Fig. 1.1 shows a schematic diagram of mobile fronthauling based on WDM-PON in a C-RAN architecture, where a pool of DUs in the CO connects to an array of OLT channel terminations (CTs) and is shared by several RUs in the RO [10]. A wavelength multiplexer (WM) such as an arrayed waveguide grating (AWG) combines the optical signals from the OLT transmitters and transmits them over a single fiber optic cable. At the receiver side, a second AWG demultiplexes the optical signals and send them to their respective ONUs. Instead of an AWG, a passive optical power splitter can also be used at the receiver side, but the ONUs in that case will require optical filters in front of them. In either case, after optical to electrical (O/E) conversion is performed by the ONU receiver, the information is relayed to the RU, to which the UE connects wirelessly.

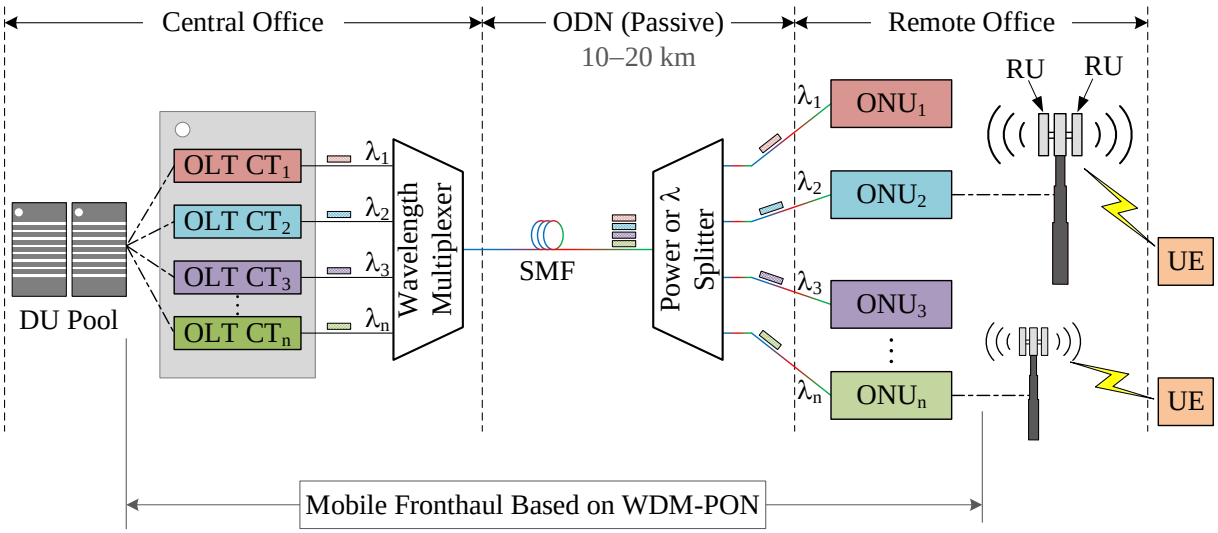


Fig. 1.1. Schematic diagram of a WDM-PON system supporting 5G fronthauling in a C-RAN architecture. CT: channel termination, SMF: single-mode fiber.

The actual implementation of the WDM-PON system (PtMP or PtP) to support 5G+ fronthauling depends on the system requirement regarding latency as well as the number of connected ONUs (number of available wavelength channels). In order to support time-critical services, a dedicated wavelength channel can be assigned to each ONU by using the PtP dense WDM (DWDM) approach defined in NG-PON2. The number of available wavelength channels can be further increased by implementing ultra-dense WDM (UDWDM) PON, which increases the channel count by reducing the spacing between neighboring channels, and it is a promising candidate for the fronthauling of emerging mobile networks [11].

On the other hand, in order to further increase the capacity of the access network and thus meet the growing bandwidth demand because of emerging technologies such as 5G+ fronthauling and data center interconnects, current PON standards are pushing the channel rate to 50 Gb/s with a nominal line rate of 25 Gb/s as recommended by IEEE's 50G EPON (Ethernet PON) [12] and 50 Gb/s as recommended by ITU's 50G PON, also known as high-speed PON (HSP) [13]. That means, to achieve the 50G capacity, the former recommends multiplexing two 25-Gb/s wavelength channels whereas the latter recommends a single-wavelength capacity of 50 Gb/s.

Both standards use simple modulation formats such as non-return-to-zero (NRZ) on-off keying (OOK) so that low-cost transceivers can be used, but NRZ-OOK is not spectrally efficient. Improving the spectral efficiency in the optical domain requires complex and expensive coherent detection, and, although it is being widely studied and getting cheaper, it is not yet the preferred option for high-speed access networks. In this thesis, we focus on NRZ modulation format, and we use PAM-4 (four-level pulse amplitude modulation) to show the capabilities of our components as a next step.

Apart from their differences in the nominal line rates (and protocols used for communication between OLT and ONU), the two standards (IEEE's 50G EPON and ITU's 50G PON) support coexistence of current PON technologies with legacy networks. As an example, Fig. 1.2 shows a simplified schematic diagram of a 50G PON system in coexistence with legacy PONs [13].

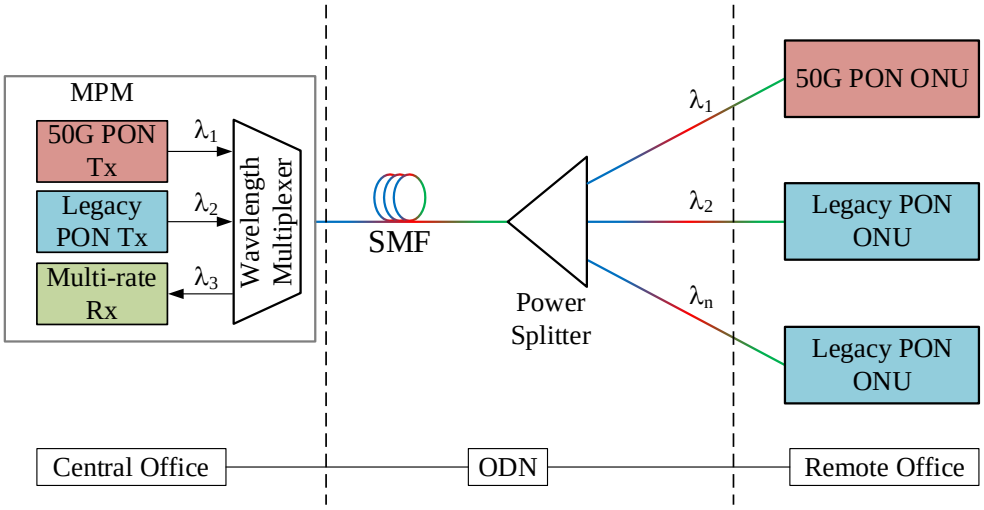
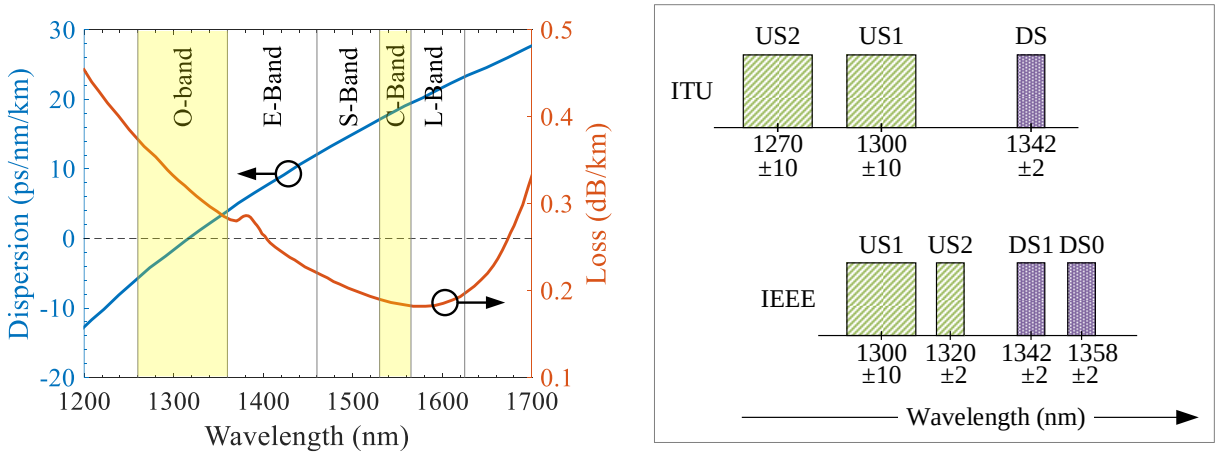


Fig. 1.2. Schematic diagram of a 50G PON system in coexistence with legacy PONs (after [13]). MPM: multi-PON module, Tx: Transmitter, Rx: Receiver.

At the OLT side, the evolution from legacy to 50G PON can be realized using a multi-PON module (MPM) that incorporates a wavelength multiplexer together with the OLT transmitters or using an external coexistence (CEx) element [13]. The optical signals from different PON transmitters are multiplexed and transmitted over a single fiber. At the receiver side, a passive splitter (power or wavelength) splits the transmitted signals and sends them to a number of connected ONUs. Then, each ONU, equipped with appropriate type of receiver (e.g., a 50G capable receiver with an optical filter for 50G PON), receives the information on its operating wavelength.

Although the wavelength plan in the NG-PON2 standard is in the C-band (1.55 μm window), which is characterized by a relatively low fiber loss and high chromatic dispersion as shown in Fig. 1.3 (a), the transmission distance in the C-band is primarily limited by dispersion, which becomes more detrimental at bit rates >10 Gb/s. For that reason, both IEEE's 50G EPON and ITU's 50G PON standards defined their WDM wavelength plans in the O-band (1.3 μm window), which is characterized by a relatively high fiber loss and very low fiber dispersion.

Fig. 1.3 (b) shows the wavelength plans for downlink and uplink transmissions defined by ITU (top) and IEEE (bottom) for 50G applications [12][13]. In both cases, the upstream transmissions take place near the zero or negative dispersion regimes so that simple and cost-effective ONU transmitters can be used without experiencing significant performance degradation because of dispersion.



(**a**) (**b**)

Fig. 1.3. (**a**) Dispersion and loss spectra of standard single-mode fiber, (**b**) wavelength plans for 50G PON applications defined by ITU's 50G PON (top) and IEEE's 50G EPON (bottom). US: upstream, DS: downstream.

In addition to minimizing the cost of the transport network by implementing WDM-PON, it is also necessary to provide low-cost optical transceivers in order to minimize the overall system cost. Moreover, the devices have to be realized using industrially compatible technologies so that they can be mass-produced for large-scale deployments.

Nevertheless, both standards (IEEE's 50G EPON and ITU's 50G PON) recommend using wavelength-tunable components on both sides of the network (at the CO and the RO) [12][13]. However, tunable devices require tight wavelength control, which in turn requires complex electronic circuitry for their operation and control at data rates >10 Gb/s. This complicates the device design and operation, making tunable devices still expensive solutions to be used in the access network with large-scale deployments. The two important challenges in using wavelength-tunable lasers in a PON system arise from: (i) the ONUs are required to operate in burst-mode transmission [8][13], which causes frequency drift during burst transmission [14]−[16], and (ii) the complexity associated with their tuning mechanisms. Both challenges are discussed in the following section using experimental results.

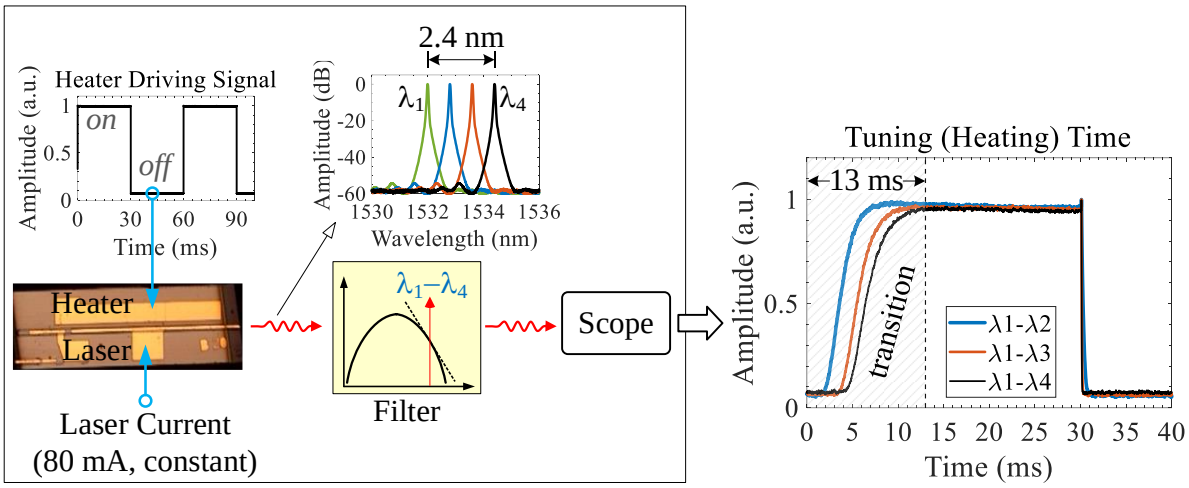
1.2. Challenges Associated with Tunable Lasers

Thermal Tuning of Lasers

For access network applications, cost-effective wavelength-tunable transmitters are mainly based on either directly modulated lasers (DMLs) or externally modulated lasers (EMLs). In the former case, the modulating electrical signal is directly applied to the laser whereas an external modulator such as an electroabsorption modulator (EAM) is integrated with the laser in the latter case. Among the two, DMLs are relatively simple, and they are widely used in short-reach applications, where the transmission distance is mainly limited by large chirp DMLs exhibit (a sudden change of laser wavelength, which causes pulse broadening and leads to intersymbol interference at the receiver side, and ultimately increases the transmission error rate) [17][18].

On the other hand, thermal tuning is the simplest wavelength tuning mechanism for such low-cost components, which can be achieved by integrating a heater on chip (for fast tuning) with a DML as illustrated in the lower part of Fig. 1.4 (a) [19]. In order to tune the laser, a DC current is applied to the heater for a duration of about 30 ms, and the emission wavelength of the laser is aligned to

the edge of a tunable filter so that the transition from one wavelength to another, within the filter bandwidth (0.25 nm ≡ 30 GHz), can be captured by a sampling oscilloscope.



(**a**) (**b**)

Fig. 1.4. (**a**) SEM image of a DML with integrated heater, and shape of the heater driving signal applied to tune the laser by 2.4 nm (4×100 GHz), (**b**) signal captured by a sampling oscilloscope after the CW light passes through a tunable optical filter. $\lambda_1 = 1532$ nm, $\lambda_2 = 1532.8$ nm, $\lambda_3 = 1533.6$ nm, $\lambda_4 = 1534.4$ nm, $V_{scope} \propto 1/f$.

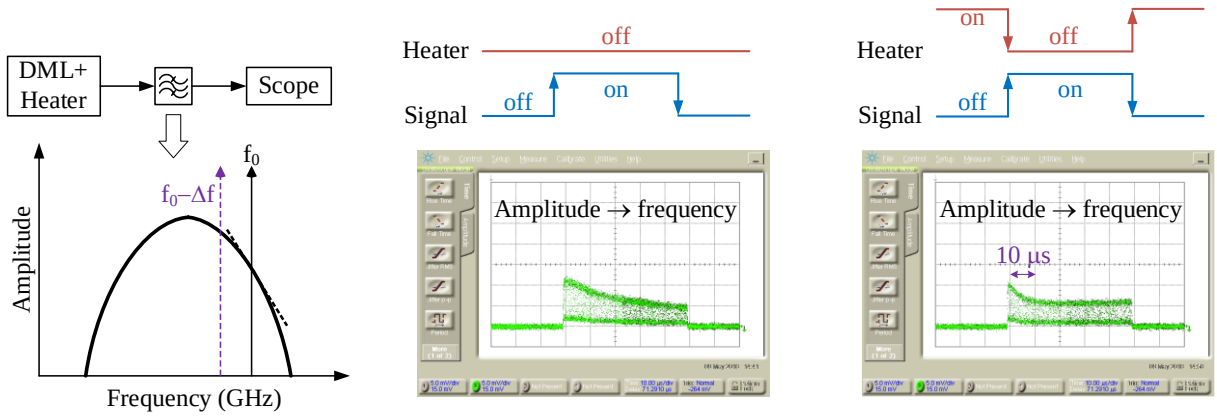
Once the laser is tuned to the desired wavelength, its output power becomes constant (stable emission) so that a flat response is observed in the oscilloscope as shown in Fig. 1.4 (b). After a fast tuning is achieved by using the integrated heater, a thermoelectric controller (TEC) can slowly take over (the TEC has a lower response time than the integrated heater), keeping the DML's operating temperature constant [19]. In this experiment, a constant DC current of 80 mA is applied to the laser whereas the heater current is varied between 0 mA and 220 mA ($\Delta T \approx 24$°C)—a higher heater current is required for a wider tuning range. Using this configuration, a tuning time of ~13 ms is achieved to tune the laser from 1532 nm to 1534.4 nm (2.4 nm range, equivalent to 4×100 GHz) as shown in Fig. 1.4 (b). This satisfies the recommended maximum tuning time of 25 ms for Class 2 applications in TWDM-PON for a 400-GHz spectral range (e.g., see Table 9-2 of [8]).

However, the heater alone consumes ~330 mW electrical power (220 mA × 1.5 V) to cover the four 100-GHz-spaced channels. Even this level of power consumption is achieved by applying several optimizations that improved the heater efficiency [19]. Therefore, in addition to the extra power consumption by the heater, thermal tuning complicates the design and driving circuitry of the device and thus increases the component cost.

Burst-Mode Operation of Lasers

When several ONUs share a single wavelength in the upstream direction of a TWDM-PON system, the output power of each ONU is required to be very low when it is not enabled (WNE) in order to minimize crosstalk on neighboring wavelength channels [8]. For example, the maximum WNE output power levels required for a 10-Gb/s symmetric transmission in the downstream and upstream directions are −63.7 dBm and −67.6 dBm, respectively [8]. Several proposed solutions are available in the literature to control the ONU output power. For example, Taguchi *et al*. demonstrated a mechanism for controlling the burst-off output power of a wavelength-tunable laser by reverse biasing an integrated SOA that acts as an optical gate [20].

Burst-mode operation of a wavelength-tunable laser also causes a frequency (wavelength) drift because of thermal variation between burst *on* and *off* states [14]. One possible solution for stabilizing the emission wavelength of a laser operating in burst-mode is to use a counter-heating technique, where the chip is intentionally heated between bursts so that its average temperature remains constant [15][16]. Fig. 1.5 (a) shows a schematic diagram of the experimental setup used to measure the frequency drift on a tunable DML operating under burst-mode transmission with and without counter-heating.



(**a**) (**b**) (**c**)

Fig. 1.5. (**a**) Schematic diagram of experimental setup for measuring emission wavelength of a laser operating in burst-mode, (**b**) measured wavelength (frequency) without counter-heating, and (**c**) with counter-heating.

By aligning the continuous wave (CW) emission wavelength (frequency) of the laser with the edge of a tunable optical filter (30 GHz bandwidth), any frequency drift caused by burst-mode operation

translates to an increase or a decrease in the output frequency. Without applying a counter-heating mechanism, the emission frequency of the laser continuously decreases (wavelength increases) until the burst ends as shown in Fig. 1.5 (b) with the worst-case performance occurring for a burst of 50% duty cycle [14][15]. When counter-heating is applied, the laser wavelength stabilizes within ~10 μs. Except for the transient frequency drift that occurs during this short period, the laser operates normally for the rest of burst transmission. However, this works well only in a system where there is sufficient gap between neighboring channels so that a certain transient frequency drift can be tolerated. Moreover, stabilizing the emission wavelength using counter-heating technique comes at the expense of extra power consumed by the heater and an additional circuitry for driving and controlling it, thereby increasing the component cost.

Another drawback of DMLs is that they exhibit large chirp (as high as +8.0) because they suffer from both adiabatic and transient chirp [18]. Although high-speed DMLs operating at bit rates ≥50 Gb/s have already been demonstrated in the O-band [21][22], the large chirp degrades their transmission performances in the C-band, limiting their usability to short-reach applications.

Therefore, in addition to the complexity associated with wavelength tuning mechanisms of lasers, both thermal and ONU power control mechanisms also increase the complexity of tunable components and increase their power consumptions, ultimately increasing the component cost, but colorless transmitters sidestep the problems associated with tunable transmitters.

In this thesis, we propose reflective EAMs (REAMs) monolithically integrated with semiconductor optical amplifiers (SOAs) as alternative transmitter solutions for low-cost and colorless access network applications, avoiding the need for wavelength tunability. Depending on the positions of the EAM and the SOA along the optical path, two photonic integrated circuit (PIC) configurations can be realized: REAM-SOA or its opposite RSOA-EAM, where the input light sees the EAM before the SOA in the former case and vice versa.

1.3. Proposed Network Architecture

Fig. 1.6 shows a schematic diagram of a WDM-PON system based on array of REAM-SOAs together with a comb-laser and a wavelength multiplexer, representing a multi-channel OLT transmitter for downlink transmission. The principle of operation is as follows: a series of CW optical lines generated by the comb-laser enters port-1 of an external optical circulator and leaves

at port-2, which is connected to an AWG (wavelength multiplexer). The AWG demultiplexes the individual optical lines and sends them to their respective REAM-SOAs. The AWG can also be used to slice wavelengths when a broad source is used instead of a comb-laser [23][24].

Inside each REAM-SOA (see inset of Fig. 1.6), the input light is first amplified by the SOA and then modulated by the EAM in its forward path. The optical carrier is reflected when it hits the rear facet of the PIC (high reflection coated), further modulated by the EAM and reamplified by the SOA in its reverse path. After going through the double modulation and amplification processes, the optical signal is coupled to the output fiber, which is the same fiber used for input coupling. The same AWG that demultiplexed the optical tones now multiplexes the modulated optical signals readied for downlink transmission over a standard single-mode fiber (SMF). The external circulator enables bidirectional transmission over a single fiber. At the receiver side, a second AWG demultiplexes the transmitted signals and sends them to their respective ONUs.

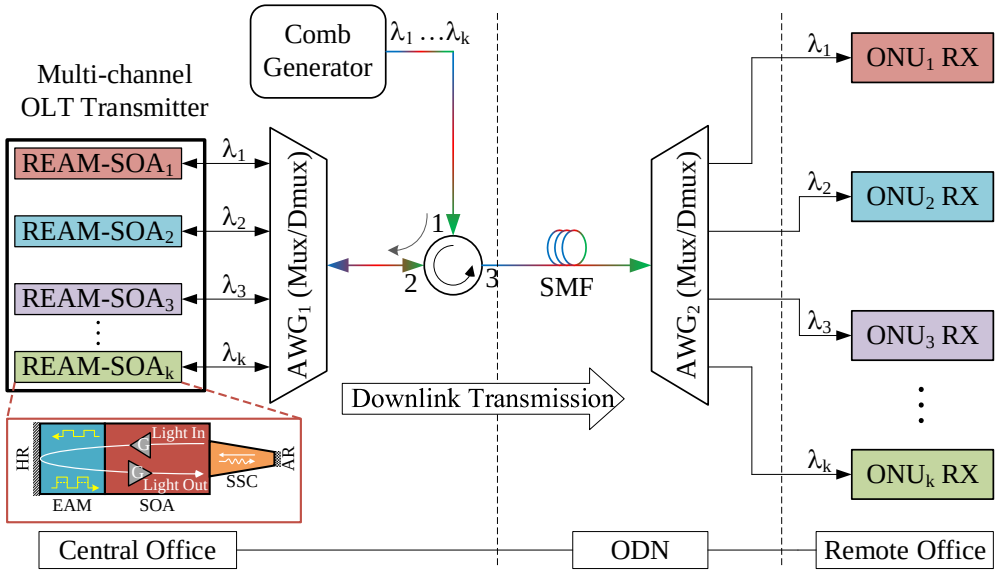


Fig. 1.6. Schematic diagram of a WDM-PON based on array of REAM-SOAs for downlink transmission. Inset: schematic of an REAM-SOA with an integrated spot-size converter.

A similar topology can be built for the uplink transmission by using the REAM-SOAs as ONU transmitters distributed across different sites as illustrated in Fig. 1.7. In this case, a remote seeding scenario can also be realized by placing the comb-laser in the central office close to the OLT and transmitting the CW optical carriers towards the ONUs to be reflected and modulated with uplink information. Moreover, since the OLT receivers exist as arrays in the central office, a pre-amplifier

having wide bandwidth can be inserted in front of the AWG so that the receivers can be realized using low-cost PIN photodiodes with their sensitivities enhanced by the pre-amplifier.

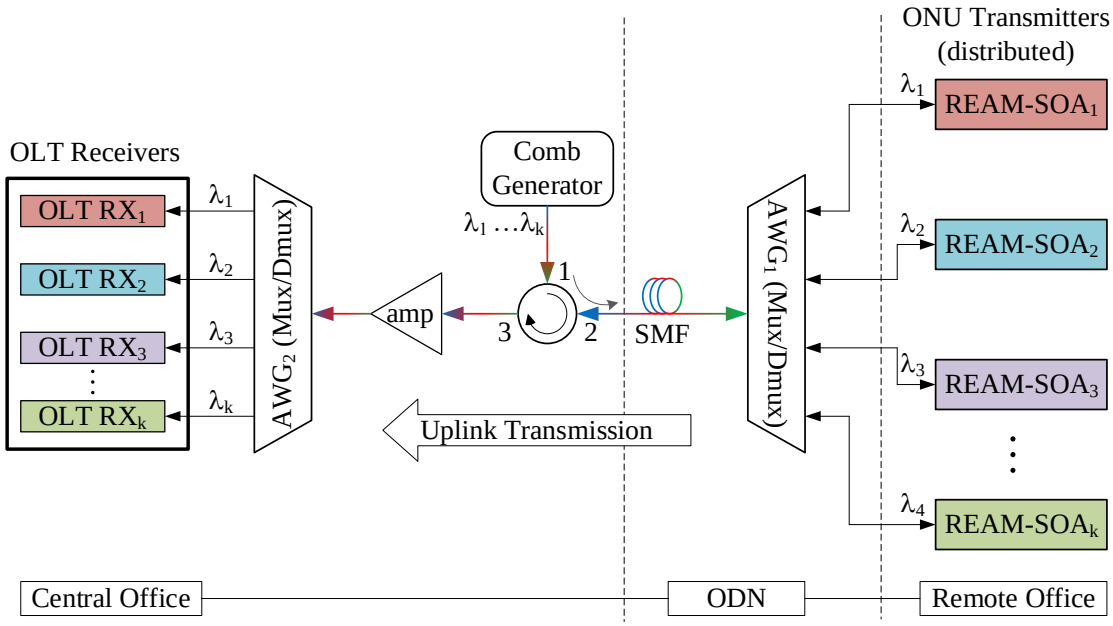


Fig. 1.7. Schematic diagram of a WDM-PON system based on REAM-SOAs as ONU transmitters.

1.4. State-of-the-Art Reflective Devices

Most research activities that dealt with reflective devices in the past focused on realizing components that are compatible with the NG-PON2 standard (10 Gb/s NRZ operation and ≥20 km transmission in the C-band), mainly for the prospect of using the devices as colorless transmitters [25]−[27]. However, because of a relatively high chromatic dispersion in the C-band, there is a tradeoff between data rate and transmission distance. For example, Lawniczuk *et al*. demonstrated a 40-Gb/s NRZ transmission using an REAM-SOA, but the transmission distance at this bit rate was limited to only 2 km at a bit error rate (BER) of 10^{-3} [28]. When operated at 10 Gb/s NRZ, the same device was able to transmit up to 25 km.

Similarly, 25 Gb/s NRZ transmissions have been demonstrated up to 20 km in [24][29]. However, both experimental demonstrations involved equalization techniques that increase the transmitter cost. Fig. 1.8 summarizes state-of-the-art REAM-SOAs showing a plot of data rate versus transmission distance. Several high-capacity transmissions based on arrays of REAM-SOAs have

been demonstrated, for example, with aggregate capacities of 113 Gb/s (10×11.3 Gb/s) [30], 400 Gb/s (40×10 Gb/s) [31], and 800 Gb/s (80×10 Gb/s) [23], all of which utilized 10G transmitters together with broad sources. Such high-density integration of reflective devices is appealing to realize multi-channel OLT transmitters for high-capacity WDM-PON systems and for bandwidth demanding short-reach data center interconnects. Therefore, increasing the achievable data rate per device is an important element to realize cost-effective transmitters for the next generation of high-speed access networks.

In this work, we demonstrate up to 16 km colorless transmission with a single-channel capacity of 25 Gb/s NRZ in the C-band [32] and up to 10 km unamplified transmission in the O-band [34]. We also show results operating the O-band device at 50 Gb/s using NRZ as well as PAM-4 modulation formats in a back-to-back (BtB) connectivity without equalization [34]. As a proof-of-concept, we also demonstrate a 1.2-m wireless V-band transmission followed by a 3-km SMF intermediate-frequency-over-fiber (IFoF) transmission at an aggregate bit rate of 10 Gb/s, which is obtained by multiplexing four 16-QAM signals (QAM: quadrature amplitude modulation) [35].

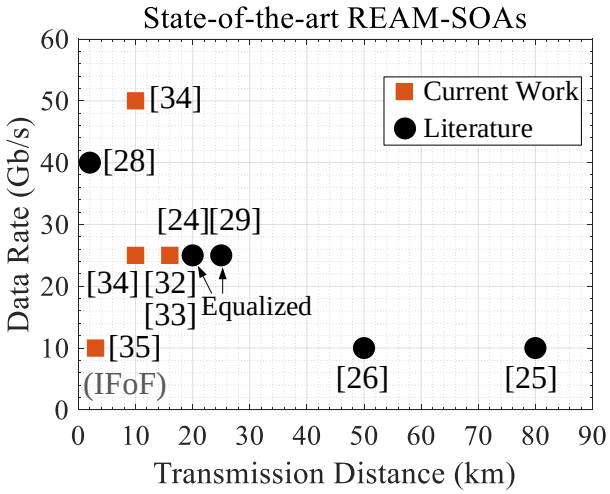


Fig. 1.8. State-of-the-art of REAM-SOAs based on NRZ modulation format ([35] is based on 16-QAM ARoF).

1.5. Context of the PhD

The objective of this PhD is to develop novel optoelectronic devices that can be used as low-cost transceivers in DWDM or even UDWDM PON systems, with a focus on 5G fronthauling, within

the context of the 5GSTEP-FWD[1] project. However, the devices can also find several application areas such as high-speed PONs and data centers. The goal is to realize those devices and demonstrate their operational capabilities in test beds representing practical systems. An important element in minimizing component cost is to realize the devices using robust and industrially compatible technologies so that they can be mass-produced for large-scale deployments. For that reason, our components leverage semi-insulating buried heterostructure (SI-BH) waveguide technology and butt-joint integration technique, both of which are compatible with indium phosphide (InP) semiconductor technology, which is mature and widely used technology for realizing active semiconductor devices.

Some of the key requirements of optical transceivers for PON applications are high power budget, high-speed operation, high device linearity, multi-wavelength or wavelength-independent (colorless) operation, less sensitivity to polarization state of light, low amplifier noise figure, low energy consumption, and minimal device footprint. The power budget depends on the average modulated output power of the transmitter (launch power), ODN losses (e.g., fiber attenuation, splitting, and connector losses), and receiver sensitivity. High-speed operation, on the other hand, depends on the types of modulators and receivers used in the system. For multi-wavelength operation, either tunable or colorless devices can be used but the former require complex device design and control circuitry as discussed above.

In this work, we propose a transmitter solution based on monolithically integrated reflective EAM-SOAs. The main technical advantage of an REAM-SOA is that it can be used as a colorless transmitter with minimal control requirements, enabling interchangeable network equipment, which minimizes the amount of network (wavelength) planning required by operators, reduces installation and inventory costs as well as operation and maintenance costs. Details of the device design and the structural differences between REAM-SOA and RSOA-EAM configurations are discussed in Chapter 2. Since the two PIC configurations have similar operating principles, the REAM-SOA configuration will be used for most of the discussions in this manuscript.

[1] 5GSTEP FWD (acronym for 5G System Technological Enhancements Provided by Fiber Wireless Deployments) is European Union's Horizon2020 innovative training network (ITN) project under grant agreement number 722429.

A reflective EAM-SOA can be used as an array (e.g., at the OLT side) or as a single transmitter element (e.g., at the ONU side), and some of its advantages are:

- Wavelength-independent (colorless) operation (avoids the need for tunability), which can have a significant impact on capital and operational expenses (CAPEX and OPEX).
- Large extinction ratio due to double absorption of light by the EAM section that occurs before and after reflection of the incident light.
- Low (or even negative) chirp, which is the primary advantages of EAMs over DMLs that allows the former to transmit relatively longer distances over a standard SMF in the C-band at bit rates beyond 10 Gb/s.
- The EAM section can be independently optimized in order to achieve very high electro-optic (E/O) bandwidth for high-speed applications without compromising the achievable extinction ratio.
- The possibility of using the REAM-SOA PIC for triple functionalities: as a transmitter, a PIN receiver, and for signal regeneration [36].
- The RSOA-EAM configuration can be used to perform bidirectional transmission using a single wavelength at the ONU side (wavelength reuse scheme), which can be achieved by splitting the downstream signal and feeding a portion of it to the RSOA-EAM (the other part goes to the ONU receiver), erasing the modulation by saturating the SOA section, and remodulating the CW optical carrier with uplink information by the EAM section [37][38].
- The devices are suitable for dense WDM integration as they require simpler driving circuitry compared to tunable devices, and they are less sensitive to thermal variations.
- The back facet of reflective devices can be used for running bonding wires, which avoids the need for complex bonding techniques such as flip-chip bonding.
- By monolithically integrating an SOA with the EAM, insertion loss of the PIC can be fully compensated, or even net device gain can be achieved through proper optimization.

The main drawback of an REAM-SOA is that it needs an external optical source. However, a multi-wavelength fixed source such as a comb-laser or a broad source can be shared by multiple

ONUs, distributing the extra cost among different remote sites. Moreover, expensive optical equipment such as the comb-laser can be centralized in order to further reduce the system cost. As such, the CW optical carriers can be generated by a comb-laser located in the central office and sent to the remote offices, realizing a remote seeding scenario [23][24]. At the ONU side, the CW light from the CO is reflected, modulated by the EAM, amplified by the SOA, and transmitted back to the OLT at the CO, realizing a sourceless and colorless ONU.

Another drawback of an REAM-SOA is that both the EAM and the SOA sections can be sensitive to polarization state of the input light, which is the case for the devices studied in this thesis. Our components are more sensitive to transverse electric (TE) polarized light than transverse magnetic (TM) polarized light, which is due to the fact that compressive strained quantum-well layers that favor TE polarization are used in their active regions. But the polarization dependence can be minimized by proper choice of material compositions so that the amount of strain applied to the epitaxially grown thin layers is reduced or even compensated by using a combination of compressive and tensile strained quantum wells (e.g., see Section 2.3.3).

In this work, we analyze the building blocks separately as well as in integrated circuits in order to achieve optimal operating conditions and satisfy different requirements of PON systems. The three building blocks in our PICs are an EAM, an SOA and a spot-size converter (SSC). The requirement for the SSC is to provide minimal tapering, insertion and coupling losses. Moreover, it is also required to minimize optical feedback to the SOA gain section. On the EAM side, the key requirements are high dynamic extinction ratio, large E/O bandwidth for high-speed applications, and low driving voltage to minimize energy consumption as well as to be compatible with complementary metal-oxide-semiconductor (CMOS) technology and thus be able to integrate low-cost driver circuits with the PICs. Similarly, the main requirements for the SOA section are high amplifier gain (to improve the system power budget), low amplifier noise figure (NF), high saturation output power, and low-current operation.

The devices presented in this manuscript are based on a continuous mastering of device design, technological aspects, and fabrication processes for realizing high-performance optoelectronic devices at III-V Lab. The main contribution of this PhD is a complete performance analysis of the PICs at component level and using the devices at system levels, demonstrating their operational capabilities. Moreover, results obtained from optical simulation of SI-BH waveguides and

quantum simulation of MQW structures can be used as inputs in the designs of the next generation of devices so as to improve their performances. The simulation results can also be used to relate experimental data to theory and validate the designs as well as any assumptions made during their theoretical treatments. Another contribution is the mask layout of the SSC section using Nazca Design[2] based on parametric cell (PCell) design approach as part of an going activity to build component library.

The following chapters present the designs and performances of the devices, and the chapters are organized as follows: Chapter 2 presents the designs of the devices, technologies applied for their realization and relevant theories. We also show numerical simulation results regarding optical properties of our SI-BH waveguides obtained using FIMMWAVE[3], and electrooptic properties of multiple quantum well (MQW) structures that make up the active regions of our components obtained using *nextnano*[4]. At the end of Chapter 2, we also present mask layouts of our PICs. Chapter 3 presents a complete performance analysis of the devices using different PIC configurations, including a comparison of simulation and measurement results for the taper section. Chapter 4 presents system-level performances of our components based on transmission experiments using both digital and analog modulation formats as proofs-of-concepts, demonstrating the capabilities of our components under different operating conditions. At each stage, we indicate various design and operational tradeoffs and analyze their impacts on device performances. The fifth chapter presents concluding remarks and perspectives for future works.

[2] Nazca is an open-source, Python-based design (scripting) tool for preparing mask layouts.
[3] FIMMWAVE is a suit of 2D+Z waveguide mode solvers by PhotonDesign.
[4] Nextnano is a quantum solver for simulating MQWs by solving Poisson-Schrödinger equations self-consistently.

Chapter 2

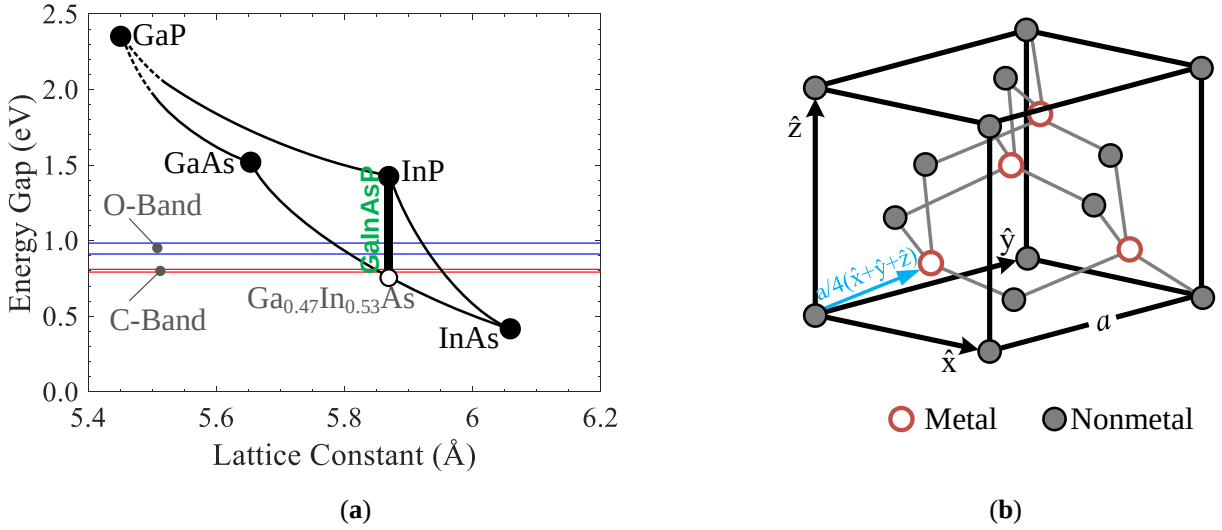
2. Device Design and Technology

This chapter presents the design of our components and the technologies applied to realize them together with some relevant theories and simulation results to show different design aspects that need to be taken into consideration. The first section presents the material system used for realizing our photonic integrated circuits (PICs). Then, the vertical designs of the devices followed by different features of multiple quantum well (MQW) structures such as quantum confinement, strain and its effect on the electronic band structure of a semiconductor material are presented in Sections 2.2 to 2.4. Sections 2.5 to 2.7 present overview of absorption coefficient of an electroabsorption modulator (EAM), polarization sensitivity, and electroabsorption effects based on quantum confined Stark effect (QCSE). Section 2.8 highlights the main characteristics of a semiconductor optical amplifier (SOA). Section 2.9 presents the fabrication process flow highlighting different epitaxial growth steps. Different waveguide technologies are presented in Section 2.10, including semi-insulating buried heterostructure (SI-BH), which is the one used in our PICs. Section 2.11 presents the structures of our devices with their schematics illustrating the two PIC configurations studied in this thesis: reflective EAM-SOA (REAM-SOA) or its opposite RSOA-EAM. Finally, Section 2.12 presents the mask layout of our integrated circuits before concluding the chapter.

2.1. Material System

Semiconductors based on III-V materials (compounds consisting of elements from groups III and V of the periodic table) are commonly used for realizing optoelectronic devices for telecom applications. Among those materials, GaInAsP grown on InP substrate is a material of choice for long distance optical transmissions mainly for two reasons: (i) GaInAsP has a direct bandgap, (ii) it provides a wide range of bandgaps between 1.0 μm and 1.6 μm, which is the region where silica fiber has minimum dispersion (1.3 μm window, O-band) and loss (1.55 μm window, C-band) [39]. Our components are based on compressive strained GaInAsP/InP MQWs and are realized using SI-BH waveguide and butt-integration technologies.

Fig. 2.1 (a) shows the bandgaps of binary constituents of GaInAsP as a function of lattice constant (distance between adjacent atoms) at 0K [39]. The binary compounds are GaAs, InAs, GaP, and InP. With the exception of GaP, which has an indirect bandgap as shown with dashed lines in Fig. 2.1 (a), the other three binaries have direct bandgaps (solid lines). However, all of them have a zincblende crystal structure formed by two interpenetrating face-centered-cubic lattices that are separated by a quarter of the lattice constant *a* as illustrated in Fig. 2.1 (b) [40].



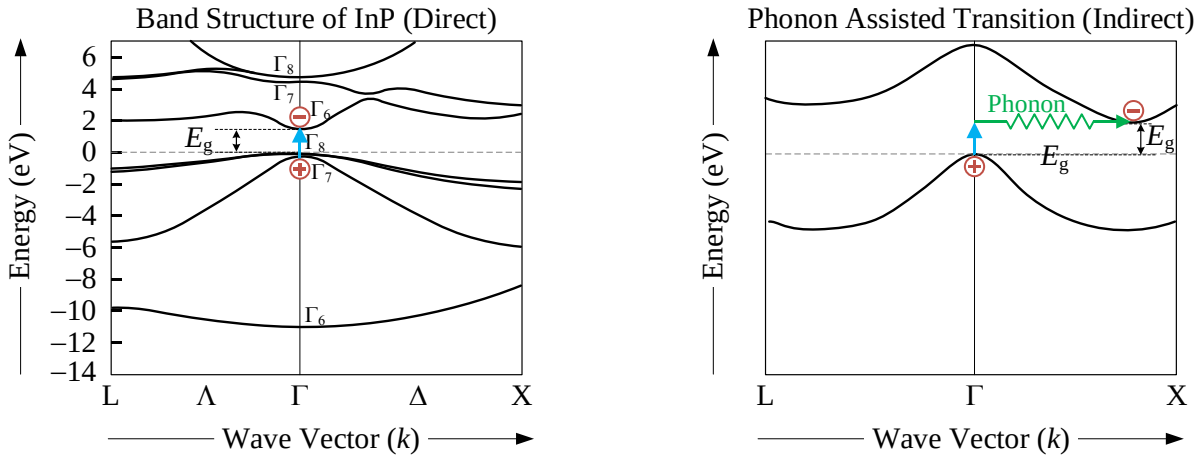
(**a**) (**b**)

Fig. 2.1. (**a**) Bandgaps of constituent binaries of GaInAsP as a function of lattice constant (after [39]), (**b**) zincblende crystal structure (after [40]).

For direct bandgap materials, the valence band (VB) and the conduction band (CB) minima occur at the same point in an energy-wave vector (*E*-*k*) space at the center of the Brillouin zone ($k = 0$, also known as the Γ point) as illustrated in Fig. 2.2. (a), for example, for InP [41]. As a result, vertical electronic transitions (from VB to CB for absorption and CB to VB for emission) occur in direct bandgap materials whereas phonon assisted transition occurs in indirect bandgap materials as illustrated in Fig. 2.2 (b), reducing the transition efficiency in the latter case. For that reason, direct bandgap materials are widely exploited to realize optoelectronic devices for telecom applications such as lasers, modulators, detectors, and amplifiers.

The relationship between the bandgap (E_g) of a given material system and its atomic transition wavelength (λ) is given by: $E_g = hc/\lambda \approx 1.24/\lambda_{\mu m}$ [eV], where *h* is Planck's constant, *c* is speed of light in vacuum, and $\lambda_{\mu m}$ is the transition wavelength in micrometers. The bandgap of

$Ga_xIn_{1-x}As_yP_{1-y}$ can be engineered by modifying compositions of the constituent binaries and thus devices operating in either of the two key telecom spectral ranges, the O-band (1260−1360 nm) or the C-band (1530−1565 nm), can be realized using the same material system (x and y are mole fractions of group III and V materials, respectively).



(**a**) (**b**)

Fig. 2.2. (**a**) Band structure of InP in the Brillouin zone centered at the Γ point ($k = 0$) (after [41]), (**b**) illustration of phonon assisted electronic transition in indirect bandgap materials.

High-performance optoelectronic devices can be realized by epitaxially growing thin layers of GaInAsP on an InP substrate. In order to grow high quality crystals on a relatively thick substrate, the lattice constant of the epitaxial layer can be matched to that of InP, which is achieved by properly controlling alloy compositions of the constituent binary materials. For ternary and quaternary alloys, their lattice constants can be calculated using Vegard's law, which is based on a linear interpolation (weighted average) of lattice constants of their binaries. For example, the lattice constant $a(x,y)$ of $Ga_xIn_{1-x}As_yP_{1-y}$ can be obtained as [42][43]:

$$a(x,y) = xya(\text{GaAs}) + x(1-y)a(\text{GaP}) + (1-x)ya(\text{InAs}) + (1-x)(1-y)a(\text{InP}), \qquad (2.1)$$

where, a(GaAs), a(GaP), a(InAs), and a(InP) are respective lattice constants of the binaries.

For GaInAsP lattice-matched to InP, $a(x,y)$ of (2.1) equates to a(InP), providing a simple matching condition expressed in terms of the mole fractions as: $x \approx 0.47y$ [42]. The thick vertical line in Fig. 2.1 (a) represents the matching condition for GaInAsP, and its lowest point (open circle) is obtained for $y = 1$, which results in $Ga_{0.7}In_{0.53}As$. For practical applications, where the quantum

well thickness is several nanometers (up to ~20 nm, below critical thickness), a lattice mismatch of ~1% is acceptable, which results in strain (compressive or tensile) on the epitaxial layers [18][39]. Strain is exploited in tailoring different characteristics of optoelectronic devices (e.g., polarization sensitivity, modulation speed of EAMs, and threshold currents of SOAs and lasers).

Although linear interpolation using Vegard's law works for calculating lattice constants of ternary and quaternary materials, it does not necessarily hold true for other parameters such as bandgap energy, lattice thermal conductivity, and effective masses [44][45]. In that case, a nonlinear factor called 'bowing parameter' is introduced for correction [44]−[46]. Its value is typically positive for III-V compounds, meaning that the actual bandgap of an alloy is less than the one that can be obtained by applying Vegard's law [39], which is the reason why the lines connecting the binaries in Fig. 2.1 (a) are slightly bent towards the lower end of the *y*-axis. For a ternary material *T* of the form AB_xC_{1-x}, its nonlinear parameters that go beyond Vegard's law (e.g., bandgap E_g) can be approximated to a quadratic function as [44][45]:

$$T_{ABC}(x) = xB_{AB} + (1-x)B_{AC} + x(1-x)C_{ABC}, \tag{2.2}$$

where, T_{ABC} is the ternary material's nonlinear parameter, B_{AB} and B_{AC} are the corresponding parameters of binaries *AB* and *AC*, and C_{ABC} is the bowing parameter.

Accordingly, nonlinear parameters of a quaternary alloy *Q* of the form $A_xB_{1-x}C_yD_{1-y}$ can be obtained from the parameters of the constituent binaries and ternaries as [44][45]:

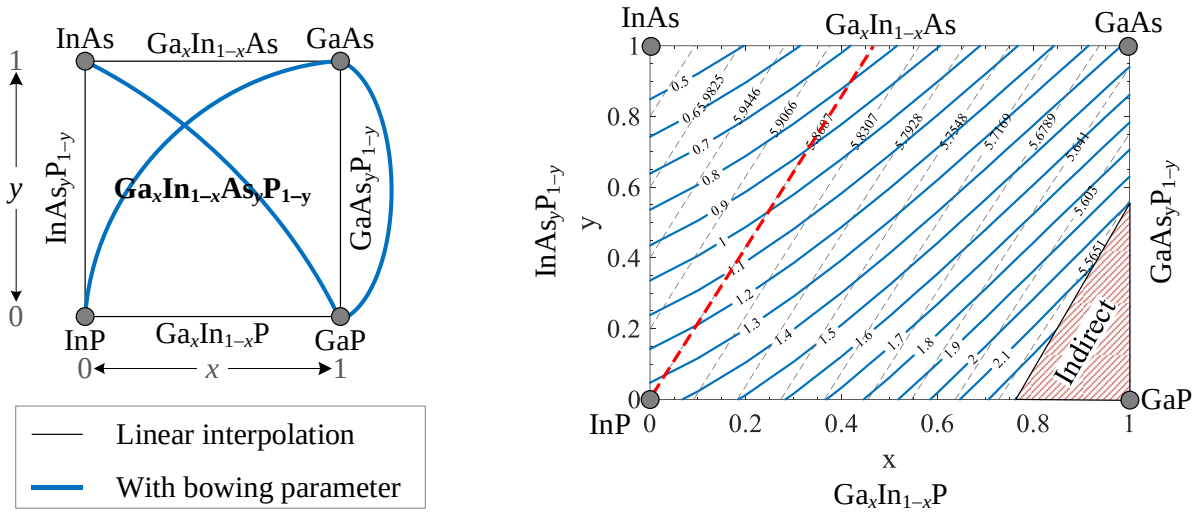
$$Q(x,y) = \frac{x(1-x)[yT_{ABC}(x) + (1-y)T_{ABD}(x)] + y(1-y)[xT_{ACD}(y) + (1-x)T_{BCD}(y)]}{x(1-x) + y(1-y)}. \tag{2.3}$$

In most analytical systems, a constant bowing parameter is used, which can be extracted by fitting experimental data to functions. In numerical simulations, however, a more complex approach is employed (e.g., by using a bowing parameter that depends on alloy compositions). For example, up to thirteen parameters are used in *nextnano*[5] for calculating the bandgap of a quaternary of the form $A_xB_{1-x}C_yD_{1-y}$ [47]−[49].

Fig. 2.3 (a) illustrates the effect of bowing parameter on the bandgap of $Ga_xIn_{1-x}As_yP_{1-y}$, which also applies to any quaternary of a similar form. The borders are defined by the binary materials

[5] Nextnano is a quantum solver software used for simulating electronic and optoelectronic devices, for example, to solve the Schrödinger-Poisson equations self-consistently.

and the lines connecting them are the ternaries, with straight lines representing linear interpolation whereas the curved lines are when bowing parameter is included.



(**a**) (**b**)

Fig. 2.3. (**a**) Schematic illustration of bandgaps with and without bowing parameter for GaInAsP (after [47]) [straight lines: linear interpolation, curved lines: with bowing parameter), (**b**) composition diagram of GaInAsP [solid lines: bandgap energies in eV, dashed lines: lattice constants in Å, hatched region: GaInAsP becomes indirect bandgap].

For analytical purposes, generalized interpolation formulas available in the literature can be used to estimate the bandgap as well as lattice constants of quaternaries, which typically are generated by fitting experimental data to functions. For example, for $Ga_xIn_{1-x}As_yP_{1-y}$, the bandgap at room temperature can be expressed in terms of alloy compositions x and y as [50]:

$$E_g(x, y) = 1.35 + 0.668x - 1.068y + 0.758x^2 + 0.078y^2 - 0.069xy - 0.322x^2y + 0.03xy^2. \quad (2.4)$$

Similarly, its lattice constant is approximated as [50]:

$$a(x, y) = 5.8688 - 0.4176x + 0.1896y + 0.0125xy. \quad (2.5)$$

Fig. 2.3 (b) shows composition diagram of GaInAsP calculated using (2.4) and (2.5). The solid lines represent bandgaps in electronvolt (eV), and the dashed lines are lattice constants in angstrom (Å). The thick dashed line (red color) represents the lattice-matching condition for GaInAsP to an InP substrate, and the hatched region on the right-hand side of the figure is the region where GaInAsP becomes an indirect bandgap material (i.e., the composition of GaP dominates).

Apart from GaInAsP, GaInAlAs is also widely exploited for the realization of thermally efficient, high-speed optoelectronic devices [39]. However, the presence of aluminum complicates the fabrication process because of its susceptibility to surface oxidation when exposed to air, which is an important issue for buried heterostructures utilizing butt-joint integration technique [18].

2.2. Vertical Device Design

Our components are based on GaInAsP MQWs grown on an *n*-doped InP substrate using gas-source molecular beam epitaxy (GS-MBE) [51]. The selection of the material system (e.g., GaInAsP/InP), the vertical structure (e.g., MQW active region), and the fabrication process are based on continued efforts by III-V Lab to realize high-performance semiconductor devices with a wide range of applications [28][51][52]. Details of the fabrication process flow and different waveguide technologies are discussed in Sections 2.9 and 2.10. For most of the discussions concerning the vertical designs of our components, the EAM's MQW structure is used since the other building blocks, namely the SOA and the spot-size converter (SSC), have similar structures.

Fig. 2.4 shows a schematic diagram of the EAM's MQW structure (vertical design). First, an n-doped buffer layer is grown on top of the InP substrate in order to minimize strain and dislocation (defects) when the relatively thin quantum well (QW) layers are grown in the following steps. Another important role of the buffer layer is to control free-carrier absorption as it is possible to control its doping level in contrary to that of the n-doped InP substrate. Following the buffer layer, an undoped GaInAsP separate confinement heterostructure (SCH) layer is grown for enhanced photon confinement. The SCH layer has an intermediate refractive index between that of the buffer layer and the QW layers as illustrated on the left-hand side of Fig. 2.4. On top of the SCH layer, alternating thin layers of GaInAsP wells and barriers are grown, defining the MQW active region. Then, a second SCH layer is grown on top of the MQW stack, embedding the active region inside SCH layers along the growth axis. The MQW structure is terminated by the growth of a p-doped InP layer (spacer or top p-InP), which has the advantage of protecting the active region from oxidation and unintentional etching during the subsequent etching and regrowth steps. Finally, a p-doped InP cladding layer is grown on top of the entire wafer, which is followed by the growth of a strongly p-doped ternary layer (p+ GaInAs) to form p-contacts of the active sections (EAM and SOA), and metallization to make them ohmic contacts.

The MQW active regions for EAMs and the gain section typically differ for the number of QWs as well as thicknesses of barrier, well, and SCH layers. For EAMs, the QWs are designed to obtain higher transition energies with respect to integrated gain sections (blue shift). Although a reasonable number of QW layers are required in each section, fewer QW layers are typically used in the gain section in order to minimize early saturation effects by reducing the optical confinement factor, which depends on the number of QW layers. Limiting the number of QW layers in the gain section also allows having efficient and homogeneous carrier injection across the MQW stack.

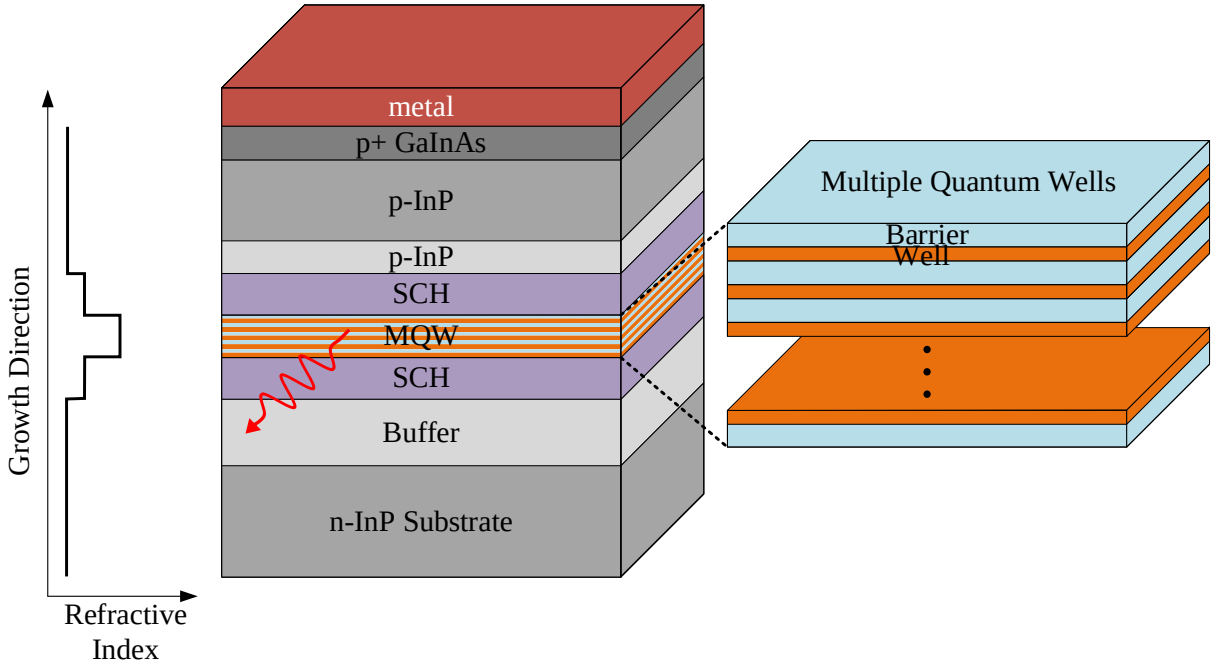


Fig. 2.4. Schematic diagram of multiple quantum well structure based on separate carrier confining heterostructures. Inset: schematic of refractive indices of the epitaxial layers (left) and enhanced view the MQW stack (right).

In our components, one less QW layer is used in the SOA section with respect to the EAM. Although using the same number of QW layers in the two sections allows growing them in a single epitaxy step, which reduces the fabrication time of the PIC, the fact that the SOA's gain peak will be close to the absorption edge of the EAM (strong absorption) reduces the modulated output power when the two components are integrated on a single chip. For that reason, the SOA's gain peak is positively detuned (in wavelength) from the absorption edge of the EAM.

On the other hand, the same MQW stack is used for both the EAM and the SSC sections, where the latter is a bent tapered waveguide used to improve the input/out coupling efficiency. As a result,

the two sections (EAM and SSC) are grown in a single epitaxy step. The main source of internal loss in a GaInAsP/InP heterostructure is intervalence band absorption between the GaInAsP active region and the p-doped InP cladding layers, which is ~20 times higher than that of the n-InP layer in the C-band (relatively weaker in the O-band: 14×) [18][53]. For that reason, an optimized cladding layer is used for the SSC section so as to minimize its insertion loss (intrinsic absorption), which is slightly different from that of the EAM and the SOA sections.

In this thesis, we studied different PIC configurations based on three modulator lengths: 80-µm and 150-µm long EAMs in the C-band, and 100-µm long EAM in the O-band. Table 2.1 and Table 2.2 summarize details of the epitaxial layers of the C- and O-band EAMs, respectively. The parameters in Table 2.1 are used to obtain the simulation results presented later in this chapter. A complete performance analyses of the devices are presented in Chapter 3.

Table 2.1. Design parameters for the C-band EAMs.

Type/Layer	**Composition**	**Thickness (nm)**	**Doping (cm^3)**	**Refractive Index**
Top InP	InP	180	p: 7×10^{17}	3.162
SCH (top/bottom)	GaInAsP	30	Undoped	3.327
MQW	GaInAsP	129	Undoped	3.460
Buffer	InP	700	n: 1×10^{18}	3.161

Table 2.2. Design parameters for O-band EAMs.

Type/Layer	**Composition**	**Thickness (nm)**	**Doping (cm^{-3})**	**Refractive Index**
Top InP	InP	100	p: 1×10^{18}	3.2062
SCH (top/bottom)	GaInAsP	30	Undoped	3.2920
MQW	GaInAsP	149	Undoped	3.4600
Buffer	InP	100	n: 1×10^{18}	3.2052

2.3. Multiple Quantum Wells

The bandgap of $Ga_xIn_{1-x}As_yP_{1-y}$ can be engineered by varying the mole fractions of its binary constituents and thus a heterostructure can be formed by growing a thin layer of narrower-bandgap GaInAsP (well) of thickness *d* sandwiched between a wider-bandgap GaInAsP (barrier) as illustrated in Fig. 2.5 for a single QW layer surrounded by two barrier layers.

There are two types of heterostructures depending on whether the bandgap of the QW is completely nestled within that of the barrier (type-I) or not (type-II) [54]. Our MQW structures are based on the former type, where a series of narrower-bandgap GaInAsP wells are surrounded by wider-bandgap GaInAsP barriers. In type-I heterostructures, electrons and holes are confined

within the same semiconductor layer (inside the well), which is desirable for efficient absorption or emission. In type-II materials, on the other hand, the electrons and the holes are confined in different layers of the heterostructure.

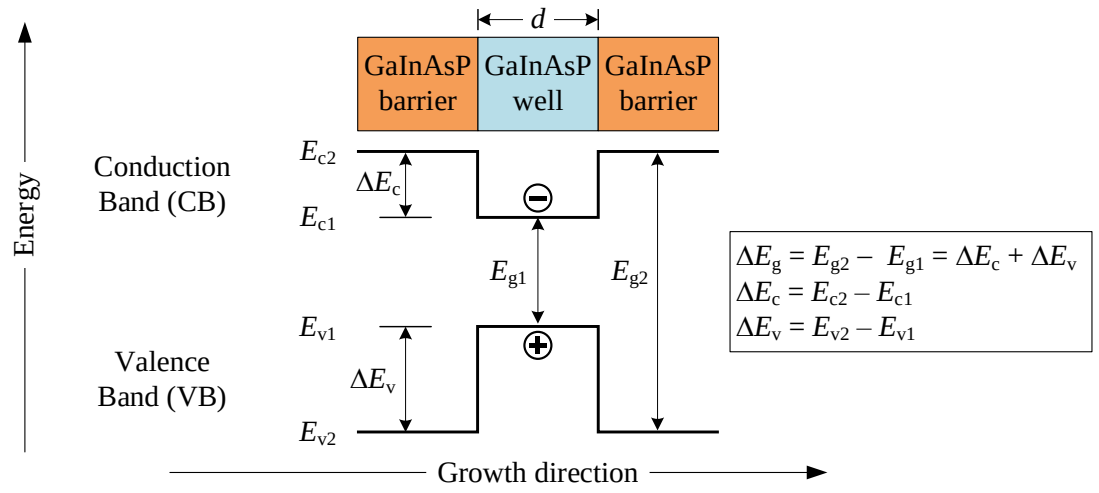


Fig. 2.5. Schematic diagram of a GaInAsP quantum-well and its bandgap profile.

MQW structures are formed by epitaxially growing a series of alternating potential wells and barriers. By using thin QW layers, the movement of electrons and holes can be limited along the growth axis (*z* axis) while they still are free to move in the growth plane (*x* and *y* axes), creating a 'quantum confinement' phenomenon in the transverse direction. MQWs are widely exploited to realize high-performance optoelectronic devices because they exhibit step-like density of states and high electroabsorption efficiency at a given bias voltage compared to their bulk counterparts [40]. The step-like density of states of MQWs allows realizing lasers and amplifiers with low threshold current and improved thermal stability whereas the high electroabsorption efficiency enables the realization of high-speed EAMs with low driving voltage [55].

In order to achieve quantum confinement along the growth axis, the thickness of the QW layer must be less than the de Broglie wavelength of electrons and holes, which is given by [56]:

$$\lambda_{\mathrm{deB}} = \frac{h}{p} \approx \frac{h}{\sqrt{mK_BT}}, \tag{2.6}$$

where, h is Planck's constant, p is momentum, m is particle mass, K_B is Boltzmann's constant, and T is temperature.

For typical III-V semiconductors used in optoelectronic devices, this requires a well thickness in the order of ~10 nm at room temperature [56]. The confinement of electrons and holes is achieved through bandgap discontinuity, which is the bandgap difference between the potential barrier and well ($\Delta E_g = E_{g2} - E_{g1}$) as shown earlier in Fig. 2.5. The distribution of the bandgap discontinuity in the conduction and valence bands depends on the actual material system, and it is an important design parameter as it plays a key role in determining device performances. For example, a GaInAsP/InP MQW system provides a valence band offset (VBO, ΔE_v) of $\sim 0.6\Delta E_g$ and a conduction band offset (CBO, ΔE_c) of $\sim 0.4\Delta E_g$ ($\Delta E_g = \Delta E_c + \Delta E_v$) [18]. In other words, electrons in the CB see a barrier height of $0.4\Delta E_g$ whereas holes in the VB see a barrier height of $0.6\Delta E_g$.

The optimization of bandgap discontinuity plays a key role in determining the performances of semiconductor devices. For example, thermal stability of optical sources (e.g., lasers and SOAs) depends on the CBO because electrons, having a relatively lower effective mass, require large binding energies (higher barrier offsets), which otherwise can easily escape the QW region when the devices operate at high temperatures [39]. On the other hand, the saturation characteristics of an EAM heavily depends on the VBO. When an EAM operates under high power condition, photogenerated holes, having a relatively higher mass than electrons, begin to accumulate in the VB of the QW (hole pile-up), increasing the hole sweepout time, which ultimately leads to a dampening of the EAM's dynamic response [57]. Moreover, because of a longer hole sweepout time, the densities of electrons and holes inside the QW region become different, causing space charge screening effect, which distorts the distribution of an externally applied electric field and thus lowers the dynamic extinction ratio (DER) of an EAM that can be achieved at a given applied field (reverse bias voltage) [57][58].

Material systems that provide large CBO are generally desirable for high-temperature operation of lasers/SOAs whereas materials with lower VBO are desired for high-speed operation of EAMs. However, a relatively strong confinement is still required in the latter case in order to have a stronger excitonic absorption, which is a key feature of EAMs based on MQW active regions. Under reverse bias condition, escaping of electrons from the QW region can still be efficient with high CBO but the high VBO limits the saturation input power of EAMs.

On the other hand, GaInAlAs/InP MQWs provide a large CBO of $\sim 0.7\Delta E_g$. As a result, aluminum-based devices show superior thermal as well as modulation speed performances

compared to their phosphorous counterparts, and they are widely studied to realize devices for uncooled or semi-cooled operations [39][59]. However, the presence of aluminum complicates the fabrication process as it is susceptible to surface oxidation, making GaInAlAs/InP MQW incompatible with multi-step butt-joint integration technique where the MQW structure is exposed to air during different etching and regrowth processes. Most devices that are realized using GaInAlAs/InP MQWs so far are fabricated using selective area growth (SAG) [18][52]. Fig. 2.6 schematically illustrates electronic band structures of the two material systems: GaInAsP (left) and GaInAlAs (right).

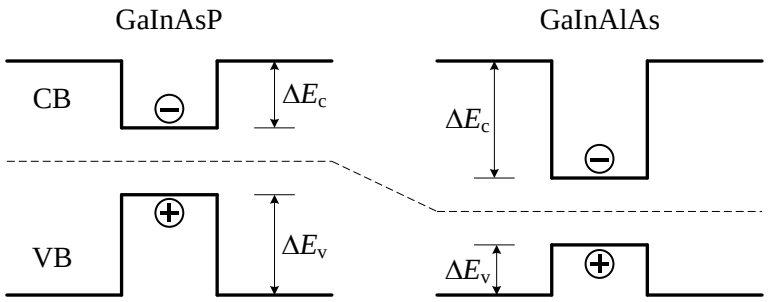


Fig. 2.6. Schematic illustration of electronic band profiles of GaInAsP (left) and GaInAlAs (right) MQWs.

A common approach for improving the high-speed performances of phosphorous-based semiconductors is to use compressive strained QWs, which reduces the VBO and thus reduces the hole sweepout time. Another possibility to improve the thermal efficiency of devices within the GaInAsP domain is to increase the bandgap of the barrier region, which then increases the CBO. However, increasing the barrier bandgap also increases the VBO, which is not desirable for the EAM section. In some cases, a combination of the two material systems is exploited, for example, using compressive strained GaInAsP wells and tensile strained GaInAlAs barriers, which results in a CBO of $\sim 0.8\Delta E_g$ [18]. Apart from increasing the CBO, using tensile strained QWs also helps to minimize polarization dependence of optoelectronic devices [60].

In summary, the confinement of electrons and holes in the transverse direction has three important consequences: (i) electron and hole confinement energies shift the bandgap to higher energies with respect to the band edges of bulk materials, providing additional flexibility to bandgap engineering, (ii) within a given confined state, density of states become independent of carrier energy, and (iii)

the existence of electrons and holes close to one another results in high electron-hole binding energy, which leads to the formation of strong excitonic effects at room temperature [56].

2.3.1. Quantization of Energy

The conduction (valence) band discontinuity can be represented by a one-dimensional finite potential (V_0) as illustrated in Fig. 2.7, for example, for an electron in the CB of a QW of thickness d, centered at $z = 0$ along the growth axis ($V_0 = \Delta E_c$ for the CB and $V_0 = \Delta E_v$ for the VB). Allowed energy levels that electrons and holes can occupy within the QW can be obtained by solving the time-independent Schrödinger equation, which is given by [54]:

$$-\frac{\hbar^2}{2m^*}\frac{\partial^2}{\partial z^2}\psi(z) + V(z)\psi(z) = E\psi(z). \tag{2.7}$$

where, $\hbar$ is reduced Planck constant ($\hbar = h/2\pi$), m^* is effective mass of electron (hole) inside the QW region, $V(z)$ is the confinement potential along the growth axis, $\psi(z)$ is the electron (hole) wave function, and E is total energy of the particle.

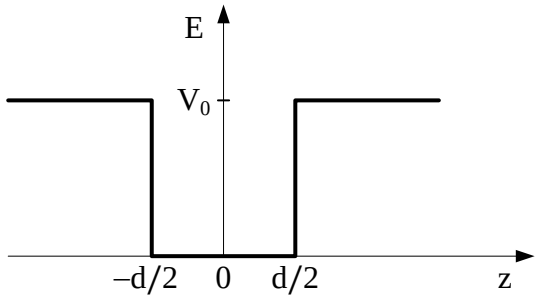


Fig. 2.7. Schematic representation of a one-dimensional finite barrier potential.

In the envelope function approximation method, the wave functions in the VB (ψ_1) and the CB (ψ_2) are expressed as a product of a slowly varying envelope function $F(\mathbf{r})$ and Bloch functions $u(\mathbf{r})$, where the latter is a complex function having a periodicity of the crystal lattice, as [39][61]:

$$\psi_1 = F_1(\mathbf{r})u_v(\mathbf{r}) \quad \text{and} \quad \psi_2 = F_2(\mathbf{r})u_c(\mathbf{r}), \tag{2.8}$$

where, the subscripts v and c stand for valence and conduction bands, respectively, and $\mathbf{r}$ is the position vector.

For quantum-wells, the wavefunctions take the form of plane waves propagating in the plane of the heterostructure (*xy* plane), and the envelope function (slow varying) is given by [39][62]:

$$F(\mathbf{r}_{xy}) = \frac{1}{\sqrt{S}} \cdot n(z) \cdot \exp(j\mathbf{k}_{xy}.\mathbf{r}_{xy}), \tag{2.9}$$

where, S is area of the crystal, $n(z)$ is bound states of the QW along the growth axis (the solution of the one-dimensional confinement potential of the QW), $\mathbf{k}_{xy}$ is the wave vector in the plane of the heterostructure, and $\mathbf{r}_{xy}$ is the position vector within the plane.

The wave function inside the QW ($-d/2 \leq z \leq d/2$ in Fig. 2.7) has a sinusoidal shape, and for confined electrons (holes) with energy $E < V_0$, it is given by [39]:

$$\psi(z) = \begin{cases} A\cos(k_w z), \text{ for symmetric solutions (even parity)} \\ A\sin(k_w z), \text{ for asymmetric solutions (odd parity)} \end{cases}, \tag{2.10}$$

where, A is amplitude of the wave function inside the QW region, and k_w is the well wave vector.

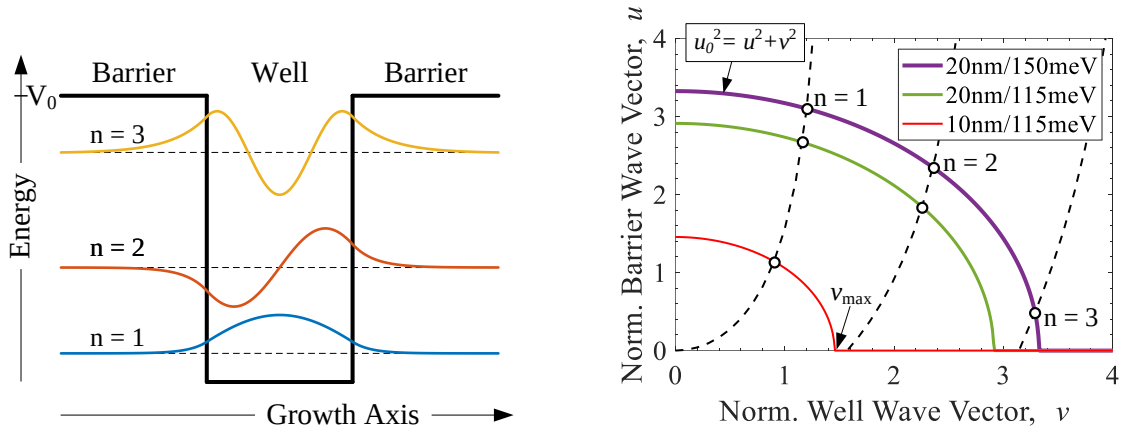
On the other hand, the wave function follows an exponentially decaying function outside the well (i.e., in the barrier region: $z \geq |d/2|$), which is given by: $\psi(z) = Bexp(-|k_b z|)$, where B is amplitude of the wave function inside the barrier. The wave vectors inside the well k_w and the barrier k_b regions are given by [54]:

$$k_w = \frac{\sqrt{2m^* E}}{\hbar}, \quad k_b = \frac{\sqrt{2m^*(V_0 - E)}}{\hbar}. \tag{2.11}$$

In most cases, where there is a coupling between different bands, amplitudes of the wave functions in (2.10) are obtained using numerical methods by solving the Schrödinger-Poisson equations self-consistently. In that case, multiband envelope function method (also known as multiband **k**.**p** model) is commonly used, which takes into account the interaction between different bands [54][62]. There are three hole-subbands in the valence band of semiconductors, namely heavy-hole (HH), light-hole (LH) and spin-orbit split-off (SO). For simulating our MQW structures, we used the 8-band **k**.**p** model, which, in addition to the HH, LH and SO bands, also includes the conduction band, and their spin degeneracies [40][54].

To analyze confined states in QWs, graphical methods are also commonly used, which are obtained by applying the boundary matching conditions at $z = |d/2|$ of Fig. 2.7 (equating the well

and barrier envelope functions and normalizing their wave vectors). Fig. 2.8 (a) illustrates wave functions of the lowest three confined electronic states ($n = 1$ being the ground state), having sinusoidal shapes inside the quantum-well and exponentially decaying in the barrier region.



(**a**) (**b**)

Fig. 2.8. Illustration of (**a**) wave functions of the first three confined states of an electron in the conduction band, (**b**) matching conditions for confined states of a GaInAsP QW of different well thicknesses (10 and 20 nm) and barrier potentials (115 and 150 meV). $m^* = 0.045m_0$ used for GaInAsP [39].

The number of confined states inside a QW is determined by the well width (a narrower well confines fewer states) as well as the confining potential V_0 (a larger V_0 confines more electronic states). Fig. 2.8 (b) shows a graphical illustration of the number of confined states for different well thicknesses and barrier heights. The figure plots normalized barrier wave vector (u) as a function of normalized well wave vector (v), which are given by [54]:

$$u = k_{\mathrm{b}}\frac{d}{2}, \quad \text{and} \quad v = k_{\mathrm{w}}\frac{d}{2}, \tag{2.12}$$

where, k_{b} and k_{w} respectively are absolute barrier and well wave vectors given in (2.11).

The radius of the circular curve (first quadrant) in Fig. 2.8 (b) contains key design parameters such as effective mass m^*, the well thickness d, and barrier height V_0, and it is given by [54]:

$$u_0{}^2 = u^2 + v^2 = \frac{m^* V_0 d^2}{2\hbar^2}. \tag{2.13}$$

Equation (2.13) shows that, the number of confined states decreases with decreasing the effective mass, thickness of the well, and/or the barrier potential. But, as it can also be seen from Fig. 2.8

(b), the ground state is always confined regardless of the well thickness and the barrier potential [54]. For example, for a 20-nm thick well surrounded by a 150-meV potential barrier, the first three states are confined (calculations are performed assuming $m^* = 0.045m_0$ for GaInAsP at 1550 nm, where m_0 is rest mass of electron [39]). The number of confined states also decreases with decreasing the barrier height. For example, only the first two electronic states are confined within the 20-nm thick well when the barrier height is reduced from 150 meV to 115 meV. Similarly, for a 10-nm thick QW surrounded by 115 meV potential barriers, only the ground state is confined at thermal equilibrium. The total number of confined states (N) can be approximated (rounded up to the closest integer) as [54]:

$$N = \left\lceil \frac{2v_{max}}{\pi} \right\rceil, \tag{2.14}$$

where, v_{max} is the maximum value of the normalized well wave vector ($v_{max} = u_{max} = u_0$).

The total energy of an electron (hole) confined inside the QW can also be obtained as [54]:

$$E = E_n + \frac{\hbar \left| k_{xy} \right|^2}{2m^*}, \tag{2.15}$$

where, k_{xy} is the in-plane dispersion, E_n is the confinement (quantization) energy of the n^{th} state, which is given by [54][63]:

$$E_n = \frac{\hbar^2 \pi^2 n^2}{2m^* d^2}, \tag{2.16}$$

where, n is the quantum number of confined states (n^{th} allowed energy level), m^* is effective mass of the particle (electron/hole), and d is the well thickness.

Equation (2.16) shows that allowed energy level of the ground state ($n = 1$) is nonzero, and it is above the minimum (lower edge) of the CB in bulk materials, which is one of the consequences of quantum confinement. Moreover, the energy levels are quadratically spaced, and the gap between confined states increases with decreasing the QW width [63].

2.3.2. Density of States

For a given number of electrons (holes) within the conduction (valence) band, their energy distribution is expressed in terms of density of states. Since there is a discrete number of allowed

energy levels that an electron (hole) can occupy in the conduction (valence) band of a QW, the density of states in QWs is no longer continuous as it is the case for bulk semiconductors. Instead, it has a step-like shape and the density of states of the corresponding bulk material forms an envelope for density of states of the QW as illustrated in Fig. 2.9 [39].

In bulk materials, electrons (holes) have three degrees of freedom, and the density of states within the conduction (valence) band is continuous (following the square root of the carrier energy), which is given by [39][54]:

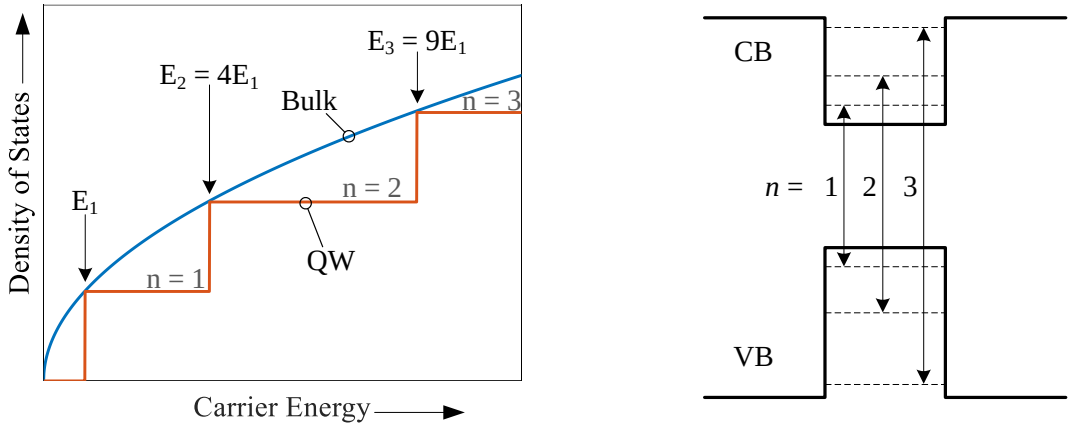
$$\rho^{3D}(E) = \frac{dN}{dE} = \frac{1}{2\pi^2}\left(\frac{2m^*}{\hbar^2}\right)^{\frac{3}{2}}\sqrt{E}, \tag{2.17}$$

where, ρ^{3D} is the three-dimensional density of states in bulk materials, N is the number of confined states, E is the total energy of electron (hole) confined in the QW.

The total density of states in QWs (ρ^{2D}), on the other hand, has a staircase shape, and it is approximated as [54]:

$$\rho^{2D}(E) = \frac{m^*}{\pi\hbar^2}\sum_{i=1}^{n}\Theta(E - E_i), \tag{2.18}$$

where, Θ is the unit step function, and n is quantum number of confined states.



(**a**) (**b**)

Fig. 2.9. (**a**) Dependence of density of states on carrier energy in bulk (smooth curve) and quantum wells (step-like curve), (**b**) schematic illustration of quantized energy levels in the valence and conduction bands of a GaInAsP QW.

Fig. 2.9 (a) schematically illustrates energy dependence of density of states of the two structures (bulk: smooth curve, QW: staircase type) for three confined states (the ground state being $n = 1$). For QWs, optical transitions from the VB to the CB (in the absence of an external influence such as a DC field) can occur only between confined states that have the same parity as illustrated in Fig. 2.9 (b). That means, $\Delta n = n_f - n_i = odd$ is strictly forbidden, where n_f and n_i are quantum numbers of the final and initial states, respectively [56]. However, this rule is broken in the presence of an electric field (externally applied or built-in).

2.3.3. Strained Quantum Wells

In MQW structures, thin layers of wells and barrier are epitaxially grown on a relatively thick substrate. If the native lattice constant of the epitaxial layer is different from that of the substrate, the lattice constant of the former is forced to change in the growth plane (perpendicular to the growth axis) in order to match the lattice constant of the substrate, causing in-plane (biaxial) strain on the epitaxial layer [39][54]. Fig. 2.10 illustrates two types of materials grown on a substrate in their unstrained (left) and strained states (right). The epitaxial layer is compressively strained if its lattice constant is larger than that of the substrate and tensile strained in the opposite case. Along the growth direction (z-axis), the lattice constant relaxes (for compressive strain QW) or tightens up (for tensile strained QW) to keep the crystal volume the same as its unstrained condition [39].

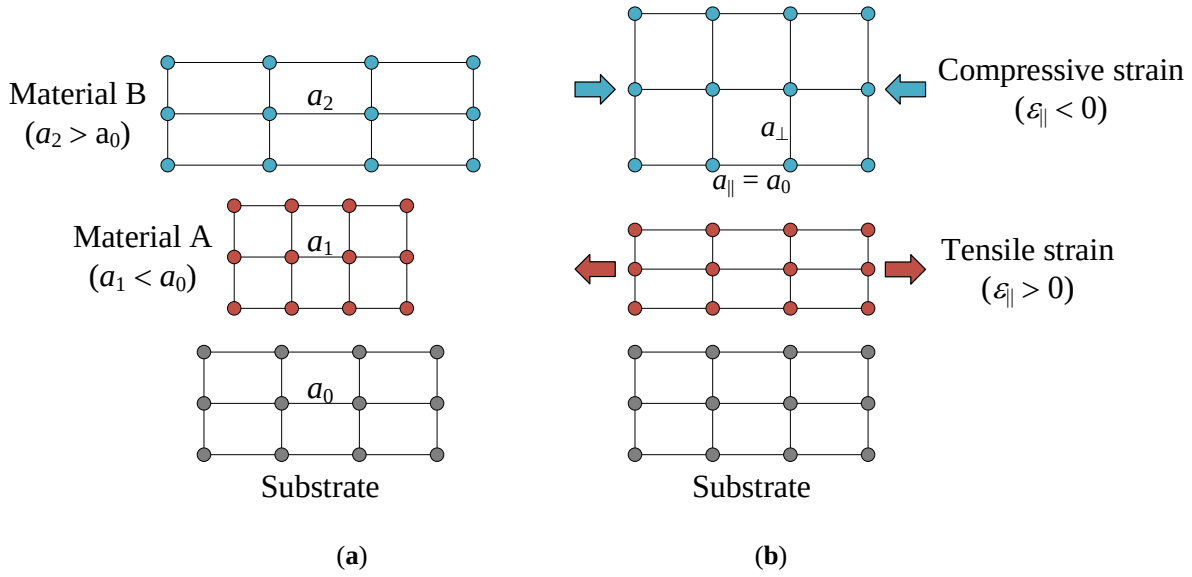


Fig. 2.10. Illustration of two types of materials, one with a larger lattice constant and another with smaller lattice constant than the substrate in their (**a**) unstrained states, (**b**) strained states (after [54]).

The crystal lattice deformation is expressed in terms of strain tensor, and the in-plane (hydrostatic) strain component ($\varepsilon_{\parallel}$) is given by [54]:

$$\varepsilon_{\parallel} = \frac{a_0 - a_l}{a_l}, \tag{2.19}$$

where, a_0 and a_l are lattice constants of the substrate and the epitaxial layer, respectively.

The in-plane strain is negative for compressively strained QWs ($a_l > a_0$), and it is positive for tensile strained QWs ($a_l < a_0$). For semiconductors having a cubic zincblende crystal structure, the strain components along the *x* and *y* directions (in-plane) are the same ($\varepsilon_1 = \varepsilon_2 = \varepsilon_{\parallel}$), and they are given by (2.19). When the epitaxial layer experiences compressive strain in the growth plane, it relaxes along the growth axis and vice versa for tensile strain. The perpendicular strain ($\varepsilon_{\perp}$) along the growth axis is given by [39][54]:

$$\varepsilon_{\perp} = \varepsilon_3 = -2\frac{C_{12}}{C_{11}}\varepsilon_1, \tag{2.20}$$

where, C_{11} and C_{12} are elastic stiffness constants.

The change in the crystal volume ΔV with respect to its original volume V is given by [54]:

$$\frac{\Delta V}{V} = \varepsilon_1 + \varepsilon_2 + \varepsilon_3 = 2\varepsilon_1\left(1 - \frac{C_{12}}{C_{11}}\right). \tag{2.21}$$

However, deformation of the epitaxial layer occurs only up to a certain 'critical thickness', after which atomic forces build up in the epitaxial layer, and it no longer deforms uniformly [54]. Instead, it tends to restore the native lattice constant. For most practical applications, a "thickness × strain" product of no more than 20nm% is required in order to grow high quality crystals [18][56], and for most semiconductor devices, a strain of ~1% is found to be an optimal value [39], which is also the case for our components (~0.81% compressive strained QWs). Table 2.3 summarizes strain and key parameters of the binaries for the EAM's GaInAsP/InP MQW [39].

Table 2.3. Parameters of binary constituents of GaInAsP and strain in the EAM's QW layer in our PICs.

Binary Alloy	***a* (Å)**	**C_{11}, C_{12}** [39]	$\varepsilon_{\parallel} = \varepsilon_1 = \varepsilon_2$	$\varepsilon_{\perp}$
GaP	5.65325	14.12, 6.253	−0.811% (compressive)	+0.849% (tensile)
GaAs	5.4505	11.88, 5.38		
InAs	6.0583	8.329, 4.526		
InP	5.8697	10.22, 5.76		

2.3.4. Effect of Strain on Electronic Band Profiles

Since the band structure of a semiconductor material is related to its lattice spacing, the crystal deformation due to strain affects its bandgap. As a result, strained QWs are widely exploited in semiconductor devices mainly for two reasons: (i) the hydrostatic strain changes the mean bandgap by pushing the conduction and valence bands in opposite directions, (ii) the axial strain lifts the HH and LH degeneracy that exists in the VB of bulk semiconductors at the center of the Brillouin zone ($k = 0$) [39][56].

Considering the first case, a compressive strain applied to a QW layer increases the bandgap by causing an upward shift to the CB edge and a downward shift to the VB edge, and vice versa for tensile strained QWs [39]. For cubic zincblende semiconductors, the shift in the conduction band edge (change in CBO) as a result of hydrostatic strain is given by [54][64]:

$$\delta E_c = -a_c(2\varepsilon_1 + \varepsilon_3), \tag{2.22}$$

where, a_c is hydrostatic deformation potential of the CB.

The shear strain component (the second effect), on the other hand, breaks the cubic symmetry of the semiconductor and moves the HH and LH subbands in opposite directions. The third subband within the VB (SO band), is separated from the other hole bands by energy Δ_{SO}. Therefore, in addition to the hydrostatic strain, the shear strain component is included in calculating the HH and LH band edge shifts, which are given by [64]:

$$\begin{aligned} \delta E_{HH} &= a_v(2\varepsilon_1 + \varepsilon_3) + b(\varepsilon_1 - \varepsilon_3) \\ \delta E_{LH} &= a_v(2\varepsilon_1 + \varepsilon_3) - b(\varepsilon_1 - \varepsilon_3) \end{aligned} \tag{2.23}$$

where, a_v and b are hydrostatic and shear deformation potentials of the valence band, respectively.

Fig. 2.11 schematically illustrates bulk-like band structures of a direct bandgap semiconductor in tensile strained (left), unstrained (middle) and compressive strained (right) states [18][65]. For unstrained QWs, the HH and the LH subbands are degenerate at the center of the Brillouin zone, and they split for nonzero wave vectors. For compressive strained QWs, the HH band edge moves upward, lowering the heavy-hole to electron (HH-E) transition energy, whereas the LH band edge moves downward, increasing the LH to electron (LH-E) transition energy. Moreover, compressive

strain reduces the in-plane particle mass, making it lighter than the perpendicular mass (along the growth axis) [65]. As a result, the highest band is the HH band along the growth axis ($k_{\perp}$) as shown on the right-hand side of Fig. 2.11 (c). For the case of tensile strained QWs, the LH band edge shifts upward, moving above that of the HH band, and the perpendicular mass becomes lighter than the in-plane mass. Therefore, strained QWs bring additional degree of freedom for device design and enable valence band engineering.

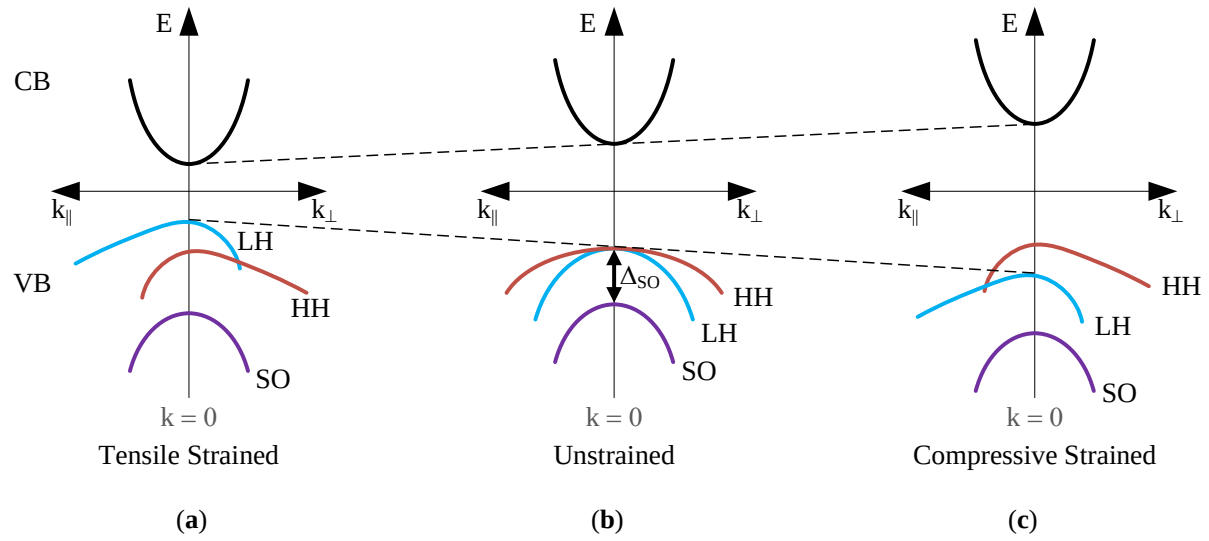
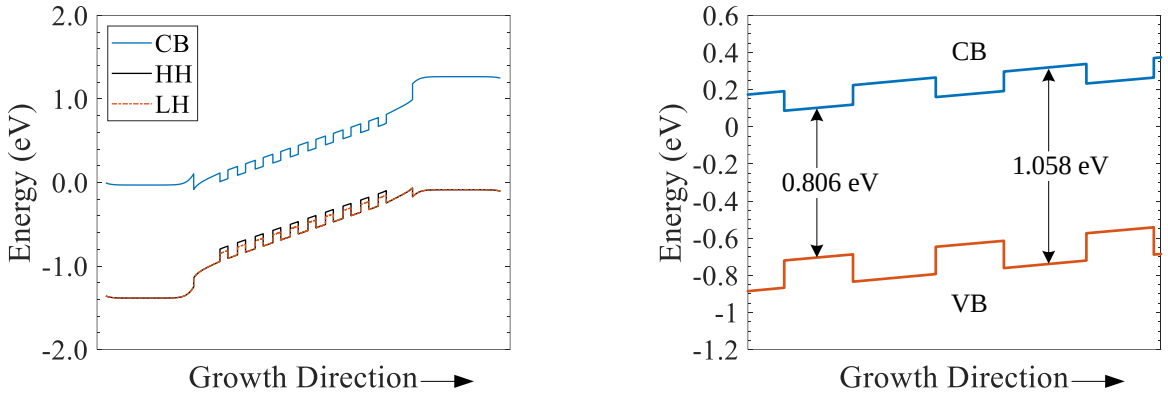


Fig. 2.11. Illustration of electronic band structures of (**a**) tensile strained, (**b**) unstrained, and (**c**) compressive strained *bulk-like* direct bandgap material. $k_{\perp}$ is the wave vector along the growth (*z*) axis whereas $k_{\parallel}$ is the in-plane (*xy*) wave vector (after [18]).

2.4. Electronic Band Structures of Compressive Strained MQWs

Fig. 2.12 shows simulated electronic band profile (native bandgap) of the compressive strained MQW structure, which has similar design parameters as our C-band EAMs, for the lowest confined states in the absence of an external DC field (simulated using *nextnano* [49]). The band structures are tilted in the direction of the growth axis (left to right) because of the built-in field. As expected, the HH and LH band edges are separated by ~53.4 meV in the well region because of the in-plane compressive strain ($\varepsilon_{\parallel} \approx 0.81\%$) as shown in Fig. 2.12 (a). The HH-E transition energy is ~0.81 eV (~0.86 eV for LH-E) as shown in the enhanced view of the band structure in Fig. 2.12 (b), corresponding to a transition wavelength of 1540 nm (1440 nm). This indicates HH-E transition occurs at a relatively lower photon energy than LH-E, making the devices sensitive to polarization

state of the input light as the two transitions contribute differently to transverse electric (TE) and transverse magnetic (TM) polarized light because of selection rules for interband optical transitions.



(**a**) (**b**)

Fig. 2.12. (**a**) Simulated *native* bandgap profile of compressive strained GaInAsP QWs surrounded by unstrained GaInAsP barriers, grown on InP substrate, (**b**) enhanced view of the band structure showing transition energies.

The QWs are surrounded by a barrier of ~1.06 eV bandgap, resulting in a bandgap difference (ΔE_g) of ~252 meV for HH-E transitions and 198.5 meV for the LH-E transitions. In other words, the well is deeper for HHs than the LHs. The CBO is ~105 meV, which is ~42% of the HH-E bandgap discontinuity, and the VBO is ~147 meV (~58% of the HH-E bandgap discontinuity). Table 2.4 summarizes simulated energies of the GaInAsP MQW structure.

Table 2.4. Simulated band edge energies for a compressive strained GaInAsP MQW.

Parameter	**HH**	**LH**
E_g (well)	0.806 eV	0.859 eV
E_g (barrier)	1.058 eV	1.058 eV
ΔE_g	252 meV	198.6 meV
ΔE_c	105.3 meV (41.8%)	105.3 meV (53%)
ΔE_v	146.7 meV (58.2%)	93.3 meV (47%)
Δ_{SO}	286.9 meV	233.5 meV

2.5. Absorption Coefficient

The absorption coefficient of an EAM is directly related to the imaginary part of the complex refractive index $\tilde{n}$ of its MQW active region, which is given by: $\tilde{n} = n + j\kappa$, where n and κ are the

real and imaginary parts of the refractive index. The latter is known as extinction coefficient, and it is related to the absorption coefficient α as [61]:

$$\alpha = \frac{4\pi\kappa\nu}{c} = \frac{4\pi\kappa}{\lambda}, \tag{2.24}$$

where, ν and λ respectively are the optical frequency and wavelength, c is speed of light in vacuum.

Fig. 2.13 shows schematic diagram of an EAM (left) and the process of exciting an electron by a photon of energy $h\nu$ (right) so that the electron transitions from its initial state of energy E_i to its final state of energy E_f in the upward direction (absorption). The photon energy required for this transition to occur is: $h\nu = E_f - E_i$. In an ideal two-level system (in the absence of defects or energy levels in the bandgap), photons having energy below $E_f - E_i$ are not absorbed.

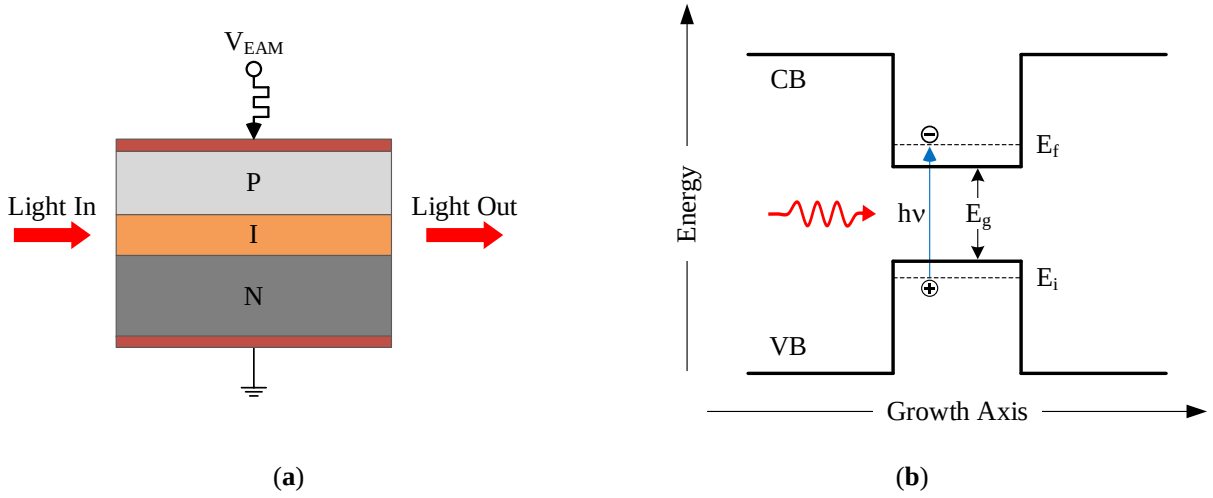


Fig. 2.13. Schematic diagram of (**a**) an EAM and (**b**) photon-assisted electronic transition through the bandgap.

The transition probability is obtained using Fermi's golden rule, and for an electronic transition from an initial state $|i\rangle$ to a final state $|f\rangle$, it is given (using dipole approximation) by [56][61]:

$$W_{i\to f} = \frac{2\pi}{\hbar}|M|^2\rho(h\nu), \tag{2.25}$$

where, $\hbar$ is reduced Planck constant, $\rho(h\nu)$ is the joint density of states at photon energy $h\nu$, which is enhanced thanks to compressive strain, and M is the transition matrix element, which quantifies strength of interaction between electrons in the CB and holes in the VB, and it is given by [39][61]:

$$M = \langle f|H'|i\rangle = \int_V \psi_f^*(\boldsymbol{r}) H'(\boldsymbol{r}) \psi_i(\boldsymbol{r})\, d^3\boldsymbol{r}, \tag{2.26}$$

where, V is the volume of the active region, and H' is Hamiltonian of the perturbation that causes the electronic transition (associated with the light wave: $H' = q\mathbf{r} \cdot \mathbf{E}$, where $\mathbf{r}$ is position vector and $\mathbf{E}$ is the perturbing electric field), and $\psi(\mathbf{r})$ is electron (hole) wave function.

Therefore, from (2.25), the interband transition rate depends on: (i) spatial overlap of wavefunctions of the initial and final states (electron-hole overlap integral), and (ii) density of states [39]. In the absence of an externally applied electric field, the value of the overlap integral in MQWs is close to unity as the electron and hole wave functions are aligned symmetrically (except for a slight displacement caused by the build-in field). Moreover, since the density of states in MQWs has a step-like shape, the transition rate as well has a step-like shape, which also applies to the absorption coefficient as well.

The perturbing electromagnetic wave can be characterized by a plane wave of the form $\boldsymbol{E}(z) = E_0(z)\exp(\mathrm{j}\omega t - k_x x)\mathcal{E}$, propagating along the x-axis (plane of heterostructure) with polarization $\mathcal{E}$. In that case, for a single QW layer centered at $z = z_0$ along the growth axis, the absorption coefficient α for given photon of energy $h\nu$ is given by [66][67]:

$$\alpha = \left[\frac{E_0(z_0)^2}{\langle E_0(z)^2\rangle}\right] \frac{q^2}{2\nu n \varepsilon_0 c m_0^2 V} \sum_{i,f} |\langle f|\mathcal{E}\cdot\boldsymbol{p}|i\rangle|^2 \times \rho(E_f - E_i - h\nu) \times \left[f(E_i) - f(E_f)\right], \tag{2.27}$$

where, ν is the optical frequency, q is elementary charge, m_0 is electron rest mass, V is normalizing volume of the optical mode ($V = L \times w \times d$), $\boldsymbol{p}$ is the electron momentum, and $\rho(x)$ is the joint density of states. The last two terms, $f(E_i)$ and $f(E_f)$, are Fermi-Dirac distributions representing the occupancy probabilities of the initial and final states, respectively.

For an electron transitioning from the VB (initial state) to the CB (final state), the Fermi-Dirac distributions at a given energy E, $f_v(E)$ and $f_c(E)$, are given by:

$$f_v(E) = \frac{1}{1 + \exp[(E - E_{Fv})/K_B T]}, \quad \text{and} \quad f_c(E) = \frac{1}{1 + \exp[(E - E_{Fc})/K_B T]}, \tag{2.28}$$

where, E_{Fv} and E_{Fc} respectively are quasi-Fermi levels in the valence and conduction bands, K_B is Boltzmann's constant, and T is temperature.

For HH-E (LH-E) transition with energy $E_{H(L)}$, (2.27) can be expressed in terms of reduced masses of the charge carriers as [66][67]:

$$\alpha = \left[\frac{E_0(z_0)^2}{\langle E_0(z)^2\rangle}\right]\frac{\beta}{d}\mu_{H(L)}M_{H(L)}^2 P_{H(L)}\Theta\big(E_{H(L)} - h\nu\big), \tag{2.29}$$

where, $H(L)$ stands for HH(LH), d is the QW thickness, μ is in-plane reduced mass of the electron-hole pair in units of conduction band effective mass (m_c), M is the overlap integral of heavy-hole (light-hole) and electron envelope functions, $M_{H(L)-E} = |\langle \psi_{\text{en}}|\psi_{\text{hn}}\rangle|$, P is variable part of the corresponding atomic dipole matrix element, $\Theta(x)$ is the unit step function, and the parameter β is a dimensionless constant with a value of 6×10^{-3} [66].

The reduced mass of an electron-hole pair (HH-E or LH-E) is given by:

$$\frac{1}{\mu} = \frac{1}{m_e^*} + \frac{1}{m_h^*}, \tag{2.30}$$

where, m_e^* and m_h^* are electron and hole effective masses, respectively.

For a MQW structure, the total absorption coefficient of the guided mode can be obtained by summing over all quantum-well positions, which is the same as replacing the prefactor ${E_0}^2/\langle {E_0}^2\rangle$ by the total optical confinement factor [66].

2.5.1. Optical Confinement Factor

The confinement factor Γ is defined as the fraction of optical field intensity that overlaps with the MQW active region. In other words, it is the ratio of optical power inside the MQW to the total input power, and it is given by [39]:

$$\Gamma = \frac{\int_{-w/2}^{w/2}\int_{-d/2}^{d/2} |U(x,y)|^2\, dxdy}{\iint_{xy} |U(x,y)|^2\, dxdy} \tag{2.31}$$

where, $U(x,y)$ is the normalized field profile of the electromagnetic wave, w is the waveguide width, and d is thickness of the QW layer.

The optical confinement factor of a single QW layer can be increased by increasing its thickness and/or the waveguide width. However, the former is constrained by the critical thickness for growing high-quality crystals and the latter by the requirement for monomode operation of optoelectronic devices. The total confinement factor of a MQW stack is obtained by multiplying the Γ value obtained using (2.31) by the number of QW layers.

In order to extract the confinement factors at different layers of our MQW structure, we simulated the SI-BH waveguides using FIMMWAVE [70]. The C-band EAMs in our PICs are based on a MQW stack having a total thickness of 189 nm (wells + barriers + SCH layers) and a ridge width of 1.5 μm. The total simulated optical confinement factor for the fundamental TE mode is ~8.9%. For the O-band devices, on the other hand, the ridge width is chosen to be 1.3 μm for monomode operation of the devices. In order to obtain a comparable confinement factor to that of the C-band devices, one more QW layer is used, resulting in an optical confinement factor of ~11%.

The optical confinement factor has an important implication in determining extinction ratio (modulation strength) as well as insertion losses of EAMs, where the latter also applies to passive sections. For planar waveguide modulators such as an EAM, the output power (P_{out}) decreases exponentially (in linear scale) with the EAM length (L_{EAM}) as follows:

$$P_{out} = P_{in} \exp(-\Gamma \alpha L_{EAM}), \tag{2.32}$$

where, P_{in} is the input optical power, Γ is the optical confinement factor, and α is absorption coefficient of the MQW active region.

The modulation strength of an EAM (the ratio of output powers in the *on* and *off* states) can be increased by increasing all or any one of the following three parameters: Γ, α and L_{EAM}. But insertion loss L_{in} of the EAM (absorption during the *on* state) also increases with increasing those parameters as waveguides always have finite intrinsic absorption coefficients [$L_{in} = P_{in}/(P_{in} - P_{out}) = 1 - exp(-\Gamma \alpha L_{EAM})$].

However, the main source of insertion loss for the EAM section comes from the p-doped InP layers grown on top of the MQW stack, which is due to intervalence band absorption between the GaInAsP MQW active region and the p-InP cladding layer. For the C-band devices, the simulated optical confinement factor in the p-InP layers (180 nm spacer and 2 μm cladding) is ~31.6%,

which results in a one-way insertion loss of ~3 dB for a 150-μm long EAM (assuming $\alpha = 150$ cm^{-1} at 1530 nm [71]). For the O-band EAMs, on the other hand, the total confinement factor in the p-doped region is ~32.8%, which results in an insertion loss of ~2 dB for a 100-μm long EAM (L_{in} in dB $= 10\log_{10}L_{in}$). Table 2.5 summarizes simulated confinement factors of the MQW and p-InP cladding layers of the EAM section for the fundamental TE mode.

Table 2.5. Simulated confinement factors of MQW and cladding layers for the fundamental TE mode.

Freq. Band	EAM Length (μm)	Waveguide Width (μm)	MQW Thickness (nm)	Confinement Factor		Insertion Loss (dB)
				MQW	p-InP	
C	150	1.5	189	8.9%	31.6%	3
O	100	1.3	209	10.9%	32.8%	2

2.6. Polarization Sensitivity

Electrons in the CB have *s*-like atomic states whereas holes in the VB have *p*-like atomic states [61]. For an electron to be excited by a photon of wave vector k_{ph} and transition from its initial state of wave vector k_i to its final state k_f (e.g., from the VB to the CB), the two wave vectors must satisfy the **k**-selection rule, i.e., $k_{ph} = k_f - k_i$ [56]. However, the photon wave vector is very small compared to that of electrons and holes (an order of magnitude lower), and it is ignored in most cases [39]. That means, transition from the VB to the CB (or the opposite) is possible only if the two states have the same wave vectors (the two states must propagate in the same direction). Direct bandgap materials satisfy this condition of $k_i = k_f$ and thus optical transitions occur vertically, improving the absorption (emission) efficiency, which is the main advantage of direct bandgap materials over indirect bandgap materials to realize active optoelectronic devices.

Another selection rule for interband transitions in MQWs is imposed by parity (the electron-hole overlap integral), where vertical electronic transitions are allowed only between confined states that have identical quantum numbers, and the rest are forbidden [39].

For light propagating along the *x* axis, it can have two polarizations, namely, TE and TM modes as illustrated in Fig. 2.14, which arises from dependence of the atomic-like transition matrix element $\langle u_v|\mathcal{E}.\mathbf{p}|u_c\rangle$ on polarization state of the incident light [62][52].

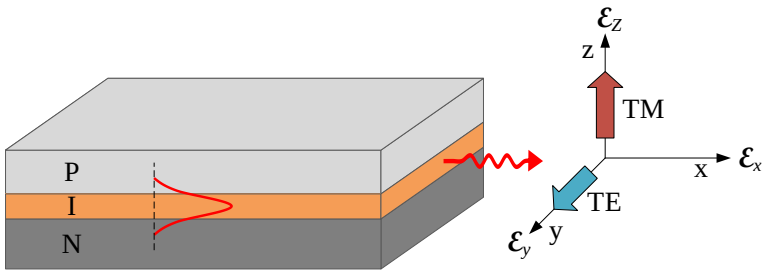


Fig. 2.14. Schematic of light propagating either in TE or TM mode (after [52]).

That means, HH-E and LH-E transitions contribute to the TE and TM modes differently. The selection for HH-E and LH-E transitions are shown in Table 2. 6 using the absolute value of the transition matrix element Π, which is given by [62]:

$$\Pi = \frac{-i}{m_0}\langle S|p_x|X\rangle = \frac{-i}{m_0}\langle S|p_y|Y\rangle = \frac{-i}{m_0}\langle S|p_z|Z\rangle, \tag{2.33}$$

where, |S⟩, |X⟩, |Y⟩, and |Z⟩ are states of the four Bloch functions (*s*-like CB and *p*-like VB edges) at $k = 0$.

Table 2. 6. Selection rules of interband optical transitions [62].

Polarization	$\mathcal{E}_x$	$\mathcal{E}_y$	$\mathcal{E}_z$
HH-E transition	Impossible	$\Pi/\sqrt{2}$	Forbidden
LH-E transition	Impossible	$\Pi/\sqrt{6}$	$2\Pi/\sqrt{6}$

At the center of the Brillouin zone, the HH-E transitions are three times stronger than the LH-E transitions [62]. The SO-E transition has an intermediate strength of $2/3$ of the HH-E transition. For TE polarization, most of the contributions $(3/4)$ come from HH-E transitions (α_{HH}) whereas only LH-E transitions (α_{LH}) contribute to the TM mode [39][66]. As a result, the absorption coefficient of an EAM for TE mode (α_{TE}) is stronger than that of TM mode (α_{TM}), i.e.,

$$\alpha_{TE} = \frac{1}{4}\alpha_{LH} + \frac{3}{4}\alpha_{HH},$$
$$\alpha_{TM} = \alpha_{LH}, \tag{2.34}$$

For compressive strained QWs, the HH band edge lies above that of the LH [cf. Fig. 2.11 (c)]. As a result, the HH-E transition requires a relatively lower energy than the LH-E transition and thus

devices based on compressive strained QWs exhibit high sensitivity to TE polarization than TM polarization. On the other hand, the LH band edge is above that of the HH in tensile strained QWs, which allows obtaining comparable TM and TE performances by exploiting the LH-E transitions. A combination of tensile and compressive strained MQW structures are being widely exploited to realize polarization-independent devices [52][65][68][69]. Since our components are based on compressive strained QWs, using mainly HH-E transitions, both the EAM and the SOA sections are sensitive to polarization state of the input light.

Polarization sensitivity may not be an issue for integrated laser modulators (e.g., DFB-EAM-SOA) as all the building blocks operate in TE mode. However, the polarization state of light in optical fibers is random, and it becomes an important issue for external intensity modulators, inline amplifiers, and photodetectors.

2.7. Electroabsorption Effects

When a semiconductor material is illuminated with light, band edge absorption of photons occurs if the photon energy is high enough to excite an electron from the VB to the CB ($h\nu > E_g$). In heterostructures, the optical transition (absorption) is enhanced by applying an external DC field perpendicular to the layers of the heterostructure, which tilts the electronic band structure in the direction of the applied field [40][56]. As a result of the tilting of the band profile, the transition energy decreases so that photons of relatively lower energy than the bandgap can now be absorbed. This phenomenon is known as Franz-Keldysh effect in bulk materials [40] and quantum confined Stark effect (QCSE) in QWs [72].

Fig. 2.15 schematically illustrates photon assisted tunneling of electrons with and without applying an external DC field. In the absence of an external electric field, the electron and hole wave functions have the maximum overlap about the center of the QW as shown in Fig. 2.15 (a). Here, a flat electronic band structure is shown for simplicity. In reality, the band profile is slightly tilted by the built-in field. As the band profile is further tilted by applying a perpendicular field, the electrons and holes move towards their respective lower energy levels, i.e., electrons to the left and holes to the right as illustrated in Fig. 2.15 (b). This displacement of charge carriers lowers the electron-hole overlap integral.

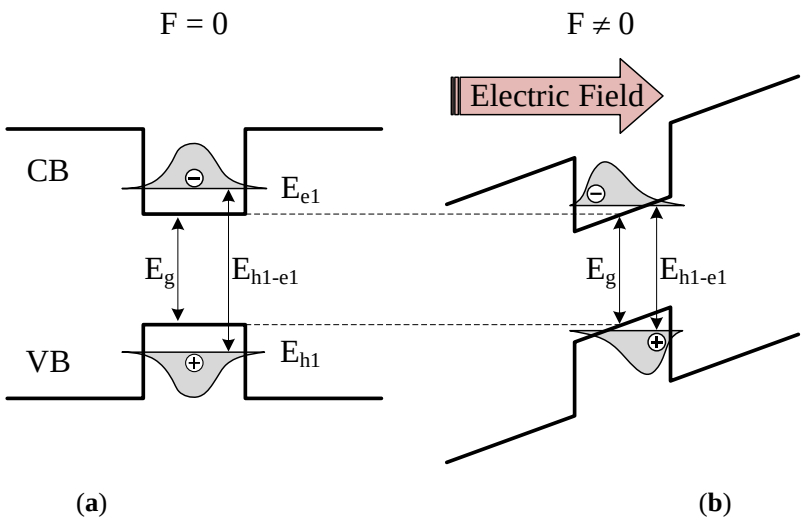


Fig. 2.15. Schematic illustration of bandgap profile and wave functions of ground state electrons and holes inside a QW (**a**) without and (**b**) with externally applied electric field.

The total electric field (F) that exists along the growth axis of a MQW structure is given by [61]:

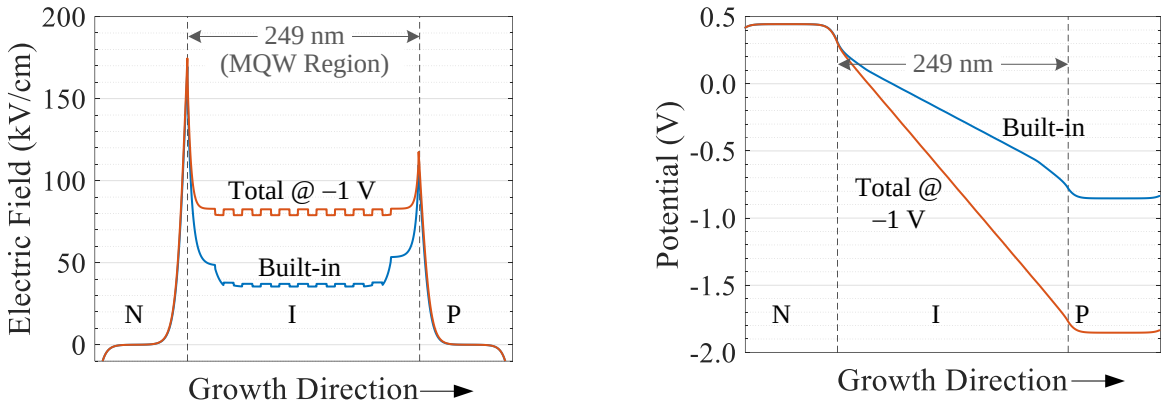
$$F = \frac{|V_{bi} - V_0|}{d}, \tag{2.35}$$

where, V_{bi} is the built-in diode potential, V_0 is the applied bias voltage, and d is the MQW active region thickness.

In a reverse biased structure such as an EAM, the external field, together with the built-in field, increases the total electric field inside the MQW active region, further tilting the electronic band structure. Fig. 2.16 (a) shows simulated electric field strength inside a GaInAsP MQW structure with and without a DC field (reverse bias voltage). The electrostatic potential is shown in Fig. 2.16 (b), which is the solution of Poisson's equation given by [61].

$$\frac{\partial^2}{\partial z^2} V(z) = -\frac{\rho(z)}{\varepsilon_0 \varepsilon_r}, \tag{2.36}$$

where, $V(z)$ is the voltage drop across the MQW region, $\rho(z)$ is the electric charge density, ε_0 is the permittivity of free space, and ε_r is the dielectric constant of the medium (MQW active region).



(**a**) (**b**)

Fig. 2.16. (**a**) Simulated electric field distribution inside a GaInAsP MQW structure with and without applying an external field perpendicular to the QW layers, (**b**) total voltage drop across the MQW structure.

The total thickness of the undoped MQW active region used for the simulation is 249 nm (including wells, barriers, and SCH layers). The built-in field is ~36 kV/cm, which corresponds to a built-in voltage drop of ~0.9 V ($V \approx F \times d$). When a reverse bias voltage of −1 V is applied perpendicularly to the MQW structure, the total field increases to ~80.5 kV/cm, out of which, the externally applied field is ~44.5 kV/cm.

Apart from the applied electric field, the electroabsorption effect in QWs is further enhanced by Coulomb interaction between bound electron-hole pairs, known as 'excitonic absorption' [72][73]. Because of strong confinement of electrons and holes in QWs that keeps them close to one another, the excitonic absorption in MQW structures is very strong [72]. As a result, the absorption spectra of MQWs exhibit sharp excitonic peaks at room temperature with those peaks occurring at photon energies [56]:

$$h\nu = E_g + E_{hn} + E_{en} - E_{xn}, \tag{2.37}$$

where, E_g is the bandgap, E_{hn} and E_{en} respectively are confining energies of holes and electrons in the n^{th} state, and E_{xn} is the corresponding exciton binding energy.

The excitons in QWs can be modeled as 2D hydrogen atoms inside a material of dielectric constant ε_r, and the exciton binding energy E_x is approximated as [56]:

$$E_{xn} = \frac{\mu}{m_0}\frac{1}{\varepsilon_r^2}\frac{1}{(n-1/2)^2}R_H, \tag{2.38}$$

where, μ is reduced mass of the electron-hole pair, m_0 is free electron mass, n is the principal quantum number, and R_H is Rydberg's constant for hydrogen atom (13.6 eV). For bulk materials, the value of E_x in (2.38) varies with $1/n^2$ instead of $1/(n-1/2)^2$ [56].

The exciton binding energy in QWs is larger than bulk materials due to the fact that the electrons and holes are kept close to one another by the relatively thin QW layers, increasing the strength of their interaction $\left(E_x^{2D} \approx 4E_x^{3D}\right)$ [54][56]. As a result, MQWs exhibit strong bandgap absorptions with sharp excitonic peaks that are resolved at room temperature and high field [72], enabling the realization of room-temperature semiconductor devices.

For a GaInAsP MQW active region operating in the C-band ($m_e^* = 0.045m_0$, $m_h^* = 0.37m_0$, $\varepsilon_r = 13.75$ [39]), equation (2.38) provides an exciton binding energy of ~12 meV for the ground state. However, the typical value of E_x in QWs is ~10 meV, which is slightly lower due to the tunneling of electrons and holes into the barriers, reducing exciton lifetime [56][61].

2.7.1. Quantum Confined Stark Effect

When an electric field is applied perpendicularly to the QW layers, electrons and holes move in opposite directions, lowering the electron-hole overlap integral. However, a strong potential barrier still keeps electrons and holes in close proximity, preventing the excitons from completely breaking apart. As a result, the excitonic peaks in QWs are resolved even at high fields, evidencing strong excitonic absorption [61][72]. Moreover, the excitons interact with the applied field and shift the optical transition energy to lower energies (longer wavelengths), which is known as QCSE [72]. When the applied field is small, the Stark shift ΔE_{shift} (the decrease in the bandgap or red-shift of the transition wavelength) has quadratic relationship with the field, i.e., [18][61]

$$\Delta E_{\text{shift}} \propto (m_e^* + m_h^*)q^2F^2d^4, \tag{2.39}$$

where, m_{e^*} and m_{h^*} respectively are effective masses of confined electrons and holes, q is elementary charge, F is the applied DC field, and d is thickness of the QW layer.

However, as the field increases, the electrons and holes move further away from the center of the QW. But the relatively small well thickness still limits the displacement of electron and hole envelope functions, and the energy shift develops a linear relationship with the applied field instead of a quadratic relationship [63].

Fig. 2.17 shows simulated band edge profiles of a compressively strained GaInAsP MQW structure for the fundamental electron and heavy-hole confined states without (left) and with (middle) an applied electric field. In the absence of an external field, the electronic band structure is tilted only by the built-in field, and the quasi-Fermi levels of electrons and holes overlap. When the MQW structure is reverse biased, for example at -1 V (44.5 kV/cm field), the electron Fermi-level moves downward, and the hole Fermi-level moves upward as shown in Fig. 2.17(b). As such, the optical transition energy lowers, allowing vertical transitions at lower photon energies that otherwise would have been impossible to take place. For comparison, the band profiles of the two conditions (with and without external field) are shown in Fig. 2.17 (c).

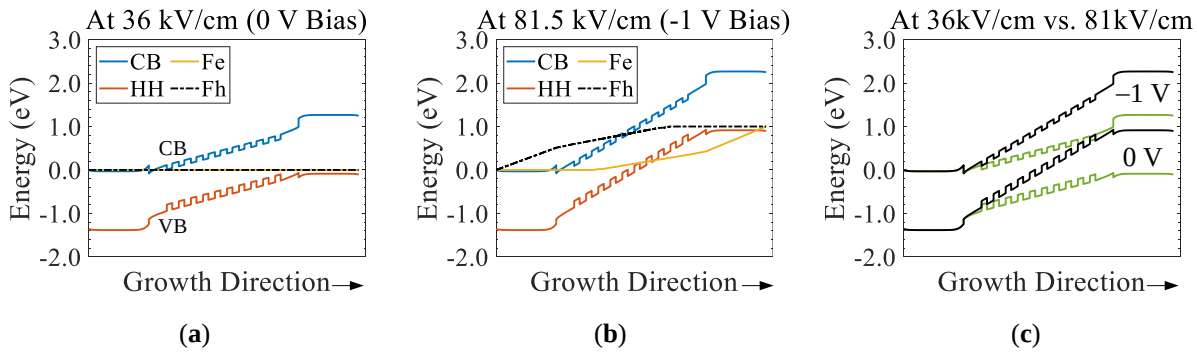
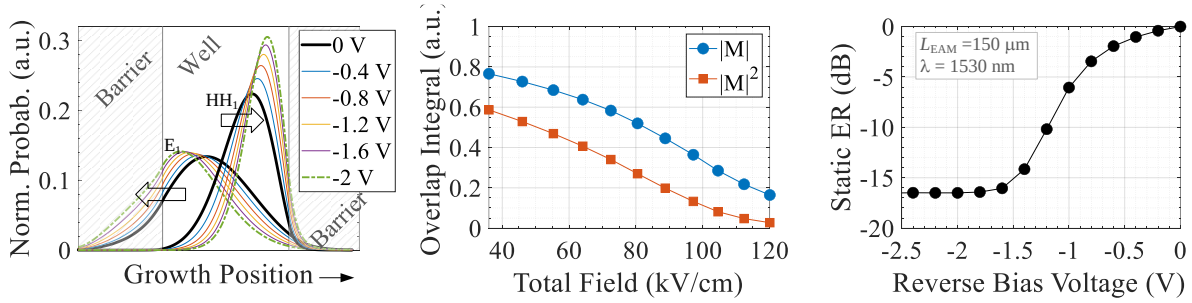


Fig. 2.17. Simulated band edge profiles of compressive strained GaInAsP MQW structure on an InP substrate (**a**) without applied field (at 0 V, 36 kV/cm built-in field), (**b**) with applied field (-1 V, 81.5 kV/cm total field), and (**c**) comparison of the band structures with and without external DC field.

The tilting of the electronic band structure increases with increasing reverse bias voltage, reducing the electron-hole overlap area. Fig. 2.18 shows the displacement of the electron and hole wave functions for the lowest confined electron and HH states (left), their overlap integrals as a function of the applied field (right), and static extinction ratio of a 150-μm long EAM. As the applied field increases, the electrons move towards the n-contact (to the left) and tunnel into the potential barrier as shown in Fig. 2.18 (a). The holes, on the other hand, move towards the p-contact (to the right) but escape at a relatively lower rate. As a result, the heavy-holes begin to accumulate at the edge

of the well, which is a direct consequence of a large VBO offered by GaInAsP MQWs (~0.6ΔE_g) that lowers the escape rate of the heavy-holes out of the QW region. The wave function of the HHs narrows as the field increases while its amplitude increases, indicating that the HHs are confined inside the QW region as they hardly penetrate into the barrier region.



(**a**) (**b**) (**c**)

Fig. 2.18. (**a**) Simulated evolution of electron and hole wave functions with applied reverse bias voltage (field) and (**b**) their overlap integrals (M and M^2) as a function of applied field, (**c**) static extinction ratio of a 150-μm long REAM at 1530 nm and 25°C.

In the absence of external electric field (only ~36 kV/cm built-in field), the HH-E overlap integral is ~0.77, which gives rise to a squared overlap integral ($M^2 = |\langle\psi_{en}|\psi_{hn}\rangle|^2$) of ~0.6 as shown in Fig. 2.18 (b). The value is lower than unity because of the built-in field. These results are obtained by applying Dirichlet boundary condition in *nextnano* (the potential at the boundary is constant). When a DC field of ~44.5 kV/cm (total 80.5 kV/cm) is applied, the overlap integral reduces to ~0.16, which indicates saturation of the EAM's absorption coefficient so that its extinction curve flattens as shown in Fig. 2.18 (c), for example, for a 150-μm long C-band REAM at 1530 nm.

As the applied field increases, the emission rate of photogenerated electrons and holes also increases because of a decrease in the potential barrier. The relationship between barrier height (H) and the applied field (F) about the center of the well is given by [58]:

$$H_{c(v)}(F) = \Delta E_{c(v)} - E_{c(v),n} - qF\frac{d}{2}. \tag{2.40}$$

where, $\Delta E_{c(v)}$ is the conduction (valence) band offset, $E_{c(v),n}$ is confinement energy of the n^{th} electron (hole) state. The last term is the change in potential energy due to the applied field.

Fig. 2.19 shows simulated transition energies of a single GaInAsP QW layer together with the electron and hole wave functions without (left) and with (right) applied field at 300K (26.85℃). The results are obtained by solving the Schrödinger-Poisson equations self-consistently using 8-band **k**.**p** model for CB, HH, LH, and SO bands in *nextnano* [49].

In the absence of an externally applied DC field, the transition energy of the MQW structure is ~0.843 eV (equivalent to ~1471 nm in wavelength) as shown in Fig. 2.19 (a), which is similar to the first excitonic peak of the C-band EAMs in our PICs at 0 V and 25℃. With respect to the native bandgap of the QW layer (~0.81 eV, cf. Fig. 2.12), the transition energy is increased by ~37 meV. According to (2.37), the total transition energy in a QW is increased by the confining potentials of electrons and holes less the exciton binding energy ($E = E_g + E_{hn} + E_{cn} - E_{xn}$), resulting in an energy difference of ~37 meV with respect to the bulk-like band edges of GaInAsP.

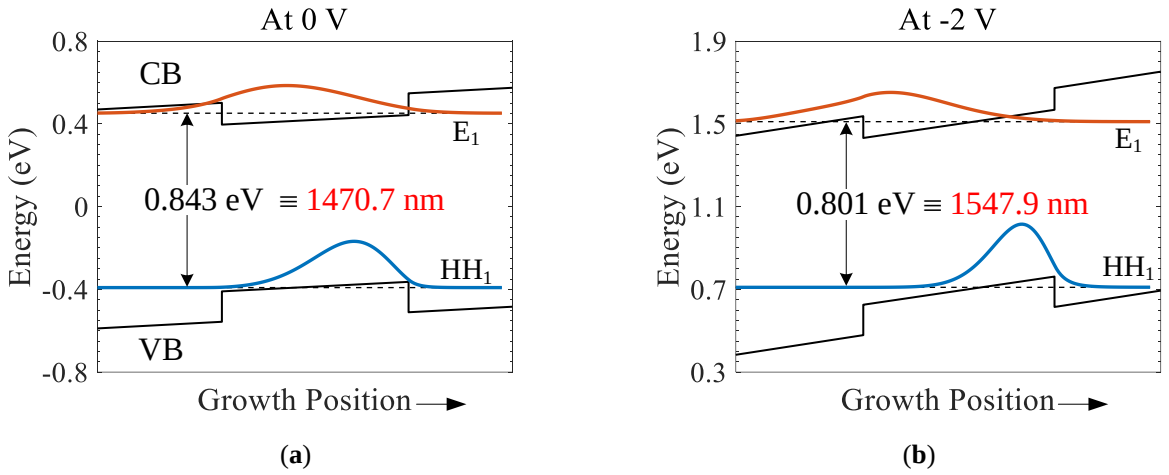


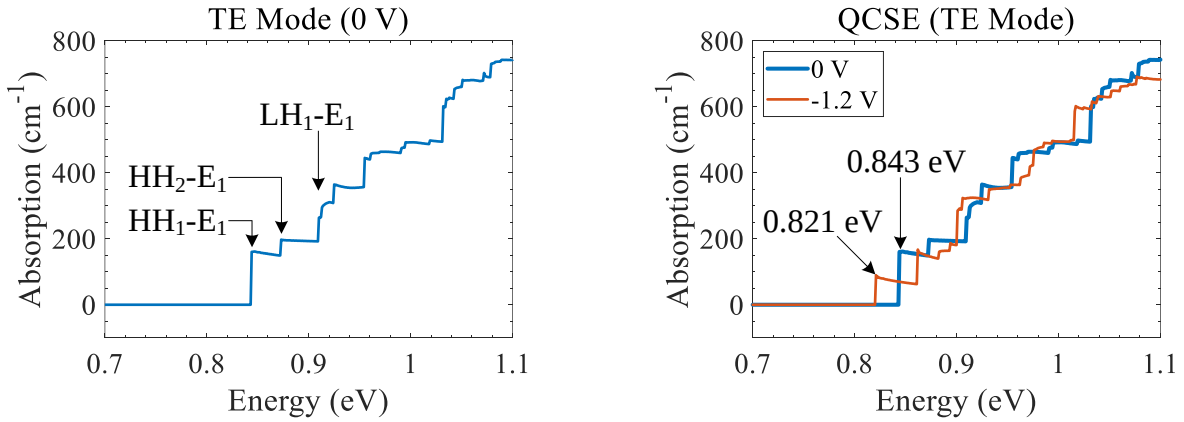
Fig. 2.19. Simulated band edge profiles of compressive strained GaInAsP QW layer at (**a**) 0 V, (**b**) −1.2 V bias.

By applying a reverse bias voltage of −2 V, the bandgap is lowered to ~0.801 eV (equivalent to 1548 nm in wavelength) as shown in Fig. 2.19 (b), which corresponds to a Stark shift of ~42.1 meV ($\Delta\lambda_{Stark} \approx 77.2$ nm). However, these results are obtained without considering exciton broadening effect, which plays a significant role in lowering the rate of electronic transitions and thus flattens the absorption spectrum of the MQW active region. Moreover, the absorption coefficient of an EAM is proportional to the squared overlap integral of the electron and hole wave functions [$\alpha \propto |M|^2 \rho(h\nu)$]. When the applied DC field increases, the electron-hole overlap

decreases because of spatial separation of the two particles, weakening exciton binding energy, which in turn lowers the peak excitonic absorption.

Fig. 2.20 shows simulated modal absorption spectra ($\Gamma \times \alpha$) of compressive strained GaInAsP MQW, for which the HH band edge lies above that of the LH. As a result, the HH-E transitions occur at lower energies (HH_1-E_1 at 0.843 eV and HH_2-E_1 at 0.872 eV) as shown in Fig. 2.20 (a) for TE mode at 300K. The LH-E transition occurs at a higher energy since the LH band edge is shifted downward in *E-k* space. The absorption coefficient has a step-like shape following that of the density of states in QWs as discussed in Section 2.3.2.

When a reverse bias voltage of -1.2 V is applied perpendicular to the QW layers, the absorption edge shifts to a lower energy as shown in Fig. 2.20 (b) due to the QCSE. However, strength of the excitonic absorption peak decreases due to reduced electron-hole overlap (e.g., 160.5/cm at 0 V vs. 89.5/cm at -1.2 V). The reduction in absorption coefficient at longer wavelengths with applied bias is the reason why the extinction ratio of an EAM is wavelength dependent. For example, for our C-band EAMs, where the absorption edge occurs around 1470 nm, a higher ER is obtained at the lower edge of the C-band and the strength decreases as the operating wavelength increases (e.g., ~17 dB static extinction ratio at 1530 nm and ~12 dB at 1550 nm. See Chapter 3, Section 3.5). By operating the EAMs at a larger detuning from the absorption edge (typically 40−60 nm detuning [59]), the insertion loss can be reduced while achieving acceptable extinction ratios in the EAM's operating region.



(**a**) (**b**)

Fig. 2.20. Simulated modal absorption spectrum of compressive strained MQW (**a**) in TE mode, (**b**) comparison of absorption spectra in TE mode with (QCSE) and without applied field (0 V vs. −0.8 V). T = 300K (26.85°C).

On the other hand, because of interband transition selection rules, the HH-E and LH-E transitions contribute to TE and TM modes differently as discussed in Sections 2.5 and 2.6. Fig. 2.21 (a) shows modal absorption spectra of the compressive strained GaInAsP MQW for TE and TM modes at 300K without applying a DC field. As expected, the TM absorption begins at a higher energy level (LH_1-E_1 transition energy), making the devices more sensitive to TE-polarized light.

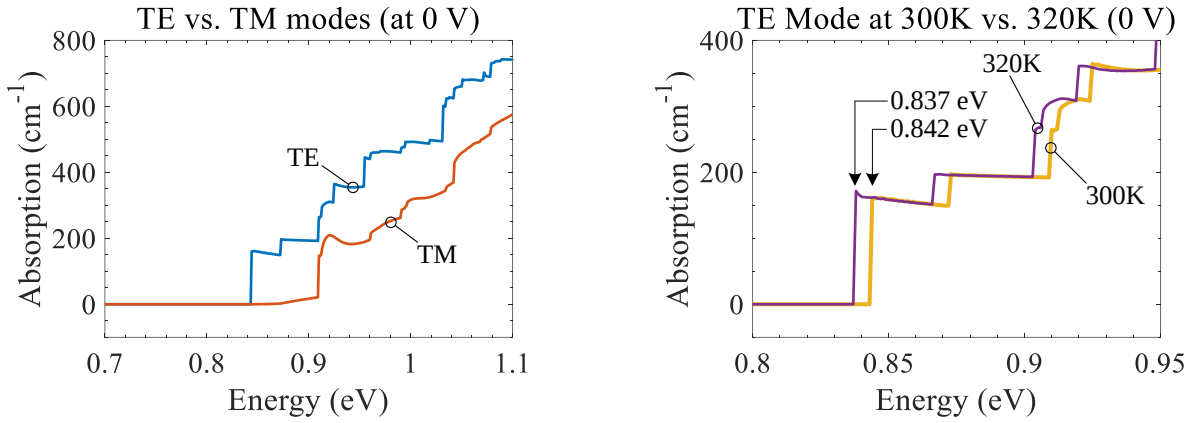


Fig. 2.21. Simulated modal absorption spectra of compressive strained GaInAsP MQW without a DC field (0 V bias): (**a**) for TE versus TM modes, (**b**) TE mode at 300K (26.85°C) vs. 320K (46.85°C).

Apart from Stark shift (decrease in the transition energy) as a result of QCSE, the bandgap of a semiconductor also tends to decrease with increasing temperature *T*, and for a bulk material, temperature-dependence of the bandgap is given by Varshni's empirical model as [74]:

$$E_g(T) = E_g(0) - \frac{\alpha T^2}{(\beta + T)}, \tag{2.41}$$

where, $E_g(0)$ is the bandgap at 0K, α and β are material constants. For quaternary QWs, the Varshni parameters are obtained by including bowing parameter as discussed in Section 2.1.

Fig. 2.21 (b) shows absorption coefficient of the compressive strained GaInAsP MQW at 300K and 320K (26.85°C and 46.85°C). For a 20°C-temperature increase, the bandgap decreases by ~6 meV ($\Delta\lambda_{thermal} \approx 10.6$ nm). That means, a thermal detuning of ~0.53 nm/°C occurs because of temperature variation. Therefore, devices that are compatible with semi-cooled or uncooled environments can be realized by properly choosing the absorption edge of the EAM. With that in mind, our C-band components are designed to operate up to 45°C whereas the O-band devices are

designed for 25°C operation. The effect of temperature on the transmission performance at a system-level is discussed in Chapter 4.

For comparison, Fig. 2.22 shows measured and simulated modal absorption spectra ($\Gamma \times \alpha$) of a C-band EAM of 189 nm thick MQW region, and measured spectrum of an O-band EAM of 209 nm thick MQWs. The simulated absorption coefficient is the same as the one shown in Fig. 2.20 (a). The experimental result in each case is obtained by subtracting (in decibel) the ASE power of an SOA integrated with an EAM from that of an SOA without an EAM. The simulation result is in a good agreement with the experimental data except for a slight broadening of the measured spectrum, which is due to exciton broadening (excitonic effects are not included/supported in the simulation). Moreover, the peak of the measured absorption is higher than that of the simulated absorption because of excitonic effects in the former case that enhance the EAM's absorption. On the other hand, the effect of a thicker MQW stack is visible in the measured absorption coefficient of the O-band EAM whose excitonic peak is higher than that of the C-band EAM. The extinction ratios of the EAMs studied in this thesis are presented in Chapter 3, Section 3.5.

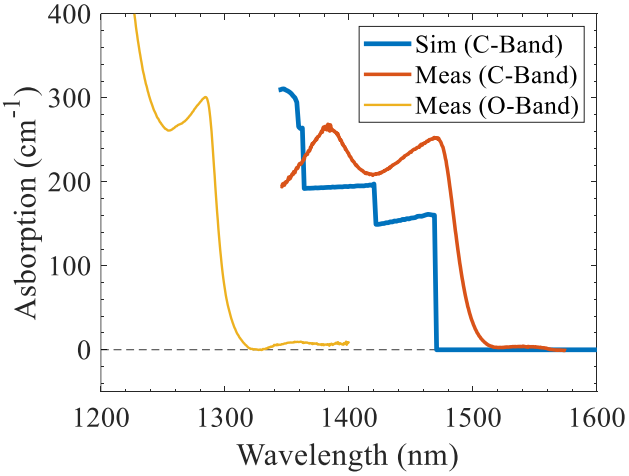


Fig. 2.22. Comparison of simulated and measured absorption spectra of a 150-µm long C-band EAM at 0 V.

2.7.2. Carrier Sweepout Time and Saturation Characteristics

Photogenerated carriers inside a MQW structure escape out of the wells (or disappear) mainly in three different ways: (i) recombination, (ii) tunneling through the barrier region, and (iii) thermionic emission as schematically illustrated in Fig. 2.23 [58].

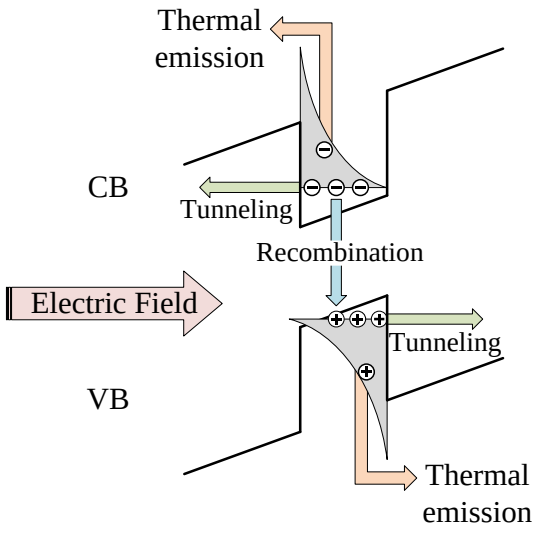


Fig. 2.23. Schematic of carrier escape mechanisms under the influence of an externally applied field (after [58]).

For an EAM, any form of recombination (spontaneous, nonradiative, Auger or stimulated recombination) is a loss mechanism and does not contribute to the photocurrent whereas the other two (thermal and tunneling escape mechanisms) contribute to the total photocurrent obtained from an EAM. The carrier sweepout time τ is determined by a combination of the three escape mechanisms, and assuming they are independent of one another, it is given by [58]:

$$\frac{1}{\tau} = \frac{1}{\tau_R} + \frac{1}{\tau_T} + \frac{1}{\tau_E}, \tag{2.42}$$

where, ${\tau_R}^{-1}$, ${\tau_T}^{-1}$ and ${\tau_E}^{-1}$ are recombination, tunneling, and thermal emission rates, respectively.

Once the carriers escape out of the wells either thermally or by tunneling through the barrier, they are accelerated by an externally applied field (saturation velocity in the order of 10^7 cm/s) to be collected by their respective metal contacts, creating a flow of electric current.

An important parameter in the operation of an EAM is its input power handling capability. As the input power increases, the density of photogenerated charge carriers also increases. The heavy-holes, having a relatively larger mass than electrons, begin to pile-up in the valence band of the QW so that the hole sweepout time increases. The saturation intensity I_{sat} (input optical power per unit area) of an EAM under the influence of a finite electric field is approximated as [58][82]:

$$I_{sat} = \frac{h\nu N_{sat}}{\alpha_0(d+L_b)} \cdot \frac{m_e^* + m_h^*}{m_e^*\tau_h + m_h^*\tau_e}, \tag{2.43}$$

where, h is Planck constant, ν is the optical frequency, N_{sat} is the saturation carrier density, α_0 is the unsaturated absorption coefficient of the EAM, d and L_b respectively are thicknesses of the well and barrier regions, m^* is effective mass (e: electron, h: hole), and τ is sweepout time.

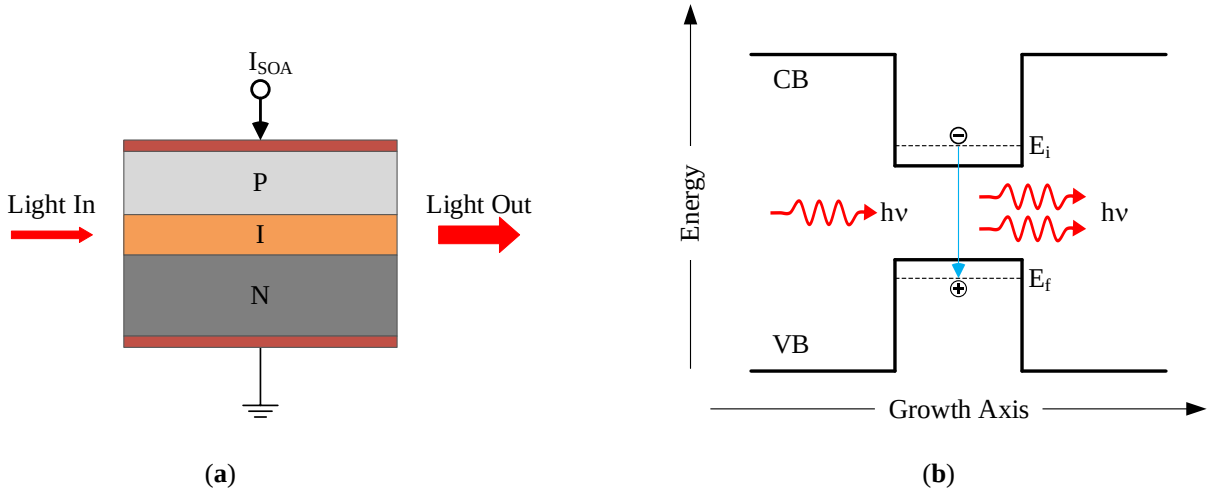
The saturation power of an EAM can be increased by: (i) increasing the applied field, (ii) decreasing the well and/or barrier thickness, and (iii) decreasing the bandgap discontinuities. Increasing the applied field allows sweeping out photogenerated charge carriers quickly by reducing the barrier height. On the other hand, decreasing the barrier thickness increases the tunneling rates of electrons and holes through it $\left[1/\tau_T \propto \frac{1}{d^2}\exp(-L_b)\right]$ [58]. However, a very thin barrier leads to an overlap in the wave functions of adjacent wells, which in turn increases the rate of recapturing of charge carriers. The third parameter (bandgap discontinuity) plays an important role in determining saturation characteristics of an EAM by increasing or decreasing the hole pile-up. Bandgap discontinuity also determines the thermal performance of semiconductor devices (e.g., SOAs and lasers) as the relatively lightweight electrons require large barrier offset when the devices operate at high temperatures. For EAMs, a reasonable CBO is still required in order to confine electrons and thus obtain strong excitonic effects at high temperatures.

Since electrons and holes have different effectives masses, they also have different sweepout times, creating an imbalance between electron and hole densities inside the active region. As a result of different electron and hole densities inside the QW region, space charge begins to build up that screen the externally applied field, causing field nonuniformity across the MQW structure, which ultimately reduces the Stark shift that can be achieved at a given bias voltage [58].

2.8. Amplifier Gain and Noise Figure

For SOAs, the downward transition (recombination), more specifically stimulated recombination, is the key process for amplifying the input light. For that reason, charge carriers are injected into the MQW region by applying a forward bias current as schematically illustrated in Fig. 2.24 (a). The injected current creates a population inversion, where the number of electrons in the CB exceeds that of the VB. Stimulated recombination occurs when a photon of energy $h\nu$ interacts

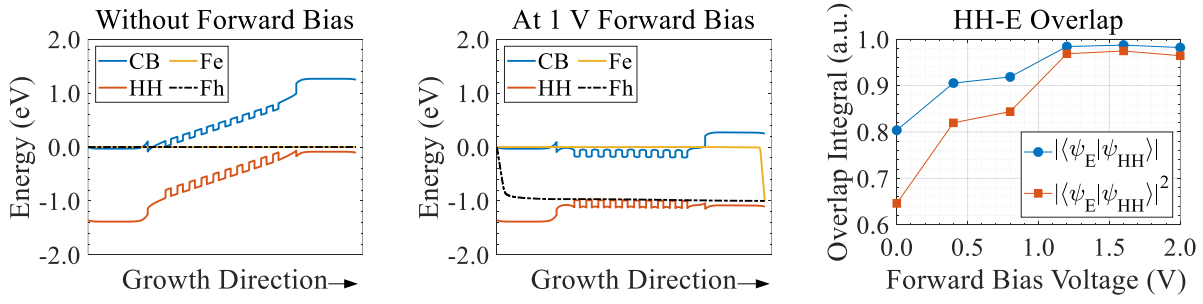
with an electron in the CB so that the electron recombines with a hole in the VB by giving off a photon of the same energy and direction as the incident photon as illustrated in Fig. 2.24 (b). Net amplification is obtained once the gain exceeds all internal losses.



(**a**) (**b**)

Fig. 2.24. Schematic diagram of (**a**) an SOA, and (**b**) the process of light amplification through stimulated emission.

In the absence of a forward bias current, the electronic band structure is tilted by the built-in voltage as shown in Fig. 2.25 (a), which is similar to the case of an EAM. However, applying a forward bias current to the SOA reverses the tilting and results in a symmetric band structure as shown in Fig. 2.25 (b). In the latter case, the electron-hole overlap approaches unity ($M \approx 0.99$, $M^2 \approx 0.98$) as shown in Fig. 2.25 (c), maximizing the probability of stimulated recombination and thus increasing the amplifier gain.



(**a**) (**b**) (**c**)

Fig. 2.25. Simulated electronic band structure of a compressive strained GaInAsP MQW (**a**) without and (**b**) with applied forward bias, (**c**) heavy-hole to conduction band overlap integral as a function of forward bias voltage.

The modal gain $g(\nu)$ of a MQW-based gain section is given by [39][52]:

$$g(\nu) = \frac{\pi q^2 \hbar}{nc\varepsilon_0 m_0^2} \frac{1}{h\nu} \sum_m \sum_n \int_0^\infty \frac{2}{V} |M|^2 [f_c(E_{cm}) - f_v(E_{vn})] \mathscr{L}(E - E_{mn}) dE, \tag{2.44}$$

where, q is the elementary charge, h ($\hbar$) is Planck's constant (reduced), n is refractive index of the active region medium, c is speed of light in vacuum, ε_0 is the permittivity of free space, m_0 is the electron mass, ν is the optical frequency, V is the normalization volume, M is the electron-hole overlap, f_c and f_v respectively are Fermi-Dirac distributions in the conduction and valence bands, and $\mathscr{L}(E)$ is the linewidth broadening factor, which is approximated to a Lorentzian function for QWs as [39]:

$$\mathscr{L}(E - E_{mn}) = \frac{1}{\pi} \frac{\hbar/\tau_{int}}{(\hbar/\tau_{int})^2 + (E - E_{mn})^2}, \tag{2.45}$$

where, τ_{int} is interband relaxation time (commonly referred to as T_2). Its typical value is 0.1−1 ps.

The SOA gain depends on both the incident photon energy and intensity of light inside the gain section (photon density). Using a simple homogenously broadened two-level system, the material gain can be expressed in terms of the signal power (P) being amplified by the SOA and the saturation power of the gain medium (P_{sat}) as [43][75]:

$$g(\nu) = \frac{g_0}{1 + (\nu - \nu_0)^2 T_2^2 + P/P_{sat}}, \tag{2.46}$$

where, g_0 is the maximum value of the material gain, ν_0 is the bandgap transition frequency.

For SOAs operating in the unsaturated regime ($P \ll P_{sat}$), the term P/P_{sat} becomes negligible, and (2.46) reduces to [43][75]:

$$g(\nu) = \frac{g_0}{1 + (\nu - \nu_0)^2 T_2^2}. \tag{2.47}$$

Equation (2.47) shows maximum amplification can be obtained by aligning the operating frequency (wavelength) of the SOA with its bandgap transition frequency (wavelength).

Some of the most important SOA performance parameters are gain, saturation output power, and noise figure (NF). The amplifier gain (G) depends on the optical confinement factor Γ as well as the cavity length L_{SOA}, and it is given by:

$$G = \frac{P_{out}}{P_{in}} = \exp\left(\Gamma g L_{SOA}\right), \tag{2.48}$$

where, P_{in} is the input optical power, P_{out} is the output signal power after amplification, g is the material gain. This shows that, for a given material system, the SOA gain can be increased by increasing: (i) the optical confinement factor, which can be achieved by increasing the number of QW layers in a MQW structure, (ii) the SOA cavity length.

Apart from gain, SOAs are also characterized by saturation output power. As the input power increases (increasing photon density), the carrier density decreases because of the stimulated emission process, reducing the population inversion as the carrier density is unable to cope with the large photon density, which ultimately leads to gain saturation. The saturation output power ($P_{o,sat}$) is defined as the output power at which the amplifier gain drops by 3 dB (half of the small-signal gain), and is given by [39][64]:

$$P_{o,sat} = ln2 \cdot \frac{G_0}{G_0 - 2} \cdot \frac{A}{\Gamma} \frac{h\nu}{a_1 \tau} = ln2 \frac{G_0}{G_0 - 2} P_{sat}, \tag{2.49}$$

where, A is the cross-sectional area of the gain medium (width × thickness), $h\nu$ is the photon energy, a_1 is differential gain of the gain medium, τ is carrier lifetime, and G_0 is unsaturated (small signal) gain of the SOA given by: $G_0 = \exp(\Gamma g_0 L_{SOA})$. The term $\frac{A}{\Gamma}\frac{h\nu}{a_1 \tau}$ is the saturation power P_{sat} of the gain medium.

Maximizing the saturation output power is important for linear operation of amplifiers for applications, for example, in wavelength division multiplexing (WDM) where the combined optical power is relatively high. For other nonlinear applications such as wavelength conversion based on four wave mixing (FWM) and self (cross) phase modulation (SPM, XPM), early SOA saturation is desirable [64]. Moreover, gain saturation of SOAs can also be exploited in bidirectional transmission over a single wavelength using reflective devices (e.g., RSOA-EAM) [37][38]. In the latter case, the SOA section can be used to erase the modulated downlink signal by saturating the SOA and remodulating the CW light with uplink information.

From (2.49) shows that $P_{o,sat}$ can be increased by decreasing the optical confinement factor and/or increasing the cross-sectional area [52]. However, decreasing the confinement factor has the opposite effect on the amplifier gain [cf. (2.48)]. Similarly, increasing the cross-sectional area

requires a wide waveguide, which can cause multimode operation of the SOA. As a result, there is a tradeoff between $P_{o,sat}$ and SOA gain. Nevertheless, for large SOA gains ($G_0 \geq 20$ dB), $P_{o,sat}$ of (2.49) becomes less dependent on the amplifier gain ($P_{o,sat} \approx 0.69P_{sat}$) [43][64]. In that case, the first step to maximize $P_{o,sat}$ is reducing the optical confinement factor. As such, fewer QWs are commonly used for SOAs than EAMs, and the amplifier gain is enhanced by increasing the cavity length. The SOAs in our PICs have one less QW layer than their respective EAMs.

Another important characteristic of an SOA is the noise figure, which provides information about the quality of the transmitted signal. As part of the amplification process, the SOA adds noise in the form of amplified spontaneous emission (ASE) light. The degradation of the signal quality is quantified using the amplifier NF, defined as the ratio of input to output signal-to-noise ratios (SNRs), i.e., [77][78]:

$$NF = \frac{SNR_{in}}{SNR_{out}} = \frac{1}{G} + \frac{2P_{ASE}}{Gh\nu B_0}, \tag{2.50}$$

where, G is the SOA gain, P_{ASE} is the ASE power co-polarized with the input light, $h\nu$ is photon energy, and B_0 is the optical bandwidth on which the ASE light is measured (P_{ASE}/B_0 is spectral density of the ASE light). Apart from increasing gain and filtering the signal at the receiver side to remove part of the ASE light, minimizing optical feedback plays an important role in achieving low NF values. The performances of the SOAs in our PICs are presented in Chapter 3, Section 3.4.

2.9. Fabrication and Epitaxial Growth Process Flow

Our components are realized using GS-MBE on an n-doped InP substrate. The fabrication process flow with the main epitaxy steps is schematically illustrated in Fig. 2.26 [51]. The first epitaxy step involves growing the EAM's MQW structure as shown in (a). Since the SSC is based on the same MQW stack as the EAM, the two sections are grown within the same epitaxy step. Following the first epitaxy step, a hard mask is deposited on top of the spacer layer (top p-InP as discussed in Section 2.2), and a pattern is transferred to the mask using photoresist as shown in (b).

In the next epitaxy step, the region outside the EAM and the SSC sections is etched using inductively coupled plasma (ICP) etching as illustrated in Fig. 2.26 (c). Then, the SOA's MQW stack is regrown as illustrated in (d) while aligning the SOA's MQW stack with that of the EAM

and the SOA sections, realizing a butt-joint (BJ) monolithic integration of the building blocks (BBs). Butt-joint integration allows optimizing the MQW structures of the EAM and the SOA sections independently. The key challenge in BJ integration is aligning the MQWs of different building blocks that have different number of QW layers, which is necessary in order to minimize reflection of light at the BJ interfaces. Moreover, refractive index continuity must be maintained at the BJ interfaces so that light propagates from one section to another smoothly.

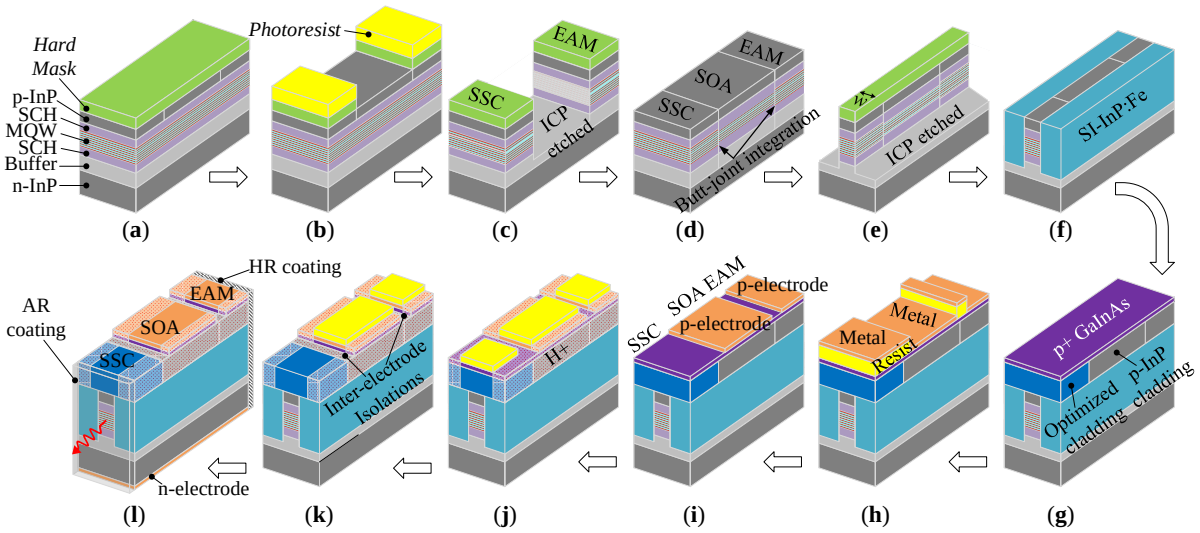


Fig. 2.26. Schematic illustration of epitaxial growth process flow based on butt-joint integration technique and SI-BH waveguide definition: (**a**) hard mask deposition on the EAM's MQW structure grown in the first epitaxy step, (**b**) hard mask etching using photoresist, (**c**) ICP etching of the region outside the EAM and the SSC, (**d**) SOA's MQW regrowth, (**e**) ICP etching to define a ridge width of w (w = 1.3−1.5 μm), (**f**) SI-BH regrowth (laterally growing Fe-doped InP layer), (**g**) growing p-InP cladding and ternary p-contact layers, (**h**) metal deposition using photoresist, (**i**) defining p-electrodes for EAM and SOA sections using lift-off, (**j**) H+ ion implantation laterally as well as in the region between BBs, (**k**) ternary opening to form inter-electrode isolations, (**l**) final PIC after removing the photoresist and AR/HR treatments.

The number of BJ interfaces depends on the actual device configuration. In the REAM-SOA configuration shown in Fig. 2.26, there are two BJ interfaces—one between the EAM and the SOA and another between the SOA and the SSC sections. When the EAM and the taper are next to one another along the optical path, for example in an RSOA-EAM configuration where the input light sees the EAM before the SOA, only one BJ interface exists (between the EAM and the SOA sections) because the EAM and the SSC have the same MQW stack. That means, BJ interface exists only when there is a difference in the number of QW layers among the photonic BBs.

Once the three MQW structures are grown, the hard mask previously transferred to the EAM and the SSC sections is removed. Then, a new hard mask is deposited, and a pattern is transferred to it using a photoresist, defining a ridge width w of 1.3−1.5 μm as shown in Fig. 2.26 (e), in preparation for the SI-BH waveguide definition. The region outside the core waveguide is etched down for a thickness of about 2 μm from the top of the wafer using ICP etching. A ridge width of 1.5 μm is used for our C-band devices whereas the ridge is 1.3 μm for the O-band devices, both of which are chosen to obtain monomode operation of the respective devices. After etching the region outside the core waveguide, an semi-insulating (SI) InP layer (iron-doped, SI-InP:Fe) is grown laterally burying the ridge and realizing an SI-BH waveguide as shown in (f). The SI-BH layer provides lateral photon and carrier confinement.

Following the SI-BH regrowth step, a p-InP (zinc or beryllium doped) cladding layer is grown covering the entire wafer as shown in Fig. 2.26 (g). An optimized cladding layer is used for the SSC section in order to minimize absorption of light by the strongly p-doped cladding layer and thus minimize insertion loss of the passive sections (e.g., the SSC). Within the same epitaxy step, a strongly p-doped ternary layer (p+ GaInAs) is grown on top of the p-InP cladding layer to form the p-contacts of the active sections (EAM and SOA) as illustrated in (g).

The p-contacts of the EAM and the SOA sections are metalized by depositing layers of titanium, platinum, and gold (Ti/Pt/Au), making them ohmic contacts as shown in Fig. 2.26 (h). The regions where metal contacts are not required are covered by a photoresist so that the metals deposited on the resist will be washed away in the following step as shown in (i). This process of covering passive sections with a photoresist and removing metal contacts from those areas is known as the lift-off process. The metal contacts are also annealed so that the deposited metals spread uniformly across the p-contact layer, providing optimal electrical connectivity (low access resistance).

Following metallization, ion implantation is performed by using a photoresist mask of ∼10 μm width to cover the BBs. Then, the p-contact area is bombarded with accelerated H+ ions as shown in Fig. 2.26 (j). Ion implantation is required to reduce the p-contact width to ∼10 μm, which improves injection efficiency of SOAs (and lasers) by localizing the injected carriers to the MQW active region. The p-contact width can even be further reduced by using a narrower mask, but the access resistance increases with decreasing electrical contact area. Moreover, bombarding the cladding layer with H+ ions very close to the active region requires further attention as it can

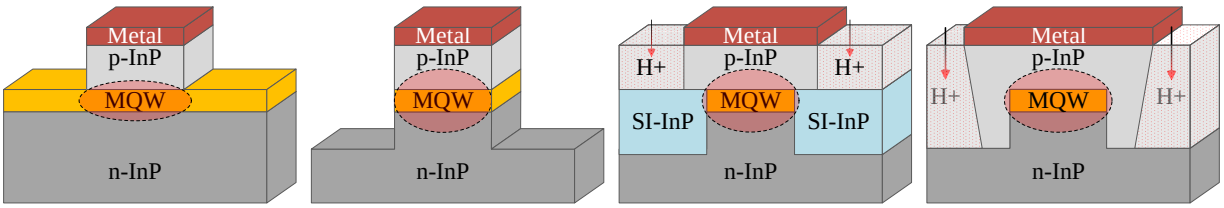
damage the core waveguide. The 10-µm p-contact provides an access resistance of as low as 4 Ω [15]. In addition to reducing the p-contact area, H+ ion implantation also reduces electrical leakage between adjacent electrodes, for example, between the EAM and the SOA sections.

Finally, a ternary etching (opening) is performed to complete the inter-electrode isolation, where the highly p-doped ternary layer (p+ GaInAs) is removed by using a resist mask and ICP etching as illustrated in Fig. 2.26 (k), forming an isolation trench. The n-electrode is formed by depositing a stack of Ti/Pt/Au metallic layers. The fabricated chips are cleaved and treated with anti-reflection (AR) and high-reflection (HR) coatings applied to the front and rear facts of the chip, respectively. The final structure of a PIC comprising an EAM, an SOA and an SSC is illustrated in (j).

2.10. Semi-Insulating Buried Heterostructure

For lateral photon confinement, there are several commonly used waveguide technologies, and the most common ones are shallow or deep ridge waveguides (RWs) and buried heterostructures (BHs) [79]. In the shallow RW case, the top cladding layer (outside the core waveguide section) is etched down up to a few micrometers as illustrated in Fig. 2.27 (a). The etching depth goes deeper for deep RWs in order to have lateral photon confinement by air as shown in Fig. 2.27 (b).

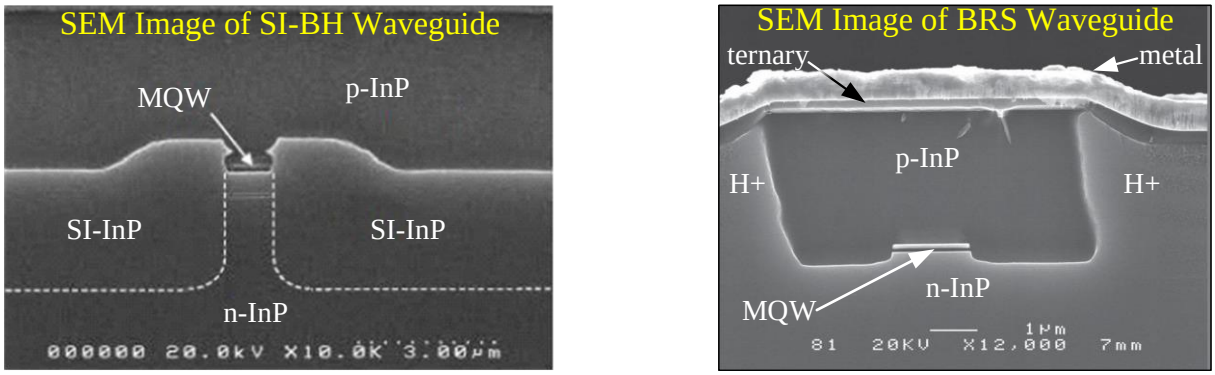
The shallow RW is the simplest and cost-effective waveguide solution as it involves fewer epitaxy steps, but it results in an asymmetric mode profile with an exaggerated elliptical shape as shown using dashed lines in Fig. 2.27 (a) [52]. The deep RW, on the other hand, provides a relatively more circular mode shape, which is comparable to that of BHs. However, low thermal conductivity of air laterally surrounding the waveguide is less efficient in terms of thermal dissipation, making it a less preferred option, especially when semi-cooled or uncooled operation of devices is required, which is the case for low-cost access and metro network transceivers.



(**a**) (**b**) (**c**) (**d**)

Fig. 2.27. Schematics diagrams of different waveguide technologies: (**a**) shallow ridge (**b**) deep ridge, (**c**) SI-BH, and (**d**) buried ridge stripe waveguides (adapted from [52]).

In BHs, the core waveguide is buried inside an InP layer. In the case of SI-BH waveguides, an SI-InP (typically Fe-doped) is grown laterally, and the top cladding layer is a p-doped InP (zinc or beryllium doped) as illustrated in Fig. 2.27 (c). For BRS, on the other hand, the same p-doped layer is grown both laterally and on the top, as shown in Fig. 2.27(d). In both SI-BH and BRS cases, H+ ion implantation is performed to increase electrical resistance of the lateral layers as well as to reduce the p-contact area to ~10 μm. As a result, SI-BH and BRS minimize electrical leakage by preventing lateral spreading of charge carriers. In the case of SOAs and lasers, improved lateral carrier confinement enables the realization of devices with low threshold currents. Fig. 2.28 shows scanning electron microscope (SEM) images of SI-BH (left) and BRS (right) waveguides [15].



(**a**) (**b**)

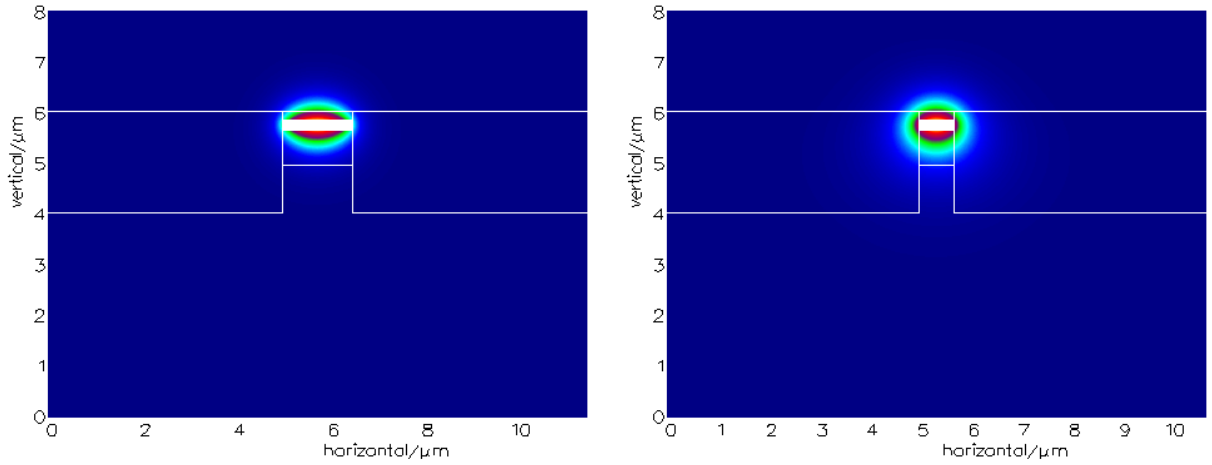
Fig. 2.28. Scanning electron microscope images of (**a**) SI-BH and (**b**) BRS waveguides (after [15]).

Compared to RWs, buried waveguides (SI-BH and BRS) result in a lower access resistance ($R \approx 4\ \Omega$) because of a relatively wider p-contact area (~10 μm for BH vs. 2−3 μm for RW) [15], which improves energy efficiency and reduces device self-heating.

Although both SI-BH and BRS suffer at high current, SI-BH has an advantage because of the SI-InP layer (higher electrical resistance) instead of a conductive p-InP for BRS. Moreover, SI-BH waveguides have lower lateral optical loss than both RWs and BRS because of the SI-InP.

BH waveguide technologies provide symmetric mode profiles. Fig. 2.29 shows simulated mode profiles of SI-BH waveguides of 1.5 μm (left) and 0.7 μm (right) ridge widths. A circular mode profile is desirable for improved fiber coupling efficiency, which also relaxes the fiber alignment process. Moreover, BH waveguides exhibit improved lateral thermal dissipation efficiency with

respect to RWs because InP has higher thermal conductivity than both GaInAsP (for shallow RWs) and air (for deep RWs), i.e., 0.68 W/cm-℃ for InP vs. 0.06 W/cm-℃ for GaInAsP [50].



(**a**) (**b**)

Fig. 2.29. Simulated mode profiles of SI-BH waveguides of (**a**) 1.5 μm and (**b**) 0.7 μm ridge widths.

Another important advantage of SI-BH over the other waveguide technologies (even though it is more complex) is that it allows reaching better performance and realize high-speed modulators by lowering the EAM's capacitance. The E/O bandwidth of an EAM is primarily limited by RC time constant, and the maximum 3-dB bandwidth ($f_{3\text{-dB}}$) is given by [59]:

$$f_{3-dB} = \frac{1}{2\pi\left[R_s + \left(\frac{1}{R_g + R_L}\right)^{-1}\right]C}, \tag{2.51}$$

where, R_s is series resistance of the EAM (in the order of a few Ohms), R_g is resistance of the signal generator (typically 50 Ω), R_L is the load resistance (EAMs are terminated with a 50 Ω resistor on chip for impedance matching with the source), and C is the total resistance of the EAM.

The capacitive contributions of an EAM come from the reverse-biased PIN junction capacitance (C_{PIN}), parasitic capacitances ($C_{parasitic}$) and bonding pad capacitance (C_{pad}) as illustrated in Fig. 2.30 (a). The three capacitances can be estimated using a parallel plate capacitor model as:

$$C = \frac{\varepsilon_0 \varepsilon_r A}{d}, \tag{2.52}$$

where, ε_0 is permittivity of free space, ε_r is dielectric constant of the medium between the parallel plates, A is the overlap area of the plates. The parameter d is the gap between the parallel plates, which is the thickness of the undoped region for C_{PIN}, the gap between the p-InP and the n-InP layers for $C_{parasitic}$, and the gap between the bonding pad and the n-InP substrate for C_{pad}.

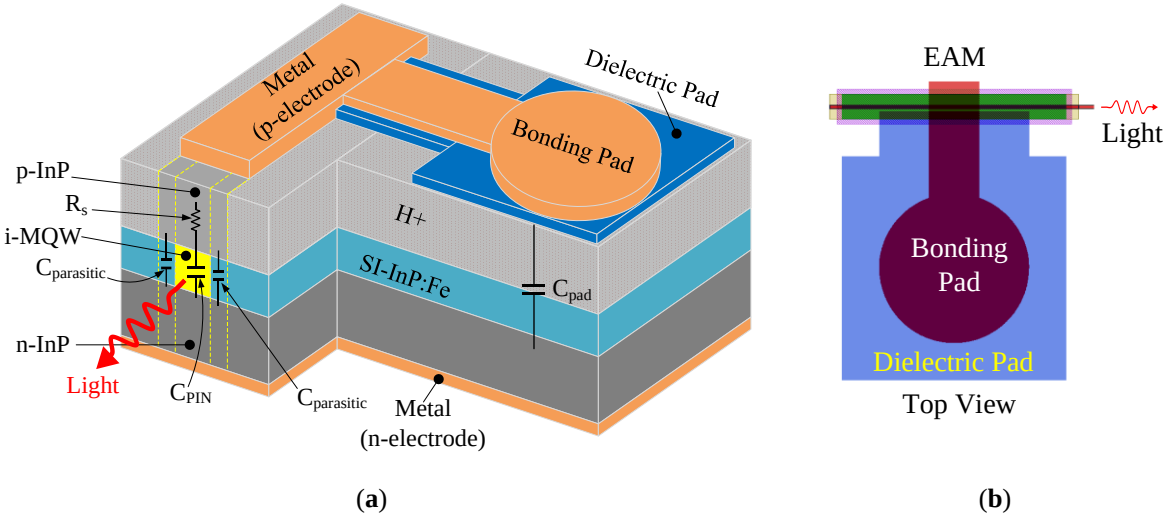


Fig. 2.30. (**a**) Schematic of an EAM showing different capacitive effects, (**b**) top view of the layout of an EAM.

The junction capacitance depends on thickness of the MQW active region, and it can be reduced by increasing the number of QW layers. However, the number of QW layers has to be increased sensibly in order to avoid the risk of EAM saturation (increased optical confinement factor, which also increases insertion loss). A thick MQW region also reduces the effective DC field (Stark shift) that can be obtained at a given reverse bias voltage. Furthermore, C_{PIN} also depends on the overlap between n- and p-doped InP regions, which is determined by the waveguide width (1.5 µm for C-band devices and 1.3 µm for O-band devices).

The parasitic capacitance, on the other hand, is due to the fact that the p-electrode is wider than the core waveguide (~10 µm vs. 1.3−1.5 µm), and it depends on the gap between the p- and n-doped InP layers, separated by the SI-InP layer (~2 µm thickness).

Similarly, C_{pad} depends on the overlap region between the bonding pad and the n-InP substrate, separated by a combination of the SI-InP and ion-implanted p-InP layers (>4 µm gap in total). In order to further reduce C_{pad}, a dielectric bonding pad (SiO_2) layer is added on top of the ion-implanted layer, which itself is on top of the SI-InP layer. Fig. 2.30 (b) shows top view of the mask

layout of an EAM with the dielectric pad. For EAMs that are several tens of micrometers long, which are the lengths of interest in our case, both $C_{parasitic}$ and C_{pad} are relatively small, and . In that case, C_{PIN} becomes the dominant contribution of the EAM's capacitance. However, as the EAM length becomes very short, where the device can no longer be considered as a lumped element, the two capacitance contributions ($C_{parasitic}$ and C_{pad}) become significant. Therefore, high-speed modulators can be realized by using shorter EAMs while taking advantage of the SI-InP layer, H+ implantation as well as the dielectric contact pad.

Fig. 2.31 shows calculated C_{PIN} and $C_{parasitic}$ for two ridge widths together with series resistance of the EAM (left) and the maximum 3-dB bandwidths of EAMs having 189 nm and 209 nm thick active regions using the RC model. The two active region thicknesses are similar to the MQW regions of our C-band and O-band EAMs, respectively. The calculated pad capacitance is ~35.1 fF. The 3-dB bandwidth increases with decreasing the EAM length because of decreasing C_{PIN} and $C_{parasitic}$. For example, the maximum 3-dB bandwidth of the 80-µm long C-band EAM is ~35 GHz (C_{total} ≈ 127 fF) and that of the 150-µm long EAM is ~25.5 GHz (C_{total} ≈ 207 fF).

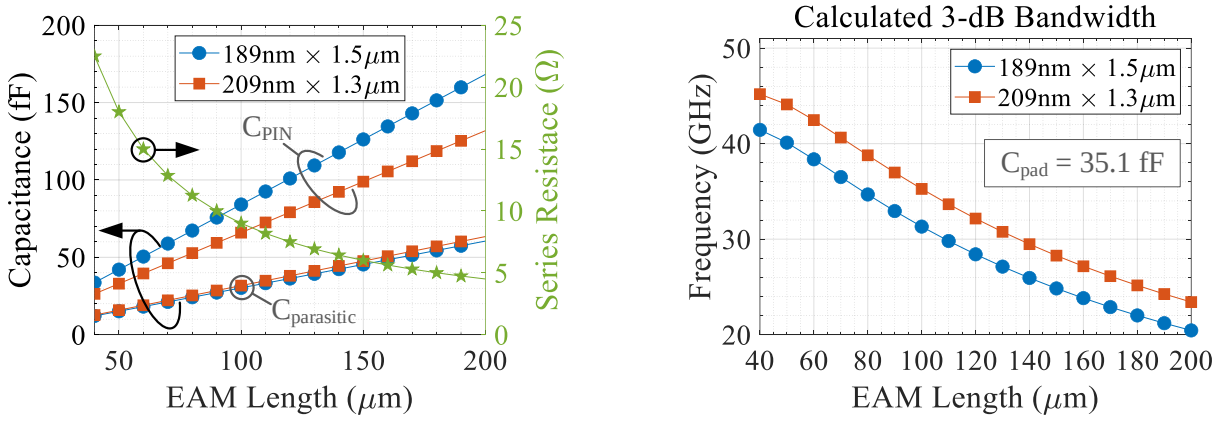


Fig. 2.31. (**a**) Calculated PIN junction and parasitic capacitances of as a function of EAM length, (**b**) maximum 3-dB bandwidth RC model (C_{pad} = 31.5 fF; $f_{3\text{-dB}} = 1/2\pi RC_{total}$, where $C_{total} = C_{PIN} + C_{parasitic} + C_{pad}$).

The E/O bandwidth of an EAM also increases with increasing the thickness of the active region as well as decreasing the waveguide width (reducing the cross-sectional area), which is the case for the O-band devices. For example, by using one more QW layer with respect to the C-band devices, calculated 3-dB bandwidth of the 100-µm long O-band EAM is ~37.5 GHz (C_{total} ≈ 125 fF), which

is comparable to the bandwidth of the 80-µm long C-band EAM (assuming the same R_s). However, the modulation strength of an EAM scales down with decreasing its length. As a result, there is a tradeoff between bandwidth and modulation strength of an EAM. The frequency responses of different device configurations studied in this thesis are discussed in Chapter 3, Section 3.6.1.

2.11. Device Structure and Schematics

Our PICs have three basic building blocks: EAM, SOA and SSC. The SSC is based on a bent tapered waveguide with a 7°-tilted output. The taper broadens the optical mode and thus improves input/output coupling efficiency whereas the tilt minimizes optical feedback to the SOA gain section. The devices are based on compressively strained GaInAsP MQWs grown on an InP substrate. To realize a reflective device configuration, the devices are cleaved and treated with AR/HR coatings applied to the front/rear facts of the integrated circuit. Depending on the positions of the EAM and the SOA along the optical path, two PIC configurations can be realized, namely, reflective EAM-SOA (REAM-SOA) and RSOA-EAM. Fig. 2.32 shows a schematic diagram of an REAM-SOA PIC with integrated SSC (the taper bending is not shown here).

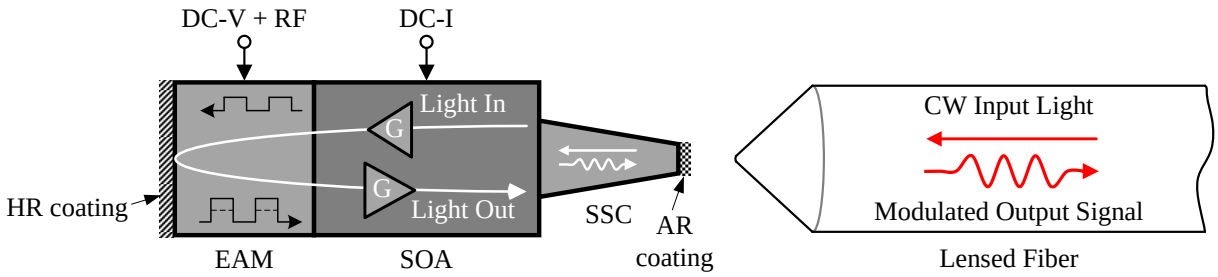


Fig. 2.32. Schematic diagram of an REAM-SOA PIC with integrated SSC. A lensed fiber is used for coupling light to and from the PIC.

The principle of operation of an REAM-SOA is as follows: a continuous wave (CW) light generated by an external monochromatic source is injected into the PIC using a lensed fiber via the SSC. Inside the PIC, the input light is first amplified by the SOA, and then modulated by the EAM in its forward path (light propagating from right to left). When the optical signal hits the rear facet of the PIC, it is reflected by the HR coating. Then, it is further modulated by the EAM and re-amplified by the SOA in its reverse path. After going through the double amplification and absorption process, the optical signal is coupled to the output fiber, which is the same lensed fiber

used for input coupling. Bidirectional transmission over a single lensed fiber is enabled by using an external optical circulator.

The operating principle of an RSOA-EAM is similar to that of the REAM-SOA except that the input light first passes through the EAM section before it reaches the SOA section as schematically illustrated in Fig. 2.33. However, because of large round-trip delay inside the SOA section in an RSOA-EAM configuration, which causes a phase difference between the modulated signals in the forward and reverse paths, an RSOA-EAM results in a lower modulation bandwidth (e.g., see Chapter 3, Section 3.6.1). From the vertical design point of view, the respective BBs in the two PIC configurations have similar designs. Hence, most of the discussions in this manuscript focus on the REAM-SOA configuration, and the RSOA-EAM is explicitly mentioned only when needed.

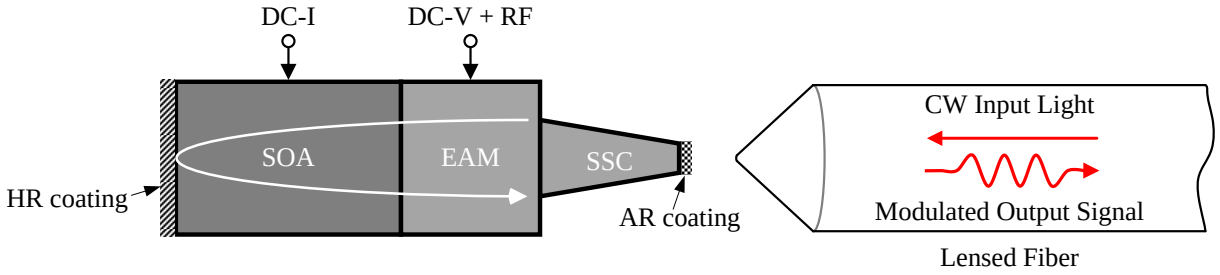


Fig. 2.33. Schematic diagrams of an RSOA-EAM and a lensed fiber used for input/output coupling.

Fig. 2.34 shows a picture of an REAM-SOA chip-on-carrier (CoC) mounted on a 23°-tilted high frequency (HF) carrier. The 23° tilt is chosen because it is the angle at which light coming out of a 7°-tilted SSC bends during input/out coupling because of diffraction at the waveguide-air interface. The refraction angle of light passing through two different media is given by Snell's law, which reads:

$$n_1 \sin\theta_1 = n_2 \sin\theta_2, \tag{2.53}$$

where, n_1 is effective refractive index of the GaInAsP MQW waveguide (~3.2), n_2 is refractive index of air (~1), θ_1 is tilt angle of the SSC (7°), and θ_2 is the refraction angle of light (~23°). Because of a tilted CoC configuration, the lensed fiber lies in the horizontal plane (along the optical axis), without the need for angled fiber holders.

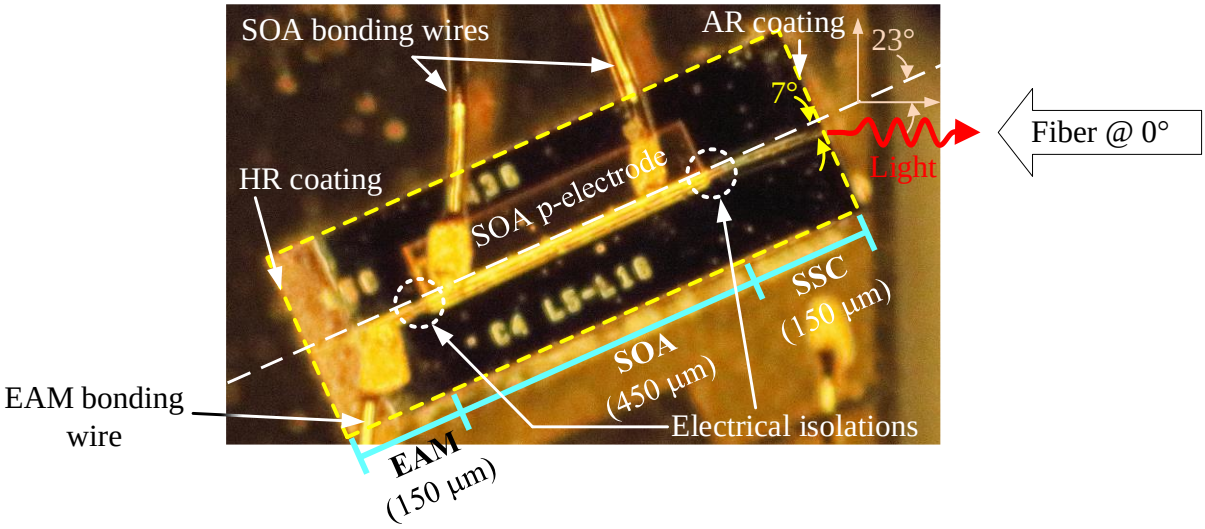
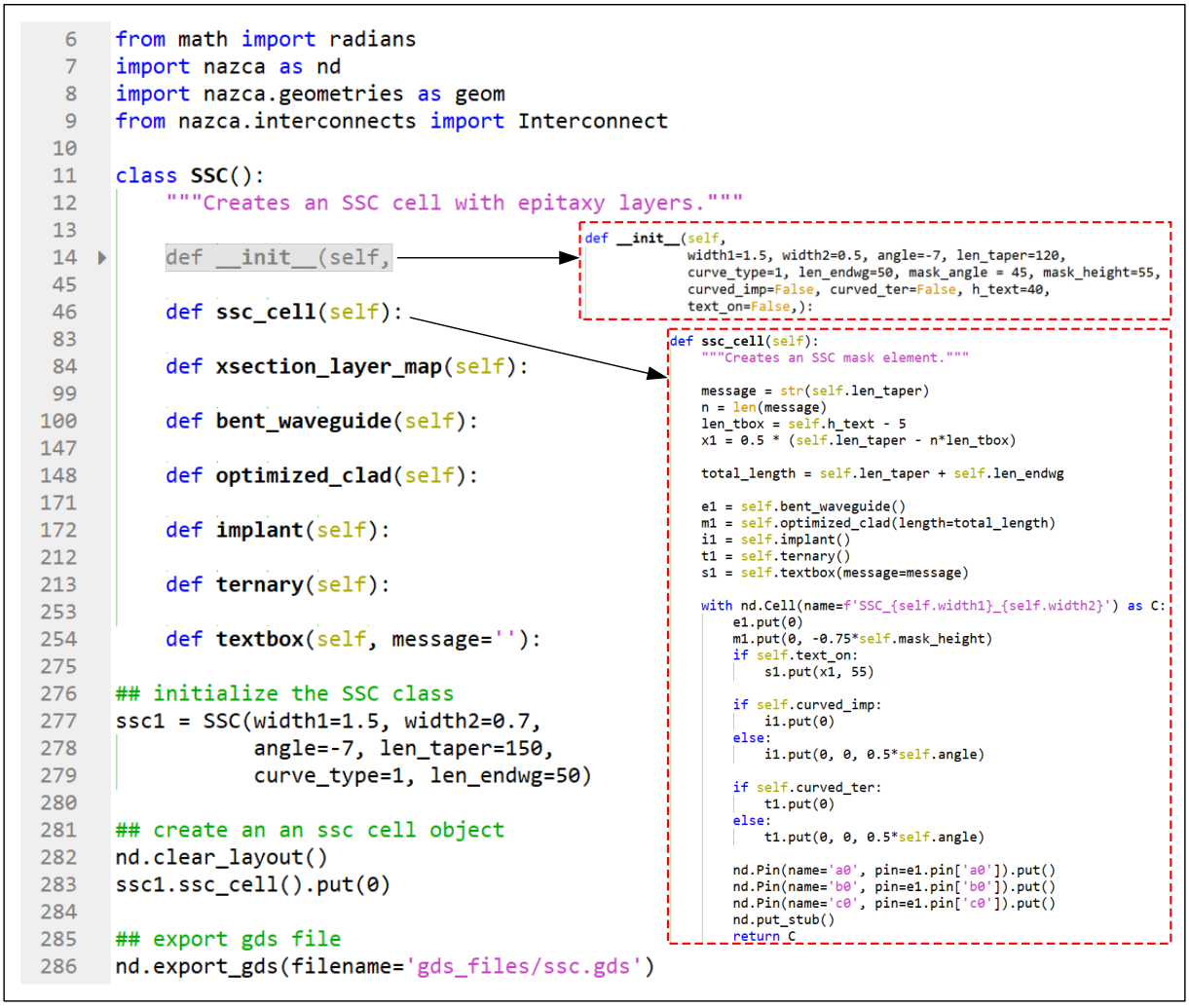


Fig. 2.34. Picture of an REAM-SOA chip-on-carrier mounted on a 23°-tilted high frequency carrier.

2.12. Optical Mask Layout

There are several industry standard tools available for preparing optical mask layouts based on either graphical user interfaces (e.g., Tanner L-Edit [83]) or scripting tools (e.g., Nazca Design [84]). Our components are designed using a licensed version of L-Edit. However, scripting tools offer more design flexibility and enable a parametric cell (PCell) design approach. In that case, one can create a BB library that can be used in a wide range of applications while the design parameters can be easily modified, and several instances of a single cell can be used to create a complex mask layout. The mask layouts shown in this section are generated using Nazca Design, which is an open-source Python-based design tool [84].

As an example of a PCell design, Fig. 2.35 shows an excerpt of a class-based SSC cell using Nazca, where the epitaxy layers are defined as functions and called when creating the PCell. For example, the SSC's parameters can be identified as input/output waveguide width, tilt angle, type of curve (single curve or cascaded curves), and length of the end waveguide used for cleaving purpose (see Chapter 3, Section 3.1.1 for more details about the SSC). Geometrically, the implant and ternary layers can also be designed to follow a curved path (similar to the waveguide section), or rectangular shapes tilted at a certain angle. The SSC cell can be created once, and its instances can be used several times to create a more complex PIC layout.



```python
from math import radians
import nazca as nd
import nazca.geometries as geom
from nazca.interconnects import Interconnect

class SSC():
    """Creates an SSC cell with epitaxy layers."""

    def __init__(self,
                 width1=1.5, width2=0.5, angle=-7, len_taper=120,
                 curve_type=1, len_endwg=50, mask_angle = 45, mask_height=55,
                 curved_imp=False, curved_ter=False, h_text=40,
                 text_on=False,):

    def ssc_cell(self):

    def xsection_layer_map(self):

    def bent_waveguide(self):

    def optimized_clad(self):

    def implant(self):

    def ternary(self):

    def textbox(self, message=''):

## initialize the SSC class
ssc1 = SSC(width1=1.5, width2=0.7,
           angle=-7, len_taper=150,
           curve_type=1, len_endwg=50)

## create an an ssc cell object
nd.clear_layout()
ssc1.ssc_cell().put(0)

## export gds file
nd.export_gds(filename='gds_files/ssc.gds')
```

```python
def ssc_cell(self):
    """Creates an SSC mask element."""

    message = str(self.len_taper)
    n = len(message)
    len_tbox = self.h_text - 5
    x1 = 0.5 * (self.len_taper - n*len_tbox)

    total_length = self.len_taper + self.len_endwg

    e1 = self.bent_waveguide()
    m1 = self.optimized_clad(length=total_length)
    i1 = self.implant()
    t1 = self.ternary()
    s1 = self.textbox(message=message)

    with nd.Cell(name=f'SSC_{self.width1}_{self.width2}') as C:
        e1.put(0)
        m1.put(0, -0.75*self.mask_height)
        if self.text_on:
            s1.put(x1, 55)

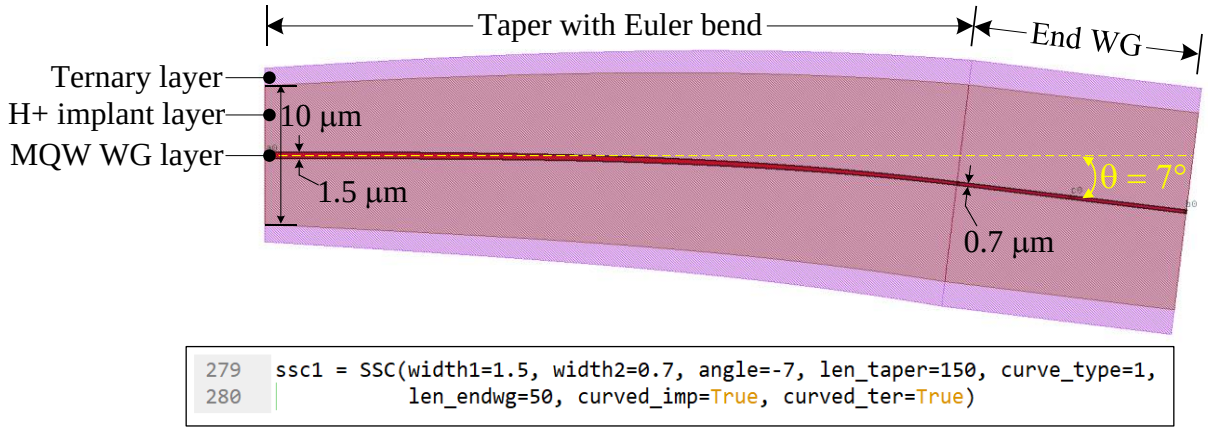
        if self.curved_imp:
            i1.put(0)
        else:
            i1.put(0, 0, 0.5*self.angle)

        if self.curved_ter:
            t1.put(0)
        else:
            t1.put(0, 0, 0.5*self.angle)

        nd.Pin(name='a0', pin=e1.pin['a0']).put()
        nd.Pin(name='b0', pin=e1.pin['b0']).put()
        nd.Pin(name='c0', pin=e1.pin['c0']).put()
        nd.put_stub()
        return C
```

Fig. 2.35. Excerpt of a Python code for creating an SSC PCell using Nazca Design.

Fig. 2.36 shows the mask layout of a 0.7-µm SSC with a 7°-tilted output created using Nazca. The taper begins with a straight section and slowly bends towards its end (following an Euler curve) until the final tangential angle becomes 7°. The SSC is terminated by a straight waveguide section (not tapered), which is used for relaxing the cleaving tolerance so that the chips are cleaved in a region where the waveguide is not changing in width as well as curvature. In this layout, both the implant and ternary layers follow the same curved path as the core waveguide section.




```
279 ssc1 = SSC(width1=1.5, width2=0.7, angle=-7, len_taper=150, curve_type=1,
280             len_endwg=50, curved_imp=True, curved_ter=True)
```

Fig. 2.36. Mask layout of a 7°-tilted SSC running from 1.5 µm to 0.7 µm with its epitaxial layers created using Nazca. Inset: excerpt of the code for creating the PCell object.

Fig. 2.37 shows mask layout of an REAM-SOA PIC comprising a 100-µm long EAM, a 300-µm long SOA and a 150-µm long SSC, which is similar to our O-band REAM-SOAs. The layout also shows the butt-joint interfaces as well as inter-electrode electrical isolation. This PIC can be a cell by itself in a more complex PIC design, allowing for a hierarchical layout design.

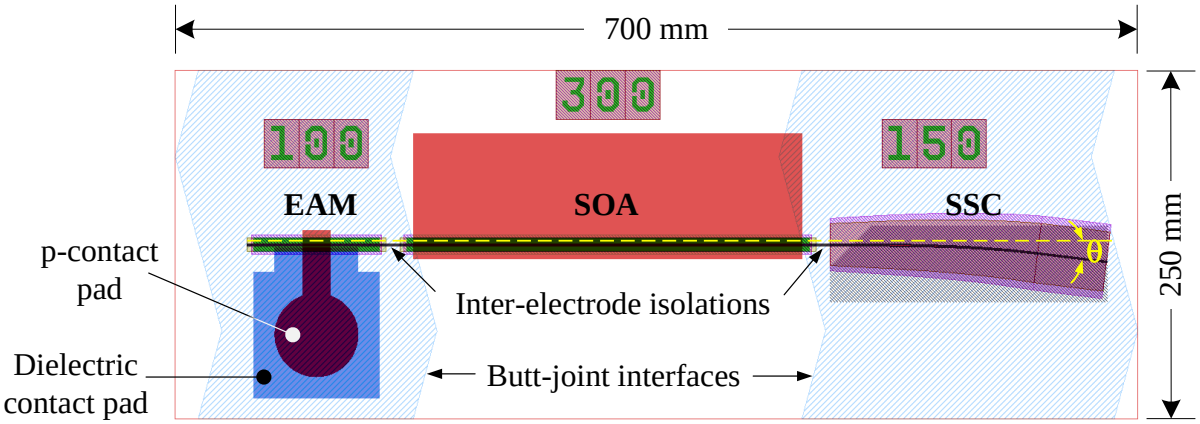


Fig. 2.37. Mask layout of a reflective EAM-SOA PIC with integrated SSC using butt-joint integration technique.

2.13. Summary and Discussion

Different design aspects of our photonic integrated circuits are presented in this chapter with relevant theoretical background about the device physics, starting from the basics and moving towards the realization of photonic integrated circuits. The material system used in our MQW

structures (GaInAsP/InP) is discussed with respect to bandgap engineering and lattice-matching conditions so that devices operating in the two telecom spectral windows (1.3 μm and 1.55 μm) can be realized using the same material system.

The vertical designs of our PICs are presented focusing on the EAM section since the principles also apply for the SOA and the passive sections. Separate-confinement MQW structures provide enhanced photon confinement, high electroabsorption efficiency, and low driving voltage for the EAM section. The effects of strain on the electronic band structures of semiconductor devices are discussed showing the advantages of compressive strained QW to improve device performances such as high-speed modulation of EAMs and low threshold current for lasers and SOAs. Because of polarization selection rules, the HH-E and LH-E transitions contribute differently to TE and TM performances of optoelectronic devices, and we recommend introducing tensile strain to the MQW structures in future works in order to minimize polarization-dependent performances of the EAM and the SOA sections [52].

Electroabsorption effect in MQWs, which is based on the QCSE, is demonstrated using numerical simulation results obtained by solving the Schrödinger-Poisson equations self-consistently. The TE and TM performances with respect to the EAM's absorption coefficient clearly indicate the devices are less sensitive to TM polarization. An overview of the SOA's key performance parameters is also presented.

The process flow applied to realize our components is presented using schematic illustration of the key process steps. Moreover, the advantages of SI-BH waveguide over other waveguide technologies are highlighted. Realizing the devices using robust and industrially compatible technologies such as SI-BH and butt-joint integration enable mass-production of cost-effective components for large scale deployments. Finally, the device structures and mask layouts are discussed as a final step in the realization of our components. The performances of different device configurations are presented in Chapter 3.

Chapter 3

3. Performance Analysis of Basic Building Blocks

Our photonic integrated circuit (PIC) comprises an electroabsorption modulator (EAM), a semiconductor optical amplifier (SOA), and a spot-size converter (SSC). In this chapter, we analyze key performances of these basic building blocks (BBs) and indicate design tradeoffs that can be exploited in the future to further improve device performances.

The first section presents waveguide optimizations performed on the SSC using both simulation and experimental results. Then, the second section presents static performances of the EAM and the SOA including insertion losses, gain and noise figure of the SOA, and static extinction ratio of the EAM. The final section presents dynamic performances of the devices such as small-signal frequency response and modulator-induced chirp (small- and large-signal).

In this thesis, we studied devices operating in both the 1.3 µm (O-band) and the 1.55 µm (C-band) spectral windows as these are the two frequency bands that are suitable for long distance telecom applications, and both are being exploited for access network applications. The C-band is characterized by a relatively higher chromatic dispersion and lower fiber loss than the O-band.

Different device configurations, based on a 100-µm long EAM in the O-band, and an 80-µm and a 150-µm long EAMs in the C-band are studied. Depending on the positions of the EAM and the SOA along the optical path, two PIC configurations are possible: reflective EAM-SOA (REAM-SOA) and its opposite, RSOA-EAM. Table 3.1 summarizes geometries and PIC configurations of the devices studied in this thesis.

Table 3.1. Summary of different device configurations studied in this thesis.

Frequency Band	EAM Length (µm)	SOA Length (µm)	Taper Length (µm)	Device Configuration	
				REAM-SOA	RSOA-EAM
C	80	500	150	×	—
	150	450	150	×	×
O	100	300	150	×	×

3.1. Optimization of Spot-Size Converter

In order to maximize the output power of an optical transmitter, and to effectively utilize the transmitted power at the receiver side of an optical communication system, it is important to minimize losses at different stages of the transmission system. One such point where power loss occurs is when the optical signal is coupled to and from optical components, primarily due to the mode mismatch between the optical fiber and the input/output waveguides of the devices. For monomode propagation, the width of the core waveguide in most PIC designs in InP technology is limited to a few micrometers (e.g., ≤2 μm in a GaInAsP/InP system).

In a planar PIC, where edge coupling is employed, tapered or lensed fibers are commonly used [18]. On the component side, a spot-size converter based on passive waveguides is typically used in order to increase the optical mode size. A simpler solution to broaden the optical mode is to use a linear taper where the waveguide width narrows laterally towards the front facet (output) of the chip as illustrated in Fig. 3.1 [18]. In our components, the taper is a building block by itself integrated with the active sections using a butt-joint integration technique. As the taper width narrows down along the optical path, the optical mode broadens because of weak guiding, which results in a less divergent beam.

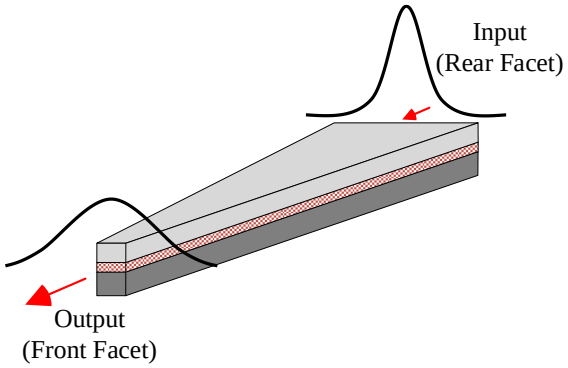


Fig. 3.1. Schematic diagram of a taper and shapes of the optical modes at its input and output (after [18]).

In addition to mode broadening, the SSC can also be optimized to minimize optical feedback related to facet reflectivities at the input/output of the PIC. In the presence of a gain medium such as an SOA (or a laser), facet reflectivity causes a Fabry-Perot (FP)-cavity like effect, affecting the

amplifier gain, commonly referred to as *gain ripple*. For an SOA, having input and output facet reflectivities of R_1 and R_2, respectively, the gain ripple is given by [85]:

$$G(\nu) = \frac{(1 - R_1)(1 - R_2)G_s}{\left(1 - G_s\sqrt{R_1R_2}\right)^2 + 4G_s\sqrt{R_1R_2}sin^2[\pi(\nu - \nu_0)/\Delta\nu]}, \tag{3.1}$$

where, G_s is single-pass gain, ν is optical frequency, ν_0 is resonance frequency of the gain medium, and $\Delta\nu$ is free spectral range of the cavity. The latter is expressed in terms of the cavity length L, effective refractive index of the active region n_{eff}, and speed of light in vacuum c as [64]:

$$\Delta\nu = \frac{c}{2Ln_{eff}}. \tag{3.2}$$

The sinusoidal term ($\sin^2 x$) in (3.1) is responsible for frequency oscillation of the SOA gain [75]. The ratio of the peak (resonant) to valley (anti-resonant) ripple amplitudes, also known as gain ripple (G_r), is given by [85]:

$$G_r = \left[\frac{1 + G_s\sqrt{R_1R_2}}{1 - G_s\sqrt{R_1R_2}}\right]^2. \tag{3.3}$$

For an ideal condition where R_1 and R_2 are both close to zero, the value of G_r becomes unity (i.e., $G_r = 0$ dB in logarithmic scale), which indicates the absence of resonance (no ripple) [75]. Very low facet reflectivities can be achieved by using a combination of the following approaches: (i) applying anti-reflection (AR) coating to the input/output facets, (ii) using a tilted input/output waveguide, and (iii) adding a transparent window region before the end facet [75].

The first approach is based on index-matching between the two media through which light propagates (waveguide and air for the case of fiber coupling). To do that, one or more layers of dielectric coatings are applied to the output facet of a PIC. Although AR coating is a widely used technique, good performance is achieved only over a small range of operating wavelengths [86]. In order to achieve low facet reflectivity over a wide range of spectrum, it requires carefully optimized multiple layers of AR coatings. Another drawback of AR coating is that the reflectivity depends on polarization state of the incoming/outgoing light [64] [75].

The second option, which is tilting the input/output waveguide of a PIC, on the other hand, minimizes facet reflectivities by preventing the reflected light from being coupled back into the

cavity of the gain medium by scattering the light at a different angle. As such, the strength of the reflected light diminishes along the way, and it ultimately vanishes to the cladding region. For a given tilt angle θ with respect to the optical (waveguide) axis and a Gaussian-like transverse electric (TE) polarized plane wave, reflectivity of an angled facet is given by [87]:

$$R(\theta) = R_f(\theta) exp\left[-\left(\frac{2\pi n_2 w_0 \theta}{\lambda_0}\right)^2\right], \tag{3.4}$$

where, n_2 is refractive index of the cladding region, λ_0 is free space wavelength of light, R_f is Fresnel reflection coefficient of the plane wave, and w_0 is width of the Gaussian beam at full power. The reflection coefficient of a TE-polarized light is given by:

$$R_f(\theta) = \frac{n_1 cos(\theta) - \sqrt{{n_2}^2 - {n_1}^2 sin^2(\theta)}}{n_1 cos(\theta) + \sqrt{{n_2}^2 - {n_1}^2 sin^2(\theta)}}, \tag{3.5}$$

where, n_1 is refractive index of the core waveguide.

The full-power-width (w_0) of a Gaussian beam can be approximated as [87][88]:

$$\frac{w}{w_0} = A + \frac{B}{\sqrt{V}} + \frac{C}{V^3} + \frac{D}{V^5}, \tag{3.6}$$

where, w is the waveguide width, $A = 9.2063\times10^{-3}$, $B = 1.7265$, $C = 0.38399$, $D = 9.1691\times10^{-3}$, and V is the normalized frequency (also known as V number).

For a step-index planar waveguide, the V number is given by [64]:

$$V = \frac{\pi w}{\lambda}\sqrt{{n_1}^2 - {n_2}^2}, \tag{3.7}$$

Detailed analysis of tilted output facets with a derivation of the V number can be found in [64][87]. Fig. 3.2 shows facet reflectivities as a function of tilt angle, calculated using Eqs. (3.4) to (3.7) for a GaInAsP/InP MQW system ($n_1 = 3.46$, $n_2 = 3.32$, $\lambda_0 = 1550$ nm). Typically, tilt angles of $7-10°$ are commonly used, resulting in facet reflectivities of the order of 10^{-3} [64].

Finally, in the buried facet (windowing) approach, a transparent window region whose bandgap energy is higher than that of the incident photons is added in front of the end facets. Light entering the transparent window diffracts at a different angle than its initial state and spreads spatially throughout the window region. When reflected, it spreads further in space reducing the amount of

light coupled back into the cavity of the gain medium. In addition to suppressing the gain ripple, the windowing approach also allows realizing polarization-independent gain when it is used with reflecting mirrors inside the gain medium [64]. Therefore, by combining a single-layer dielectric coating (AR) with window facets, low reflectivities in the order of 10^{-5} can be achieved [64].

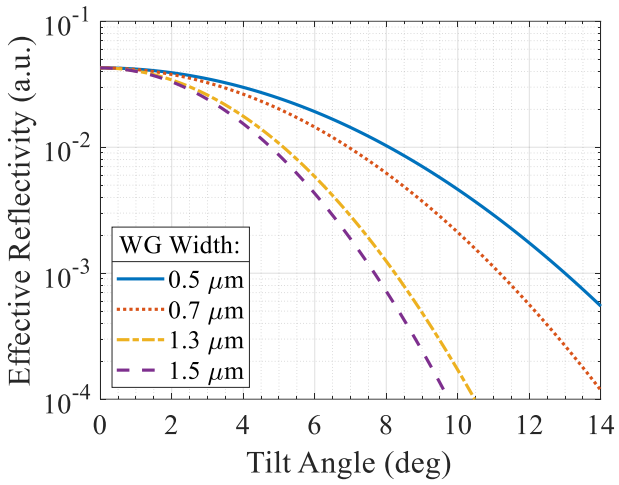


Fig. 3.2. Calculated facet reflectivity versus tilt angle for different waveguide widths at 1550 nm ($n_1 = 3.46$, $n_2 = 3.32$).

The first two approaches—AR coating and tilted output waveguide—are implemented in our components. The SSC in our components is based on a bent tapered waveguide with a 7°-tilted output waveguide. The 7° tilt provides a good compromise between bending loss and optical feedback. The front facet is treated with AR coating whereas the rear facet is treated with high-reflection (HR) coating, realizing a reflective device configuration. The next generation of devices can be realized by combining all the three mechanisms discussed above so as to achieve very low facet reflectivity as well as gain ripple.

In order to demonstrate the advantages of integrating SSC with the PICs, Fig. 3.3 shows ripple observed in the amplified spontaneous emission (ASE) spectra of two gain cavities with and without an SSC, and a third one from a reflective SOA in an RSOA-EAM configuration. Without an SSC (a cleaved and AR coated output facet), the peak-to-peak ripple is >4.5 dB, and it is reduced to ~1.5 dB by integrating an SSC with the gain section. The ripple in a reflective device configuration is further reduced to <1 dB, which is the level of ripple required for practical devices [75]. Therefore, a tilted SSC, treated with low-reflectivity dielectric coatings, improves fiber

coupling efficiency, relaxes the fiber alignment tolerance, and suppresses optical feedback to the SOA gain section.

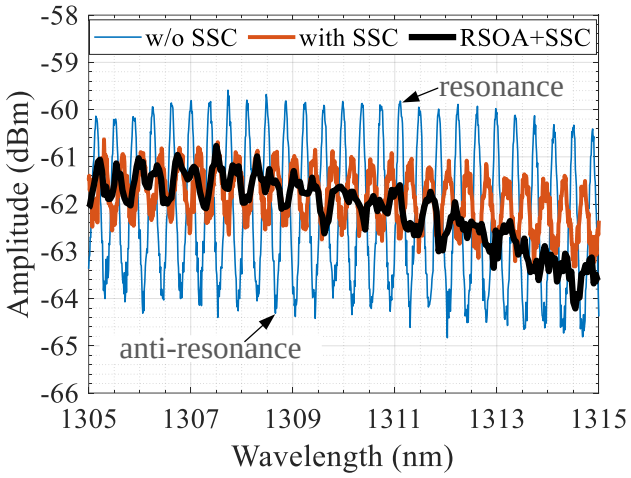


Fig. 3.3. ASE ripple in a single-pass (transmittive) Fabry-Perot cavity with and without a tilted output waveguide, and a double-pass (reflective) SOA with an integrated SSC.

3.1.1. Simulation of Waveguide Structures

The taper in our PICs is based on a linear taper running from 1.5 µm (for the C-band devices) or 1.3 µm (for the O-band devices) at the input side to 0.7 µm at the output side. In order to avoid abrupt change of curvature in the optical path, the taper starts with a straight waveguide section and slowly bends towards its end until the final tangential angle becomes 7°. More specifically, the taper follows a partial Euler spiral (also known as clothoid curve) whose radius of curvature changes linearly with the taper length so that the transition from a straight to a bent waveguide occurs slowly, minimizing the bending loss [89]. The *x*- and *y*-coordinates of a normalized Euler curve are given by Fresnel integrals as:

$$x = \int_0^L \cos(s^2)ds\,, \qquad \text{and} \qquad y = \int_0^L \sin(s^2)ds\,, \tag{3.8}$$

where, L is the physical length of the taper.

The radius of curvature R can be obtained using the taper's physical length and the tangential angle at the output of the taper in radians (θ_{rad}) as: $R = L/2\theta_{\text{rad}}$.

In order to estimate the mode size of the SSC in our PICs, we simulated our SI-BH waveguide structures using FIMMWAVE [70], a vectorial mode solver for 2D+Z waveguide structures . For 3D simulations, its propagation module FIMMPROP can be used. For comparison, we simulated tapers with and without a bend as shown in Fig. 3.4.

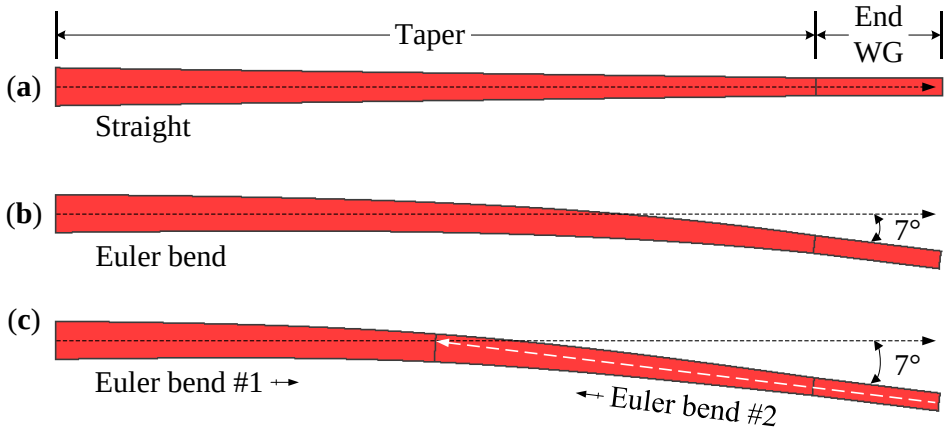


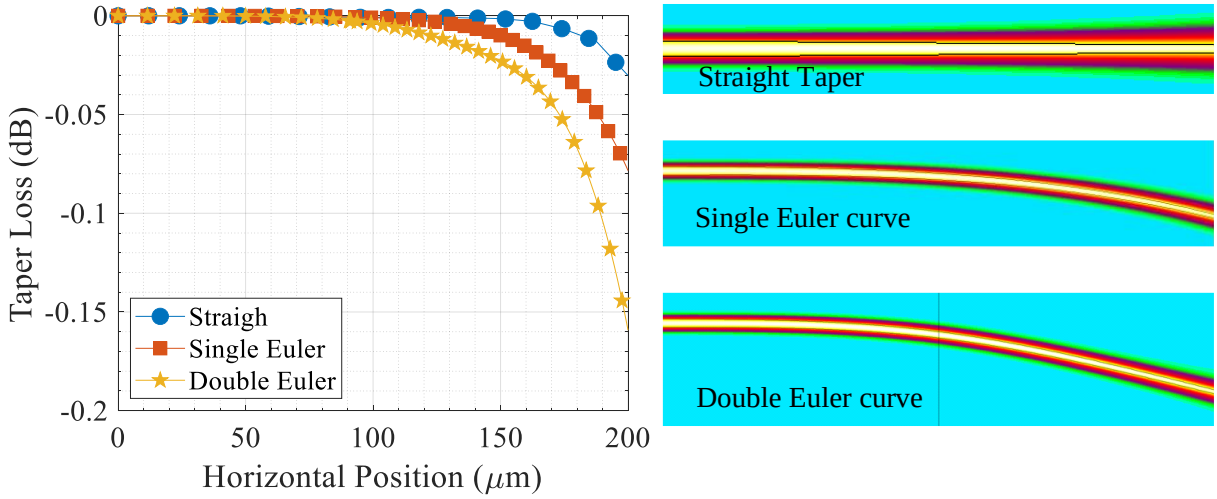
Fig. 3.4. Tapers with and without a bend: (**a**) straight taper, (**b**) taper with a single clothoid curve, and (**c**) taper with double clothoid curves.

We added a 50-µm long straight waveguide of uniform width after the taper (labelled 'End WG' in Fig. 3.4) so that, according to cleaving tolerances, we avoid any uncertainty on curvature and width of the output SSC configuration. However, there still is a change of curvature at the interface between the taper (bending) and the end waveguide (straight). To study the effect of this change of curvature on the optical path, we simulated a third configuration by combining two Euler curves. In this case, the second stage is flipped from right to left so that the combined SSC begins and ends with straight waveguide sections. The total taper length is maintained at the same the same value of 200 µm between the three configurations and the final tilt angle in the case of bent waveguides is 7°. The simulation parameters are summarized in Table 3.2 (for C-band EAMs).

Table 3.2. Parameters used for simulating C-band SI-BH waveguides 1550 nm.

Type	**Layer Thickness (nm)**	**Refractive Index**
InP top	180	3.163
SCH	30	3.321
MQW	129	3.460
SCH	30	3.321
Buffer	700	3.168

Fig. 3.5 shows simulated losses for the fundamental TE mode of the three SSC configurations without considering material absorption. The simulated modal propagations inside the two bent waveguides are shown on the right-hand side of the figure. Compared to the straight taper, bending loss of the taper with a single Euler curve is negligible (<0.08 dB). The double Euler curve, on the other hand, forces the waveguide bend faster introducing an additional loss of ~0.1 dB. This indicates that despite the anticipated advantage of a double Euler curve in improving smooth transition of light from the taper to the final waveguide, it increases the SSC loss. All the PICs studied in this thesis are based on a single Euler curve with a 7°-tilted output waveguide.



(**a**) (**b**)

Fig. 3.5. (**a**) Simulated loss of an SSC based on SI-BH waveguides, without considering material absorptions, (**b**) simulated modal propagations inside the SCC.

In order to estimate the mode size of the SSC in our PICs, we also performed 2D simulation of our SI-BH waveguides using FIMMWAVE [70]. By knowing the mode size, we can choose a lensed fiber of appropriate dimension so as to match its beam diameter with that of the SSC and thus improve input/output coupling efficiency. Fig. 3.6 (a) shows simulated full width at half maximum (FWHM) divergence angles of the fundamental TE mode as a function of waveguide width. Contour plots of the far-field intensity distributions of 1.5 μm and 0.7 μm waveguides are shown in Fig. 3.6 (b) and (c), respectively. For a 1.5-μm waveguide, the FWHM divergence angles of the beam in the horizontal and the vertical directions are ~23° and ~27°, respectively. For a 0.7-μm wide waveguide, the respective divergence angles are reduced to ~15.0° × 18.5°.

The divergence angle can be further reduced by using a narrower taper, but the mode may no longer be guided, which can be seen from Fig. 3.6 (a) for waveguide widths below 0.5 µm. As the taper gets much narrower, the tapering loss also increases, increasing the fabrication complexity since it requires a very high lithographic resolution. Moreover, a narrow taper requires a larger bend angle as shown earlier in Fig. 3.2 (b), which also requires a longer SSC, ultimately increasing insertion loss of the SSC as the waveguide loss increases exponentially with its length.

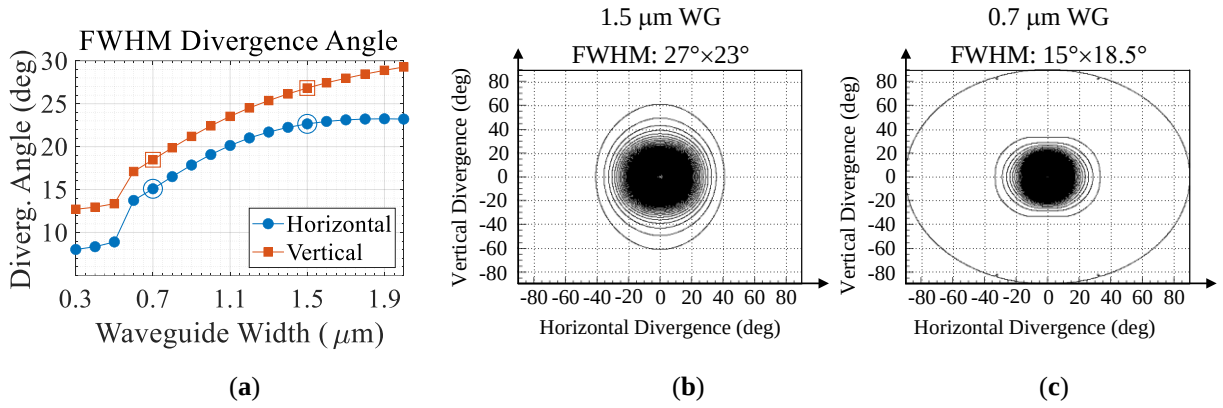


Fig. 3.6. Simulated FWHM divergence angles as a function of waveguide width, and contour plots of far-field intensity distributions of the optical modes of (**b**) a 1.5-µm, and (**c**) a 0.7-µm waveguides.

The beam waist (radius) can be estimated using the divergence angles obtained from the far-field intensity distributions as illustrated in Fig. 3.7(a). An optical beam propagating in the z direction with a minimum waist w_0 at position z = 0 diverges at a certain angle θ during propagation.

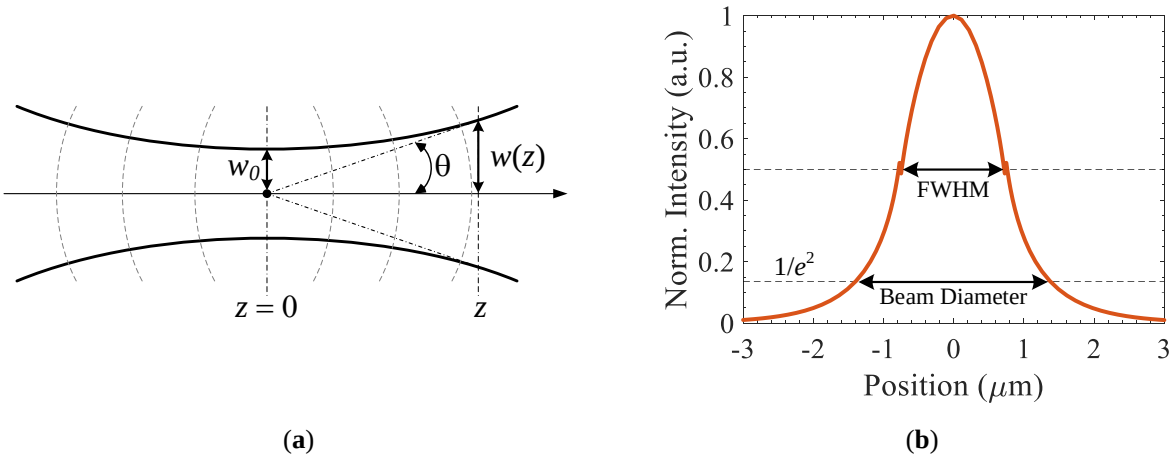


Fig. 3.7. (**a**) Schematic representation of an optical beam propagation, (**b**) its intensity field profile.

For a Gaussian beam, its radius w at any point z away from the source is given by [90]:

$$w^2 = {w_0}^2 \left[1 + \left(\frac{\lambda z}{\pi n {w_0}^2}\right)^2\right], \tag{3.9}$$

where, λ is free space wavelength, and n is refractive index of the medium ($n \approx 1$ for air).

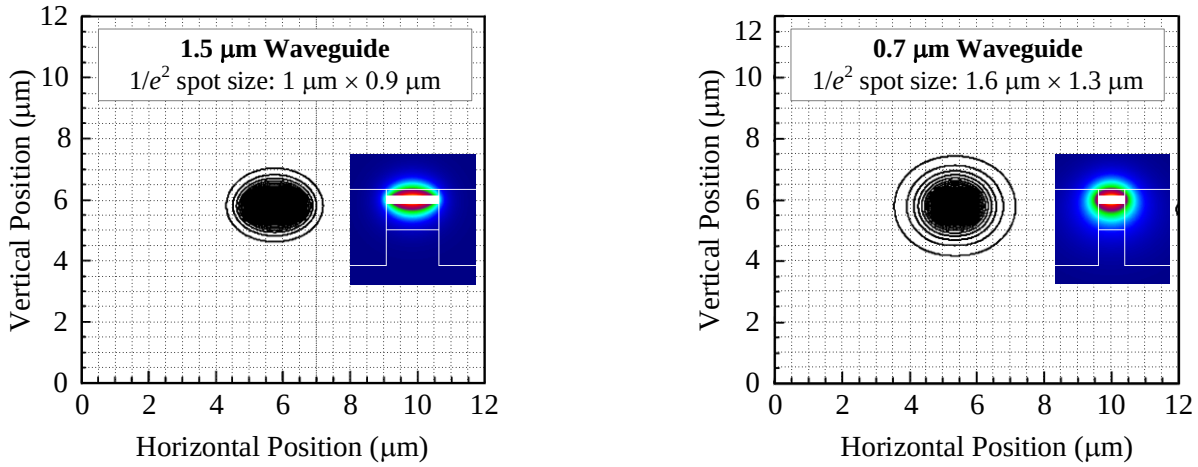
For most practical applications, the beam diameter at $1/e^2$ point is considered, where ~86% of the total beam power is included as illustrated in Fig. 3.7(b). The $1/e^2$ diameter of a Gaussian beam (d_{1/e^2}) is expressed in terms of the FWHM diameter (d_{fwhm}) as:

$$d_{1/e^2} = \frac{d_{fwhm}}{\sqrt{2ln2}}, \tag{3.10}$$

$$d_{fwhm} = \frac{\lambda}{n\pi\theta_{rad}}, \tag{3.11}$$

where, θ_{rad} is the FWHM divergence angle in radians.

Fig. 3.8 shows contour plots of simulated intensity profiles for 1.5 μm (left) and 0.7 μm (right) waveguides, which are respective dimensions of the taper in our PICs at its input and output, respectively. The corresponding color plots are also shown in the insets of the figures.



(**a**) (**b**)

Fig. 3.8. Simulated intensity profiles of (**a**) 1.5 μm and (**b**) 0.7 μm waveguides expressed in terms of horizontal and vertical waveguide dimensions. Insets: color plots of the mode profiles.

The optical mode has an elliptical cross section at the input side of the taper with $1/e^2$ beam diameter of ~1 μm in the horizontal direction and ~0.9 μm in the vertical direction, calculated using (3.10) and (3.11). At the output of the taper, on the other hand, the optical mode has a more symmetric shape with $1/e^2$ diameters of 1.6 μm × 1.3 μm. The mode symmetry is partly attributed to the SI-BH waveguide structure as discussed in Chapter 2 (e.g., see Section 2.10) [15][18].

3.1.2. Far-Field Measurement

To compare the simulated mode profiles with that of fabricated devices, we performed far-field measurements using a goniometric radiometer from Photon Inc. Fig. 3.9 shows plots of measured and simulated far-field intensity distributions of a 1.5-μm waveguide (without tapering or tilting), and a 0.7-μm SSC with a 7°-tilted output waveguide.

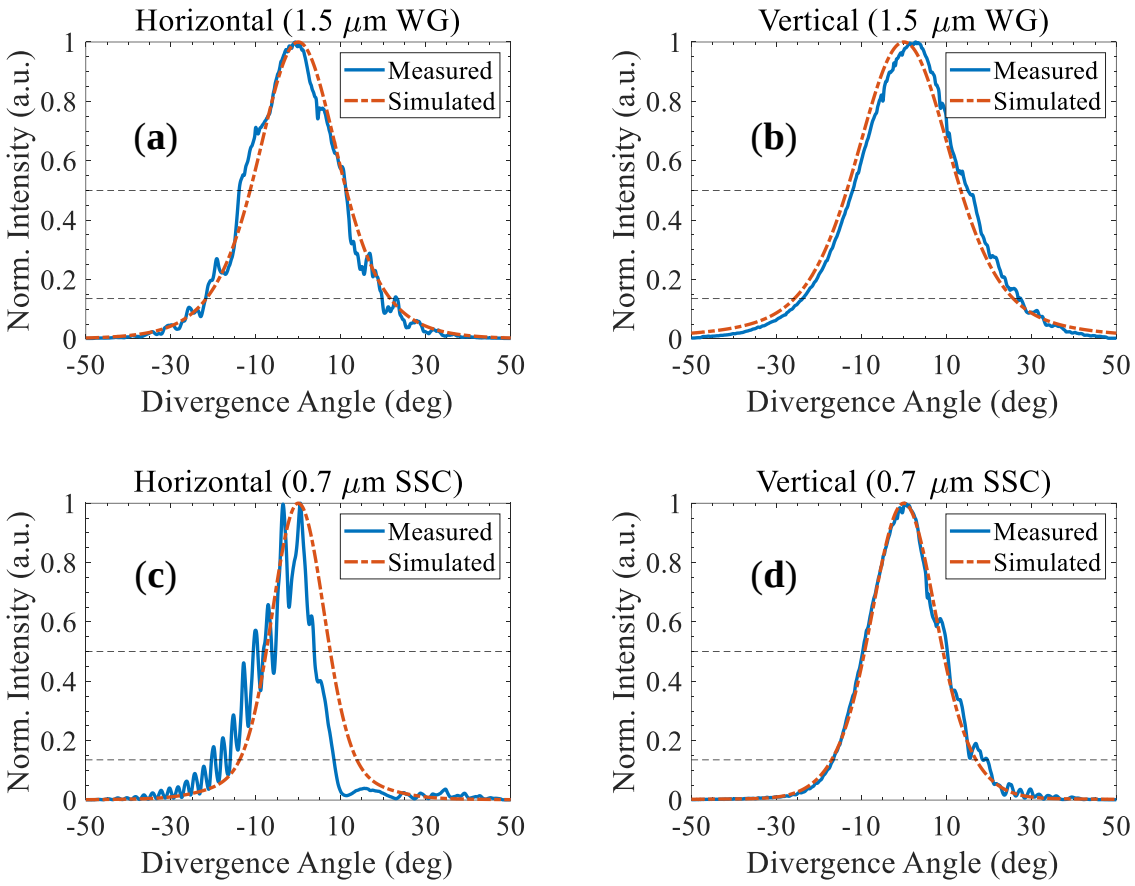


Fig. 3.9. Simulated and measured far-field intensity distributions of (**a**), (**b**) 1.5 μm (straight output waveguide without a taper), (**c**), (**d**) 0.7 μm waveguide (7°-tilted output waveguide) in the horizontal (left) and vertical (right) directions.

The simulation results are in good agreement with the experimental data in both cases. Without an SSC, measured FWHM divergence angles of the 1.5-μm waveguide are ~25° and 27.2° in the horizontal and the vertical directions, respectively [Fig. 3.9 (a) and (b)]. The 0.7-μm SSC reduces the divergence angles to 14.5° × 20° [Fig. 3.9 (c) and (d)]. Fringes observed in the experimental results (especially in the horizontal far-field of the 0.7-μm SSC) are attributed to reflections inside the far-field analyzer, and they may affect accuracy of divergence angles estimated using measured far-field intensity profiles.

For comparison, measured far-field intensity profiles of the 0.7-μm SSC and a lensed fiber are shown in Fig. 3.10 (a) and (b) in the horizontal and vertical directions, respectively. Although the shape of the horizontal far-field profile of the SSC is affected by fringes, the vertical intensity profile reveals that the lensed fiber with estimated FWHM beam divergence angles of 23.5° × 21.5° is a good match for the PICs based on a 0.7-μm SSC.

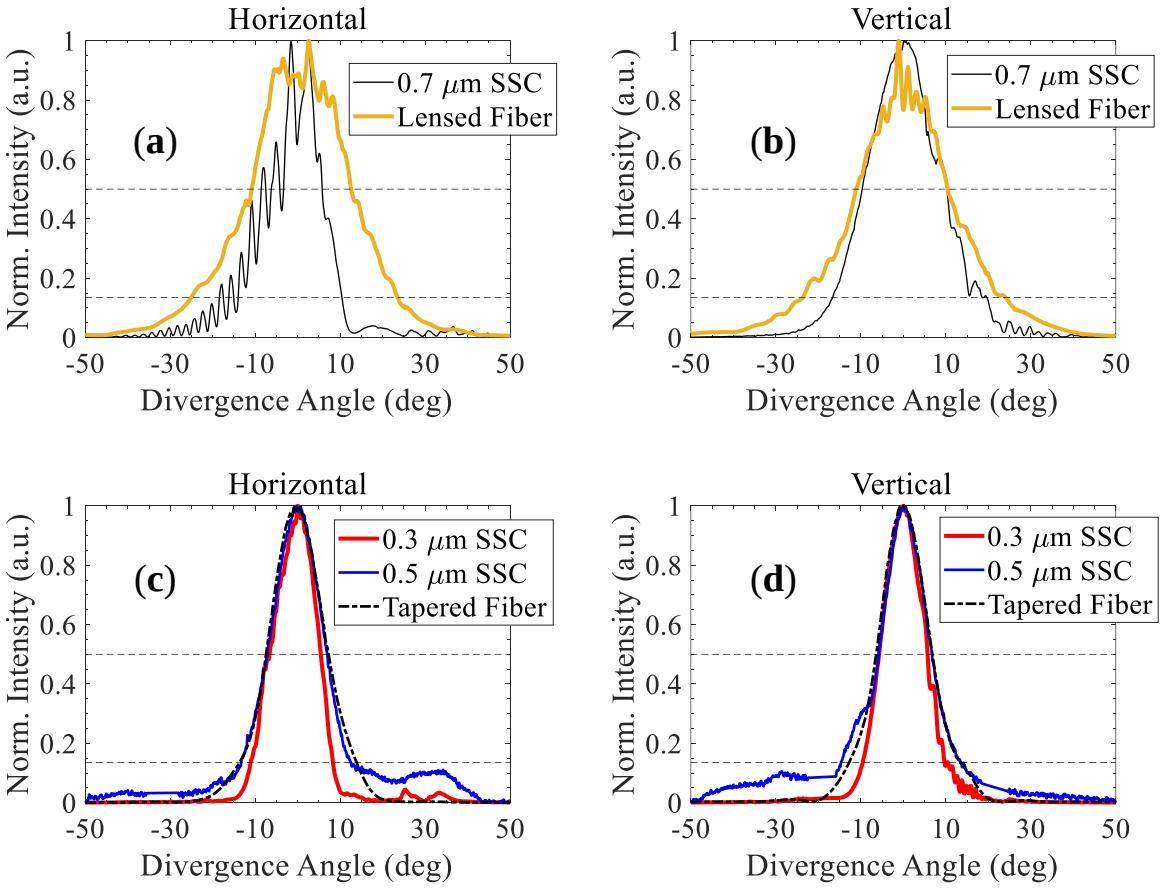


Fig. 3.10. Measured far-field intensity profiles of (**a**), (**b**) 0.7-μm SSC and a lensed fiber, (**c**), (**d**) 0.3-μm SSC, 0.5-μm SSCs and a commercial tapered fiber in the horizontal (left) and vertical (right) directions.

Based on the various optimizations performed so far on the spot-size converter, the next generation of devices were realized using a 0.5-μm SSC as well as a 0.3-μm SSC. Far-field intensity profiles of the beams from the two SSCs are shown in Fig. 3.10 (c) and (d) for the horizontal and the vertical directions, respectively. Measured FWHM divergence angles of the 0.5-μm SSC are ~14.1° × 12.5° and that of the 0.3-μm SSC are 12° × 10.9°. This shows that the divergence angle is almost halved by using a 0.5-μm SSC. On the other hand, the 0.3-μm SSC not only increases the mode size but also provides a symmetric mode profile approaching the shape of a fiber, which maximizes fiber alignment tolerances. For comparison, far-field intensity distribution of a commercial tapered fiber of advertised 4-μm mode diameter is also shown in Fig. 3.10 (c) and (d). Its estimated divergence angles are 14.7° × 13.2°, which is the closest match to the 0.5-μm SSC. Table 3.3 summarizes divergence angles of the SSCs and fibers shown in Fig. 3.9 and Fig. 3.10.

Table 3.3. FWHM divergence angles of SSCs and fibers.

Component		**Divergence Angle (deg)**	
		Horizontal	Vertical
0.3 μm SSC		12.0	10.9
0.5 μm SSC		14.1	12.5
0.7 μm SSC	Simulated	15.0	18.5
	Measured	14.5	20.0
1.5 μm WG	Simulated	23.0	27.0
	Measured	25.0	27.2
Lensed fiber		23.4	21.6
Tapered fiber		14.7	13.2

3.2. Insertion Loss

3.2.1. Insertion Loss Estimation

For a waveguide modulator such as an EAM, the output power (P_{out}) decreases exponentially with the waveguide length following the relation:

$$P_{out} = T(V)P_{in}, \tag{3.12}$$

where, P_{in} is the input power and $T(V)$ is the transmission coefficient at a given bias voltage V, which is expressed in terms of the optical confinement factor Γ, absorption coefficient of the EAM $\alpha(V)$, and its length L_{EAM} as:

$$T(V) = e^{-\Gamma \cdot \alpha(V) \cdot L_{EAM}}. \quad (3.13)$$

Insertion loss (L_{in}) is the amount of power lost during propagation of light inside the waveguide, which is given by [40]:

$$L_{in} = \frac{P_{in} - P_{out}(0)}{P_{in}} = 1 - T(0) = 1 - e^{-\Gamma \cdot \alpha_i(0) \cdot L_{EAM}}, \quad (3.14)$$

where, $P_{out}(0)$ is the output power at 0 V bias (*on* state), $T(0)$ is the transmission coefficient, and $\alpha(0)$ is absorption coefficient of the active region material.

The absorption coefficient $\alpha(0)$ has a finite value because of intrinsic material absorption associated with QW interband absorption as well as intra-valence band and free-carrier absorption in doped layers [18][40]. Equation (3.14) works for any waveguide structure including the EAM and the SSC sections of our components. Input and output coupling efficiencies are neglected in the equation so that insertion loss calculated using (3.14) simply is the propagation loss of the waveguide. As a result, we will use the term '*total insertion loss*' when considering all loss contributions including coupling as well as waveguide losses in an integrated circuit.

The main loss contributions in a reflective EAM-SOA with integrated SSC come from input/output facet coupling efficiencies, EAM absorption in the *on* state, and intrinsic absorption of the SSC section as illustrated in Fig. 3.11. Facet coupling losses arise from mode mismatch between the SSC and the lensed fiber. The SSC in our components is based on the same MQW stack as the EAM section whereas a separately optimized MQW structure is used in the SOA section. As a result, the SSC is not completely transparent to the input light, it rather has a finite absorption and contributes to the insertion loss. In a reflective device configuration, the effective lengths of both the EAM and the SSC sections are doubled because of the double-pass configuration. As a result, the insertion loss of the EAM is also doubled. Since the optical signal also passes through the same SSC, the SSC loss is also doubled. Other sources of losses such as the butt-joint interfaces, and finite reflectivities of the HR and AR coatings are negligible, and they are not considered in our analysis of insertion loss.

Fig. 3.11 schematically illustrates the different loss contributions in an RSOA-EAM PIC. The lossy elements remain the same between REAM-SOA and RSOA-EAM configurations. The latter is chosen here for demonstration purpose as it allows identifying all losses before the input light

arrives at the SOA section and gets amplified. The same configuration is also used to extract the intrinsic SOA gain (to be discussed in Section 3.3).

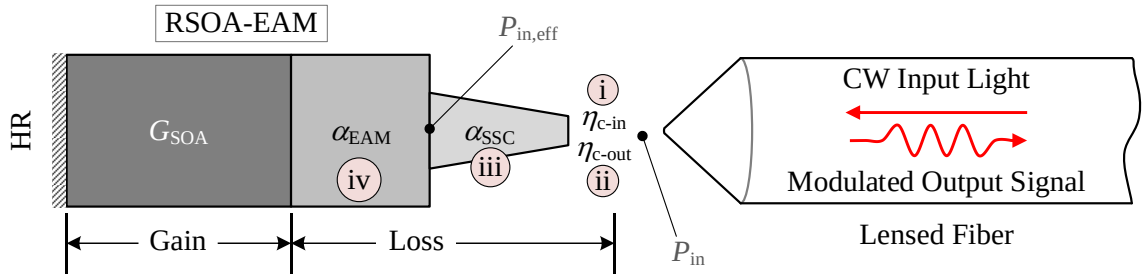


Fig. 3.11. Schematic diagram of an RSOA-EAM with integrated SSC, and the various insertion loss contributions. The labels represent losses: (i) input coupling loss, (ii) output coupling loss, (iii) SSC loss (absorption and bending), (iv) EAM absorption loss at 0 V. Coupling losses in dB are obtained as: $C_{in/out}$ [dB] = $10\log_{10}(\eta_{c\text{-}in/out})$.

By using a lensed fiber, we estimated 2 dB facet coupling loss in each direction. To estimate the input coupling loss, we injected a continuous wave (CW) light from a tunable laser source to the PIC while reverse biasing the EAM section ($V_{bias} = -3$ V). The photogenerated current is obtained by subtracting the EAM's dark current from the total current obtained from EAM: $I_{photo} = I_{EAM} - I_{dark}$. Then, the photocurrent is converted into an equivalent absorbed optical power, which is the effective input power arriving at the EAM section ($P_{in,eff}$), and it is related to the optical power via the EAM's responsivity $\Re$ as:

$$P_{in,eff} = I_{photo}/\Re. \tag{3.15}$$

The responsivity depends on the incident photon energy hv as well as internal quantum efficiency η, which quantifies the amount of light power converted into photocurrent, and it is given by:

$$\Re = \frac{\eta q}{hv} \approx \frac{\lambda_{\mu m}}{1.24}, \tag{3.16}$$

where, q is elementary charge, h is Planck's constant, v is optical frequency, and $\lambda_{\mu m}$ is free space wavelength of the input light in micrometers.

We assumed perfect absorption (100% internal quantum efficiency, $\eta = 1$) for our calculations, which in reality is not the case as the conversion efficiency of PIN heterostructures is always less than unity. As a result, our approach, which we call the '*photocurrent method*', overestimates the input coupling loss.

The difference between the input power from the laser source P_{in} (obtained at the output of the fiber) and the effective input power calculated using (3.15) gives the *one-way loss* of the PIC, which is a combination of the input coupling loss and the SSC loss. The latter can be estimated using (3.8) for waveguide propagation loss and Fig. 3.1 for a combination of tapering and bending losses. For the 150-µm long SSC in our PICs, which is based on a 189-nm thick GaInAsP MQWs, we estimated a *one-way loss* of ~1 dB ($\Gamma \approx 9\%$, $\alpha \approx 150$ cm^{-1} for GaInAsP near 1530 nm). Once the SSC loss is determined, the input coupling loss (C_{in}) can be obtained in decibel as follows:

$$C_{in}\,[\mathrm{dB}] = P_{in} - P_{in,eff} - L_{SSC}. \tag{3.17}$$

The powers in (3.17) are expressed in dBm and the coupling loss is in dB, which is also the case for the upcoming equations in this subsection.

For the output coupling loss estimation, we measured the average power of the ASE light generated by the SOA at a given pump current in two different configurations: (i) using a broadband detector (P_{broad}), and (ii) fiber-coupled power using an optical power meter together with a lensed fiber (P_{fiber}). Assuming the broad detector collects all the output light, which again is not the case in reality, the output coupling loss (C_{out}) can be obtained in decibel as:

$$C_{out}\,[\mathrm{dB}] = P_{broad} - P_{fiber}. \tag{3.18}$$

In this case, the taper loss is automatically removed from the calculation as it is embedded in both measurements. The procedure is repeated using a PIC that has the same SSC structure as the reflective devices but with an integrated laser source, and similar results are obtained.

In a reflective device configuration, the same SSC couples light to and from the PIC, which results in the same input and output coupling losses. As a result, the 1-dB loss of the SSC (L_{SSC}) estimated earlier can be validated using experimental results based on (3.17) and setting $C_{in} = C_{out}$ as:

$$L_{SSC}\,[\mathrm{dB}] = P_{in} - P_{in,eff} - C_{out}. \tag{3.19}$$

Table 3.4 summarizes estimated loss contributions of a PIC comprising a 150-µm long SSC and a 150-µm long EAM, keeping the EAM in an *on* state ($V_{EAM} = 0$ V). We used a lensed fiber having an estimated FWHM divergence angle of 23.5° × 21.5° to couple light to and from the chip. The total *two-way* loss of the PIC is ~12 dB, out of which the EAM contributes a *two-way* loss of 6 dB

(3 dB in each direction). Therefore, a minimum SOA gain of ~12 dB is required to fully compensate the insertion losses of the PIC.

Table 3.4. Total insertion loss of a C-band PIC at1530 nm estimated using a lensed fiber.

Label in Fig. 3.11	Loss Element	Loss (dB)	Remark
(i)	Input facet coupling	2	—
(ii)	Output facet coupling	2	—
(iii)	SSC (150 µm long)	2	Two-way losses
(iv)	EAM (150 µm long)	6	
	Total Insertion Loss	**12**	

3.2.2. Insertion Loss Spectrum

The absorption coefficient α of an EAM used in (3.14) depends not only on the bias voltage but also on the operating wavelength . More specifically, the EAM's absorption coefficient increases with increasing photon energy (decreasing wavelength) as discussed in Chapter 2 (e.g., see Section 2.7). As a result, a higher insertion loss is expected at shorter wavelengths.

Fig. 3.12 shows the total one-way loss spectrum of an O-band PIC comprising a 100-µm long EAM and a 150-µm long SSC, obtained using a lensed fiber. Since a narrower ridge width (1.3 µm) is used for the O-band devices compared to the C-band devices (1.5 µm), one more QW layer is used in the former case in order to obtain comparable optical confinement factors from the devices operating in the two frequency bands. The results shown in Fig. 3.12 are obtained using a lensed fiber based on the photocurrent method discussed above.

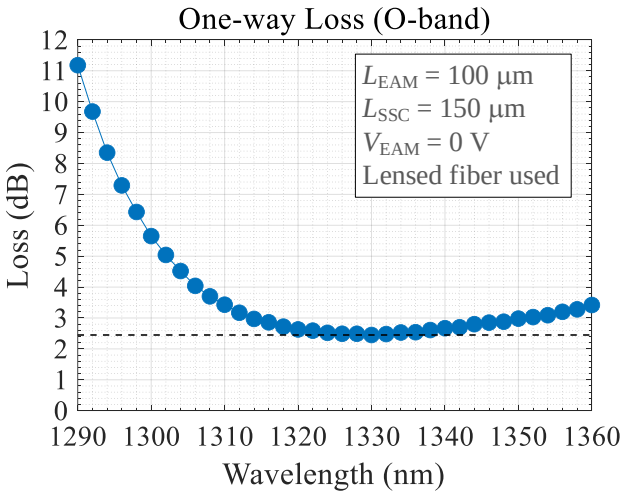


Fig. 3.12. Measured one-way loss spectrum of an O-band PIC based on a 100-µm EAM and a 150-µm SSC.

Over the 70-nm range considered here, the total one-way loss, which is the sum of input coupling loss, SSC loss and EAM absorption, lies between ~2.4 dB and ~11.2 dB, the minimum occurring near 1330 nm and the maximum at 1290 nm (lower limit of the tunable laser source used). The O-band components are designed to operate near 1310 nm ±10 nm, and they are tested in this range. The *one-way* losses of the PIC at 1300 nm and 1320 nm are about 5.6 dB and 2.6 dB, respectively. At 1310 nm, where the amplifier gain peak occurs (to be discussed in the next section), the one-way insertion loss is about ~3.5 dB, which gives a total two-ways loss of ~7 dB.

At longer wavelengths, the MQW structures are transparent to the input light. As a result, the total loss is primarily due to input/output coupling losses. A minimum one-way loss of 2.4 dB observed in Fig. 3.12 is close to the input/output coupling loss estimated by measuring the EAM's photocurrent. Another way of measuring input coupling losses is by injecting light at a relatively longer wavelength and applying the photocurrent measurement technique discussed in the previous section, but the input coupling loss estimation can result in an exaggerated value since the EAM does not completely absorb the input light. The slight increase in the total loss of the PIC observed in Fig. 3.12 after 1330 nm is attributed to a less optimized AR coating at longer wavelengths.

The effect of facet reflectivity is more pronounced in the C-band devices as shown in Fig. 3.13. The spacing between the longitudinal modes of the cavity is ~15 nm (see inset of Fig. 3.13), the equivalent of ~80 μm physical distance for light propagating in air, which is the typical gap between the chip and the fiber [$\Delta\lambda = \lambda^2/(2nL)$, $n \approx 1$ for air, $\lambda = 1550$ nm, and $\Delta\lambda = 15$ nm].

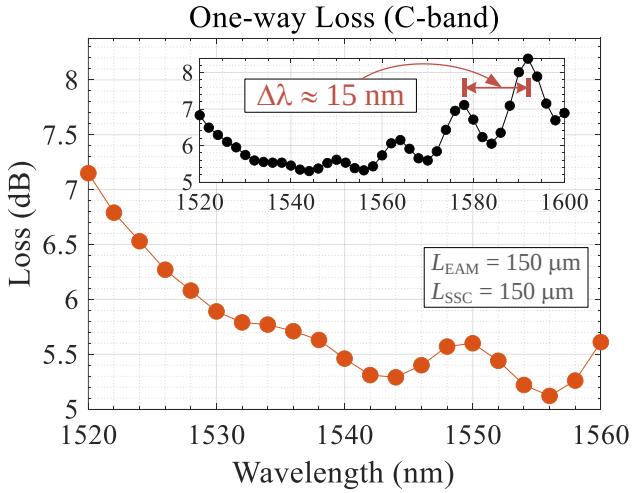


Fig. 3.13. Measured one-way loss spectrum of a C-band PIC based on a 150-μm long EAM and a 150-μm long SSC. Inset: extended view of the loss spectrum showing ripples up to 1600 nm.

For an input wavelength of 1530 nm, the total loss in a reflective configuration is ~12 dB (~5.9 one-way loss), which is in a good agreement with the result obtained using the approaches outlined in the previous section (e.g., see Table 3.4). The total loss of the C-band PIC is relatively higher than that of the O-band PIC within their respective operating regions (e.g., 10.5 dB at 1545 nm vs. 5 dB at 1330 nm) mainly because of high input/output coupling losses in the former case.

In order to fully compensate the total insertion losses of the PICs a minimum SOA gain of ~12 dB is required. Moreover, for demonstrating colorless operation over a wide range of spectrum (typically, 1300−1320 nm in the O-band, and 1530−1550 nm in the C-band), the SOA should also be able to compensate losses in that range.

Finally, the results shown in Fig. 3.12 and Fig. 3.13, which are obtained in the input direction, are also used for calibrating their respective setups in the output direction so as to extract the intrinsic gains of the reflective SOAs in our PICs.

3.3. Amplifier Gain

The gain G of an SOA (or amplification factor) is the ratio of the output to the input optical powers ($G = P_{\text{out}}/P_{\text{in}}$). It depends on both the material system and the SOA's geometry. For a given pump current that determines the density of injected carriers N, the unsaturated gain G_0 of an SOA of cavity length L_{SOA} is given by [39][43]:

$$G_0 = exp[\Gamma g(N) - \alpha]L_{SOA}, \tag{3.20}$$

where, Γ is the optical confinement factor, $g(N)$ is the material gain per unit length of the active region at a given carrier density N, and α is the total cavity loss.

3.3.1. Experimental Setup

Fig. 3.14 shows a schematic diagram of the experimental setup used to measure gain and noise figure (NF) of the SOAs in our PICs (reflective device configuration). We used a tunable laser source to generate a CW light, which is amplified by a fiber amplifier when high input power is required. Our components are sensitive to the polarization state of the input light (compressively strained QWs). For that reason, we inserted a polarization controller to inject TE-polarized light into the PICs. The amount of input power is controlled by a variable optical attenuator (VOA) so

that the SOA's operating condition (small or large signal) can be determined by varying the level of attenuation.

Two optical switches (SW#1 at the input side and SW#2 at the output side) control the type of signal that arrives at the optical spectrum analyzer (OSA), which can be ASE light from the SOA, light from the laser source, or a combination of amplified signal and ASE. In order to characterize the reflective SOAs, an external optical circulator is used that enables bidirectional transmission over a single lensed fiber. The input light from the laser first enters the circulator at port-1 and leaves at port-2 to be injected into the device under test (DUT), which in this case is an RSOA-EAM. Once the optical signal is reflected and amplified by the SOA section of the PIC, it again enters the circulator at port-2 and leaves at port-3.

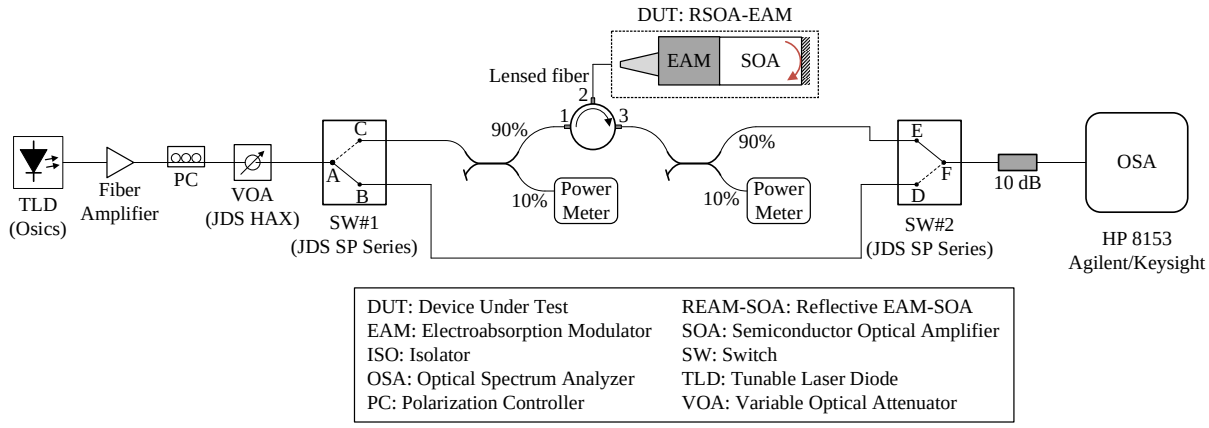


Fig. 3.14. Experimental setup for SOA gain and noise figure measurement in a reflective device configuration.

Power splitters are used on both sides of the chip to monitor the input and output power levels. Finally, a 10-dB optical attenuator is inserted before the OSA for equipment protection. All external losses related to the setup are calibrated so that the analyzer can accurately estimate the amplifier gain and NF based on the input and output signals. In this section, gain performances of the SOAs are presented, and then their NFs are presented in the next section.

3.3.2. Amplified Spontaneous Emission Spectrum

A significant amount of information about SOA gain (e.g., the position of the gain peak, amplification bandwidth, and the gain ripple) can be extracted from the ASE spectrum. The ASE power is related to the amplifier gain as well as device geometry, and it is given by [43]:

$$P_{ASE} = \frac{hvfwdBN^2(G-1)}{\Gamma g - \alpha}, \tag{3.21}$$

where, f is the fraction of spontaneous emission light that gets amplified, w is the ridge width, d is thickness of the active region ($area = w \times d$), B is radiative (bimolecular) recombination coefficient, N is the carrier density, G is the signal gain, Γ is the optical confinement factor, g and α are gain and absorption coefficients of the active region material.

SOAs based on MQWs exhibit superior bandwidth compared to bulk semiconductors mainly because of a step-like density of states in MQWs, where the carrier density becomes independent of photon energy, which is in contrary to bulk materials where the density of states is a continuous function of the carrier energy (depends on the square root of energy) [64]. However, when integrated with an EAM, the usable region of an SOA's gain spectrum is limited by the strong absorption of the EAM at a lower detuning from its absorption edge.

Fig. 3.15 shows ASE spectrum of an O-band SOA when it exists as a standalone element as well as when it is integrated with an EAM in an RSOA-EAM PIC configuration, the EAM being in an *on* state (biased at 0 V). The ASE spectra (with and without an EAM) are normalized to the longest wavelength (1400 nm) in the *x*-axis. For the purpose of demonstration, the EAM's absorption spectrum (the ASE power difference in the two configurations) is also shown in the figure.

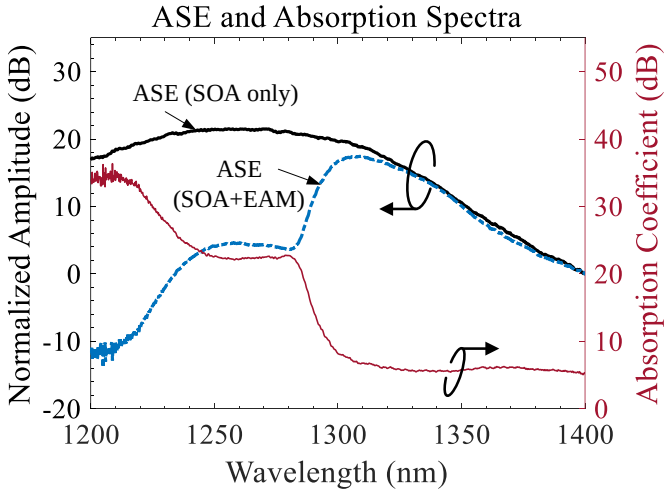


Fig. 3.15. ASE spectra of an O-band RSOA as a standalone element and in an integrated circuit in an RSOA-EAM configuration together with the EAM's absorption spectrum. The ASE amplitudes are normalized to 1400 nm.

In an integrated circuit, the ASE spectrum follows the EAM's absorption spectrum, and the usable amplifier bandwidth is narrowed to about 35 nm at the 3-dB point. The most common optimization approach to obtain maximal amplification within this limited range is positively detuning (red shift) the SOA's gain peak from the EAM's absorption edge.

Fig. 3.16 shows ASE spectra of a 300-µm long O-band SOA (left) and a 450-µm long C-band SOA (right), with their respective high-resolution ASE ripples shown at the bottom. The ASE light power increases with increasing pump current [increasing the carrier density N in (3.21)], and the spectrum slightly shifts to shorter wavelengths, which is due to band filling caused by an increase in carrier density [40][43]. For example, the ASE peak of the O-band SOA shifts from 1311 nm at 20 mA to 1306 nm at 140 mA (i.e., a 5-nm shift).

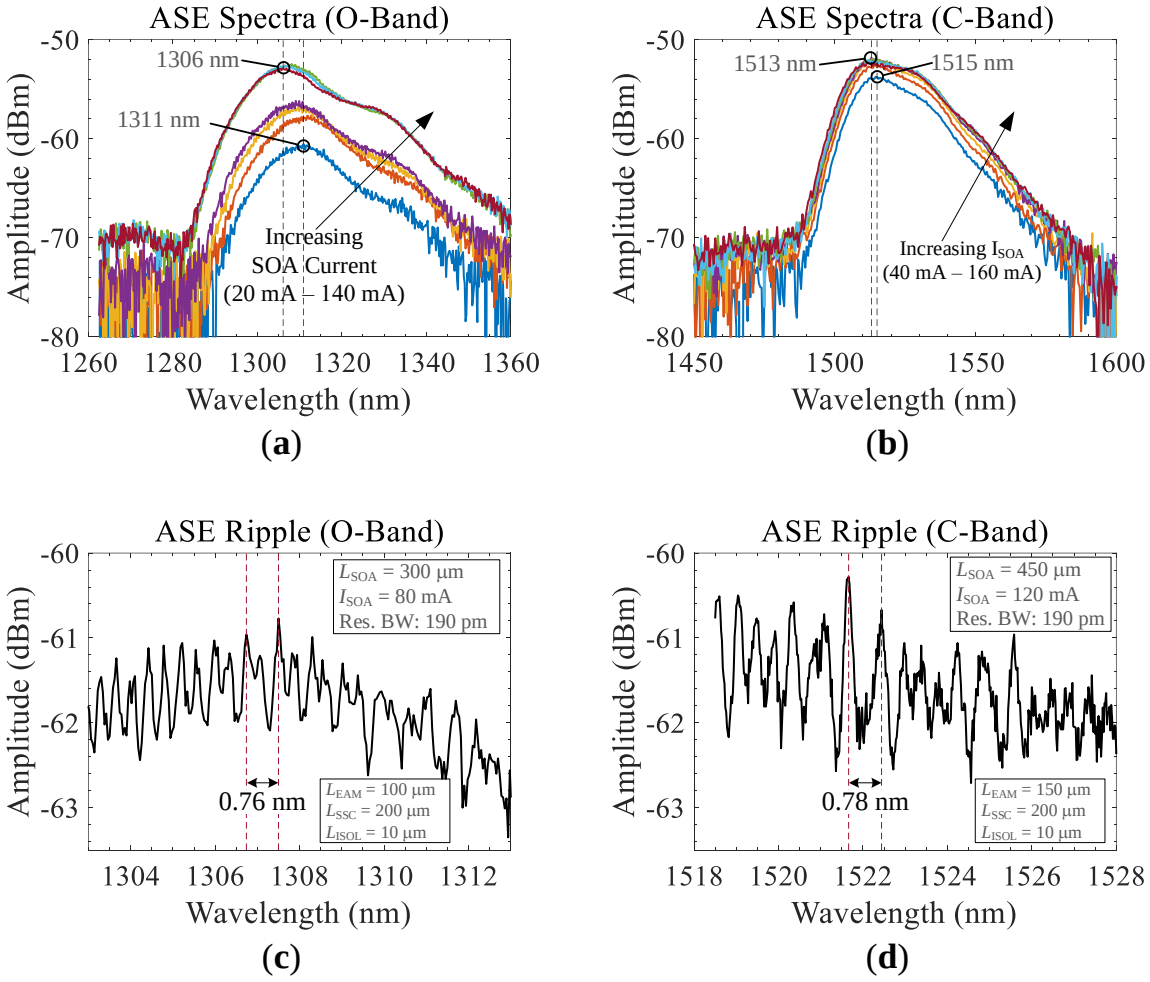


Fig. 3.16. ASE spectra of reflective SOAs at different pump currents: (**a**) 300-µm long O-band SOA, (**b**) 450-µm long C-band SOA, and ASE ripples of (**c**) the O-band SOA at 80 mA, (**d**) the C-band SOA at 120 mA. Res. BW: 190 pm.

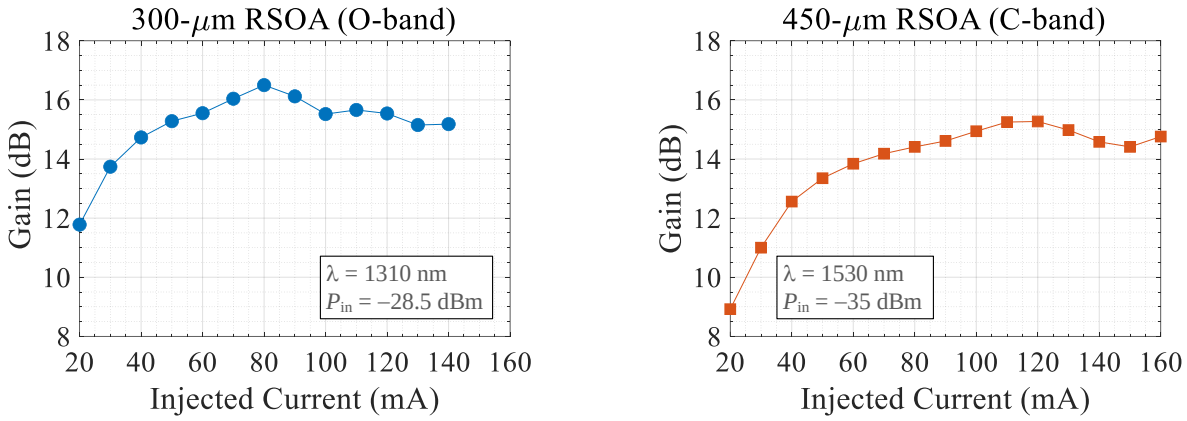
On the other hand, the shift in the spectrum of the C-band SOA is only ~2 nm (1515 nm to 1513 nm) when the pump current is increased from 40 mA to 160 mA. Despite a large difference in the applied current (120 mA difference), the ASE amplitudes are close to one another. Moreover, the maximum ASE amplitude of the C-band SOA is comparable to that of the O-band SOA although the latter has a shorter cavity length (450 μm vs. 300 μm). The anomaly observed from the C-band SOA is attributed to lateral current leakage, which is also observed in other components on the same wafer (e.g., integrated laser modulators).

A high-resolution view of the ASE spectrum reveals ripple arising from facet reflectivities as shown in Fig. 3.16 (c) at 80 mA for the O-band SOA and (d) at 120 mA for the C-band SOA. The spacing of the longitudinal modes of the ripple in the O-band devices (bottom-left) is ~0.76 nm and that of the C-band devices (bottom right) is ~0.78 nm. The difference between the two is due to the difference in EAM lengths (100-μm in the O-band vs. 150-μm in the C-band) as well as a slightly different effective refractive indices of the corresponding waveguides. On the other hand, the peak-to-peak ripple amplitudes in the two frequency bands are ~1.3 dB (O-band) and ~2.3 dB (C-band). As shown earlier in Fig. 3.13 using the insertion loss spectrum, the gain ripple of the C-band SOA is even worse at longer wavelengths, and this affects the amplifier noise figure (to be discussed in Section 3.4).

3.3.3. Current-Dependent Small-Signal Gain

For a given intensity of light inside the gain medium, the amplifier gain increases with increasing the pump current, which in turn increases the number of charge carriers that participate in the amplification (stimulated emission) process. However, the amplifier gain saturates at some point as the pump current increases because the carrier density exceeds the photon density, reaching a point where the injected carriers no longer contribute to the stimulated emission process and thus gain saturation occurs.

Fig. 3.17 (a) shows measured signal gain as a function of SOA pump current obtained from the 300-μm long O-band RSOA operating at 1310 nm for an effective input power of −28.5 dBm at 25°C submount temperature. At this wavelength, the SOA exhibits a maximum gain of ~16.5 dB and saturates at a pump current of 80 mA.



(**a**) (**b**)

Fig. 3.17. Signal gain as a function of SOA pump current: (**a**) 300-µm long O-band SOA operating at 1310 nm (effective $P_{in} = -28.5$ dBm), (**b**) 450-µm long C-band SOA operating at 1530 nm ($P_{in} = -35$ dBm). $T = 25$℃. Both SOAs are in a reflective configuration.

On the other hand, the peak gain of the 450-µm long C-band SOA is ~15.5 dB at 1530 nm, for an effective input power of −35 dBm as shown in Fig. 3.17 (b). The gain saturates at a pump current of 120 mA. Despite having a longer SOA cavity and a higher pump current required to saturate the SOA, the C-band SOA exhibits a lower gain than its O-band counterpart, which is attributed to lateral current leakage that arises from of dopant diffusion in the semi-insulating buried heterostructure (SI-BH) waveguide, which was observed in that particular wafer.

3.3.4. Gain Spectrum

In addition to the pump current, the gain of an SOA depends on the operating wavelength and the power of the input signal, and its gain spectrum can be approximated using a two-level system model (Lorentzian profile) whose gain coefficient is given by [43] [75]:

$$g(\nu) = \frac{g_0}{1 + (\nu - \nu_0)^2 {T_2}^2 + P/P_s}, \tag{3.22}$$

where, ν is the optical frequency, ν_0 is the molecular transition frequency, T_2 is carrier relaxation time (typical values are between 0.1 ps and 1 ps), P is the signal power being amplified by the SOA, P_s is saturation power of the gain medium, and g_0 is steady-state gain coefficient of the gain medium, which is given by:

$$g_0 = a\left(\frac{\eta_i I}{qV_{MQW}} - N_{tr}\right), \tag{3.23}$$

where, a is the differential gain (dg/dN), η_i is injection efficiency of the pump current, I is the forward bias (pump) current, q is elementary charge, V_{MQW} is volume of the MQW active region, and N_{tr} is steady-state (transparency) carrier density.

The minimum value for P is the incident power at the input facet of the SOA $P(0)$ and its maximum value is the power at the output facet of the SOA $P(L_{SOA})$. The saturation power P_s of the gain medium is given by [39][43]:

$$P_s = \frac{Ah\nu}{a\Gamma\tau_c}, \tag{3.24}$$

where, A is the cross-sectional area of the waveguide mode ($A = w \times d$), h is Planck's constant, ν is the optical frequency, a is differential gain of the medium, Γ is optical confinement factor, and τ_c is carrier lifetime in the active region.

For SOAs operating in the unsaturated regime ($P_{in} \ll P_s$), (3.22) is reduced to:

$$g(\nu) = \frac{g_0}{1 + (\nu - \nu_0)^2 {T_2}^2}. \tag{3.25}$$

This shows that maximum amplification can be achieved by operating the SOA close to its bandgap transition (at $\nu = \nu_0$). For a reflective EAM-SOA integrated circuit, maximum amplification can be achieved by matching the SOA's gain peak with the EAM's operating wavelength (i.e., near 1310 nm in the O-band and near 1550 nm in the C-band).

Fig. 3.18 shows gain spectrum of the 300-µm long O-band SOA and the fiber-to-fiber gain obtained using a lensed fiber in an RSOA-EAM configuration. The SOA's gain peak occurs around 1298 nm, with a maximum value of ~18 dB at 60 mA SOA pump current, and its value decreases with increasing wavelength of the input signal. However, a maximum fiber-to-fiber gain of ~8.8 dB is obtained at 1310 nm, which is in a good agreement with the ASE spectra shown earlier in Fig. 3.16 (a). The difference between the intrinsic RSOA gain and the fiber-to-fiber gain is due to input/output coupling losses as well as absorption losses of the EAM and the SSC sections. Moreover, the fiber-to-fiber gain remains more than 5 dB over a 25-nm spectral range (between 1300 nm and 1325 nm), which is desirable for colorless operation of the PIC.

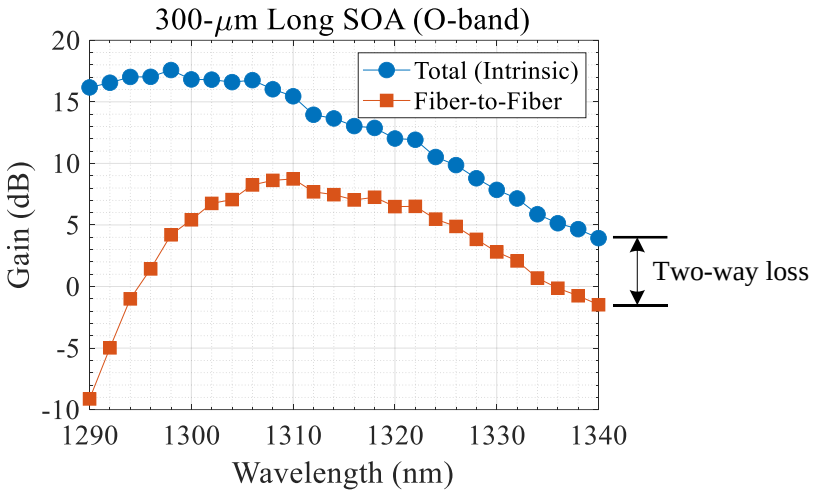


Fig. 3.18. Intrinsic and fiber-to-fiber gain spectra of a 300-μm long RSOA. $I_{SOA} = 60$ mA, $P_{in} = -28.5$ dBm, $T = 25$°C.

The gain spectrum of the 450-μm long C-band SOA is shown in Fig. 3.19, for a forward bias current of 120 mA and −35 dBm input power at 25°C submount temperature. The peak amplifier gain occurs near 1525 nm, exhibiting a maximum value of around 15.5 dB. The fiber-to-fiber gain is about 3.5 dB at 1530 nm, which is lower than that of the O-band amplifier (almost 5 dB less).

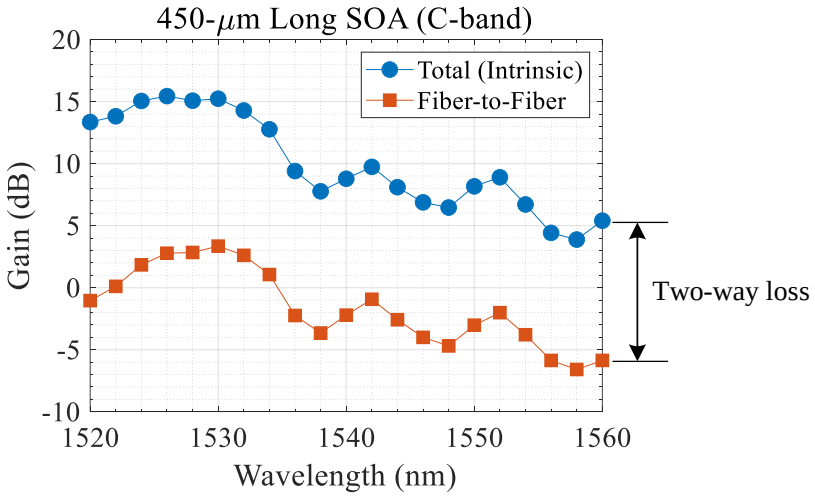


Fig. 3.19. Intrinsic and fiber-to-fiber gain spectra of the 450-μm long SOA in a reflective configuration at a pump current of 120 mA. $P_{in} = -28.5$ dBm, $T = 25$°C.

The lower fiber-to-fiber gain of the C-band SOA compared to the O-band SOA is due to a relatively higher insertion loss of the PIC (high coupling loss, higher EAM absorption loss), and a

relatively lower intrinsic gain of the SOA. Moreover, net device gain is achieved only near 1530 nm. Because of the residual facet reflectivities, the gain ripple of the SOA is also stronger as discussed in the previous section. Therefore, the C-band PIC requires two important optimizations that can be incorporated into the next generation of devices: (i) optimizing the AR coating at longer wavelengths, (ii) improving the SI-BH waveguide so as to maximize lateral carrier confinement.

3.3.5. Gain Saturation

As the input optical power to the SOA section increases, stimulated emission also increases, increasing the output signal power. However, further increase in the incident power leads to depletion of charge carriers in the active region (reduction in population inversion), which ultimately reduces the amplifier gain, a phenomenon commonly known as '*gain saturation*' [64]. This can be seen from (3.22) that as P_{in} increases and becomes comparable to the saturation power of the gain medium (P_{s}), the gain coefficient decreases, lowering the amplifier's large-signal gain, which is given by: $G = \exp(\Gamma g L_{\text{SOA}})$ [43]. However, the amplifier gain G decreases faster than the gain coefficient g because of the exponential relationship between the two. The large-signal gain of an SOA can be obtained using the small-signal gain following the relation [43][64]:

$$G = G_0 exp\left[-\frac{G-1}{G}\frac{P_{\text{out}}}{P_{\text{s}}}\right], \tag{3.26}$$

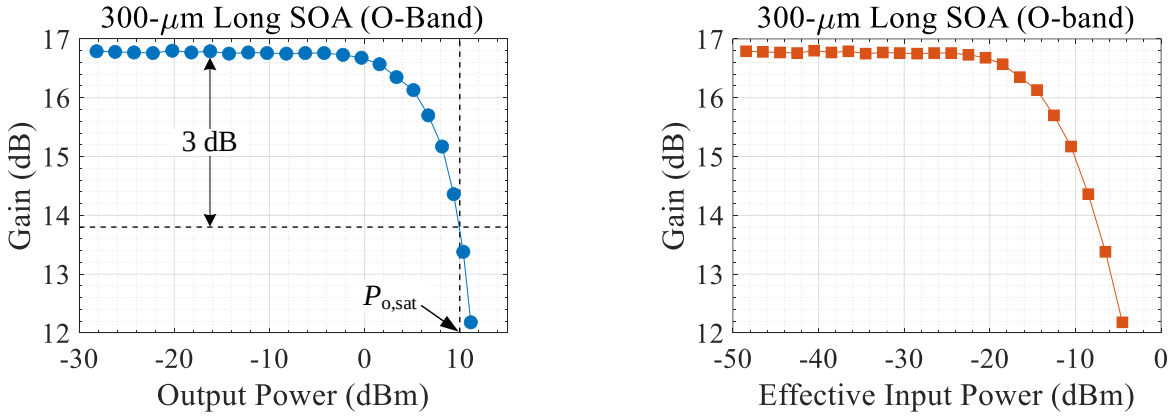
where, G_0 is the unsaturated gain (for $P \ll P_{\text{s}}$), and P_{out} is the output signal power.

Equation (3.26) shows that the signal gain decreases as the output power P_{out} becomes comparable to the gain medium's saturation power P_{s}. A common figure of merit to quantify amplifiers is the saturation output power $P_{\text{o,sat}}$, defined as the output power at which the amplifier gain drops by 3 dB from the maximum value (i.e., the large-signal gain becomes half of the small-signal gain). That means, by using $G = G_0/2$ in (3.26), $P_{\text{o,sat}}$ becomes [43][64]:

$$P_{\text{o,sat}} = \ln(2)\frac{G_0}{G_0-2}P_s. \tag{3.27}$$

Equation (3.27) shows that $P_{\text{o,sat}}$ is lower than P_{s} and it becomes independent of G_0 for large SOA gains ($P_{\text{o,sat}} \approx 0.69P_{\text{s}}$ for $G_0 \geq 30$ dB), which is due to the fact that not all the gain obtained in the optical cavity is coupled to the output facet as some of the light is lost via scattering [39][75].

Fig. 3.20 shows measured gain of the 300-µm long O-band SOA at 1310 nm for a pump current of 80 mA as a function of the output signal power (left) and effective input power (right) at 25°C. The *effective* input power is obtained by subtracting a *one-way* loss of 3.5 dB from the CW light power of the laser source at 1310 nm (cf. Fig. 3.13). The amplifier exhibits a saturation output power of about 10 dB, and saturation begins at an effective power of around about −20 dBm.



(**a**) (**b**)

Fig. 3.20. Signal gain of a 300-µm long O-band SOA in a reflective configuration as a function of (**a**) output power, (**b**) effective input power. λ = 1310 nm, I_{SOA} = 80 mA, T = 25°C.

For Fig. 3.21 shows the gain of the 300-µm long RSOA as a function of the output power for different input wavelengths at 60 mA pump current and 25°C submount temperature.

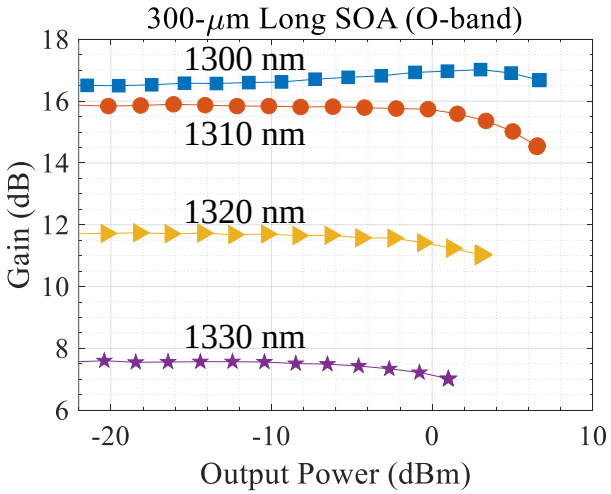
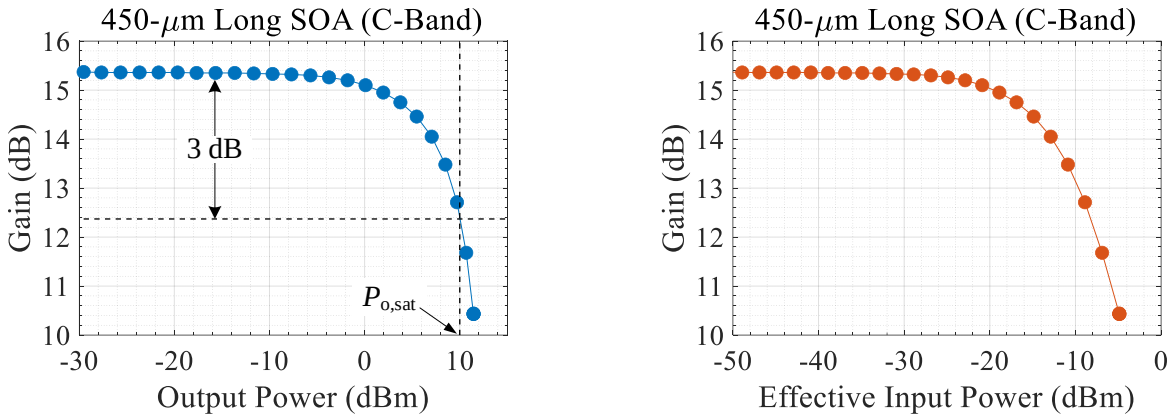


Fig. 3.21. Gain as a function of output signal power at different operating wavelengths. I_{SOA} = 60 mA, T = 25°C.

The output power of the laser source used in the setup is limited to 0 dBm and the experiment was performed without an external amplifier. As a result, the effective input power arriving at the PIC is limited, which limits the amplified signal power. As expected, the SOA gain decreases with increasing wavelength, with >8 dB difference between 1300 nm and 1330 nm. Although the signal gain is lower at longer wavelengths, the insertion loss is also low, which results in a comparable net fiber-coupled output power (>5 dB over a 20-nm range) as shown earlier in Fig. 3.18.

For completeness, the gain of the 450-µm long C-band SOA as a function output power (left) and effective input power (right) is shown in Fig. 3.22 for an input wavelength of 1530 nm and 25℃ submount temperature.



(**a**) (**b**)

Fig. 3.22. Signal gain of a 450-µm long C-band SOA in a reflective configuration as a function of (**a**) output power, (**b**) effective input power. $\lambda = 1530$ nm, $I_{SOA} = 120$ mA, $T = 25$℃.

The saturation output power of the SOA is ~10 dBm, and gain saturation begins at an effective input power of −20 dBm, both of which are the same as that of the O-band SOA. This is due to the fact that the two amplifiers have similar designs. Table 3.5 Summarizes characteristics of the two representative SOAs studied in this thesis.

Table 3.5. Key parameters and performances (TE-polarized) of the SOAs in a reflective configuration.

Operating Frequency Band	**O-band**	**C-band**
SOA length (µm)	300	450
Saturation pump current (mA)	80	120
Selected wavelength ($\lambda_{selected}$, in nm)	1310	1530
Peak SOA gain @ $\lambda_{selected}$ (dB)	17	15.5
P_{in} at which gain saturation begins (dBm)	−20	−20
Saturation output power (dBm)	10	10
Noise figure (dB) [chip-level measurement]	4	6

3.4. Amplifier Noise Figure

In an intensity-modulation/direct-detection (IM/DD) system, the major sources of transmission impairments are noise and jitter. In an unamplified system, the first one primarily comes from the relative intensity noise (RIN) of the optical source such as a tunable laser, and it leads to vertical closure of the eye diagram at the receiver side [77]. Timing jitter, on the other hand, is due to fiber dispersion as well as transmitter-induced chirp, both of which cause pulse broadening as the transmitted pulses propagate inside a dispersive medium such as an optical fiber, ultimately leading to intersymbol interference (ISI). As a result, timing jitter leads to horizontal eye closure, which, together with noise, increases the transmission bit error rate (BER).

When amplifiers, such as SOAs and fiber amplifiers (e.g., erbium-doped fiber amplifier, EDFA), are involved at the transmitter side (booster amplifier), inline, and/or at the receiver side (pre-amplifier), the ASE noise they generate couple to the RIN noise of the optical source and degrade the signal quality. The signal quality degradation is commonly expressed in terms of signal-to-noise ratio (SNR), which is the ratio of signal power to noise power [77][78].

In order to define the SNR, we can use the electrical noise determined by an ideal photodetector (unity quantum efficiency) of responsivity $\mathcal{R}$(A/W). For an input optical power P_{in}, the equivalent signal photocurrent is $I_{\text{sig}} = \mathcal{R}P_{\text{in}}$, and the input SNR ($SNR_{\text{in}}$) is given by [43][77]:

$$SNR_{in} = \frac{\langle I_{sig} \rangle^2}{\sigma^2} = \frac{P_{in}}{2h\nu B_e}, \tag{3.28}$$

where, σ^2 is the variance (root mean square) of the shot noise of the detector, $h\nu$ is photon energy, and B_{e} is electrical bandwidth of the photodetector.

At the SOA's output, the ASE noise beats with the signal (co-polarized) as well as itself. However, for large amplifier gains, the signal-spontaneous beating and shot noise are the dominant noise contributions, and neglecting other sources of noise, which is the case for gain measurements using optical spectrum analyzer, the output SNR (SNR_{out}) is given by [64][77]:

$$SNR_{out} = \frac{GP_{in}}{2h\nu B_e + \sigma_{ASE} B_e}, \tag{3.29}$$

where, σ_{ASE} is spectral density of the ASE power ($\sigma_{\mathrm{ASE}} = P_{\mathrm{ASE}}/B_{\mathrm{o}}$, where P_{ASE} is the ASE power and B_{o} is the optical bandwidth in which the optical signal is measured).

A common figure of merit for quantifying the noise performances of amplifiers is the noise figure, defined as the ratio of input and output SNRs, which is obtained by taking the ratio of (3.28) and (3.29) as [64][77]:

$$NF = \frac{SNR_{in}}{SNR_{out}} = \frac{1}{G} + \frac{2\sigma_{ASE}}{h\nu G}. \tag{3.30}$$

Here, the input coupling efficiency (η_{in}) is not included, which can be removed through setup calibration. Otherwise, the right-hand sides of (3.29) and (3.30) must be multiplied by $1/\eta_{\mathrm{in}}$.

The first term in (3.30) is the shot-noise NF of the amplifier whereas the second term is the signal-to-spontaneous beating NF. Spectral density of the ASE light σ_{ASE} is also expressed in terms of the amplifier gain, spontaneous emission (population inversion) factor [$N_{\mathrm{sp}} = N_2/(N_2 - N_1)$, where N_1 and N_2 are carrier densities in the valence and conduction bands, respectively], and photon energy $h\nu$ as [64]:

$$\sigma_{ASE} = (G-1)N_{sp}h\nu. \tag{3.31}$$

For large values of SOA gain ($G \gg 1$), the first term in (3.30) becomes negligible, and inserting the expression of (3.31) to (3.30), the amplifier's excess NF can be approximated as $NF = 2N_{\mathrm{sp}}$. The minimum value N_{sp} takes is 1 (for $N_1 = 0$). Therefore, the minimum achievable NF of an amplifier is 2 (i.e., 3 dB). Typical intrinsic noise figures of practical SOAs are $7-12$ dB (without considering insertion losses) [64].

In order to measure the NFs of the SOAs in our PICs, we used an optical spectrum analyzer (OSA) that measures σ_{ASE} and calculates the NF using (3.30), which is referred to as the "*optical method*" and a detail description of the NF measurement is available in [77][78]. Within this measurement technique, there are several options available for extracting the SOA NF with their pros and cons in terms of accuracy and the amount of time required to obtain measurement results. In our case, the "*source subtraction*" technique is employed, which involves measuring the spontaneous source emission (SSE) noise and applying a correction to remove it from the total noise measured by the analyzer [77]. The same experimental setup shown earlier in Fig. 3.14 is used for the NF

measurement. A simplified version of the setup is shown in Fig. 3.23. The SSE noise is first measured by bypassing the SOA using the path labelled '*Path*-1'. Similarly, the ASE noise is measured by following the second path, labelled '*Path*-2'.

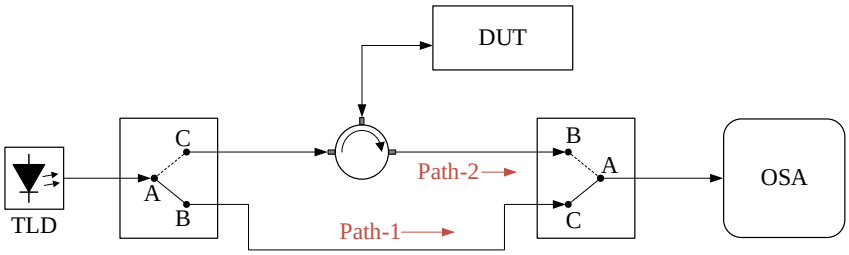


Fig. 3.23. A simplified schematic of the experimental setup used for RSOA gain and NF measurement (cf. Fig. 3.14).

When measuring the amplified signal, the total power measured by the spectrum analyzer is the sum of the signal amplified by the SOA (GP_{in}), the ASE noise power (σ_{ASE}) and amplified version of the SSE noise ($G\sigma_{\text{SSE}}$). That means, $P_{\text{out}} = G(P_{\text{in}} + \sigma_{\text{SSE}}) + \sigma_{\text{ASE}}$. Therefore, the SOA's NF can be determined by modifying (3.30) and applying a correction as follows [77]:

$$NF = \frac{SNR_{in}}{SNR_{out}} = \frac{1}{G} + \frac{2\sigma_{ASE}}{h\nu G} - \frac{2\sigma_{SSE}}{h\nu}. \tag{3.32}$$

Fig. 3.24 shows measured spectra of the input and the output signals of the O-band SOA in a reflective configuration operating at 1310 nm, for a pump current of 80 mA. The noise floor which initially is defined by the SSE noise of the source is increased to the sum of the ASE and amplified SSE noise, thereby degrading the signal quality (lower SNR_{out}).

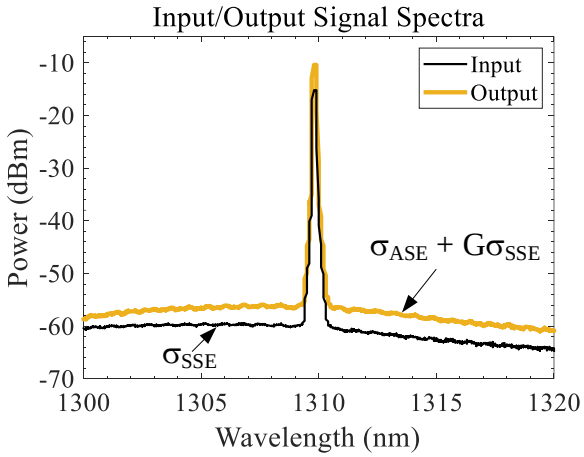
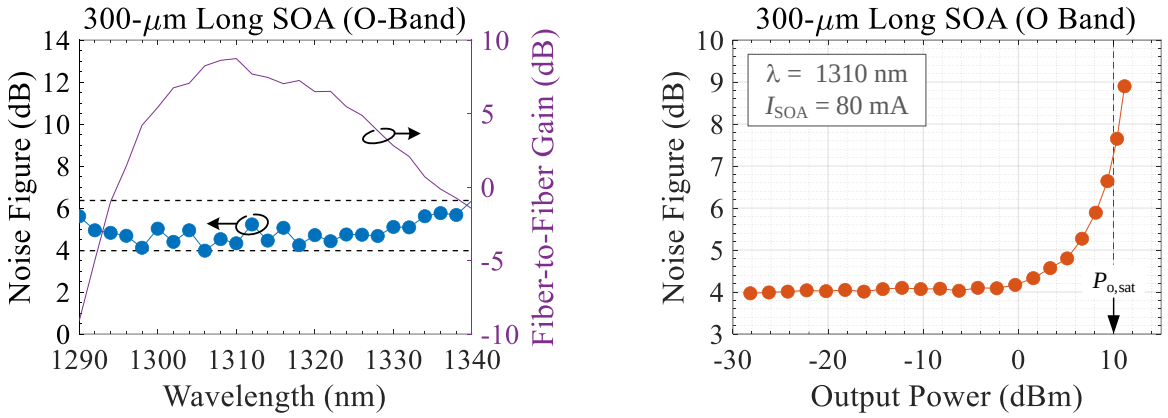


Fig. 3.24. Spectra of input and output signals which are used in estimating amplifier noise figure.

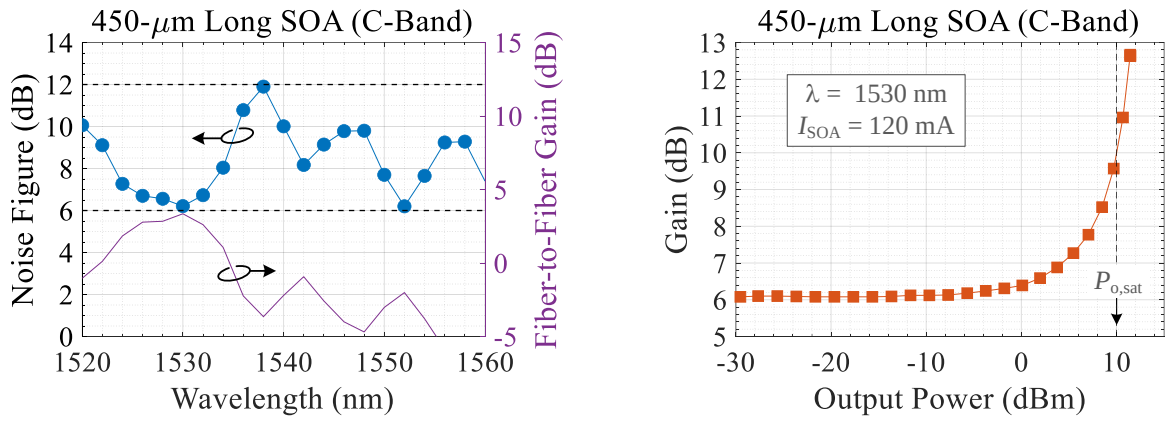
Fig. 3.25 (a) shows noise figure of the 300-µm long O-band RSOA as a function of wavelength for an input power of −15 dBm and 80 mA SOA pump current. The fiber-to-fiber gain shown earlier in Fig. 3.18 is also drawn here (solid line) along with the NF. According to (3.32), the NF has an inverse relationship with the amplifier gain. As a result, minimum NF is obtained in the region where the SOA gain is maximum. For example, the O-band SOA exhibits a minimum single-polarization (TE mode) NF of ~4 dB near 1310 nm, where the amplifier's fiber-to-fiber gain is maximum. Nevertheless, the NF remains below 6 dB over the 50-nm range (between 1290 nm and 1340 nm). The NF also increases with increasing output power because of gain saturation, which lowers the SOA gain, as shown in Fig. 3.25 (b). At 1310 nm, the SOA's NF is ~7.5 dB at the 10-dBm saturation output power of the SOA.



(**a**) (**b**)

Fig. 3.25. Noise figure of the 300-µm long O-band SOA in a reflective configuration as a function of (**a**) wavelength of the input light ($P_{in} = -15$ dBm), (**b**) output power ($\lambda = 1310$ nm,). $I_{SOA} = 80$ mA, $T = 25$℃.

For the 450-µm long C-band SOA, on the other hand, the NF fluctuates between ~6 dB and ~12 dB as shown in Fig. 3. 26 (a). The fluctuation is due to gain ripple that originates from facet reflectivities (cf. Fig. 3.13). A minimum of ~6 dB NF is obtained at 1530 nm where the SOA gain is maximum, and its value at $P_{o,sat}$ is ~9.5 dB as shown in Fig. 3. 26 (b). The effect of strong gain ripple observed earlier from the C-band SOA is clearly visible in degrading is its noise figure performance. That means, the AR coating of the C-band PIC requires further optimization in order to maximize the signal gain and reduce the amplifier noise figure.



(**a**) (**b**)

Fig. 3. 26. Noise figure of the 450-µm long C-band SOA in a reflective configuration as a function of (**a**) wavelength of the input light ($P_{in} = -15$ dBm), (**b**) output power (λ = 1530 nm,). $I_{SOA} = 120$ mA, $T = 25$℃.

Therefore, the O-band SOA with a higher amplifier gain and lower gain ripple than the C-band SOA provides a better NF performance. Its Gain and NF performances are comparable to state-of-the art SOAs although the results presented here are for a bare chip (unpackaged). The C-band SOA, on the other hand, requires further optimization in the SI-BH waveguide (to minimize SOA current leakage) as well as in the AR coating (to minimize SOA gain ripple).

3.5. Modulator Static Extinction Ratio

For waveguide modulators such as an EAM, the output power (P_{out}) decreases exponentially with increasing the modulator length, and it is related to the input power (P_{in}) via the transmission coefficient $T(V)$ at a given bias voltage V following the relation: $P_{out} = T(V)P_{in}$. Taking facet reflectivities and coupling losses into consideration, the transmission coefficient is given by [91]:

$$T(V) = \gamma(1-R)^2 \exp\left(-\Gamma\alpha(V)L\right), \tag{3.33}$$

where, γ is facet coupling efficiency, R is effective facet reflectivity ($R = \sqrt{R_1 R_2}$), Γ is optical confinement factor of the MQW active region, $\alpha(V)$ is its absorption coefficient at the bias voltage V, and L is the modulator length.

Extinction ratio (ER) of an EAM is the ratio of output powers in the *on* and *off* states (also known as on/off ratio), which is expressed in linear scale as:

$$ER = \frac{P_{on}}{P_{off}} = \frac{T(V_{on})}{T(V_{off})}, \tag{3.34}$$

where, V_{on} and V_{off} are the EAM's reverse bias voltages for the *on* and *off* states.

In logarithmic scale, the ER is given by:

$$ER\ [\text{dB}] = 4.343 \times \Gamma \left[\alpha(V_{off}) - \alpha(V_{on})\right] \times L. \tag{3.35}$$

where, $\alpha(V_{on})$ and $\alpha(V_{off})$ are absorption coefficients in the EAM's *on* and *off* states, respectively.

Equation (3.35) shows that the ER of an EAM can be increased by increasing any of the following three parameters: (i) the differential absorption coefficient [$\Delta\alpha = \alpha(V_{off}) - \alpha(V_{on})$], (ii) the EAM length, (iii) the optical confinement factor. However, for a given MQW structure, the insertion loss also increases with increasing the EAM length. Furthermore, the EAM length has the opposite effect on its electrical bandwidth because of increased EAM capacitance (to be discussed in Section 3.6.1).

The ER of an EAM also depends on the wavelength of the input light, which originates from the operating principle of EAMs where photons of energies equal to or greater than the bandgap of the active region material are easily absorbed contributing to the flow of electric current. That means, the absorption coefficient $\alpha(V)$ has wavelength-dependent behavior, increasing with increasing photon energy (decreasing wavelength). As a result, a higher ER is expected at shorter wavelengths, and the ER decreases at a larger detuning from the absorption edge of the EAM.

Fig. 3.27 shows extinction ratio spectrum of a 150-μm long C-band EAM in a reflective configuration at different bias voltages. As the reverse bias voltage increases, the absorption edge shifts to longer wavelengths (Stark shift) and the absorption spectrum broadens as well because of excitonic broadening effects. In order to minimize insertion losses, EAMs are typically designed to operate with 40−50 nm detuning from their absorption edges [57].

In our case, the absorption edge of the O-band EAM occurs near 1275 nm and that of the C-band EAMs near 1475 nm. The two EAMs are intended to operate at 1310±10 nm and 1540±10 nm, respectively. For example, the 150-μm long REAM provides a static ER of 8.5−17 dB over the entire C-band (the region shown in between dashed lines in Fig. 3.27) while keeping the insertion loss minimum (e.g., 3 dB one-way EAM insertion loss at 1530 nm, see Sect. 3.2).

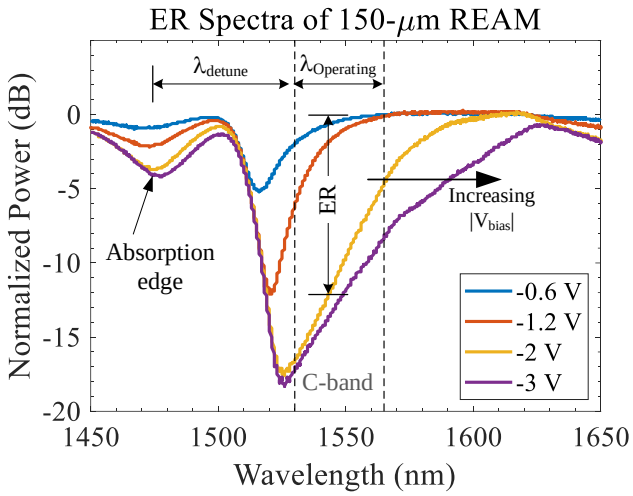


Fig. 3.27. Spectrum of static extinction ratio of a 150-μm long REAM as a function of reverse bias voltage. T = 25°C.

Another important figure of merit in designing EAMs is the differential absorption coefficient per unit applied reverse bias voltage, i.e., [40][92]:

$$\frac{\Delta\alpha}{\Delta V} = \frac{\alpha(V_{off}) - \alpha(V_{on})}{|V_{off} - V_{on}|}, \tag{3.36}$$

A modulator design that provides large $\Delta\alpha\ /\Delta V$ is desirable as it allows minimizing the modulator drive voltage. Reducing the driving voltage of an EAM has two advantages: (i) it minimizes energy consumption of the component, (ii) it allows realizing CMOS-compatible components with low-cost driving circuitry, which also reduces the device footprint. One possible option for increasing the differential absorption coefficient is by using MQWs with SI-BH waveguide structures, where quantum confined Stark effect (QCSE) [73] together with enhanced carrier and photon confinement results in high $\Delta\alpha$ at a relatively low applied DC field ($F = V/d$, where d is thickness of the MQW active region). Using equations (3.34) and (3.35), the relationship between ER, $\Delta\alpha$, and ΔF is given by [40]:

$$\frac{ER}{\Delta V} = \frac{4.343\Gamma\Delta\alpha}{\Delta F}. \tag{3.37}$$

Fig. 3.28 shows static extinction ratio of an 80-μm long EAM in an REAM-SOA configuration as a function of reverse bias voltage at different wavelengths in the C-band. The EAM's active region

has 129-nm thick MQWs embedded in two 30-nm thick separate confinement layers (a total of 189-nm thick undoped region). The MQW stack provides an optical confinement factor of ~8.9% (simulated value) for an SI-BH waveguide of 1.5 μm ridge width.

Between 0 V and −3 V, the EAM exhibits a static extinction ratio of ~11 dB at 1530 nm and ~7.5 dB at 1550 nm, and the ER remains within the two extremes for wavelengths in-between (e.g., ~8.5 dB ER at 1540 nm). The applied field reaches across the full thickness of the MQW stack at a bias voltage of around −2 V, which can be seen in the excitonic peaks of the ER curves, indicating compatibility of the device for low-voltage operation while achieving acceptable ERs. For example, the excitonic peak at 1530 nm occurs at about −1.6 V, after which the EAM's absorption flattens or slightly decreases due to field ionization of the excitons.

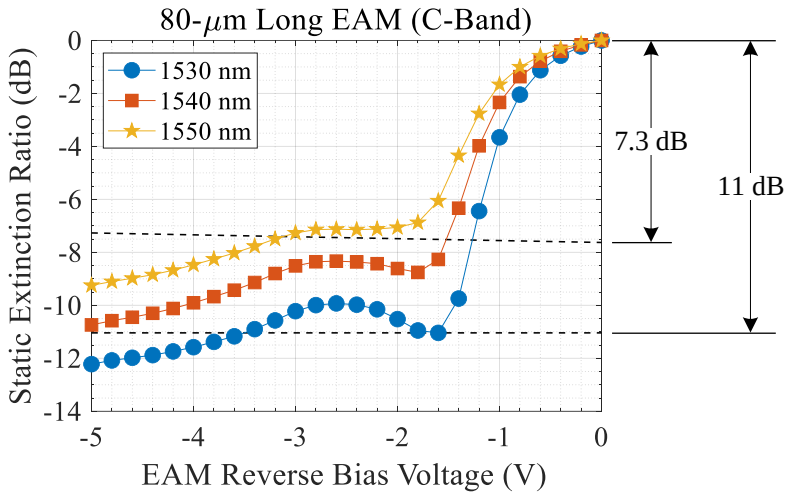


Fig. 3.28. Static extinction ratios of an 80-μm long C-band EAM in a reflective configuration at different operating wavelengths (1530−1550 nm). $T = 25$℃.

In a reflective device configuration, the effective modulator length is doubled as the EAM absorbs the input light before and after reflection. As a result, a higher ER can be achieved by using a reflective EAM compared to its single-pass counterpart for the same modulator length, which is one of the advantages gained by using reflective EAMs. For most access network applications, ERs in the range between 6 dB and 10 dB are required depending on the transmission bit rate, where a higher ER is generally required at lower bit rates in order to minimize receiver complexity and thus realize low-cost transceivers [93][94].

For an EAM with a given MQW structure, the ER can also be increased by increasing the modulator length as shown earlier in (3.34). Fig. 3.29 shows static ER of a 150-μm long EAM in a reflective configuration, operating in the C-band. Except for the length difference (150 μm vs. 80 μm), the two EAMs have the same vertical design (189 thick MQW active regions). Between 0 V and −3 V, the 150-μm long EAM exhibits a very high ER of ~17 dB at 1530 nm and ~12 dB at 1550 nm, which is nearly a 5-dB increase in each case compared to that of the 80-μm long EAM.

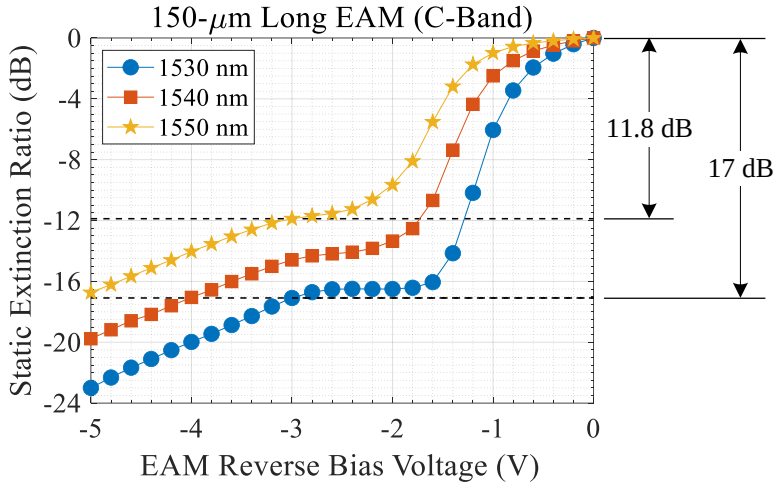


Fig. 3.29. Static extinction ratios of a 150-μm long C-band EAM in a reflective configuration at different operating wavelengths (1530−1550 nm). T = 25°C.

The third option for increasing the ER of an EAM is to increase the optical confinement factor, which is achieved by using a larger number of QW layers. Increasing the number of QWs also increases the EAM's bandwidth by lowering the modulator capacitance (to be discussed in Section 3.6.1). Therefore, a comparable ER to the 150-μm long EAM can be achieved by using a shorter EAM but with a larger number of QW layers. At the same time, high modulation bandwidth can be achieved without compromising the ER. For that reason, the O-band EAMs studied in this thesis have a length of 100-μm and a 209-nm thick MQW active region (MQW + SCH), resulting in an optical confinement factor of ~10.9% (simulated value, see Chapter 2, Section 2.5). Static ER of the 100-μm EAM in a reflective configuration is shown in Fig. 3.30.

Despite its relatively short length, the 100-μm long O-band EAM exhibits high ERs that are comparable to that of the 150-μm C-band EAM because of a higher optical confinement factor. For example, between 0 V and −3 V, the EAM exhibits a static ER of ~16.5 dB at 1300 nm and 10 dB at 1320 nm. The ER at the EAM's typical operating wavelength of 1310 nm is ~12.8 dB.

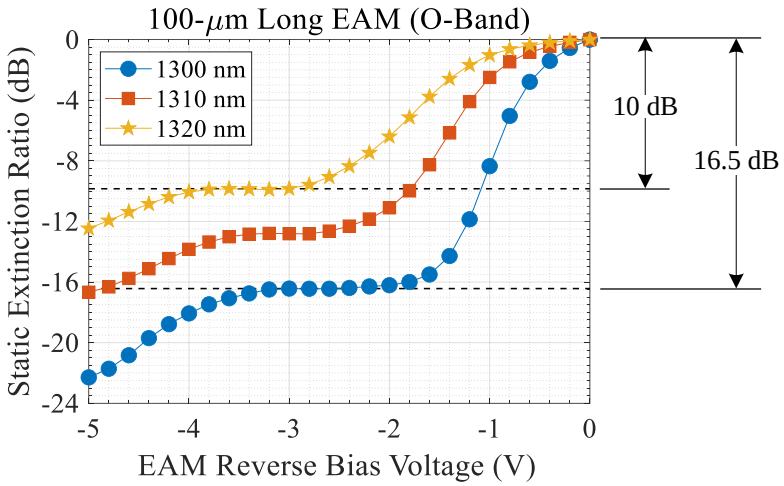
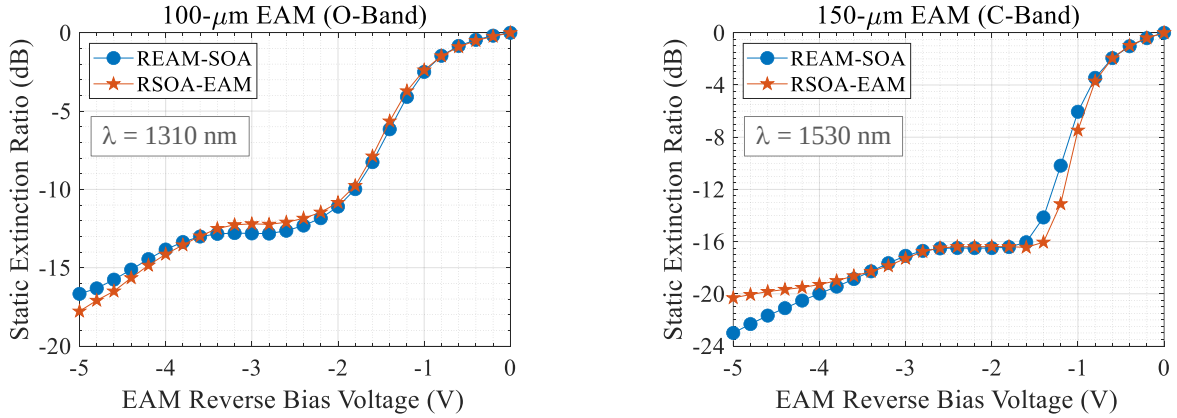


Fig. 3.30. Static extinction ratios of a 100-μm long O-band REAM at different operating wavelengths. $T = 25$℃.

For the same EAM length and number of QW layers, there is no difference in static extinction ratios between REAM-SOA and RSOA-EAM configurations as shown in Fig. 3.31 for the 100-μm long O-band EAM (left) and the 150-μm long C-band EAM (right). Static performances of the three EAMs (80 μm, 100 μm and 150 μm) are summarized in Table 3.6.



(**a**) (**b**)

Fig. 3.31. Comparison of static extinction ratios of REAM-SOA and RSOA-EAM configurations for (**a**) 100-μm long O-band EAM at 1310 nm, (**b**) 150-μm long C-band EAM at 1530 nm.

Table 3.6. Static extinction ratios of reflective EAMs.

Freq. Band	**EAM Length (μm)**	**MQW Thickness (nm)**	**ER (dB) at −3 V**	**Wavelength (nm)**
C	80	189	11	1530
	150	189	17	1530
O	100	209	16.5	1300

3.6. Dynamic Characteristics

3.6.1. Small-Signal Frequency Response

For an EAM which is long enough to be considered as a lumped element, it can be modelled as a lumped RC circuit of series resistance R_s and capacitance C_{EAM}, with a photocurrent I_{ph} flowing through it and connected to a load resistance R_L as illustrated in Fig. 3.32 (a) [57]. The electro-optic (E/O) bandwidth of an EAM is primarily limited by RC time constant, where the maximum 3-dB bandwidth is given by:

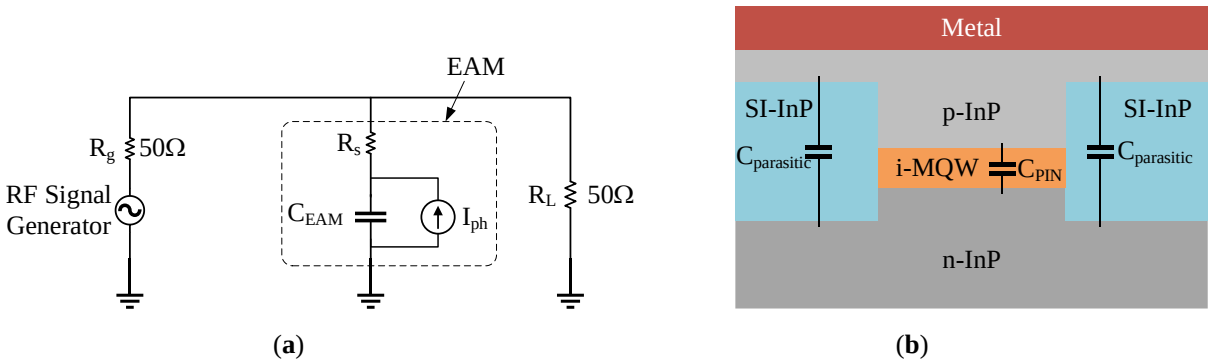
$$f_{3-dB} = \frac{1}{2\pi\left[R_s + \left(\frac{1}{R_g + R_L}\right)^{-1}\right]\left(C_{PIN} + C_{parasitic} + C_{pad}\right)}, \tag{3.38}$$

where, R_g is resistance of the RF signal generator, C_{PIN} is reverse biased junction capacitance of the EAM, $C_{parasitic}$ is the parasitic capacitance, and C_{pad} is the bonding pad capacitance ($C_{EAM} = C_{PIN} + C_{parasitic} + C_{pad}$).

The capacitive effects of the EAM can be modelled by a parallel plate capacitor model given by:

$$C = \varepsilon_0 \varepsilon_r \frac{A}{d}, \tag{3.39}$$

where, ε_0 is permittivity of free space, ε_r is dielectric constant of the medium between the parallel plates, A is their overlap area, and d is the gap between them. For calculating C_{PIN}, d is thickness of the undoped MQW active region (SCH layers and MQW stack) and ε_r is relative permittivity of undoped GaInAsP.



(**a**) (**b**)

Fig. 3.32. (**a**) Equivalent circuit model of an EAM as a lumped element, (**b**) schematic illustration of modulator capacitances due to reverse biased PIN junction as well as parasitic contributions (pad capacitance not shown).

For the bonding pads, on the other hand, the gap is larger (>4 μm) and the SI-InP reduces the capacitance because of reduced dielectric constant through Fe-doping. As a result, the main capacitive contribution comes from the reverse biased PIN junction. In any case, reducing the EAM's capacitance is desirable in order to achieve high E/O bandwidth.

The junction capacitance is determined by thickness of the intrinsic MQW region, the ridge width, and the EAM length. As a result, C_{PIN} can be reduced by using a shorter EAM (reducing overlap area A) and a thick MQW active region (increasing d), but at the expense of a reduced extinction ratio and applied electric field for a given bias voltage ($F = V/d$) [57]. In other words, a shorter EAM results in a lower ER and a thicker active region lowers the DC field that can be obtained from a given bias voltage. Therefore, there is a tradeoff between the E/O bandwidth, extinction ratio, and operating voltage of an EAM.

In order to lower the bonding pad capacitance, a commonly used approach is to use dielectric contact pads (beneath the contact pads) together with an SI-InP layer between the p- and n-doped layers. Apart from that, on-chip impedance matching technique is also commonly employed to minimize electrical reflections to the driver circuit [95].

On the other hand, the input power handling capability of an EAM is limited by hole pile-up in the valence band of the QW. This is the case in material systems such as GaInAsP, where most of the bandgap discontinuity occurs in the valence band. Since QCSE depends not on carriers but electric field, hole pile-up has more impact on the dynamic extinction ratio of an EAM than its bandwidth.

Table 3.7 summarizes calculated capacitive contributions of the three EAMs studied in this thesis together with their estimated 3-dB bandwidths using RC model. The total capacitance of the 80-μm long C-band EAM is ~127 fF and that of the 150-μm long EAM is ~207 fF, which result in ~36 GHz and ~26 GHz 3-dB bandwidths, respectively. Similarly, for the 100-μm long O-band EAM, the total capacitance is ~133 fF and the 3-dB bandwidth is ~34 GHz.

Table 3.7. Calculated capacitances and maximum 3-dB bandwidths of EAMs.

Freq. Band	L_{EAM} **(μm)**	d_{MQW} **(nm)**	w_{ridge} **(μm)**	C_{EAM} **(fF)**				R_s **(Ω)**	R_L, R_g **(Ω)**	$f_{3\text{-dB}}$ **(GHz)**
				C_{PIN}	$C_{parasitic}$	C_{pad}	C_{total}			
C	80	189	1.5	67.3	24.2	35.1	127	10	50	35.9
	150	189	1.5	126	45.4	35.1	207	5	50	25.7
O	100	209	1.3	66	31.7	35.1	133	10	50	34.2

The E/O response of an EAM can be obtained by measuring the scattering (S) parameters in a two-port system. The S_{11} parameter, which is a purely electrical characteristics, represents the input match (input reflection) of the driver circuit. It is the ratio of reflection coefficients at an operating frequency $G(\omega)$ to the DC value $G(0)$, and it is expressed in decibel as [18]:

$$S_{11}(\omega)[\mathrm{dB}] = 10\log_{10}\left|\frac{G(\omega)}{G(0)}\right|^2 . \tag{3.40}$$

The S_{21} parameter (gain), on the other hand, is the output power at port-2 as a result of input power at port-1, and it is determined by the EAM's response. It is expressed as the ratio of the transfer functions at a given frequency $H(\omega)$ to the DC value $H(0)$, and is given in decibel by [39]:

$$S_{21}(\omega)[\mathrm{dB}] = 10\log_{10}\left|\frac{H(\omega)}{H(0)}\right|^2 . \tag{3.41}$$

In order to estimate the modulation bandwidths of our PICs, we measured small-signal frequency responses of the EAMs. The responses of all C-band devices and the O-band RSOA-EAM were measured on a setup whose upper limit is 26.5 GHz whereas the O-band REAM-SOA was characterized on a different test bench using Agilent-67GHz (N5227A PNA) and a commercial photodiode of 70 GHz bandwidth [95]. The responses of the transmission lines and the photodiode were calibrated using a standard procedure. For electrical access from the top, the devices were mounted on an HF carrier with a ceramic submount for efficient heat sink. The EAMs have a 150-µm pitch of ground-signal-ground (GSG) electrical connections, and they are terminated with a 50-Ω resistor as illustrated in Fig. 3.33.

In order to avoid the need for angled fiber holders due to refraction of the output light at the interface between the 7°-tilted SSC and air, the chips are mounted on a 23°-tilted HF carrier, following Snell's law, which is given by:

$$\frac{n_1}{n_2} = \frac{\sin\theta_2}{\sin\theta_1}, \tag{3.42}$$

where, n_1 and n_2 are refractive indices of the waveguide and air ($n_1 \approx 3.2$ for GaInAsP/InP MQW, $\theta_1 = 7°$, $n_2 \approx 1$ for air, and $\theta_2 = 23°$). Therefore, the input/output fiber lies parallel to the optical axis on the plane of propagation.

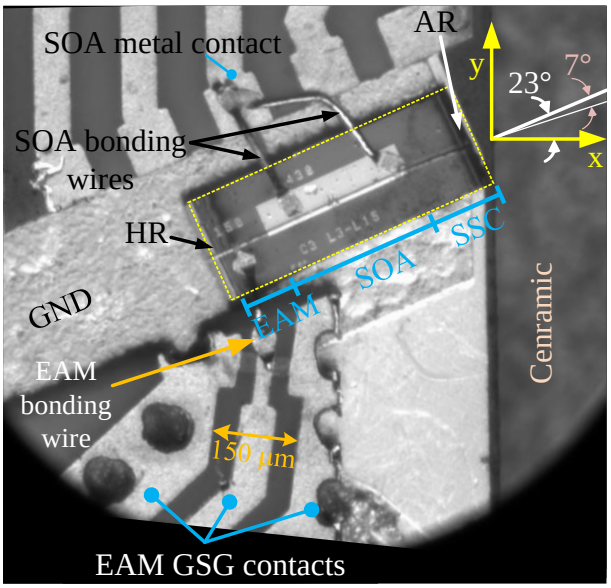
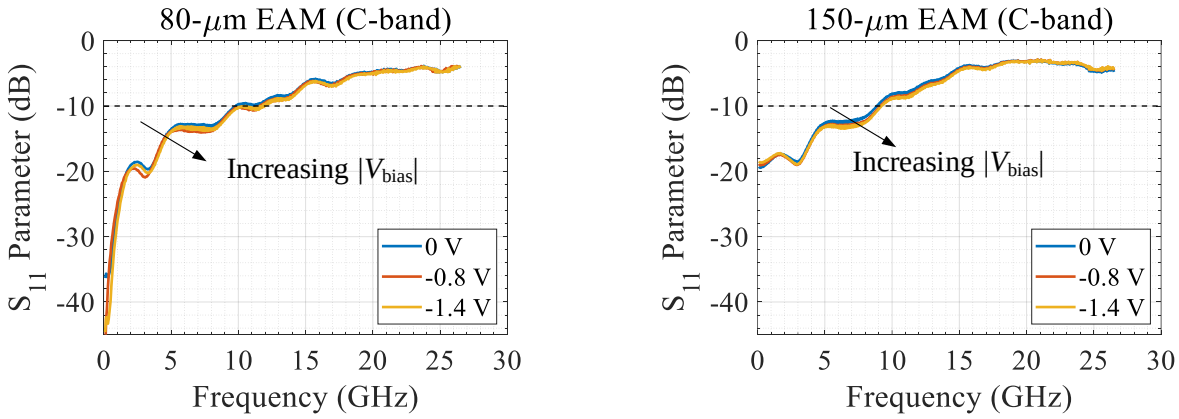


Fig. 3.33. Picture of an REAM-SOA mounted on a 23°-tilted HF carrier.

Fig. 3.34 shows measured reflection coefficients (S_{11} parameters) of the HF carrier for the two C-band EAMs: 80-µm (left) and 150-µm long (right). The S_{11} parameter is below −10 dB only up to ~10 GHz and below −5 dB up to ~15 GHz, indicating that further optimization of the HF carrier is necessary in order to minimize electrical reflections.

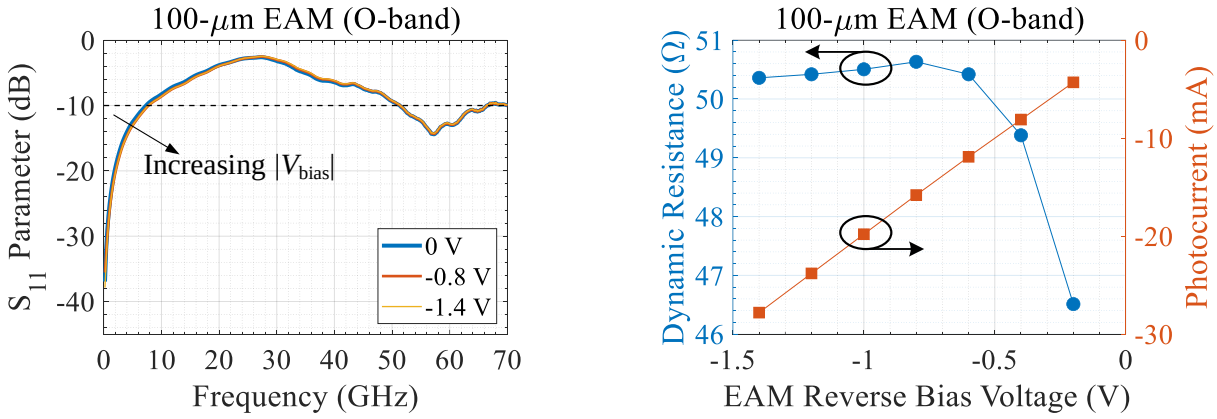


(**a**) (**b**)

Fig. 3.34. Reflection (S_{11}) parameters of the driving circuits of (**a**) 80-µm long and (**b**) 150-µm long C-band EAMs.

Small-signal frequency response of the 100-µm O-band EAM, on the other hand, is measured on a different test bench capable of measuring responses up to 70 GHz. The S_{11} parameter of the EAM

is shown in Fig. 3.35 (left) together with dynamic resistance of the circuit as a function of reverse bias voltage (right). Since the same CuW HF carrier is used, the electrical behavior does not change except for some differences that may arise from variations in length and straightness of the bonding wires, which determine its electrical characteristics (resistance and inductance). For reverse bias voltages higher than −0.5 V, dynamic resistance of the circuit approaches 50 Ω, which validates the previous assumption for a 50-Ω load resistance.



(**a**) (**b**)

Fig. 3.35. (**a**) S_{11} parameter of the driving circuit of the 100-µm long O-band EAM, (**b**) effective resistance of the circuit as a function of reverse bias voltage.

Nevertheless, the S_{21} parameter is the one that provides actual information about the E/O response of an EAM. The S_{21} parameters of our EAMs were measured by injecting a CW light of 0 dBm power (less than −5 dBm effective input power). The SOA integrated with the 150-µm long C-band EAM has a cavity length of 450 µm whereas the one with 80-µm long C-band EAM has 500 µm cavity length. SOA active region was designed in order to find a compromise between high gain and high saturation power. Based on the vertical structure design, we made components with different SOA lengths (between 300 and 500 µm), and we found the best compromise for the lengths shown here. The SOAs are forward biased by applying 120 mA to the longer SOA and 90 mA to the shorter one, providing comparable current densities. The EAMs are reverse biased between −1 V and −1.4 V, depending on the operating wavelength. Finally, the modulating electrical waveform (small signal) is generated by a vector network analyzer (VNA) with a peak-to-peak voltage swing of ~200 mV (equivalent to −10 dBm RF power).

Fig. 3.36 shows measured S_{21} parameters of the 150-µm (left) and the 80-µm (right) long C-band EAMs at different operating wavelengths (between 1530 and 1550 nm) and 25°C submount temperature. Both EAMs are in an REAM-SOA PIC configuration.

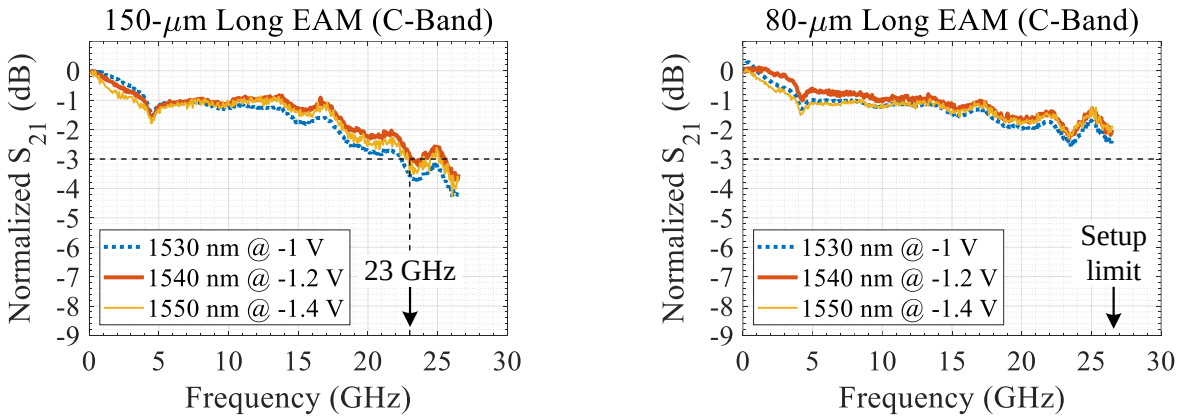


Fig. 3.36. Small-signal frequency responses (S_{21} parameters) of REAM-SOAs based on (**a**) 80-µm long EAM, and (**b**) 150-µm long EAM at 25°C. $P_{in} \approx 0$ dBm, $I_{SOA} = 90$ mA for (a) and 120 mA for (b).

The 150-µm long EAM exhibits 3-dB cutoff bandwidth of ~23 GHz whereas the frequency response of the 80-µm long EAM is still flat at 26.5 GHz (setup upper limit). The E/O bandwidth of the shorter EAM suggests that it can support bit rates ≥50 Gb/s using non-return-to-zero (NRZ) modulation format. This shows that the E/O bandwidth of an EAM indeed can be increased by using shorter EAMs.

On the other hand, the frequency responses of the EAMs are independent of the operating wavelength, which is desirable for colorless operation of the devices over a wide range of spectrum. A slight shift in the frequency response of the 150-µm long EAM at 1530 is attributed to the beginning of saturation effects occurring inside the EAM section ($\Delta f_{3\text{-dB}} \approx 1$ GHz).

Fig. 3.37 compares the frequency responses of the two C-band EAMs at 25°C and 45°C for an input wavelength of 1540 nm. The performance of the 80-µm long EAM is not degraded by temperature up to 45°C. The 3-dB bandwidth of the 150-µm long EAM, on the other hand, is reduced by ~1 GHz at 45°C, which is attributed to saturation effects similar to the one observed for an input wavelength of 1530 nm when the EAM operates at 25°C.

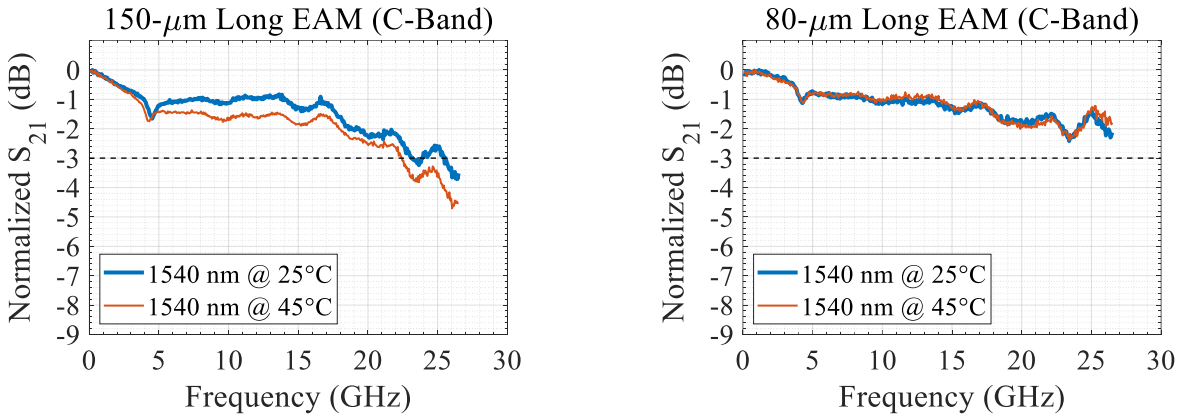
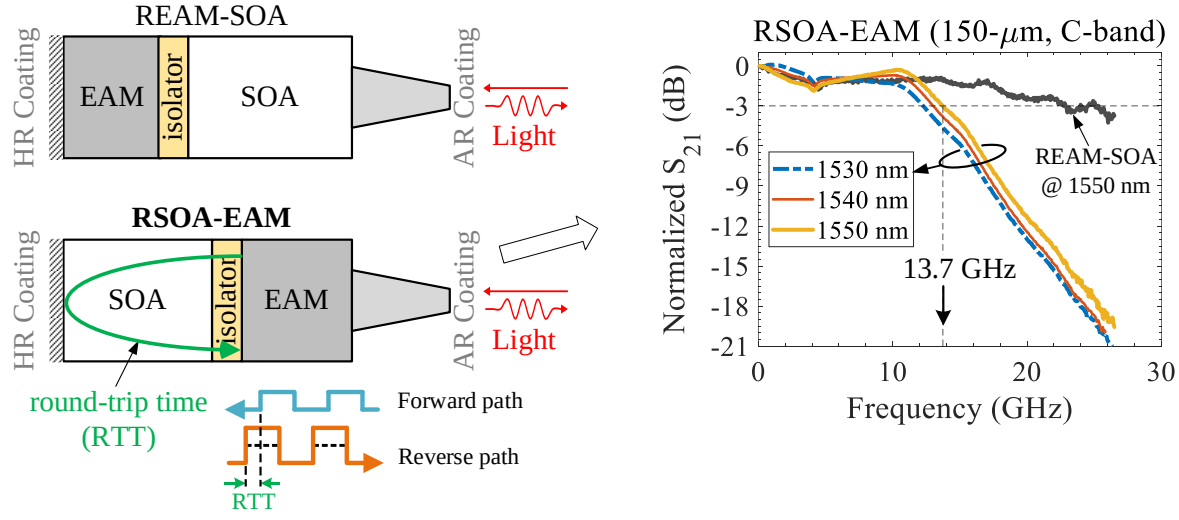


Fig. 3.37. Comparison of S21 parameters at 25C vs. 45C for (**a**) 150-µm long EAM, (**b**) 80-µm long EAM. Both PICs are in an REAM-SOA configuration. $V_B = -1$ V to -1.2 V, $P_{in} \approx 0$ dBm, $I_{SOA} = 90$ mA for (a) and 120 mA for (b).

On the other hand, for the same EAM length, the RSOA-EAM configuration significantly affects the modulator's frequency response due to the round-trip delay inside the SOA section, which is schematically illustrated in Fig. 3.38(a). The frequency response of the 150-µm long EAM is shown in Fig. 3.38 (b). The 3-dB cutoff bandwidth of the EAM is reduced to ~13.5 GHz at 1550 nm and slightly higher than 12 GHz at 1530 nm, which is an approximately 9-GHz reduction compared with the one obtained in from an REAM-SOA. For comparison, the EAM's response in an REAM-SOA configuration for an input wavelength of 1550 nm is also shown in the figure.



(**a**) (**b**)

Fig. 3.38. (**a**) Schematics of REAM-SOA (top) and RSOA-EAM (bottom) PIC configurations, (**b**) small-signal frequency response (S_{21} parameter) of the 150-µm long EAM in an RSOA-EAM configuration ($L_{EAM} = 150$ µm, $L_{ISO} = 10$ µm). $P_{in} = 0$ dBm, $I_{SOA} = 90$ mA, $T = 25$°C. *Isolator*: inter-electrode isolation.

Considering the 450-µm length of the SOA and a 10-µm inter-electrode isolation between the EAM and the SOA sections, the round-trip time (RTT) is ~10 ns (n = 3.2), which large enough to cause a degradation to the EAM's frequency response (10 ps vs. 73 ps, equivalent of 13.7 GHz). The RTT causes a phase shift between the forward and reverse modulations when the bit rate is very high, degrading dynamic response of the PIC. Therefore, the maximum bit rate an RSOA-EAM can support is limited to a few tens of Gb/s (e.g., up to 25 Gb/s NRZ) regardless of the EAM's length.

In order to further analyze the effects of modulator length and thickness of the MQW active region on the EAM's bandwidth, we also measured the frequency response of the 100-µm long EAM in both REAM-SOA and RSOA-EAM configurations. Fig. 3.39 shows small-signal frequency response of the 100-µm long O-band EAM in an REAM-SOA configuration, for different input wavelengths and two operating temperatures: 25°C (left) and 45°C (right). At 25°C, the PIC is tested between 1300 nm and 1320 nm.

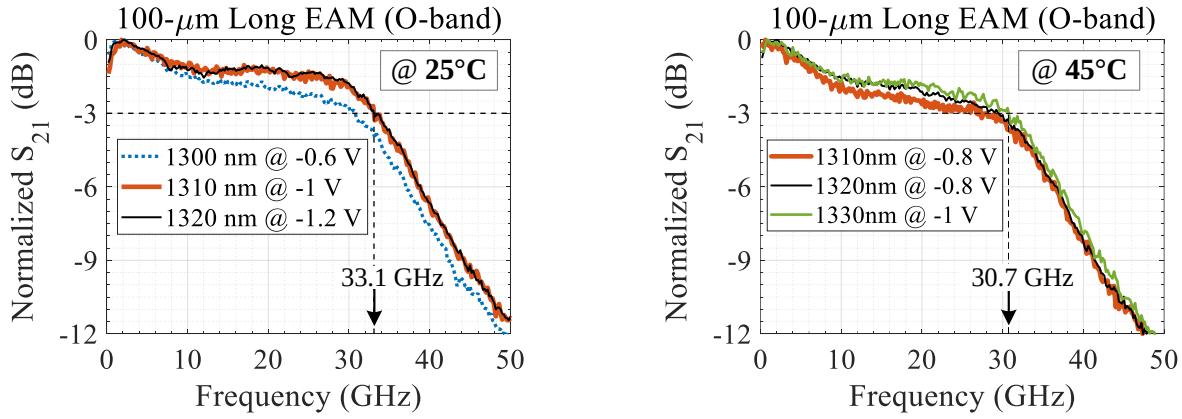


Fig. 3.39**.** Small-signal frequency response (S_{21} parameter) of a 100-µm long O-band EAM for different input wavelengths, operating at (**a**) 25°C, (**b**) 45°C. P_{in} = 0 dBm, I_{SOA} = 40 mA.

The effect of saturation, which already is visible at 25°C for an input wavelength of 1300 nm, becomes stronger at 45°C. Moreover, insertion loss of the EAM at a given wavelength increases as the temperature increases because the EAM's absorption edge shifts towards the red end of the spectrum. For example, for a thermal detuning of ~0.7 nm/°C, the EAM's absorption at 1300 nm and 25°C now becomes the equivalent of 1290 nm at 45°C (i.e., 10 nm red shift in the absorption edge of the EAM). With that in mind, the 45°C experiments are performed for wavelengths form

1310 nm to 1330 nm while keeping the 20-nm spectral range. The SOA is forward biased by applying 40 mA DC current ($L_{SOA} = 300$ μm) and injecting 0 dBm optical power.

When operated at 25℃, the 100-μm long EAM exhibits a 3-dB cutoff bandwidth of ∼33 GHz at 1310 nm as shown in Fig. 3.39 (a). Saturation of the EAM's absorption is clearly visible in this case, reducing its response when operated at shorter wavelengths. For example, the E/O bandwidth at 1300 nm is reduced to ∼30.5 GHz even at a relatively lower bias voltage of −0.6 V. Nevertheless, the bandwidth remains >30 GHz over the 20-nm range considered here, which allows the device to be effectively modulated at least at 50 Gb/s NRZ while operating it in a colorless mode.

The device is designed for 25℃ operation, centered at 1310 nm, as one can see from the both the SOA's gain peak (cf. Fig. 3.18) and the EAM's maximum E/O bandwidth in Fig. 3.39 (a). When the device operates at higher temperature of 45℃, the E/O bandwidth is reduced by ∼3 GHz ($f_{3\text{-dB}} \approx 27$ GHz at 1300 nm and ∼30.5 GHz at 1330 nm). The performances of the EAM and the SOA are affected at high temperatures. In the amplifier case, thermally excited electrons having a lower effective mass than holes can easily escape from the MQW region, resulting in electron leakage current and thus reducing the amplifier gain. Conduction band offset is the primary physical parameter that controls electron leakage current [39]. As a result, enhanced photon confinement is necessary for high temperature operation of SOAs. For the EAM, on the other hand, performance degradation is primarily due to the broadening of its absorption spectrum where photogenerated electrons and holes tunnel through the barrier region [58].

At low to moderate input powers, the E/O response of an EAM has a linear relationship with the input power before it saturates. To demonstrate the effect of the intensity of light inside the EAM section on its frequency response, we measured S_{21} parameters at different input powers as well as SOA pump currents. Fig. 3.40 shows the response of the 100-μm long O-band EAM in an REAM-SOA configuration at 1310 nm for two input power levels, i.e., −5 and 0 dBm, with respective SOA pump currents of 40 mA and 60 mA. The EAM's reverse bias voltage is fixed at −1 V.

The frequency response reveals that at 0 dBm/60 mA, the EAM is not saturating since the power level is not high enough to saturate the modulator. The EAM exhibits a 3-dB cutoff bandwidth of ∼34 GHz, which is slightly higher than what we obtained earlier for the same input power but at

40 mA SOA current ($\Delta f_{3\text{-dB}} \approx 1$ GHz, cf. Fig. 3.39). When the intensity of light inside the EAM is lowered by reducing both the input power and the SOA current (−5 dBm/40 mA), the E/O bandwidth is reduced to ~30.5 GHz, which is ~3.5 GHz lower than the 0-dBm case.

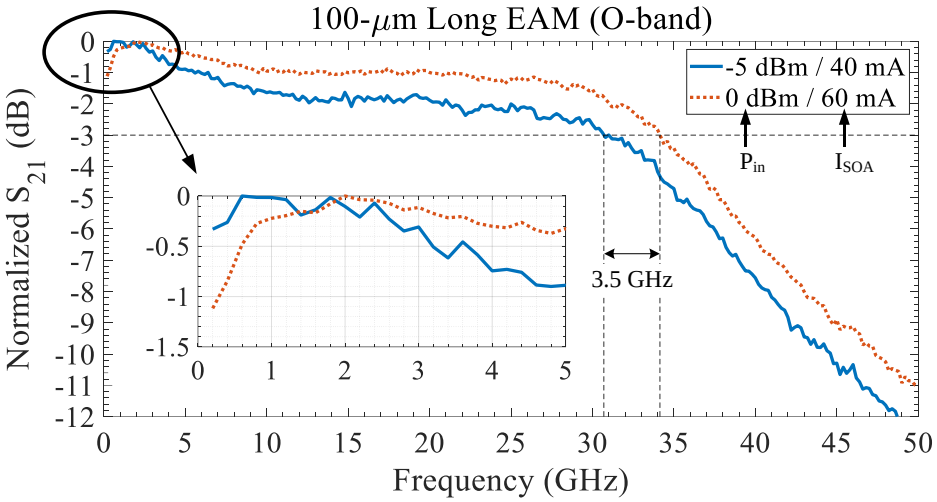
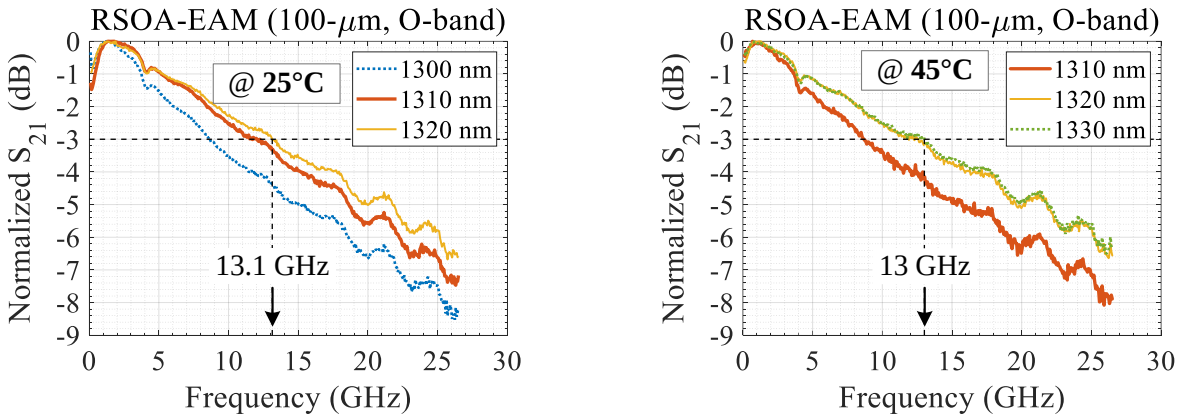


Fig. 3.40. S_{21} parameter of a 100-µm long O-band EAM in an REAM-SOA configuration for different input power levels (−5 dBm and 0 dBm) and SOA pump currents (40 mA and 60 mA) at 1310 nm. $V_{bias} = -1$ V, $T = 25$°C.

On the other hand, the SOA acts as a low-pass filter at a relatively high input power because of gain saturation, and it is clearly visible in the 0dBm/60mA case as shown in the inset of Fig. 3.40. We attribute the slight overshoot in the EAM's frequency response around 2 GHz to the filtering effect of the SOA. For that reason, the S_{21} parameters of the O-band devices are normalized to the maximum gain, not to the DC value. If one normalizes the responses to amplitude at the lowest frequency, the 3-dB bandwidth will increase by ~2 GHz. Low frequency filtering is not observed in the C-band devices because of two reasons: (i) the effective input power arriving at the EAM section is relatively lower because of higher input coupling loss (cf. Fig. 3.13), (ii) the intrinsic SOA gain is relatively lower because of lateral current leakage (cf. Fig. 3.19).

An SOA under saturation causes patterning effect when the transmission bit rate is comparable to the inverse of carrier lifetime $1/\tau_c$ (its value is in the order of 0.1 ns for GaInAsP). Patterning effect is due to change in carrier density following the bit pattern so that the SOA's gain moves back and forth between saturation and small-signal gain values [64]. But the severity of pattern effect depends on bit rate, $P_{o,sat}$, and modulation format. For example, for bit rates beyond 10 Gb/s

NRZ-OOK, the effect is less significant because there is not enough time for the carrier density to reach steady state condition.



(**a**) (**b**)

Fig. 3.41. Small-signal frequency response of a 100-µm long O-band EAM in an RSOA-EAM configuration for different input wavelengths, operating at (**a**) 25°C and (**b**) 45°C. $P_{in} = 0$ dBm, $I_{SOA} = 40$ mA. The EAM's reverse bias voltages are −0.6 V, −0.8 V, and −1.2 V in order of increasing wavelength for both (a) and (b).

Finally, as expected, the frequency response of the 100-µm long EAM in an RSOA-EAM configuration is also significantly reduced by the round-trip delay inside the SOA section as shown in Fig. 3.41. Since a higher power is involved in the O-band devices, because of a higher amplifier gain and lower insertion loss, saturation of the EAM is more pronounced as the operating wavelength decreases. As a result, the EAM exhibits a maximum 3-dB cutoff bandwidth of ~13 GHz for an input wavelength of 1320 nm when operating at 25°C, and 1330 nm at 45°C. Moreover, because of SOA saturation, an overshoot occurs in the frequency response at low frequencies, which is similar to the REAM-SOA case.

Table 3.8 summarizes performances of the various device configurations studied in this thesis. Because the EAMs in RSOA-EAM configuration exhibit lower bandwidth than their REAM-SOA counterparts, we used the latter configuration for high-speed digital transmissions (25 Gb/s NRZ in the C-band and 50 Gb/s NRZ in the O-band). However, the O-band RSOA-EAM is used for 10 Gb/s analog transmission anticipating that it provides a relatively linear amplifier response, which is critical for analog radio-over-fiber (A-RoF) applications.

Table 3.8. Small-signal frequency responses of reflective EAMs.

Frequency Band	EAM Length (μm)	Thickness of MQWs (nm)	PIC Configuration	3-dB E/O Bandwidth (GHz)
C	80	189	REAM-SOA	>26.5*
	150	189	REAM-SOA	23
	150	189	RSOA-EAM	13.7
O	100	209	REAM-SOA	33
	100	209	RSOA-EAM	14

** Upper limit of the experimental setup used for that particular measurement.*

3.6.2. Modulator Induced Chirp

The transmission distance in the C-band is no longer limited by fiber loss, thanks to EDFAs. It rather is limited by chromatic dispersion and transmitter-induced chirp. In an IM/DD system, the intensity modulator such as an EAM induces a transient chirp at the rising and the trailing edges of the transmitted pulse, setting an upper limit to the transmission bandwidth of optical fibers [96]. For an EAM, chirp originates from the change in refractive index of the active region material under the influence of an externally applied electric field.

Depending on the sign of the chirp parameter, the carrier frequency either increases or decreases. Positively chirped pulses broaden during propagation, causing intersymbol interference (ISI) at the receiver side [97]. Up to a certain extent, negatively chirped pulses experience compression (until the pulse width reaches the Fourier limit), enhancing the transmission distance through a constructive interplay between the negative chirp and the positive fiber dispersion.

Small-Signal Chirp Parameter

Chirp parameter, also known as Henry factor α_H, is a common figure of merit to quantify the chirp performances of transmitters [98]. It is the ratio of changes in the real (n) and imaginary (κ) parts of the complex refractive index ($\tilde{n} = n + i\kappa$) [17]. For an external intensity modulator such as an EAM, the chirp parameter is given by [96]:

$$\alpha_H = \frac{dn/dE}{d\kappa/dE}, \tag{3.43}$$

where, dn/dE and $d\kappa/dE$ respectively are changes in the real and imaginary parts of the refractive index under the influence of an externally applied field. The change in the complex refractive index is given by [57]:

$$\frac{d\kappa}{dE} = \frac{\lambda}{4\pi}\frac{d\alpha}{dE}, \tag{3.44}$$

where, λ is wavelength of the input light, and $d\alpha/dE$ is change in absorption coefficient of the MQW active region. Inserting (3.44) into (3.43) gives the expression for the small-signal chirp parameter of an EAM [18]:

$$\alpha_H = \frac{4\pi}{\lambda} \cdot \frac{dn/dE}{d\alpha/dE} \equiv \frac{4\pi}{\lambda} \cdot \frac{\Delta n}{\Delta \alpha}. \tag{3.45}$$

The numerator in (3.44) represents change in the carrier frequency (wavelength), which also determines the phase of the transmitted pulse, and the denominator represents strength of intensity modulation. Hence, the chirp parameter can be considered as the ratio of *phase modulation* (PM) to *intensity modulation* (IM). For an external intensity modulator, the *frequency modulation* (FM) component appears only at the leading and trailing edges of the transmitted pulse.

The exact absorption coefficient of an EAM can be calculated by numerically solving Schrödinger equations (see Chapter 2, Section 2.5 for further details). For analytical estimation, its spectrum can be approximated as a Lorentzian using the relation [98]:

$$\Delta\alpha = \frac{\alpha_p \cdot (\Delta\lambda/2)^2}{\left(\lambda - \lambda_p\right)^2 + (\Delta\lambda/2)^2}, \tag{3.46}$$

where, α_p is the peak absorption coefficient, λ_p is the wavelength at which α_p occurs, and $\Delta\lambda$ is spectral broadening of the absorption spectrum.

The change in the real part of the refractive index can be calculated using the differential absorption coefficient from (3.46) using Kramers−Krönig relationship as [57][98]:

$$\Delta n = \frac{\lambda^2}{2\pi^2} P \int_0^\infty \frac{\Delta\alpha}{\lambda^2 - \lambda'^2} d\lambda', \tag{3.47}$$

where, *P* is Cauchy principal value.

Fig. 3.42 shows the differential absorption coefficient and the corresponding refractive index calculated using (3.46) and (3.47) [98]. With increasing the EAM's reverse bias voltage, the absorption coefficient increases whereas the differential refractive index decreases, the latter

entering the negative regime after −1.5 V. As a result, the chirp parameter in (3.44) decreases as the reverse bias voltage increases, crossing the zero-chirp line at a certain bias point.

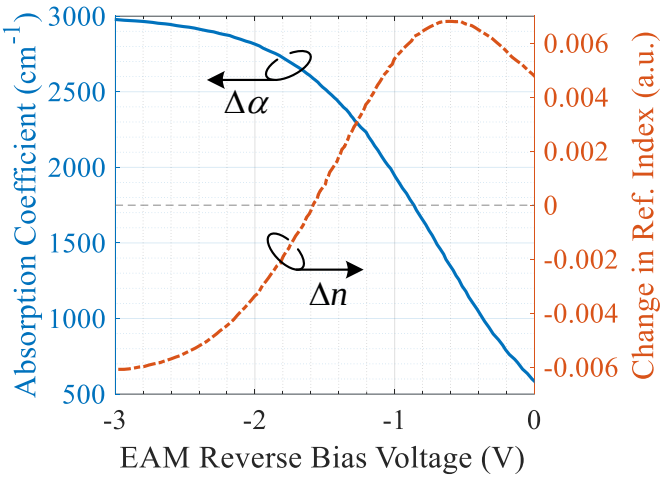


Fig. 3.42. Calculated changes in absorption coefficient (left *y*-axis) and refractive index (right *y*-axis) as a function of reverse bias voltage of an EAM (after [98]).

In order to characterize chirp performances of our components, we used a fiber-based Mach-Zehnder (MZ) interferometer as an optical discriminator [97] using a similar experimental setup as explained in [100]. The setup is reconfigured for testing reflective devices by inserting an optical circulator between the laser source and the device under test (REAM-SOA or RSOA-EAM). For small-signal chirp measurement, the modulating signal is generated by a network analyzer with a typical voltage swing of around 200 mV (equivalent of −10 dBm RF power). For large-signal chirp measurement, on the other hand, the electrical signal is generated by a signal quality analyzer with a bit pattern of 2^7-1 pseudorandom binary sequence (PRBS7). The network analyzer measures the time-resolved chirp, and a sampling oscilloscope is used to monitor the output signal.

Fig. 3.43 illustrates transmission curve of the MZ interferometer having a free spectral range (FSR) of ~48 GHz. By fixing the control point at the middle of the transmission curve (points A and B for the positive and negative slopes, respectively), any deviation in the carrier frequency as a result of EAM-induced chirp translates to an increase (positive chirp) or decrease (negative chirp) in the amplitude of the output signal, swinging between the MZ's minimum and maximum transmissions. In order to accurately measure the modulator chirp with a better linear response, FSR of the MZ must be larger than four times the anticipated frequency deviation [97].

The IM and FM components of the transmitted signal can be extracted from the signals captured at the positive (M_+) and negative (M_-) slopes of the transmission curve. The former contains the sum of the two contributions whereas the latter is the difference between the two [97][100], i.e.,

$$\begin{aligned} M_+ &= V_{IM} + V_{FM}, \\ M_- &= V_{IM} - V_{FM}, \end{aligned} \tag{3.48}$$

where, V_{IM} and V_{FM} are the intensity and frequency modulation components of the transmitted signal, respectively, and they can be obtained by manipulating the above two equations, resulting:

$$\begin{aligned} V_{IM} &= \frac{1}{2}(M_+ + M_-), \\ V_{FM} &= \frac{1}{2}(M_+ - M_-). \end{aligned} \tag{3.49}$$

The chirp parameter of an EAM can be extracted from signals recorded at the two slopes as [100]:

$$\alpha_H = \frac{1}{\mathrm{j}} \cdot \frac{1}{tan\left(\frac{\pi f_m}{FSR}\right)} \cdot \left(\frac{M_+ - M_-}{M_+ + M_-}\right), \tag{3.50}$$

where, f_m is the modulation frequency and FSR is free spectral range of the MZ interferometer.

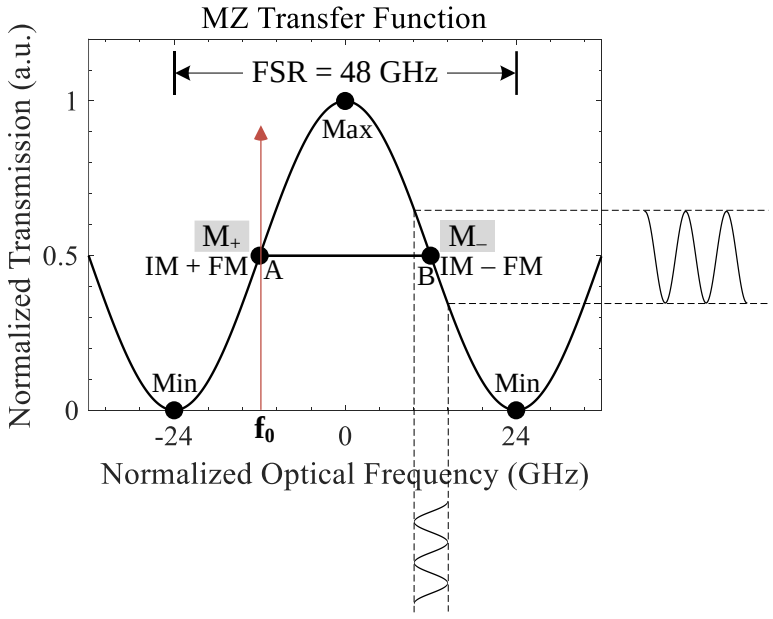


Fig. 3.43. Schematic illustration of the transfer function of a Mach-Zehnder interferometer and the control points for chirp measurement.

The instantaneous phase shift induced by an EAM can also be obtained using the time-varying small-signal chirp parameter $\alpha_H(t)$ as [17][100]:

$$\frac{d\phi}{dt} = \frac{\alpha_H}{2} \cdot \frac{1}{P(t)} \cdot \frac{dP(t)}{dt}, \tag{3.51}$$

where, ϕ and $P(t)$ are instantaneous phase and power of the output signal, respectively.

In order to analyze for any frequency dependent behavior of the chirp parameter, we performed a frequency sweep on the RF signal from a few MHz to 20 GHz while injecting a monochromatic light at 1545 nm. Fig. 3.44 shows the chirp parameter of the 150-µm long C-band EAM in an REAM-SOA configuration for a reverse bias voltage of −1.3 V and 90 mA SOA pump current, measured at 25°C submount temperature (V_{PP} = 200 mV).

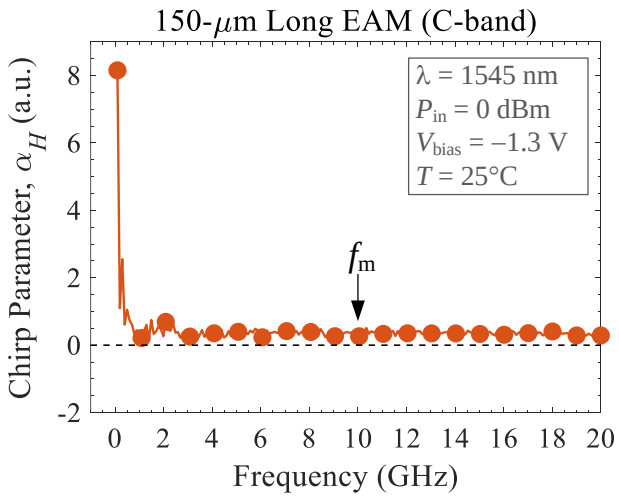
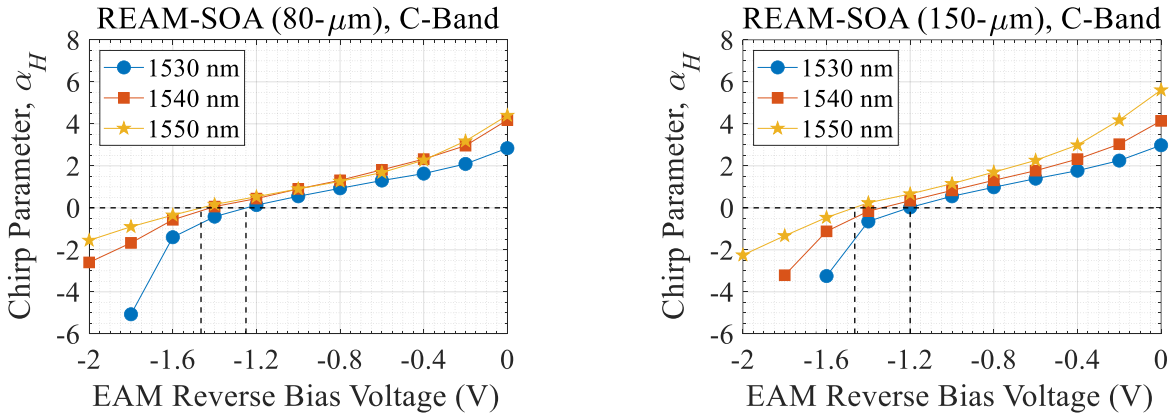


Fig. 3.44. Small-signal chirp parameter as a function of modulation frequency obtained from a 150-µm long EAM in an REAM-SOA configuration.

Except for a small variation observed at very low frequencies, which is attributed to lower limit of the setup, the chirp parameter is independent of the modulation frequency. The chirp parameter at −1.3 V and 1545 nm is positive, and its value is about +0.35. Afterwards, we applied a 10-GHz RF signal for the rest of our chirp measurements.

Fig. 3.45 shows small-signal chirp parameters of the 80-µm (left) and the 150-µm (right) long EAMs in an REAM-SOA configuration. In both cases, the chirp parameter is positive for the *on* state and moves to the negative regime as the reverse bias voltage increases towards the *off* state.

Since the EAMs have identical vertical structures (the same number of QW layers), the small-signal chirp performances are similar in the two cases, except for small differences in the *on*-state performances. This similarity is due to the fact that α_H is an average value encountered between the *on* and *off* states. However, the instantaneous chirp performances are different, which will be discussed in the next section.



(**a**) (**b**)

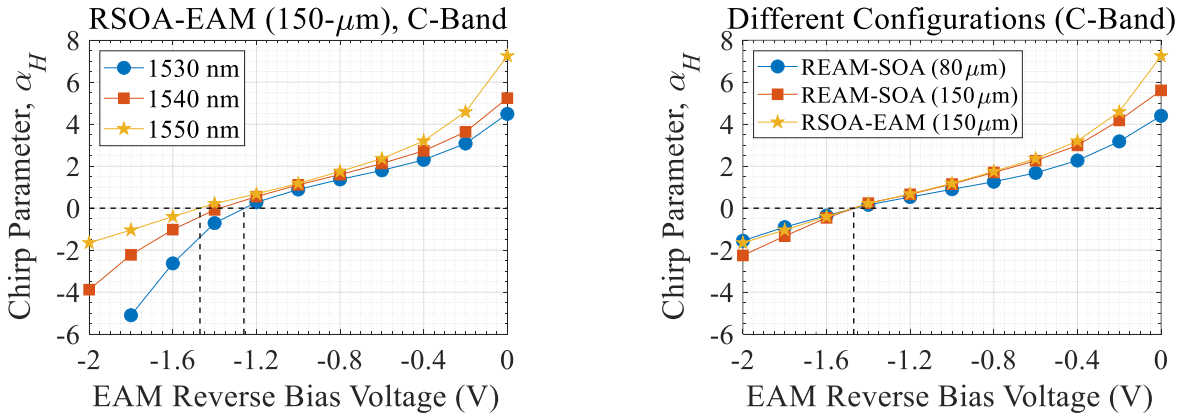
Fig. 3.45. Small-signal chirp parameters of (**a**) 80 µm (**b**) 150 µm long EAMs, both devices being in an REAM-SOA PIC configuration. $T = 25$°C. $I_{SOA} = 120$ mA for (a) and 90 mA for (b).

Over the 20-nm range considered here (between 1530 nm and 1550 nm), the chirp parameter crosses the zero line for reverse bias voltages in the range between -1.2 V and -1.5 V. For a given bias voltage, the EAMs exhibit a higher chirp parameter at longer wavelengths because the differential absorption coefficient term $\Delta\alpha$ in (3.44) is relatively lower. As a result, a higher reverse bias voltage is required to achieve a zero or even negative chirp parameter as the wavelength increases (i.e., for a larger detuning from an EAM's absorption edge).

In most cases, optimal transmission is achieved for $\alpha_H \leq 0$. This however increases the required reverse bias voltage, which is a compromise to be made for optimal transmissions at bit rates ≥25 Gb/s. Nevertheless, fixing the bias reverse voltage, for example at -1.2 V, the EAMs still exhibit low chirp values of $+0.02$, $+0.34$ and $+0.66$ respectively at 1530, 1540 and 1550 nms.

For the same EAM length, and under similar operating conditions, there is no significant difference in the chirp performances of REAM-SOA and RSOA-EAM configurations. Fig. 3.46 (a) shows small-signal chirp parameter of the 150-µm long EAM in an RSOA-EAM configuration at 25°C.

For comparison, the chirp performances of the three device configurations in the C-band, the 80 μm EAM in REAM-SOA and the 150-μm in both REAM-SOA and RSOA-EAM configurations, are shown in Fig. 3.46 (b) for an input wavelength of 1550 nm at 25℃. All of the EAMs have the same zero-crossing points occurring at a reverse bias voltage of around −1.5 V. The difference in their on-state chirp performances is attributed to different contributions from the SOA sections due to gain saturation when the input power is relatively higher for *on* state (i.e., $V_{\mathrm{EAM}} = 0$).



(**a**) (**b**)

Fig. 3.46. Small-signal chirp parameters of (**a**) 150 μm long EAM in an RSOA-EAM configuration (I_{SOA} = 90 mA), (**b**) comparison of chirp performances of the 80-μm long EAM in REAM-SOA and the 150-μm long EAM in both REAM-SOA and RSOA-EAM configurations (λ = 1550 nm). T = 25℃. I_{SOA} = 90−120 mA.

In addition to the EAM, the SOA also induces chirp as its carrier density varies between the *on* and *off* states, and the chirp parameter has a similar form to that of a DML, and it is given by [101]:

$$\alpha_{H,SOA} = \frac{dn/dN}{dk/dN} = -\frac{4\pi}{\lambda}\frac{dn/dN}{dg/dN}, \tag{3.52}$$

where, dn/dN and $d\kappa/dN$ are carrier-induced changes in real and imaginary parts of the complex refractive index, dg/dN is differential gain, and λ is wavelength of the input light.

Since the SOAs operate at a constant DC current, the change in the carrier density is not because of change in the pump current but rather is due to change in the photon density during the *on* and *off* states of the EAM. Furthermore, when the input power is high enough to push the SOA to its saturation regime (during the *on* state), the carrier density also changes because of a reduction of

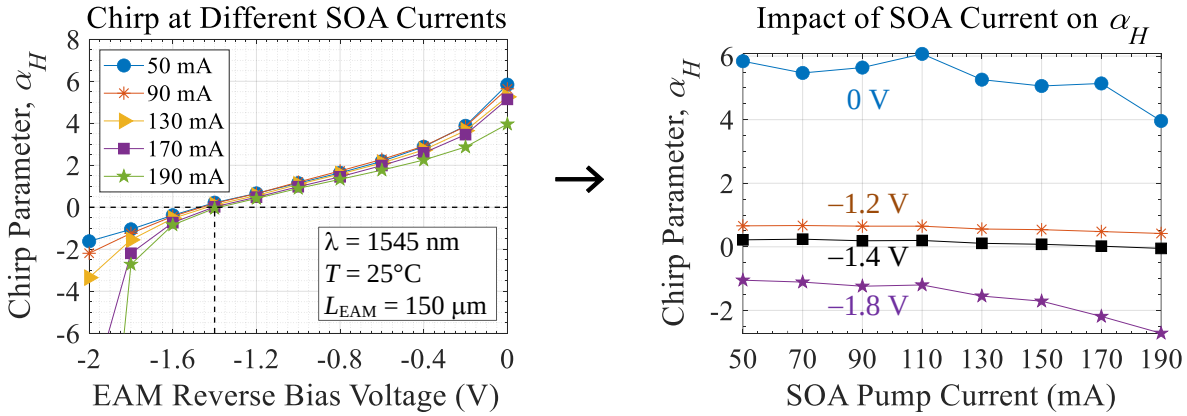
population inversion. The extra chirp added by the SOA to the transmitted signal $\alpha_{H,SOA\text{-}sig}$ is given by [101]:

$$\alpha_{H,SOA-sig} = \alpha_{H,SOA} \cdot \left(\frac{dN}{dP}\right) \cdot \left(\frac{dg}{dN}\right) \cdot P \cdot L_{SOA}, \tag{3.53}$$

where, dN/dP is change in the carrier density due to a change in the optical power P arriving at the SOA section, and L_{SOA} is the SOA cavity length.

The EAM-induced chirp can be slightly compensated by operating the SOA at a higher pump current [102]. However, extracting the chirp contribution of an SOA in a reflective configuration is complicated as the optical carrier passes through both the EAM and the SOA sections twice—before and after reflection. That means, the chirp parameters measured so far are a convolution of the two contributions since they are measured using integrated circuits.

To study the effect of SOA pump current on the overall chirp performance, we varied the SOA current between 50 mA and 190 mA. Fig. 3.47 (a) shows small-signal chirp performance of the 150-µm long EAM in an REAM-SOA configuration as a function of the reverse bias voltage at different SOA currents, for an input wavelength of 1545 nm and 25°C submount temperature.



(**a**) (**b**)

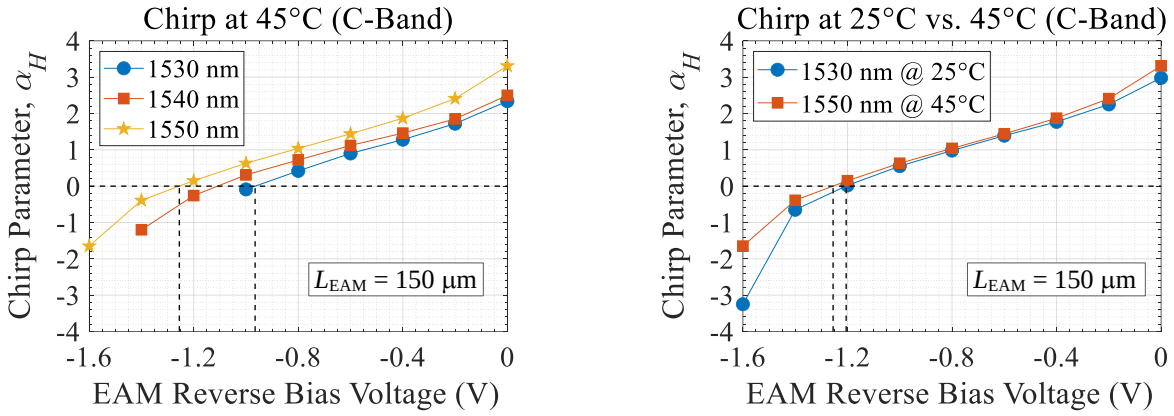
Fig. 3.47. Small-signal chirp parameter of a 150 µm long EAM (**a**) as a function reverse bias voltages at different SOA currents, (**b**) as a function of SOA pump current for different EAM reverse bias voltages. λ = 1545nm.

The impact of SOA current on the EAM's chirp parameter is visible at low and high reverse bias voltages (*on* and *off* states). For example, the chirp parameter at 0 V is reduced from about +5.8 to +4 by increasing the SOA pump current from 50 mA to 190 mA. The effect of SOA current

can be more clearly seen by plotting the chirp parameter as a function of SOA pump current as shown in Fig. 3.47 (b). In this case, the curves roll off faster at 0 V and −1.8 V as the SOA current increases, decreasing the chirp parameter by approximately 2 units.

Near the zero-crossing point (e.g., between −1.2 V and −1.4 V), the SOA current has a lesser impact on the EAM's chirp performance (about 0.25-unit reduction in α_H) than the two extrema. On the other hand, increasing the SOA current to such high values has its own side effects such as gain saturation, high ASE noise, high power consumption, and increased device temperature.

Finally, in order to analyze compatibility of our components for semi-cooled or uncooled operations, we performed chirp measurements at 45°C. Fig. 3.48 (a) shows small-signal chirp parameters of the 150-µm long EAM in an REAM-SOA configuration at 45°C for different input wavelengths. For a given wavelength, the zero-crossing point as well as the *on*-state chirp parameter are reduced because of thermal detuning of the EAM's absorption edge to longer wavelengths. For example, the zero-chirp bias point at 1530 nm is reduced (in absolute value) from −1.2 V at 25°C to −1 V at 45°C.



(**a**) (**b**)

Fig. 3.48. (**a**) Small-signal chirp parameter of the 150 µm long EAM as a function of revers bias voltage at 45°C for different input wavelengths, (**b**) comparison of chirp performances at 25°C and 45°C.

For comparison, Fig. 3.48 (b) shows the chirp performances of the 150-µm long EAM at 25°C/1530 nm and 45°C/1550 nm. The chirp performance at a longer wavelength of 1550 nm becomes comparable to the one at 1530 nm when the temperature increases from 25°C to 45°C.

This indicates that the chirp performance of the EAM for a given operating wavelength improves when it operates at a higher temperature than its 25℃.

Therefore, the C-band EAMs can operate at 45℃ without experiencing a significant performance degradation. They also operate at a relatively lower bias voltage while achieving zero or even negative chirp parameters. However, the SOA's performance degrades as the operating temperature increases mainly because of thermal emission of electrons. System-level transmission performances of the PICs up to 65℃ are presented in Chapter 4. Table 3.9 summarizes the zero-chirp bias conditions of the 150-μm long EAM at 25℃ and 45℃, which are representative operating conditions of the C-band EAMs.

Table 3.9. Small-signal chirp performances of a PIC based on a 150-μm long EAM.

Wavelength (nm)	**Required Bias Voltage (V) for Zero-Chirp**	
	@ 25℃	**@ 45℃**
1530	1.20	0.90
1540	1.35	1.10
1550	1.45	1.25

Large-Signal Frequency Chirp

The small-signal chirp parameter discussed above is an average value encountered between the *on* and *off* states. In order to analyze the instantaneous carrier frequency deviation (also known as *frequency chirp*) as a result of EAM-induced chirp, we measured the time-resolved chirp under large-signal operation for a single rectangular pulse of 2 ns period.

The instantaneous frequency chirp $\Delta\nu(t)$ is related to the instantaneous phase change $d\phi/dt$ given in (3.51) as follows:

$$\frac{d\phi}{dt} = 2\pi\Delta\nu(t). \tag{3.54}$$

This provides the relationship between instantaneous frequency chirp and the time-varying small-signal chirp parameter $\alpha_H(t)$ as [17][100]:

$$\Delta\nu(t) = \frac{\alpha_H(t)}{2\pi} \cdot \frac{1}{P(t)} \cdot \frac{dP(t)}{dt}, \tag{3.55}$$

where, $P(t)$ is the time-varying modulated output power.

Equation (3.55) shows that the frequency chirp depends on both the shape of the transmitted pulse and the EAM's extinction ratio where the latter determines the modulated output power $P(t)$. Using a similar MZ discrimination technique described in [100], the frequency chirp can be calculated using the IM and FM components as [97]:

$$\Delta\nu = \frac{FSR}{2\pi}\arcsin\left(\frac{V_{FM}}{V_{IM}}\right), \tag{3.56}$$

where, *FSR* is free spectral range of the MZ's longitudinal mode, V_{IM} and V_{FM} are the intensity and frequency modulation components given in (3.49).

Fig. 3.49 shows time-resolved frequency chirp of the 80-µm and 150-µm long C-band EAMs under large-signal operating conditions at 1545 nm and 25℃. The first column is for the longer EAM whereas the second one is for the shorter one. Similarly, the results in the first row are obtained at -0.8 V/1.6 V_{PP} whereas the ones in the second row at -1.3 V/2.6 V_{PP}. Both PICs are in an REAM-SOA configuration. The SOA pump current is 90 mA for the PIC integrating a 150-µm long EAM ($L_{SOA} = 450$ µm) and 120 mA for the one integrating an 80-µm long EAM ($L_{SOA} = 500$ µm).

The shapes of the intensity modulated rectangular pulses in each case are also shown in the figures. At -0.8 V/1.6V_{PP}, dynamic extinction ratio of the 80-µm long EAM is ~4 dB and that of the 150-µm long EAM is ~6 dB as shown in Fig. 3.49 (a) and (b), respectively. Under this bias condition, the instantaneous frequency chirp moves from zero to positive and then returns back to zero at the rising edge of the transmitted pulse, and it changes from zero to negative and then back to zero at the falling edge, which is the characteristic of a positively chirped pulse.

Since the transmitted pulse has a finite transition time (rising and falling) that originates from finite photon lifetime, the transient chirp also has a finite width, with a peak and intermediate values. When the bias voltage is increased to -1.3 V/2.6 V_{PP}, the intermediate states become complex as shown in Fig. 3.49 (c) and (d). For example, at the rising edge, the frequency chirp first moves from zero to negative, then from negative to positive before it returns back to zero. Under this bias condition, the frequency component of the rectangular pulse inside the 150-µm long EAM is shifted by a maximum of $+3.2/-3.7$ GHz at the rising/falling edge and the one inside the 80-µm long EAM by $+1.5/-2.2$ GHz.

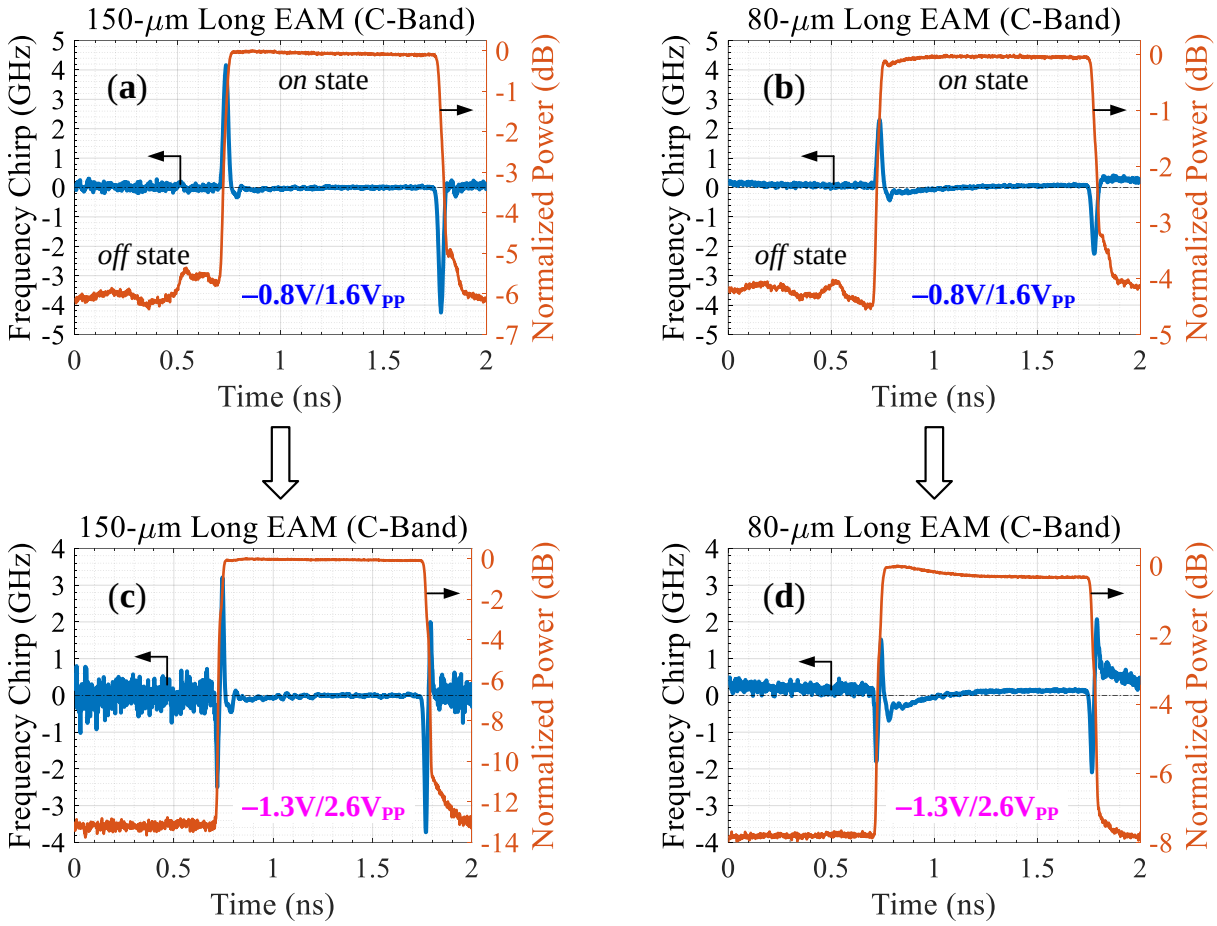
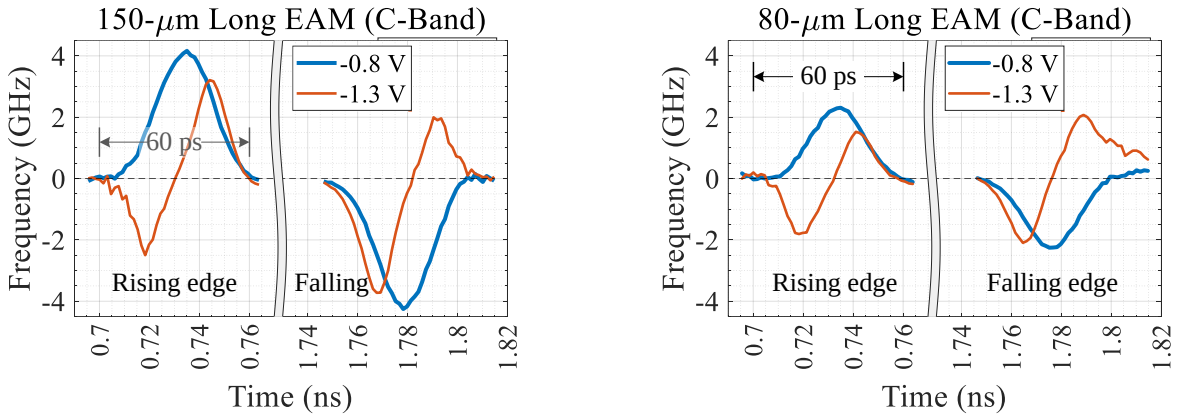


Fig. 3.49. Time-resolved frequency chirp induced by (**a**), (**c**) 150-µm EAM (I_{SOA} = 90 mA), (**b**), (**d**) 80-µm EAM (I_{SOA} = 120 mA) under large-signal operating condition. The top figures are obtained at −0.8 V/1.6 VPP whereas the bottom ones are at −1.3 V/2.6 V_{PP}. λ = 1545 nm, T = 25℃. Both PICs are in an REAM-SOA configuration.

The difference in the peak frequency chirp values between the two EAMs is due to the fact that the pulse spends more time inside the longer EAM than the shorter one while experiencing EAM-induced chirp. This can be better understood by analyzing the instantaneous phase shift $d\phi/dt$ given in (3.51), which is also related to the instantaneous frequency chirp $\Delta\nu(t)$ given in (3.54). The total phase shift induced by an EAM at the rising and falling edges of the transmitted pulse can be obtained by integrating the instantaneous phase shift of (3.54) over the time it takes to rise and fall. The phase shift is commonly expressed as a fraction of π-radians (i.e., π-rad = ϕ/π).

Fig. 3.50 shows enhanced view of the frequency chirp induced by the two EAMs (from Fig. 3.49). The transient chirp roughly takes 60 ps to rise or fall in each case, i.e., 0.7−0.76 ns at the rising edge and 1.75−1.81 ns at the falling edge of the rectangular pulse.



(**a**) (**b**)

Fig. 3.50. Enhanced view of the large-signal frequency chirp of (**a**) the 150-µm long EAM and (**b**) the 80-µm long EAM, both in an REAM-SOA PIC configuration. $\lambda = 1545$ nm, $T = 25$°C.

In general, the EAMs induce low chirp with respect to π-radians, and as expected, the phase shift induced by the shorter EAM is lower than that of the longer EAM. In each case, the induced phase shift decreases with increasing reverse bias voltage and the corresponding voltage swing. For example, the 150-µm long EAM induces a phase shift of $+0.22/-0.22$ π-rad (rising/falling edges) at -0.8 V/1.6 V_{PP} and $+0.03/-0.07$ π-rad at -1.3 V/2.6 V_{PP}. The respective values for the 80-µm long EAM at the two bias conditions are $+0.12/-0.11$ and $+0.01/+0.03$, respectively. Table 3.10 summarizes calculated phase shift at the rising and the falling edges of the transmitted pulse obtained by integrating the TRC in Fig. 3.50 (a) and (b). Since the EAMs induce a very low chirp, the transmission distance in the C-band will be primarily limited by chromatic dispersion as it always exists with silica fibers.

Table 3.10. Transient phase shift (large signal) caused by 80-µm and 150-µm long C-band REAMs.

EAM Length (µm)	**Bias/Voltage Swing**	**DER (dB)**	**Transient Phase Shift (π-rad)**	
			Rising Edge	**Falling Edge**
150	-0.8 V/1.6 V_{PP}	6	0.22	-0.22
	-1.3 V/2.6 V_{PP}	13	0.03	-0.07
80	-0.8 V/1.6 V_{PP}	4	0.12	-0.11
	-1.3 V/2.6 V_{PP}	7.8	0.01	0.03

Therefore, modulator-induced chirp (or phase shift) can be reduced by using a shorter EAM, which also provides larger modulation bandwidth by lowering the EAM capacitance. The only drawback of a short EAM is the relatively lower extinction ratio it provides, which is the case especially at

longer wavelengths. But the extinction ratio can be compensated by using an optimized vertical design with a larger number of QW layers. In a reflective configuration, the ER is reasonably high because of the double-pass configuration, which is one of the advantages of using reflective EAMs. Therefore, a PIC based on an 80-μm long EAM provides a good compromise between E/O bandwidth, modulation strength (extinction ratio), and modulator-induced chirp.

3.7. Summary and Discussion

In this chapter, the performances of basic building blocks are presented while indicating different design tradeoffs that can be exploited in the future to improve device performances. In the first section, the spot-size converter is analyzed using both simulation and experimental results. It is shown that the FWHM divergence angle of an SSC can be significantly reduced by using narrow tapers. For example, the divergence angle of a 1.5-μm wide waveguide can be halved by using a 0.5-μm taper. Based on that, the next generation of devices were realized using 0.5 μm and 0.3 μm tapers whose measured FWHM divergence angles are found to be about 14°×12.5° and 12°×11°, respectively (horizontal × vertical directions). This shows that a more symmetric mode profile can be obtained by using narrower tapers and thus improve the input/output coupling efficiency.

In the second section, amplifier gain and noise figure performances are analyzed using two SOAs, one from the C-band and another from the O-band. The performance of the C-band SOA is degraded by both current leakage and high gain ripple originating from facet reflectivities, indicating that further optimization of both the SI-BH waveguide and the AR coating is necessary. The intrinsic gain of the 450-μm long C-band RSOA is about ~15.5 dB at 1530 nm and the fiber-to-fiber gain is ~3.5 dB at the same wavelength, for SOA pump current of 120 mA. The difference between the intrinsic RSOA gain and the fiber-to-fiber gain is due to input/output coupling losses, EAM absorption loss, and SSC absorption and tapering losses.

The 300-μm long O-band SOA, on the other hand, exhibits a relatively high intrinsic gain of ~17 dB at 1310 nm with a fiber-to-fiber gain of >5 dB over a 25-nm spectral range, with a maximum fiber-to-fiber gain of ~8.5 dB near 1310 nm at 80 mA SOA pump current. Since the two SOAs have similar vertical structures, they exhibit the same saturation output power of ~10 dB. Typical saturation output powers of practical SOAs are in the range between 5 dBm and 20 dBm [64], and the typical value for MQW SOAs is in the range from 0 dBm to 13 dBm [39]. The amplifier gain

can be further improved by using a longer SOA with optimized optical confinement factor for applications that have stringent power budget requirements such as passive optical networks.

Concerning noise figure, the C-band SOA exhibits an unsaturated (small-signal) NF of ~6 dB at 1530 nm, and ~9.5 dB NF at the saturation output power. However, the small-signal NF fluctuates between 6 dB and 12 dB at longer wavelengths, which is due to high gain ripple. The O-band SOA, on the other hand, exhibits a very low small-signal NF of ~4 dB at 1310 nm, and it remains between 4 dB and 6 dB over a 50-nm spectral range. At the 10-dBm saturation output power, the NF is ~7.5 dB at 1310 nm, which is comparable to the performances of state-of-the-art SOAs.

On the modulator side, the key performance requirements are high extinction ratio at low operating voltage, large bandwidth, and low chirp. For a given modulator length, a reflective EAM provides a higher extinction ratio than its single-pass counterpart because of the dual absorption that occurs before and after reflection of the input light. The ER of an EAM can be increased by increasing its length as well as the optical confinement factor.

However, there is a tradeoff between extinction ratio and modulation bandwidth, both of which depend on the EAM length. Increasing the optical confinement factor also leads to strong EAM absorption which in turn increases insertion loss. Therefore, the number of QW layers in a MQW structure must be carefully chosen. Furthermore, improved saturation and thermal performances of EAMs can be achieved by using aluminum-based material systems such as GaInAlAs because of its high conduction band offset ($\sim 0.7\Delta E_g$), which is favorable for SOAs (the low VBO is favorable for EAMs). For GaInAsP MQWs, the performances of the EAM and the SOA can be tailored by using strained QW layers (e.g., compressive strained QWs for high-speed applications and tensile strained QWs for polarization-independent performances).

Since a reflective EAM allows achieving a relatively high ER, large electrical bandwidth can be achieved by using a shorter EAM as it results in a lower modulator capacitance. Furthermore, the frequency response can also be improved by increasing the thickness of the MQW active region, which also increases the optical confinement factor. Therefore, there is a tradeoff between E/O bandwidth, modulation strength and insertion loss of an EAM.

At system level, the chirp performance of an EAM determines the maximum distance that can be achieved without applying dispersion compensation techniques. Low chirp is the primary

advantage of EAMs over directly modulated lasers, where the latter suffer from adiabatic chirp (strong) in addition to transient chirp. The effect of chirp becomes detrimental with increasing transmission bit rate as narrower pulses are easily affected by inter-symbol interference. EAM-induced chirp, depending on its sign, plays the role of enhancing or degrading dispersion-limited transmission, and its effect can be seen using the frequency response of a fiber, which at the receiver side is given by [103]:

$$I_{det} = I_{opt} m \sqrt{1 + {\alpha_H}^2} \left| cos\left(\frac{\pi \lambda^2 D L_{fiber} {f_m}^2}{c} + \arctan\left(\alpha_H\right) \right) \right|, \tag{3.57}$$

where, I_{det} is the detected photocurrent, I_{opt} is intensity of the optical signal, m is modulation index of the transmitter, α_{H} is chirp parameter, λ is wavelength of the optical carrier, D is dispersion coefficient of optical fiber, L_{fiber} is the fiber length, f_{m} is the modulation frequency, and c is speed of light in vacuum.

The fiber response can be enhanced by decreasing the argument of the cosine term in (3.57), which can be achieved by transmitting a negatively chirped pulse ($\alpha_H < 0$). The chirp parameter of an EAM can be pushed further into the negative regime by increasing the reverse bias voltage. However, negatively chirped pulses experience compression only up to a certain extent, i.e., until the pulse width reaches the Fourier limit. For that reason, optimal transmission performance is achieved for chirp parameters in the range between -1 and 0 [104].

A common figure of merit for characterizing dispersion-limited transmission systems is the bandwidth-length (BL) product, which provides information about how far error-free transmission can be achieved at a given bit rate. The highest BL product is achieved using higher-order modulation formats based on coherent detection in long-haul transmission systems.

As an example, the B^2L product of a standard SMF at 1550 nm using NRZ-OOK coding is shown in Fig. 3.51 as a function of chirp parameter on the left y axis and estimated transmission distance at 25 Gb/s on the right y axis [104]. In the absence of chirp ($\alpha_H = 0$), the transmission distance is primarily limited by fiber dispersion. The transmission performance is enhanced by negative, and optimal transmission is achieved for α_H values in the range between 0 and -1 (the region between the dashed lines). For chirp parameters outside the optimal range, the transmission is limited by vertical eye closure due to noise and horizontal eye closure due to fiber dispersion. For example,

the dispersion-limited transmission distance at 25 Gb/s NRZ is in the order of 10 km. For positive chirp, on the other hand, the transmission performance is degraded at a faster rate. Therefore, for high-speed transmissions beyond 25 Gb/s NRZ, one has to either use dispersion compensation techniques or move the transmission window to near the zero-dispersion regime in the O-band so that long distance transmission can be achieved.

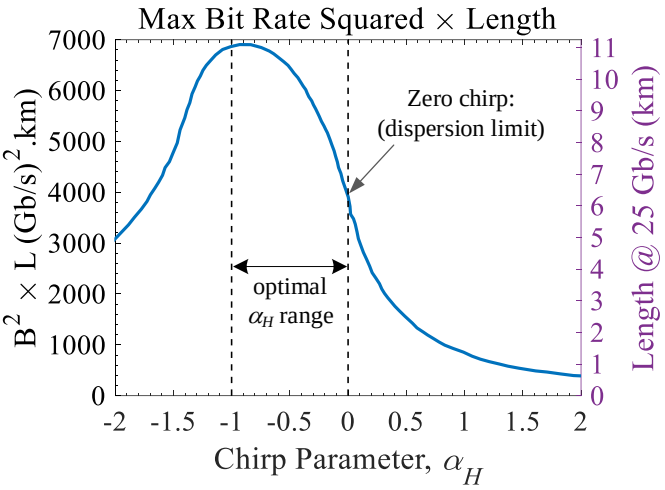


Fig. 3.51. Bandwidth squared-distance product of a standard SMF at 1550 nm (17 ps/nm/km dispersion) using NRZ modulation format and estimated fiber length for 25 Gb/s transmission (after [104]).

Using our components, we performed up to 50 Gb/s digital and 10 Gb/s analog transmissions in the O-band, and 25 Gb/s digital transmission in the C-band. The system-level demonstrations in both frequency bands are discussed in Chapter 4.

Chapter 4

4. System-Level Demonstrations

This chapter presents system-level demonstrations focusing on eye diagrams and transmission bit error rates (BERs). The devices are based on electroabsorption modulators (EAMs) monolithically integrated with semiconductor optical amplifiers (SOAs). Depending on the positions of the EAM and the SOA along the optical path, two photonic integrated circuit (PIC) configurations are possible: reflective EAM-SOA (REAM-SOA) or its opposite RSOA-EAM. Devices operating either in the C-band (1.55 μm window) or the O-band (1.3 μm window) are characterized in both PIC configurations. Our components are realized using GaInAsP multiple quantum wells (MQWs) grown on InP substrate. The C-band EAMs are based on a 189-nm thick MQW active region whereas the ones operating in the O-band are based on a 209-nm thick MQW structure.

The first section presents the performances of the C-band devices operating at 25 Gb/s using non-return-to-zero (NRZ) modulation format. The devices are tested over a wide range of spectrum at different operating temperatures (up to 65°C), where the former is to demonstrate wavelength-independent (colorless) operational capabilities of our components devices whereas the latter is to analyze compatibility of the devices to semi-cooled or uncooled environments.

The second section presents transmission performances of the O-band devices. First, preliminary results at 25 Gb/s NRZ are presented, based on which colorless operations of the devices are demonstrated. Then, high-speed transmissions at 50 Gb/s using NRZ as well as PAM-4 (25 GBaud symbol rate for PAM-4) modulation formats are presented. Since the electrooptic (E/O) bandwidth of the RSOA-EAM configuration is limited by the round-trip delay inside the SOA section, we focus on the REAM-SOA configuration for our high-speed transmission experiments.

The third section presents application of the devices in a 5G fronthaul system using a multi-channel analog radio-over-fiber (ARoF) transmission with fiber-wireless (FiWi) transmission capability. The ARoF transmission experiments are performed in collaboration with Aristotle University of Thessaloniki (AUTH) in Greece. The system represents a typical 5G fronthaul network in the

upstream direction, where the user information is first transmitted over the wireless channel and then over a fiber optic cable.

4.1. Digital Transmissions in the C-Band at 25 Gb/s

In the C-band, devices based on an 80-µm long EAM in an REAM-SOA configuration and a 150-µm long EAM in both REAM-SOA and RSOA-EAM configurations are characterized. The shorter EAM exhibits a bandwidth of >26.5 GHz (setup limited) whereas the longer EAM exhibits a 3-dB cutoff bandwidth of ~23 GHz in REAM-SOA and ~14 GHz in RSOA-EAM configurations (e.g., see Chapter 3, Section 3.6). First, the 25 Gb/s NRZ performance of the longer EAM is presented for temperatures between 25℃ and 65℃. Then, transmission improvements that can be achieved by using a shorter EAM are demonstrated using the BER performances of the 80-µm long EAM at 25 Gb/s NRZ. Published results based on the C-band devices can be found in [32][33].

4.1.1. Experimental Setup

Fig. 4.1. shows a schematic diagram of the experimental setup used for BER measurement at 25 Gb/s NRZ. A continuous wave (CW) monochromatic light is generated by a tunable laser (TL) to be injected into the PICs. Our components are sensitive to polarization state of the input light. For that reason, we used a polarization controller (PC) in order to inject transverse electric (TE) polarized light into the PICs.

For bidirectional transmission over a single fiber, we used an external optical circulator where the CW light enters at port-1 of the circulator and leaves at port-2 to be injected into the device under test (DUT), which is an REAM-SOA for the digital transmissions. Our components integrate a spot-size converter (SSC) based on a linear taper running from 1.5 µm to 0.7 µm with a 7°-tilted output waveguide. Different optimizations performed on the SSCs and their performances are discussed in Chapter 3, Section 3.1. We used a lensed fiber of estimated mode diameter ~2 µm to couple light to and from the PIC. The 25 Gb/s NRZ signal is generated by a signal quality analyzer (Anritsu MP1800A) with a bit pattern of $2^{31}-1$ pseudorandom binary sequence (PRBS31). A representative eye diagram of the electrical signal (2 V peak-to-peak amplitude) captured at the output of the PRBS generator is also shown in Fig. 4.1.

The modulating electrical signal is combined with a DC offsetting voltage using a bias-T and applied to the EAM section. The SOA is forward biased by applying a DC current in the range between 90 mA to 120 mA in order to maintain a constant current density for different SOA cavity lengths. The submount temperature is controlled by using a Peltier thermoelectric cooler (TEC). Inside the PIC, the optical carrier is modulated by the EAM and amplified by the SOA, in both the forward (before reflection) and the reverse (after reflection) paths.

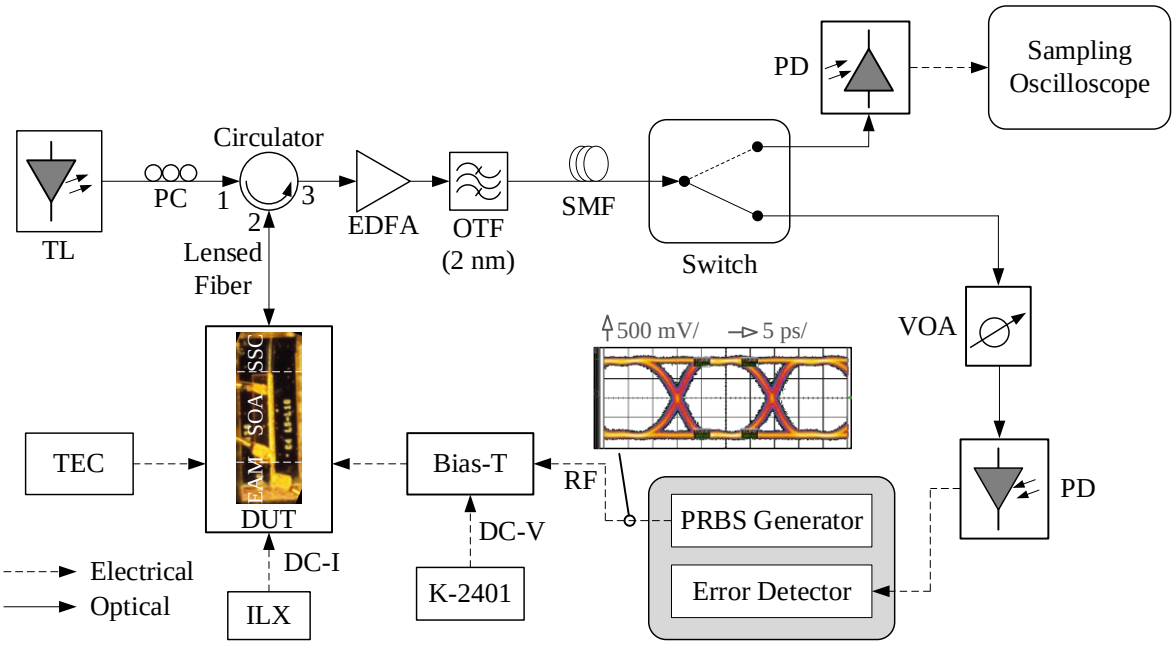


Fig. 4.1. Schematic diagram of a standard experimental setup for 25 Gb/s NRZ transmission.

The modulated signal is coupled to the lensed fiber and enters at port-2 of the circulator and leaves at port-3, which is then amplified by an erbium-doped fiber amplifier (EDFA) required to compensate external losses (e.g., circulator, filter, and switch losses). Following the EDFA, a tunable optical filter (OTF) of 2 nm bandwidth is used to remove part of the amplified spontaneous emission (ASE) noise generated by the SOA as well as by the EDFA. The filtered optical signal is then transmitted over a standard SMF. In a back-to-back (BtB) configuration, a short fiber patch cable is used between the transmitter and the receiver. For longer transmission distances, the optical signal is transmitted over a fiber loop spanning a few tens of kilometers. An optical switch is used to control the optical path to a sampling oscilloscope (for capturing eye diagrams), or to a BER tester integrated with the signal quality analyzer (for counting transmission error rates). In

the latter case, a variable optical attenuator (VOA) is used to vary the received power and thus analyze the transmission penalty, which is inserted before the high-speed photodiode (PD) that converts the optical signal to electrical signal for further processing (DSC-R409: 25 Gb/s NRZ sensitivity is around −13.5 dBm at 10^{-12} BER and −17.5 dBm at 10^{-3} BER).

Transmission Performance of 150-µm Long Modulator

In order to demonstrate colorless operation of our components, the devices are tested over a wide range of spectrum (e.g., between 1530 nm and 1545 nm, $\Delta\lambda = 15$ nm). Fig. 4.2 shows the 25 Gb/s NRZ eye diagrams obtained from the 150-µm long C-band EAM in an REAM-SOA configuration at 25°C. We obtained clearly open eye diagrams in both BtB and 10 km configurations. The first row is for 1530 nm and the second one is for 1545 nm operating wavelengths.

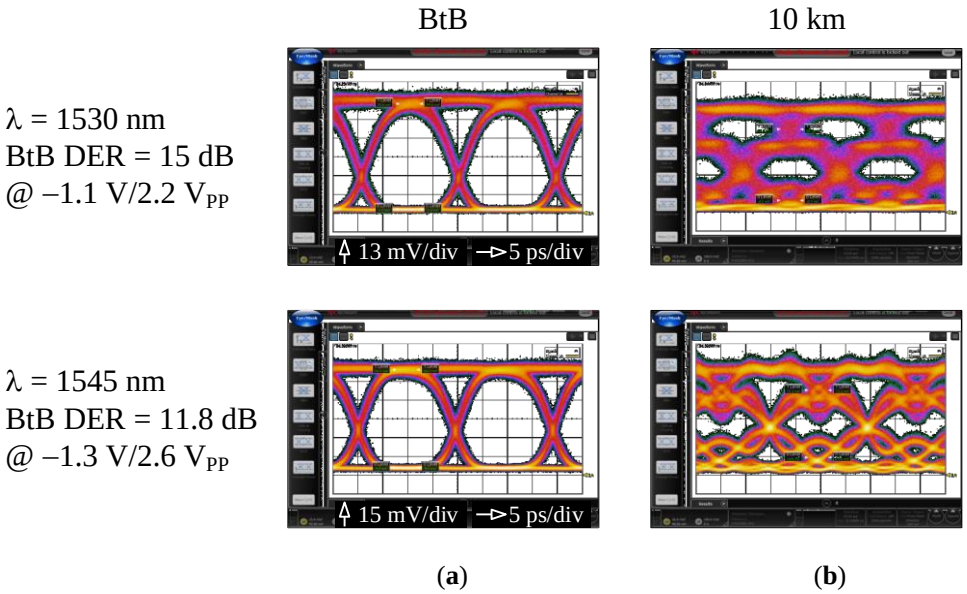


Fig. 4.2. Eye diagrams of a 150-µm long EAM in an REAM-SOA PIC configuration operating at 25 Gb/s NRZ in (**a**) back-to-back, (**b**) 10 km configurations. $T = 25$°C, $I_{SOA} = 90$ mA.

In BtB, the EAM exhibits a very high dynamic extinction ratio (DER) of ~15 dB at 1530 nm for a reverse bias voltage of −1.1 V and 2.2 V voltage swing. At a longer wavelength of 1545 nm, the EAM still exhibits high DER of ~12 dB at −1.3 V/2.6 V_{PP} , which is the advantage gained by using reflective EAMs compared to single-pass EAMs. Since the EAM's operation is based on quantum confined Stark effect (QCSE), a relatively higher reverse bias voltage is required at longer wavelengths in order to shift the absorption spectrum and achieve stronger absorption. For that

reason, the optimal bias condition for the 150-µm EAM at 1545 nm is −1.3 V for a peak-to-peak voltage of 2.6 V, which is higher (in absolute value) than the one at 1530 nm (−1.1 V/2.2 V_{PP}).

Fig. 4.3 shows the 25 Gb/s NRZ BER performances of the 150-µm long EAM in an REAM-SOA configuration at 1530 nm and 1545 nm for the eye diagrams shown above. The SOA pump current is 90 mA (L_{SOA} = 450 µm). Under the bias conditions shown above for the two wavelengths, the EAM's chirp parameter is close to zero as discussed in Chapter 3 (e.g., see Sect. 3.6.2). That means, the transmission is primarily limited by chromatic dispersion. As a result, the maximum transmission distance at 25 Gb/s NRZ is limited to 12 km with a dispersion penalty of ~4.5 dB at 10^{-3} BER, which is the typical input BER required for low-cost forward error correction (FEC) algorithms in the access network [13][94]. For 10 km transmission (without any error floor), which is the typical fiber length for time-sensitive applications (e.g., 5G fronthaul networks) [94], the dispersion penalty is ~3 dB at the same BER of 10^{-3}.

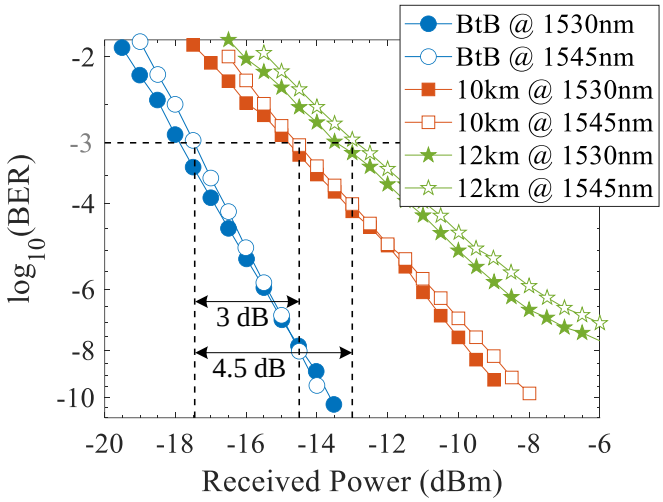


Fig. 4.3. BER performance of a 150-µm long EAM in an REAM-SOA configuration operating at 25 Gb/s NRZ. T = 25°C, I_{SOA} = 90 mA, EAM bias: −1.1 V/2.2 V_{PP} at 1530 nm and −1.3 V/2.6 V_{PP} at 1545 nm.

An important feature of the BER performance of EAM shown in Fig. 4.3 is that the penalty is independent of the operating wavelength over the 15-nm spectral range considered here—overlapping BER curves at 1530 nm and 1545 nm in both BtB and 10 km configurations. The BER curves after 12 km are slightly separated, which is due to a combination of a lower DER at 1545 nm (in BtB, 15 dB vs. 12 dB) and a relatively higher dispersion at longer wavelengths. Even in that case, the wavelength-dependent penalty is around 0.5 dB. This proves that our components

can be used as wavelength-independent (colorless) transmitters over the 15-nm spectral range considered here without experiencing a significant performance degradation.

In order to analyze the compatibility of our components for semi-cooled or uncooled environments, we characterized the PIC based on the 150-µm long EAM in an REAM-SOA configuration at different operating temperatures. Fig. 4.4 shows BER performances of the PIC between 25°C and 65°C for an input wavelength of 1545 nm while operating at 25 Gb/s NRZ. The BtB eye diagrams at 45°C and 65°C are also shown in the figure (results obtained without an optical filter at the receiver side). The bias conditions are adjusted for optimal transmission depending on the operating temperature as follows: −1.3 V/2.6 V_{PP} at 25°C, −1.1 V/2.2 V_{PP} at 45°C, and −0.8 V/1.6 V_{PP} at 65°C. This is due to the fact that the absorption edge of the EAM is shifted to longer wavelengths as temperature increases (~0.7 nm/°C), requiring a relatively lower reverse bias and swing voltage for a given wavelength.

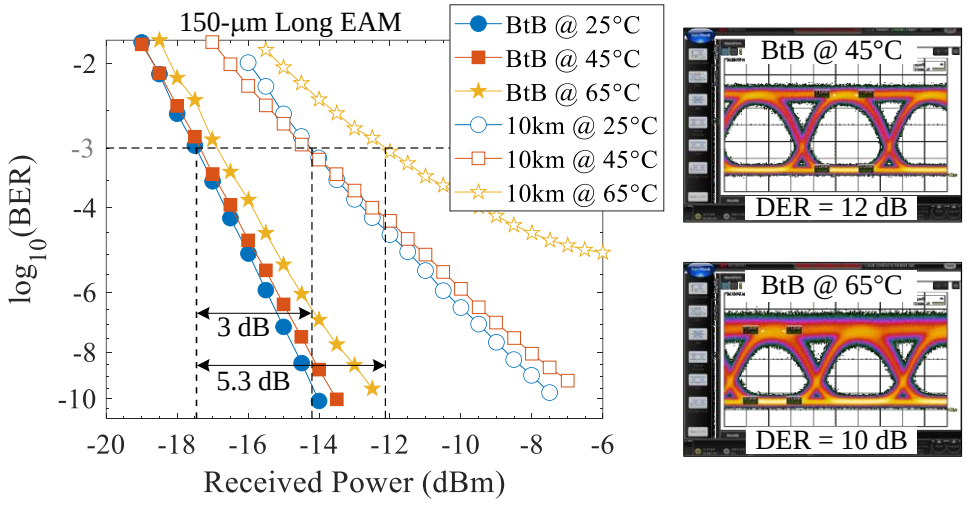


Fig. 4.4. BER performances of a 150-µm EAM in an REAM-SOA between 25°C and 65°C submount temperatures, at 25 Gb/s NRZ. λ = 1545 nm, I_{SOA} = 90 mA. EAM bias conditions: −1.3 V/2.6 V_{PP} at 25°C, −1.1 V/2.2 V_{PP} at 45°C, −0.8 V/1.6 V_{PP} at 65°C. [Inset: unfiltered 25 Gb/s NRZ BtB eye diagrams at 45°C (top) and 65°C (bottom).]

The BtB DER of the EAM at 45°C is ~12 dB, which is comparable to (or even slightly better than) the DER performance at 25°C (12 dB vs. 11.8 dB). On the other hand, the BtB DER at 65°C is ~10 dB, which is ~2 dB lower than the 25°C performance. The lower DER at a higher temperature is because of exciton broadening as well as reduced signal quality. As the operating temperature increases, the signal quality decreases because of a degradation of the SOA's gain as a result of

increased thermionic emission of injected carriers, which results in a lower signal-to-noise ratio (SNR). For example, for the same input power and SOA pump current, the average modulated output power of the PIC at 25℃, 45℃ and 65℃ is −6.2 dBm, −7 dBm and −12 dBm, respectively. Because of a lower SNR, the *one*-level (*on* state) at 65℃ is thicker than the one at 45℃, which results in a lower DER as the DER is estimated by taking the average voltage levels of the *on* and *off* states, and ultimately leads to vertical eye closure.

The BER results shown in Fig. 4.4 reveal that the device operates up to 45℃ without experiencing a significant performance degradation (overlapping BER curves at 25℃ and 45℃ in BtB and after 10 km), without any sign of developing error floor. The dispersion penalty for 10 km transmission remains the same as that of 25℃ (3 dB penalty at 10^{-3} BER). On the other hand, the effect of a lower DER at 65℃ is visible even in the BtB BER, which results in a slightly shifted BER curve towards the right-hand side of the figure (∼0.5 dB difference). After 10 km transmission, the dispersion penalty at 65℃ is ∼5 dB (with respect to its BER in BtB), which is a 2-dB higher penalty than the one at 45℃. As a result, the transmission requires ∼2 dB more input power at the receiver side when operating the PIC at 65℃ in order to achieve the same BER performance as 25℃. Moreover, an error floor begins to develop after 10 km SMF transmission at 65℃.

Transmission Performance of 80-µm Long Modulator

One way of reducing the transmission penalty (or increasing the transmission distance) is by using a shorter EAM, which, apart from providing larger modulation bandwidth, induces a lower frequency chirp (or phase shift) at the rising and falling edges of the transmitted pulses as discussed in Chapter 3 (e.g., see Sect. 3.6.2). Fig. 4.5 shows BER performance of the 80-µm long EAM in an REAM-SOA configuration at 1530 nm (−1.1 V/2.2 V_{PP}) and 25℃ submount temperature. The 25G NRZ eye diagrams are also shown on the right-hand side of the figure (BtB and 10 km). The BtB DER of the EAM at 1530 nm is ∼8.1 dB, which is lower than that of the 150-µm EAM (8.1 dB vs. 15 dB), but it still is a high value for an EAM of such a short length, which is one of the advantages gained by using reflective EAMs in comparison to single-pass EAMs.

The dispersion penalty for 16 km transmission is ∼2.5 dB at a BER of 10^{-3}, which is lower than the penalty observed with the 150-µm long EAM (cf. Fig. 4.3). For the same 10 km transmission, the penalty of the shorter EAM is only ∼1 dB, which is ∼2 dB lower than that of the longer EAM.

Even after 16 km, the transmission penalty of the 80-µm long EAM is less than the 10-km penalty of the 150-µm long EAM (2.5 dB after 16 km vs. 3 dB after 10 km). That means, the shorter EAM increases the transmission distance while it still reduces the power penalty.

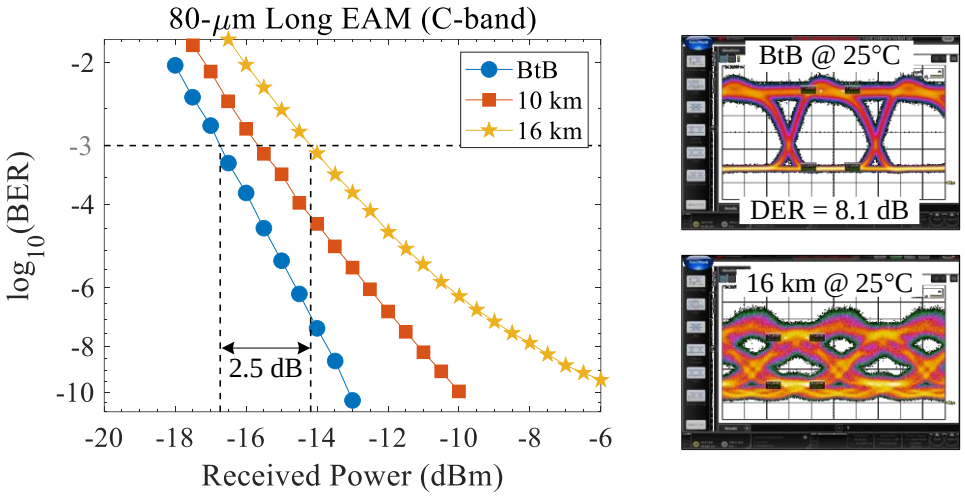


Fig. 4.5. BER performances of an 80-µm long EAM in an REAM-SOA configuration at 1530 nm (−1.1 V/2.2 V_{PP}). T = 25°C. I_{SOA} = 120 mA. [Inset: 25 Gb/s NRZ eye diagrams in BtB (top) and after 16 km (bottom).]

In order to analyze thermal stability of the REAM-SOA PIC based on the 80-µm long EAM, we performed BER measurements at 45°C, transmitting a 25-Gb/s NRZ signal at 1545 nm (−1.3 V/2.6 V_{PP}). BER performances and the corresponding eye diagrams are shown in Fig. 4.6. We obtained clearly open eye diagrams after 10 km as shown on the right-hand side of the figure.

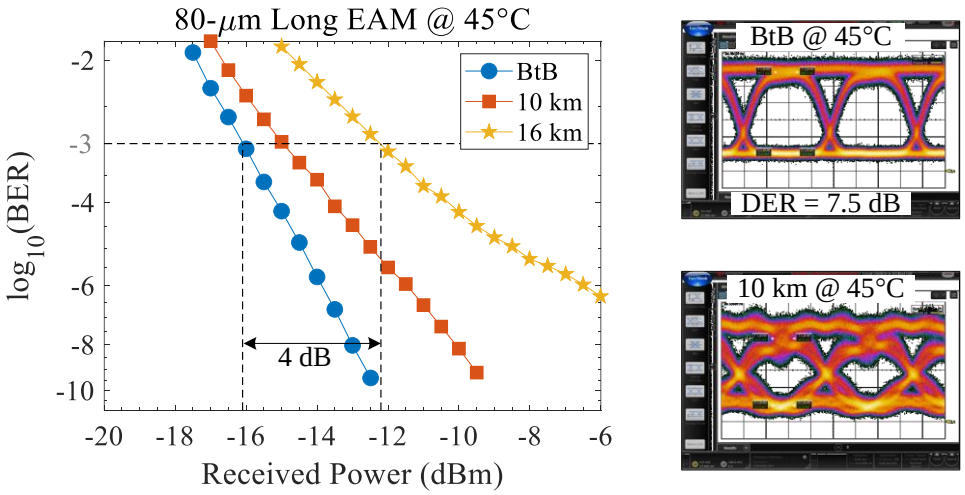


Fig. 4.6. BER performance of an 80-µm long EAM in an REAM-SOA configuration at 45°C and 1545 nm (−1.3 V/2.6 V_{PP}). I_{SOA} = 120 mA. [Inset: unfiltered 25G NRZ eye diagrams in BtB (top) and after 10 km (bottom).]

The DER of the EAM at 45℃/1545 nm is ~7.5 dB, which is slightly lower than the DER at 25℃/1530 nm (~0.6 dB difference). The difference is attributed to the fact that the 45℃ eye diagrams are obtained without filtering the optical signal at the receiver side.

The SOA's gain degrades as temperature increases, leading to a lower SNR. Compared to the EAM's performance at 25℃, the BER is not affected by temperature for transmission distances up to 10 km, and the penalty remains the same (~1 dB penalty at 10^{-3} BER). However, the dispersion penalty at 45℃ increases by ~3 dB for 16 km transmission (~4 dB penalty in total), which is ~1.5 dB higher than the case of 25℃ for the same fiber length. The higher penalty at 45℃ is attributed to a combination of reduced DER (causes vertical eye closure) and chromatic dispersion, which becomes detrimental as the signal propagates over a longer distance (causes horizontal eye closure).

Comparison of 80 µm and 150 µm Long Modulators

For comparison, Fig. 4.7 shows BER performances of the two C-band EAMs discussed above (80-µm and 150-µm) in BtB and after 10 km transmission over a standard SMF. The results are obtained at 45℃ for an input wavelength of 1545 nm. Both EAMs are in an REAM-SOA configuration, and they are modulated at 25 Gb/s NRZ.

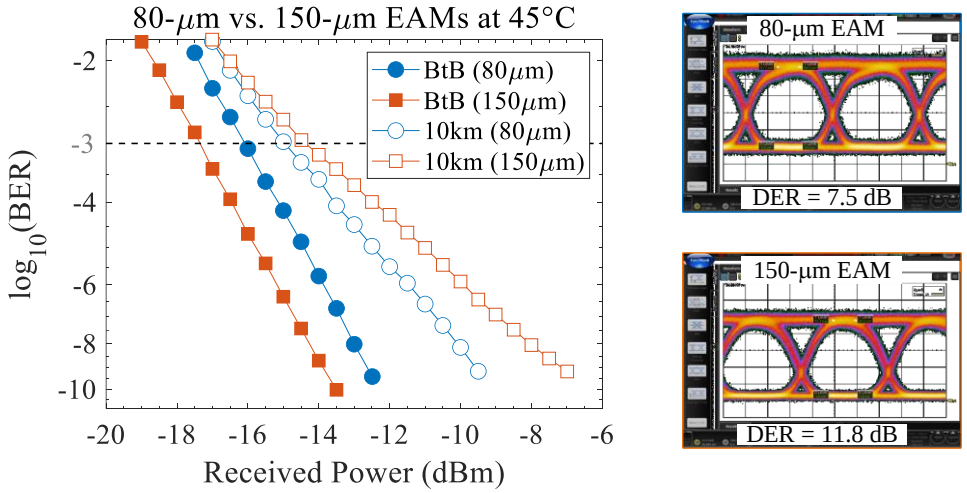


Fig. 4.7. BER performances of 80-µm and 150-µm long EAMs in an REAM-SOA configuration at 25 Gb/s NRZ and 45℃ for an input wavelength of 1545 nm (−1.3 V/2.6 V_{PP}). I_{SOA} = 90 mA for the PIC based on a longer EAM and 120 mA for the one based on a shorter EAM. [Inset: 25G NRZ BtB eye diagrams obtained from the 80-µm long EAM (top) and the 150-µm long EAM (bottom).]

Because of a lower DER obtained from the shorter EAM than the longer EAM (7.5 dB vs. 12 dB at 1545 nm), the BtB BER curve of the former is shifted to right-hand side of the figure. However, after 10 km transmission over a standard SMF, the dispersion penalty is higher for the longer EAM than the shorter one (3 dB vs. 1 dB). As a result, the 80-µm EAM can transmit a longer distance while achieving the same BER performance as that the 150-µm long EAM. This shows that there is a tradeoff between modulation strength and transmission distance (or penalty) at a given data rate. Table 4.1 summarizes dynamic performances of the C-band REAM-SOAs studied in this thesis that are promising to realize low-cost access network transmitters at bit rates ≥25 Gb/s.

Table 4.1. Dynamic performances of C-band EAMs in an REAM-SOA configuration at 25 Gb/s NRZ.

L_{EAM} (µm)	$f_{3\text{-dB}}$ (GHz)	At 25°C (λ = 1530 nm)		At 45°C (λ = 1545 nm)	
		BtB DER (dB)	Penalty	BtB DER (dB)	Penalty
80	>26.5	8.1	1 dB @ 10 km 2.5 dB @ 16 km	7.5	1 dB @ 10 km 4 dB @ 16 km
150	23	15	4.5 dB @ 12 km 3 dB @ 10 km	12	3 dB @ 10 km

Therefore, a PIC based on the 80-µm long EAM provides a good compromise between extinction ratio, E/O bandwidth and chirp. The shorter EAM can be used as a high-speed transmitter at bit rates ≥50 Gb/s (e.g., 50G PON [13]), or as a 25G-class transmitter in the access network (e.g., 5G fronthaul, 25G EPON [12]) with a relatively low penalty. However, the achievable fiber length is expected to be shorter at such high bit rates. By the time of writing this manuscript, the 50G or beyond performances of the C-band EAMs are not characterized because of the limitation of the current experimental setup—the PRBS generator is capable of generating only up to 32 Gb/s NRZ signals (e.g., see Section 4.3 for a custom-built test setup for 50G NRZ and PAM-4 transmissions).

4.2. Digital Transmission in the O-Band at 25 Gb/s

As a preliminary test, we first characterized the O-band REAM-SOA based on a 100-µm long EAM at 25 Gb/s NRZ using a similar setup shown earlier in Fig. 4.1. However, no external amplification is used in this case, which is desirable for passive optical network (PON) applications. The RSOA exhibits a large intrinsic gain of ~17 dB at 1310 nm (TE-polarized) and a noise figure of ~4 dB (small-signal) for a pump current of 60 mA (e.g., see Chapter 3, Sections 3.3 and 3.4). In order to achieve a better amplifier linear response, we operated the SOA at 40 mA. The 3-dB bandwidth of the EAM is >30 GHz over the 20-nm spectral range we considered

(between 1300 nm and 1320 nm), which indicates the PIC is capable of operating at very high bit rates over a wide range of spectrum.

Since fiber dispersion is very low in the O-band, the transmission distance is rather limited by high fiber loss (attenuation). Because of external losses in the setup (e.g., filter, switch, and connector losses), and since there was no external amplification in our experimental setup, the transmission distance in our case is limited to 10 km. Published results in relation to the O-band REAM-SOA can be found in [34].

Fig. 4.8 shows BER performance of the 100-µm long O-band EAM in an REAM-SOA configuration at 1310 nm and 25°C in BtB and 10 km connectivity. The corresponding eye diagrams are also shown on the right-hand side of the figure. The BtB DER of the EAM at 1310 nm is ~10.8 dB for a reverse bias voltage of −1.3 V and 2.6 V voltage swing.

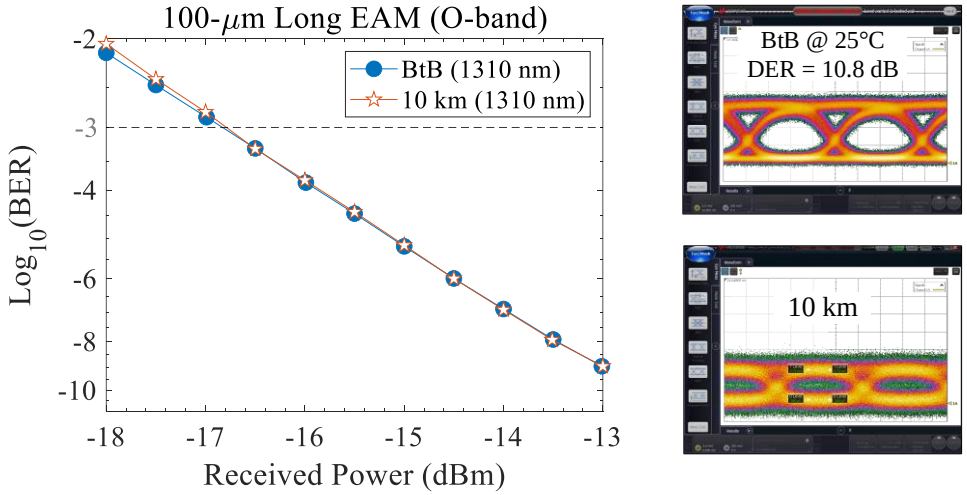


Fig. 4.8. BER performance of a 100-µm long EAM in an REAM-SOA configuration at 25 Gb/s NRZ, for an input wavelength of 1310 nm. T = 25°C, EAM bias: −1.3 V/2.6 V_{PP}, I_{SOA} = 40 mA.

The 10-km BER curve perfectly overlaps with the one in BtB, which is a clear indication of the absence of fiber dispersion in this region so that the transmitted waveform is only attenuated by the relatively high fiber loss, reducing the amplitude of the transmitted signal, which is also visible in the noisy eye diagram after 10 km.

The overlapping BER behavior is consistent over the 20-nm range where the device is tested (1300−1320 nm) as shown in Fig. 4.9 (a). The slight shift in the BER curves of the EAM at 1320

nm is due to a relatively lower DER at longer wavelengths (13.5 dB at 1300 nm vs. 8.1 dB at 1320 nm). Even with a 5.5-dB difference in DER between 1300 nm and 1320 nm, wavelength-dependent penalty of the PIC at 25 Gb/s NRZ is only ~0.5 dB. For an intermediate wavelength of 1310 nm, the BER curve after 10 km SMF transmission lies between the two extrema as shown in Fig. 4.9 (b). This proves that our components can be used to realize low-cost and high-speed colorless transmitters with at least a 20-nm WDM window requiring only 0.5 dB power tolerance, for example for ITU's 50G PON [13] and IEEE's 50G EPON upstream window 2 (UW2) applications [12]. Table 4.2 summarizes dynamic performances of the O-band REAM-SOA PIC at 25℃.

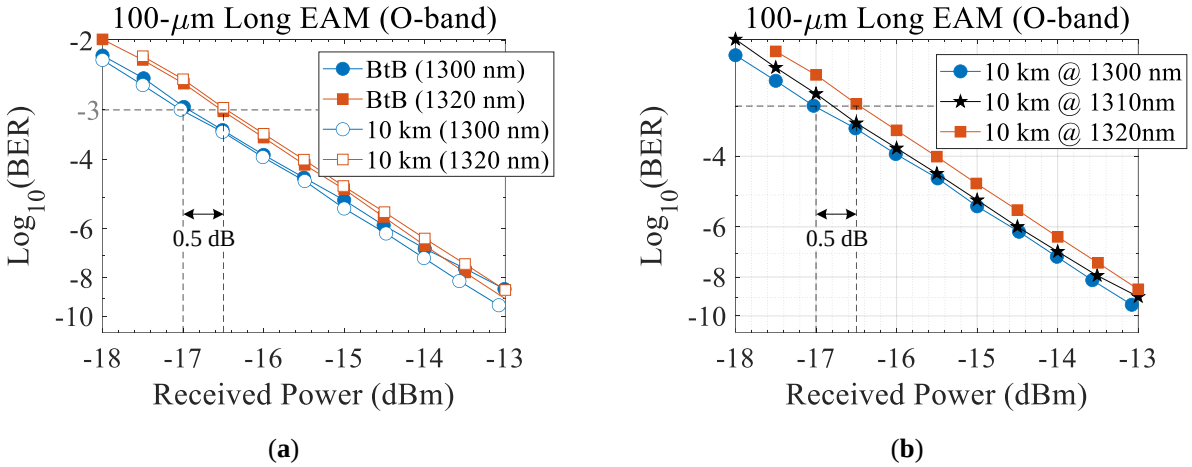


Fig. 4.9. BER performance of a 100-μm long EAM in an REAM-SOA configuration (**a**) at 1300 nm (−1 V/2 V_{PP}) and 1320 nm (−1.4 V/2.8 V_{PP}) nm in BtB and after 10 km, (**b**) 10-km BER performances with an intermediate wavelength of 1310 nm between the two extrema (i.e., 1300, 1310, and 1320 nms). T = 25℃, I_{SOA} = 40 mA.

Table 4.2. Dynamic performances of a 100-μm long O-band EAM in REAM-SOA at 25℃, 25 Gb/s NRZ.

Wavelength (nm)	3-dB Bandwidth (GHz)	BtB DER (dB)	@ Bias Condition
1300	30.5	13.5	−1.0 V/2.0 V_{PP}
1310	33	10.8	−1.3 V/2.6 V_{PP}
1320	33	8.1	−1.4 V/2.8 V_{PP}

4.3. Beyond 50G Digital Transmission in the O-Band

Using Non-Return-to-Zero Modulation Format

In order to demonstrate the high-speed capability of our components, we performed a 50-Gb/s transmission using NRZ as well as PAM-4 modulation formats. Fig. 4.10 shows schematic diagram of the experimental setup used to generate and transmit the 50G signals. The 50 Gb/s

signals are generated by multiplexing two 25-Gb/s NRZ signals from a signal quality analyzer (Anritsu MP1800A) with a bit pattern of PRBS31. A delay line is connected to one arm so that the signals are interleaved in time inside the multiplexer. For generating the 50G NRZ signal, we used a 2:1 selector (multiplexer) module from III-V Lab whereas the 25 GBaud PAM-4 signal is generated by using a digital to analog converter (DAC), a module also from III-V Lab [35].

For synchronization, the clock output of the signal quality analyzer is split into two using a 1:2 splitter (bandwidth = 26.5 GHz) and applied one part to the multiplexer module (for NRZ) or the DAC (for PAM-4) and the other part to a sampling oscilloscope at the receiver side. Then, the 50G signal is amplified by an RF amplifier (bandwidth = 40 GHz), combined with a DC offsetting voltage using a bias-T and applied to the EAM section. The rest is similar to the standard setup discussed in Section 4.1.1. At the receiver side, the 50G NRZ (or PAM4) signal is O/E converted by a high-speed photodiode whose output is fed to a sampling oscilloscope for further processing. The setup is customized only for capturing eye diagrams (not BER), and by the time of writing this manuscript, the 50G BER test has not been performed because of the setup limitation.

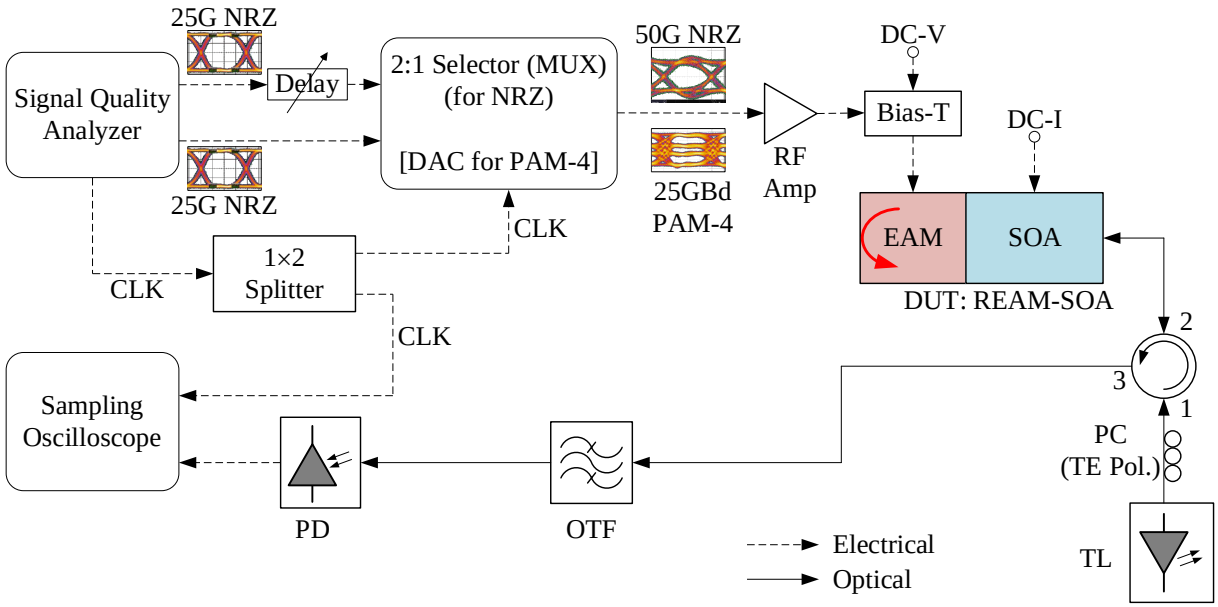


Fig. 4.10. Schematic diagram of experimental setup for generating and transmitting 50 Gb/s NRZ and PAM-4 signals.

Fig. 4.11 shows the eye diagram of the 50 Gb/s NRZ electrical signal generated by the above experimental setup. The eye amplitude is limited by the RF amplifier, and the maximum value

obtained from the driver is ~2.4 V_{PP}, and a fixed V_{PP} value is used over the 20-nm spectral range of testing. The SNR of the electrical signal is ~6 dB, and it has almost the same rise and fall times of ~9.3 ps with a root mean square (RMS) jitter of ~737.5 fs.

The crossing point of the eye diagram can be adjusted by varying the driving voltage of the multiplexer (or the DAC) module, which can bring an advantage in C-band transmissions by compensating the EAM chirp, but its impact in the O-band is not significant. Moreover, the crossing point of the optical signal can also be adjusted by appropriately choosing the EAM's bias voltage in conjunction with the peak-to-peak electrical signal. Since dispersion is very low in the O-band, we kept the crossing point of the 50G NRZ electrical signal close to 50%.

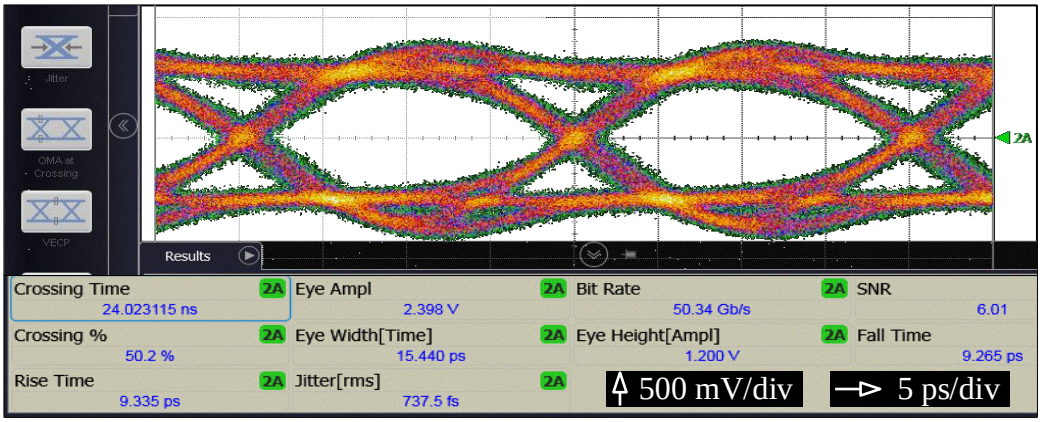


Fig. 4.11. Eye diagram of 50 Gb/s NRZ electrical signal generated using the experimental setup shown above.

Fig. 4.12 shows the 50 Gb/s NRZ eye diagrams obtained from the 100-µm long O-band EAM in a BtB connectivity without equalization. The 20-nm spectral range is the same as the 25G case (1300−320 nm). The first three eye diagrams are obtained at 25℃, and they have the same vertical scale (5 mV/div), whereas the fourth one is obtained at 45℃, and it has a vertical scale of 3 mV/div.

The eye diagrams in all cases are clearly open and the DERs are comparable to their respective values at 25 Gb/s NRZ. For example, at 1310 nm, the difference in DER between 25 Gb/s and 50 Gb/s NRZ is only 0.5 dB (10.8 dB vs. 9.7 dB). Table 4.3 summarizes DER performances of the EAM at 25G and 50G NRZ. The DER at 1320 nm/25℃ is slightly lower than the expected value

because of a lower peak-to-peak voltage (fixed 2.4 V_{PP} used), which is below the required value for this wavelength. The typical voltage swing at 1320 nm is around 2.8 V (cf. Table 4.2).

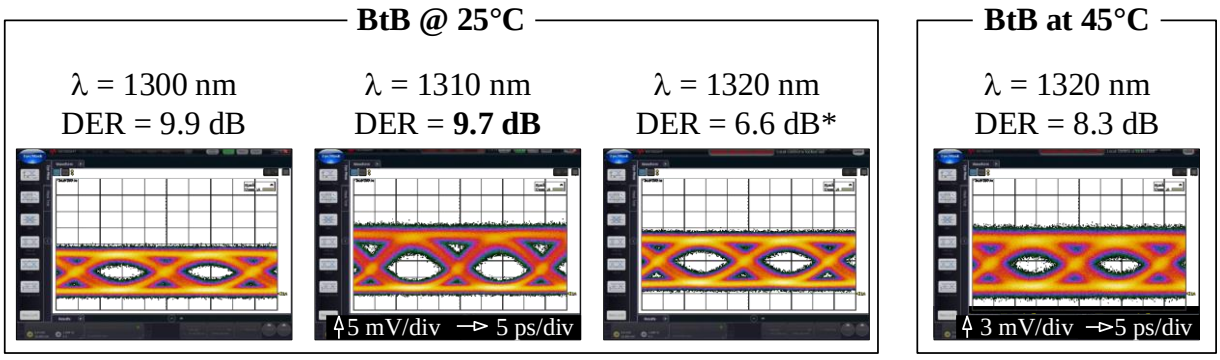


Fig. 4.12. Back-to-back 50G NRZ eye diagrams obtained from a 100-µm long EAM in an REAM-SOA configuration at 25°C for input wavelengths of (**a**) 1300 nm at −0.6 V, (**b**) 1310 nm at −1.3 V, (**c**) 1320 nm at −1.4 V, (**d**) 1320 nm at 45°C and −1 V. I_{SOA} = 40 mA. [* Lower DER at 1320 nm because of limited voltage swing, ~2.8 V_{PP} required.]

On the other hand, the eye amplitude at 1310 nm has the maximum value because it is the wavelength at which the SOA's gain peak occurs (e.g., see Chapter 3, Section 3.3). Moreover, the output power at 1320 nm/45°C is lower than the one at 25°C as a result of degraded SOA gain at a higher temperature. When the temperature increases, the absorption edge of the EAM is red shifted so that, for a given operating wavelength, a lower bias voltage is required. For example, at 45°C, the EAM's optimal operating bias condition for an input wavelength of 1320 nm is found to be −1 V/2 V_{PP}, which results in a DER of ~8.3 dB. Nevertheless, the O-band devices are designed to operate at 25°C centered at 1310 nm.

Since dynamic performances of the EAM at 50 Gb/s NRZ at different wavelengths are comparable to the ones at 25 Gb/s NRZ, we expect similar BER performances after 10 km transmission without a significant degradation of the 50G NRZ eye diagrams.

Table 4.3. Dynamic extinction ratios of the 100-µm long EAM at 25G and 50G NRZ.

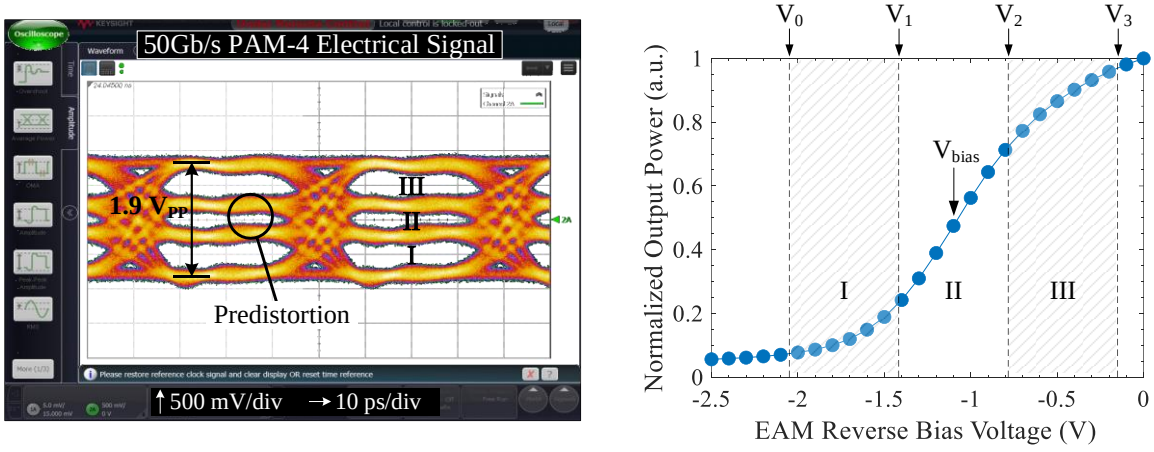
Wavelength (nm)	**DER (dB) at 25°C**		**ΔDER (dB)**
	@ 25 Gb/s NRZ	**@50 Gb/s NRZ**	
1300	13.5	10	3.5
1310	10.8	9.7	0.5
1320	8.1	6.6*	1.5

* *Lower DER because of limited output voltage of the RF amplifier* (*lower* V_{PP}).

Using PAM-4 Modulation Format

The frequency response of the 100-μm long O-band EAM in an REAM-SOA configuration (i.e., >33 GHz) suggests that it can support bit rates beyond the 50G line rate even in NRZ format. On the other hand, its high DER suggests that it can be effectively modulated with higher order modulation formats (e.g., PAM-4) to realize a 100G class colorless transmitter. To demonstrate compatibility of the PIC with such modulation formats, we modulated the EAM using a 25 GBaud PAM-4 signal (50 Gb/s in total) as a starting point, which can be achieved using the experimental setup shown earlier in Fig. 4.10. Instead of a 2:1 selector (multiplexer) that we used for 50G NRZ signal generation, we used a DAC to generate the 50 Gb/s PAM-4 signal. Similar to the 50G NRZ case, neither external amplification nor equalization is used for the 25GBd PAM-4 transmission.

Fig. 4.13 shows eye diagrams of the 25 GBaud PAM-4 electrical signal after RF amplification (left) and the EAM's absorption response in linear scale as a function of reverse bias voltage (right). The peak-to-peak voltage this time is limited to 1.9 V as shown in Fig. 4.13 (a) so that EAM operates in its linear regime while providing acceptable eye amplitudes. The EAM's response is quasilinear in the region between −0.1 V and −2 V as illustrated using the dashed lines in Fig. 4.13 (b). By biasing it at the center of the quasilinear region ($V_{bias} = -1.1$ V), the four voltage levels of the PAM-4 signal become: $V_0 = -2.05$ V, $V_1 = -1.42$ V, $V_2 = -0.78$ V, and $V_3 = -0.15$ V.



(**a**) (**b**)

Fig. 4.13. (**a**) Eye diagram of 25 GBaud PAM-4 electrical signal generated by combining two 25 Gb/s NRZ signals using a DAC in the experimental setup shown above, (**b**) absorption response of a 100-μm long O-band EAM in an REAM-SOA configuration at 1310 nm in linear scale ($T = 25$°C).

The electrical signal is slightly predistorted in order to compensate for the EAM's operation in the nonlinear regions (shaded regions, also labelled I and III). That means, the middle eye amplitude (region II) is slightly reduced compared to that of the bottom and the top eyes. Otherwise, one might need to lower V_{PP} for a better linearity, which also lowers the amplitude of each eye diagram—a compromise to be made between EAM linearity and eye openings.

Fig. 4.14 shows the 50G PAM-4 eye diagrams obtained from the 100-µm long EAM in REAM-SOA configuration without equalization, at 1310 nm (-1.1 V/1.9 V_{PP}). Even without equalization, we obtained open and almost equally spaced PAM-4 eye diagrams. For transmissions involving equalization techniques, eye closures are analyzed using standard procedures such as transmitter and dispersion eye closure for PAM-4 (TDECQ) [106]. Since the current results are obtained without equalization, we expect a significant improvement in the PAM-4 signal quality when they are refined by applying post-detection equalization.

The outer extinction ratio (OER) for PAM-4 signals is defined as the ratio of the highest (V_3) and the lowest (V_0) eye amplitudes, which is expressed in decibel as [108]:

$$OER\ [\text{dB}] = 10log_{10}\left(\frac{V_3}{V_0}\right). \tag{4. 1}$$

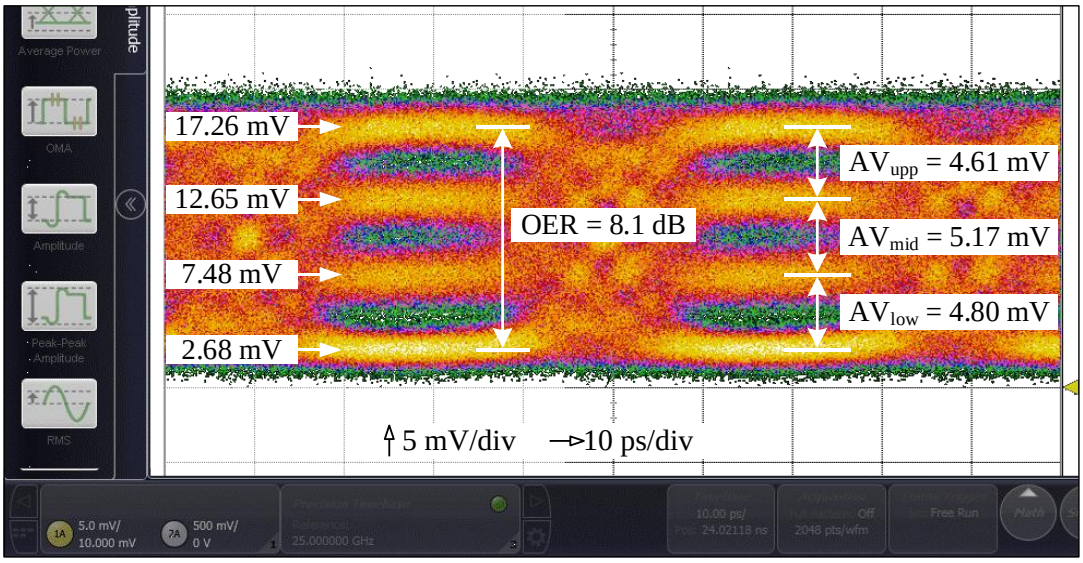


Fig. 4.14. 25 GBaud PAM-4 eye diagrams obtained from a 100-µm long EAM in an REAM-SOA configuration operating. $\lambda = 1310$ nm, $V_{bias} = -1.1$ V, $V_{PP} = 1.9$ V, $T = 25$°C.

For the 100-µm long EAM, the lowest PAM-4 signal level occurs at around 2.7 mV and the highest level at around 17.3 mV, providing an OER of ~8 dB, which is slightly lower than the DER obtained in NRZ format because of a lower V_{PP} used here (2.4 V vs. 1.9 V).

The eye diagrams are almost equally spaced with the narrowest (top) and widest (middle) eyes having amplitudes of about 4.6 mV and 5.2 mV, respectively. The bottom eye has an intermediate amplitude of about 4.8 mV. In practice, the relative PAM-4 eye openings (the average transmitted signal levels) are quantified using the eye linearity parameter defined as [108]:

$$\text{Eye Linearity} = \frac{\min(AV_{low}, AV_{mid}, AV_{upp})}{\max(AV_{low}, AV_{mid}, AV_{upp})}, \quad (4.\ 2)$$

where, AV_{low}, AV_{mid}, and AV_{upp} are amplitudes of the lower, middle, and upper eyes, respectively.

Using (4. 2), linearity of the PAM-4 eyes obtained from the 100-µm long EAM roughly becomes 89%. This indicates that the REAM-SOA PIC is a promising candidate for 100G-class PAM-4 transmission where equalization techniques are is typically used.

4.4. Analog Radio-over-Fiber Transmission

In order to demonstrate the compatibility of our components with both analog and digital transmission systems, we performed a multichannel wireless transmission in the V-band (60 GHz range) followed by intermediate-frequency-over-fiber (IFoF) transmission over a standard SMF using an RSOA-EAM based on the 100-µm long O-band EAM. The system represents a typical 5G fronthauling in the upstream direction. The results shown in this section are obtained in collaboration with Aristotle University of Thessaloniki in Greece.

Although the RSOA-EAM configuration results in a relatively lower modulation bandwidth compared to its REAM-SOA counterpart, which is due to a large round-trip delay inside the SOA section (16 GHz vs. 33 GHz, e.g., see Chapter 3, Section 3.6), it also provides a better amplifier linearity¸ which is critical for analog transmissions, because a uniform amount of light enters the SOA section before and after reflection. On the contrary, for an REAM-SOA, the optical power that enters the SOA section in the forward path is different from the one in the reverse path because of the EAM's absorption in the latter case, which can affect the SOA's linear response, especially if the incident light in either direction is strong enough to cause gain saturation.

Similarly, the EAM is also operated in its linear regime by limiting the peak-to-peak voltage swing to 1.1 V (equivalent to +5 dBm RF power), where the bias voltage is similar to the case of PAM-4 discussed above. However, the peak-to-peak voltage is significantly reduced here (1.1 V_{PP} for ARoF vs. 1.9 V_{PP} for PAM-4) because analog signals require high component linearity. Fig. 4.15 shows absorption response of the EAM in linear scale, operating at 1310 nm. The EAM's response is quasilinear in the region between the dashed lines (between −0.5 V and −1.6 V), which results in a static extinction ratio of ~7.5 dB.

By biasing the EAM at the center of the quasilinear region (−1.1 V), a better linear response can be achieved. The main drawback of operating the EAM at a relatively high reverse bias voltage for the *on* state (e.g., −0.5 V) is that it increases the insertion loss, which is a compromise to be made for linear operation of the EAM. The EAM's linearity can be improved by further reducing the voltage swing but the extinction ratio becomes small. Therefore, a V_{PP} of 1.1 V provides a good compromise between linearity, extinction ratio and insertion loss for the ARoF transmission.

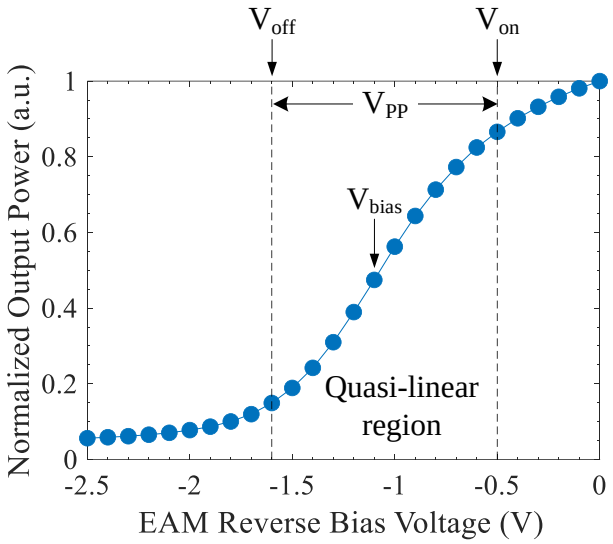


Fig. 4.15. Extinction ratio of a 100-μm long EAM in linear scale at 1310 nm. T = 25°C.

Fig. 4.16 shows schematic diagram of the experimental setup used for a multichannel V-band/IFoF uplink transmission using RSOA-EAM as the optical transmitter. Four 16-QAM subcarriers are generated by an arbitrary waveform generator (AWG), digitally multiplexed by Keysight IQ tools installed on the AWG, amplified by an external linear RF driver, and finally injected into the

transmitter horn antenna. The transmitted signal represents the user information towards a cellular base station.

An external clock source operating at 9.5 GHz is used as a local oscillator (LO) whose power is split into two and fed to the transmitter (Tx) and receiver (Rx) horn antennas. The Tx is equipped with electronic circuit for upconverting the intermediate frequency (IF) signal in the range of 5 GHz to the 60-GHz range (V-band), where the LO signal is first multiplied by six and mixed with the IF signal ($6\times9.5\text{GHz} + 5\text{GHz} = 60\text{GHz}\pm2$, i.e., V-band). The upconverted 60-GHz signal is transmitted over a wireless distance of ~1.2 m and received by another horn antenna.

The received wireless signal is downconverted to its original multi-IF state, amplified to +5 dBm RF power, combined with a DC offsetting voltage using a bias-T, and applied to the EAM section of the RSOA-EAM PIC. Finally, the modulated signal is transmitted over a 3-km standard SMF, realizing a multi-IFoF transmission.

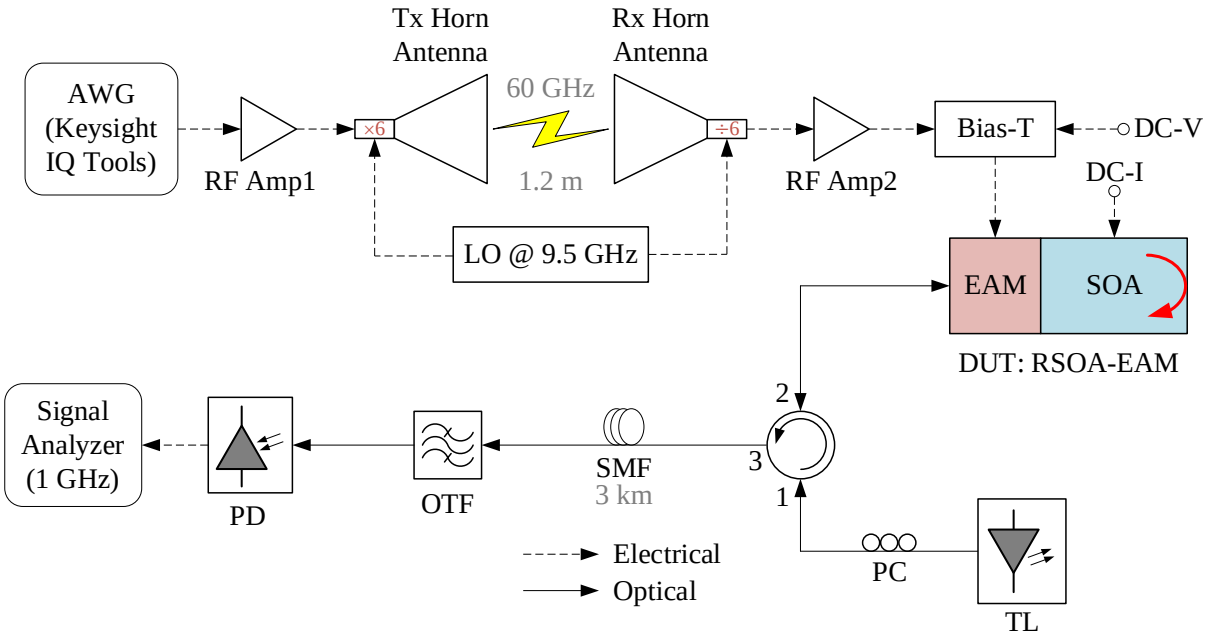


Fig. 4.16. Schematic diagram of experimental setup for a multichannel V-band/IFoF uplink transmission.

At the optical receiver side, a 10G PIN photodiode is used for optoelectronic (O/E) conversion of the Fiber-Wireless (FiWi) signal, and its output is fed to a signal analyzer for monitoring the transmission performance. The bandwidth of the AWG is ~5 GHz and that of the signal analyzer

is ~1 GHz. As a result, we limited the baud rate per subcarrier to 625 MBaud, in order to obtain an aggregate bit rate of 10 Gb/s using four 16-QAM signals ($4 \times 4 \times 625\text{MBaud} = 10$ Gb/s). Published results in relation to this section can be found in [35]. Fig. 4.17 shows spectrum of the four-channel 16-QAM signal and constellation diagrams of the subcarriers (worst-case) obtained after 1.2-m V-band/3-km SMF transmission using the RSOA-EAM as the optical transmitter.

In order to obtain uniform SNR across all subcarriers, their relative amplitudes were adjusted in IQ tools, resulting an SNR of roughly 20 dB per subcarrier. The constellation diagrams reveal that all the four subcarriers have comparable signal qualities, and they are clearly demodulated after the joint 1.2-m V-band and 3-km IFoF propagation. The signal quality in wireless transmission systems is commonly characterized in terms of error vector magnitude (EVM), which quantifies the number of erroneously received symbols by taking the difference between transmitted (ideal) symbols and received symbols after equalization [109]. The required end-to-end EVM for 5G fronthauling based on 16-QAM signals, as defined by 3GPP, is 12.5% [109].

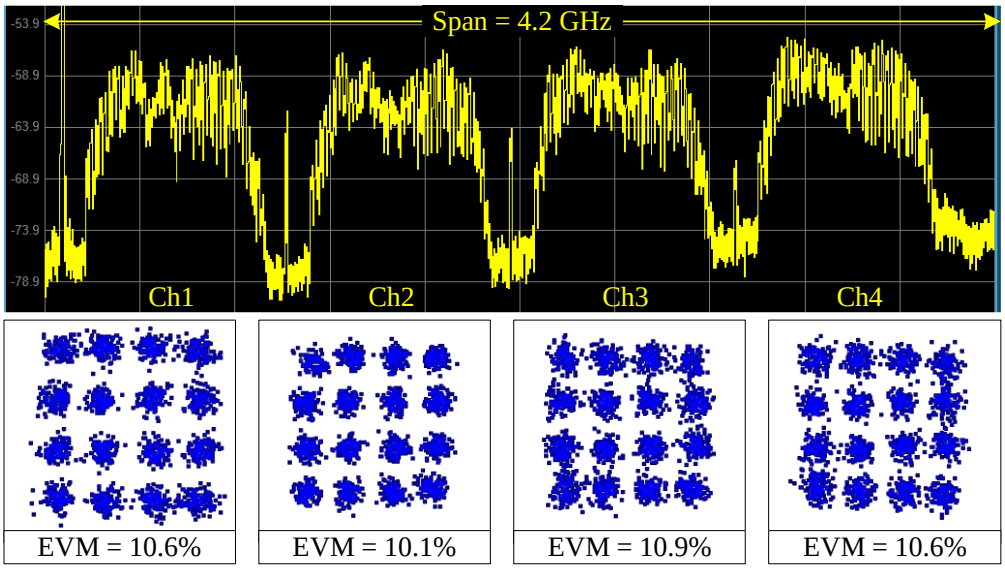


Fig. 4.17. Received spectrum (top) of a four-channel 16-QAM signal after V-band/IFoF uplink transmission using an RSOA-EAM, and the corresponding constellation diagrams (bottom). ↑ 5 dB/div, → 420 MHz/div.

In order to identify individual EVM contributions of the wireless and the optical links, we analyzed the signals by transmitting them over the two channels separately as illustrated in Fig. 4.18. First, EVM of the multiplexed 16-QAM signal is applied to the signal analyzer and EVMs of the four

subcarriers are recorded, which serve as the reference EVM (EVM_{ref}). Then, the 16-QAM signals are transmitted over the wireless channel and EVM of the received signal is recorded. In the next step, the output of the AWG is directly applied (after bias-T) to the EAM section of the REAM-SOA PIC. Following that, the modulated optical signal is transmitted over a short fiber patch cable (BtB ARoF) or a 3-km SMF loop (3km ARoF), and the EVM is measured using the signal analyzer. For the final end-to-end FiWi transmission, the wireless link is used in conjunction with the optical link as discussed above (e.g., see Fig. 4.16 for the complete setup).

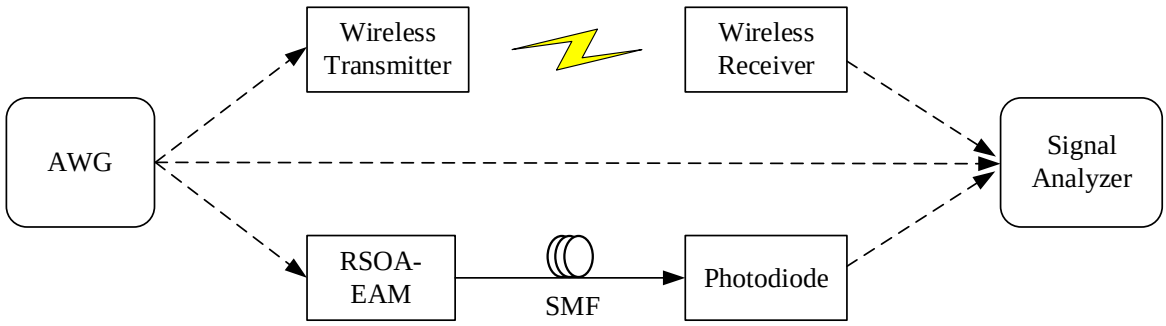


Fig. 4.18. Schematic of the experimental setup for analyzing EVM contributions of the wireless and optical links.

Fig. 4.19 shows the evolution of the transmitted IQ signals as they propagate through the wireless and optical transmission channels, where the performance of the worst performing channel at each stage is shown here. Visual inspection of the demodulated constellation diagrams from left to right reveals the degradation of the signal quality during transmission. The 16-QAM signal from the AWG has a measured EVM of ~2%, which can be used as a reference value for analyzing the performances of the wireless and the optical links.

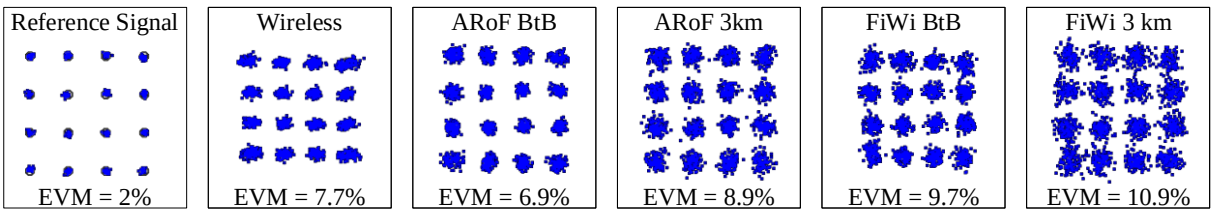


Fig. 4.19. Constellation diagrams of worst-performing channels, and measured EVMs of the corresponding subcarriers at different stages of the transmission system.

Fig. 4.20 shows measured EVMs of all subcarriers at various stages of the FiWi transmission link. The worst case EVM of the wireless link is ~7.7% (Ch4) and that of the optics part (REAM-SOA with a short fiber patch cable) is ~6.9 (Ch4). Using the 2% EVM of the source as a reference, EVM contribution of the wireless channel alone is ~5.7% and that of the REAM-SOA is ~4.9%. When a 3-km SMF is inserted between the REAM-SOA and the photoreceiver, the worst case EVM becomes ~8.9%, indicating that EVM contribution of the 3-km SMF is around 2% (i.e., 8.9% − 6.9%). Since the transmission is performed in a region where chromatic dispersion is very low, the EVM contribution (penalty) of the 3-km SMF is because of a relatively high fiber attenuation in the O-band.

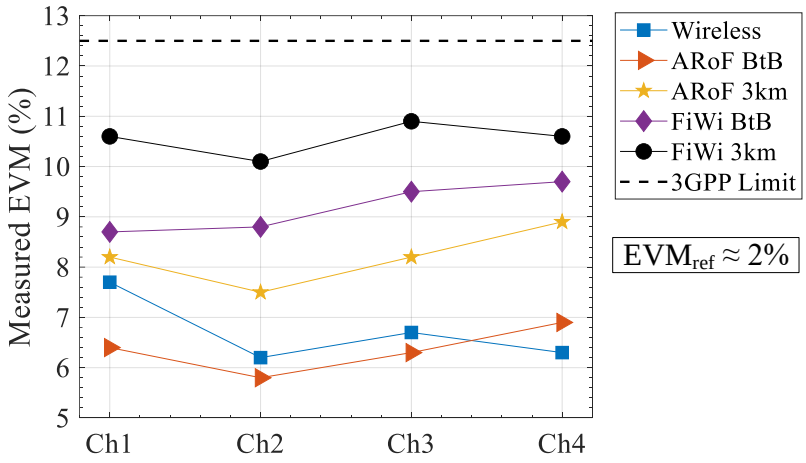


Fig. 4.20. Measured error vector magnitudes (EVMs) of the four 16-QAM subcarriers at different stages of transmission. EVM_{ref}: measured EVM of the signal generated by the AWG (used as a reference).

In a BtB connectivity for the optical link, the worst case EVM of the FiWi transmission is ~9.7% (BtB FiWi). This shows that summation of EVM contributions of the wireless and optical links acting separately does not give the actual performance when the two links work in conjunction. The worst-case end-to-end EVM of the FiWi transmission is ~10.9% (Ch3), which is below the standard 12.5% EVM upper limit defined by 3GPP for 16QAM signals. Therefore, our components can be used to realize low-cost optical transmitters for 5G fronthauling based on analog transmission while satisfying the aggregate bit rate (10 Gb/s) and EVM (11.9%, which is below 3GPP's 12.5% upper limit for 16-QAM signals) requirements for ARoF transmissions.

4.5. Summary and Discussion

In this chapter, the system-level performances of our components are presented, in both digital and analog domains. In the C-band, the transmission distance is primarily limited by chromatic dispersion, which becomes detrimental at high bit rates (e.g., ≥25 Gb/s NRZ). In addition to that, EAM-induced chirp also plays the role of degrading or enhancing (to some extent) the dispersion-limited transmission. We demonstrated the impact of EAM-induced chirp using two modulator lengths: 80-µm and 150-µm long EAMs. Since transmitted pulses spend more time inside a longer EAM, while experiencing more chirp (phase shift) during their rising and falling edges, the transmission distance of the 150-µm EAM is limited to 12 km with a dispersion penalty of about 4.5 dB at 25 Gb/s NRZ and 10^{-3} BER (3 dB penalty at for 10 km transmission at the same rate). A lower chirp can be obtained by using shorter EAMs, and we obtained a good compromise between EAM-induced chirp, modulation strength and E/O bandwidth by using a PIC based on an 80-µm long EAM, which extends the fiber length to 16 km at 25 Gb/s NRZ with only 2.5 dB penalty at a BER of 10^{-3} without applying any dispersion compensation technique.

We also demonstrated the colorless operation of our components over a 15-nm range in the C-band (between 1530 and 1545 nm), where the devices exhibit no wavelength-dependent penalty. The components are also thermally stable up to 65°C, with only 2-dB extra power penalty compared to the device performance at 25°C, making them suitable for semi-cooled or uncooled indoor/outdoor environments.

In the O-band, the transmission distance is rather limited by fiber loss as dispersion is very low in the region. By using a 100-µm long EAM in an REAM-SOA configuration, we achieved 10 km unamplified transmission over a standard SMF at 25 Gb/s NRZ. The BER curves after 10 km perfectly overlap with the ones in a BtB connectivity, and this behavior is observed over a 20-nm range (between 1300 nm and 1320 nm). Except for a 0.5-dB wavelength-dependent penalty, which is attributed to a relatively lower DER at longer wavelengths, the O-band devices demonstrated their suitability for colorless transmission over the 20-nm spectral window. In order to demonstrate the high-speed capabilities of our components, we also performed 50 Gb/s NRZ and 25 GBaud PAM-4 transmissions in BtB using the same 100-µm long EAM in an REAM-SOA configuration, achieving comparable DER performances to the ones obtained at 25G NRZ without applying any equalization techniques. The BtB eye diagrams obtained at 50G NRZ suggest that similar

performances can be obtained after 10 km to that of the 25G NRZ case without a significant degradation to the 50G eye diagrams.

Finally, as a proof-of-concept, we demonstrated a multi-channel V-band/IFoF uplink FiWi transmission using the 100-μm long O-band EAM in an RSOA-EAM configuration as the optical transmitter at the remote office—a system representing a typical 5G fronthaul network. We achieved <11% EVM across the four channels at an aggregate bit rate of 10 Gb/s, which satisfies the EVM and data rate requirements of fronthaul networks based on 16-QAM signals using ARoF modulation scheme.

In conclusion, our components can be used to realize low-cost and high-speed colorless transmitters over a wide range of operating spectrum either in the C- or the O-band, supporting both analog and digital modulation schemes, with minimum thermal and wavelength control requirements for indoor or outdoor applications.

Chapter 5

5. Conclusion and Perspectives

5.1. Summary and Conclusion

We studied different configurations of reflective EAM-SOA PICs based on three modulator lengths (80, 100 and 150 micrometers) and analyzed their performances, identifying different design tradeoffs that have to be made in order to realize cost-effective, colorless, and high-speed access network transmitters. The designs of the devices, relevant device physics, and epitaxial growth process used for their realization are presented in a brief but self-sufficient way. The devices are realized using robust and industrially compatible SI-BH waveguide technology and they are combined using butt-joint integration technique.

Optical and optoelectronic properties of the devices are studied using numerical simulation results, and the results can be used as inputs in future designs. In both cases, we observed a good agreement between simulation and experimental results. Furthermore, we performed a complete performance analysis of our components in order to identify optimal transmission conditions by optimizing the building blocks separately so that optimal performances can be obtained when they are brought together on a single chip.

On the amplifier side, we obtained an intrinsic RSOA gain of >17 dB from a 300-µm long O-band SOA, a very low unsaturated noise figure of 4 dB, and high saturation output power of 10 dBm. At wavelengths close to the SOA's gain peak, we obtained a fiber-to-fiber gain (net device gain) of >8.5 dB, which also is >5 dB over a 20-nm spectral range in the O-band.

On the EAM side, we obtained a very high dynamic extinction ratio of ~15 dB using a 150-µm long C-band EAM (>12 dB DER for a 100-µm long O-band EAM) at a relatively low driving voltage of -1.1 V/2.2 V_{PP} (e.g., at 1530 nm). In order to demonstrate the tradeoff between modulator length and achievable E/O bandwidth, we analyzed the frequency response of a shorter C-band EAM (80 µm length), and we observed that its frequency response is still flat after 26.5

GHz (setup limit), suggesting that the EAM can be effectively operated at bit rates ≥50 Gb/s, and it can be used to realize 50G-class transmitters using NRZ modulation format (or even 100G-class transmitter using PAM-4). Moreover, to demonstrate the tradeoff between extinction ratio and modulation bandwidth of an EAM, we analyzed the performance of an EAM having an intermediate length of 100 μm but a slightly thicker MQW active region, and we obtained >33 GHz bandwidth (comparable to that of the 80-μm long EAM) and 8−12 dB dynamic extinction ratios over a 20-nm range (comparable to that the 150-μm long EAM). Both performances are favorable for realizing high-speed access network transmitters in a cost-effective manner. Therefore, large E/O bandwidth can be achieved by using shorter EAMs without compromising the achievable extinction ratio, taking the advantage gained by using reflective EAMs, with a small penalty in the applied field at a given bias voltage.

In order to identify optimal transmission conditions in the C-band at bit rates ≥25 Gb/s, we thoroughly analyzed the chirp performances of our components, and we obtained zero chirp at a relatively low reverse bias voltage (between −1.2 V and −1.5 V over a 20-nm range). We also experimentally demonstrated that the modulator-induced chirp scales with the EAM length. In the case where the EAM-induced chirp is very low, the C-band transmission distance generally is limited by chromatic dispersion and fiber attenuation, requiring dispersion compensation techniques, which is an expensive solution for access network applications. Otherwise, one has to change the operating spectrum to the O-band (region of very low chromatic dispersion).

As a proof-of-concept, we demonstrated up to 50 Gb/s transmissions using our components as the optical transmitters. In the C-band, we achieved up to 16 km colorless transmission over a standard SMF at 25 Gb/s NRZ with a dispersion penalty of 2.5 dB. We also analyzed thermal stability of our components by operating them at higher submount temperatures, and we showed that the devices operate up to 45°C without any performance degradation. Based on the transmission performances, we conclude that a PIC based on an 80-μm long EAM provides a good compromise between modulation strength, E/O bandwidth, and modulator-induced chirp.

Since chromatic dispersion is very low in the O-band, the transmission distance is rather limited by a relatively high fiber loss. We achieved 10 km unamplified transmission at 25 Gb/s NRZ without any transmission penalty at a given wavelength (overlapping BtB and 10 km BER curves per wavelength) and <0.5 dB wavelength-dependent penalty over a 20-nm range. We also

demonstrated 50 Gb/s operation of an REAM-SOA PIC based on a 100-µm long EAM without equalization using both NRZ and PAM-4 modulation formats in a BtB connectivity. Dynamic extinction ratio of the EAM at 50 Gb/s NRZ is comparable to the one at 25 Gb/s NRZ. Based on the BtB DER performances, we expect similar transmission performances after 10 km without a significant degradation of the 50G eye diagrams.

Finally, we demonstrated the compatibility of our components to ARoF transmissions by inserting an RSOA-EAM PIC in a test bed that represents a 5G fronthaul network in the upstream direction. By transmitting four 16-QAM signals first over a 1.2-m V-band wireless channel and then over a 3-km SMF, we achieved an end-to-end EVM of $<11\%$, satisfying the EVM requirement defined by 3GPP for 16-QAM signals.

Therefore, our components are suitable for both analog and digital transmission systems, and they are compatible with semi-cooled indoor/outdoor environments. The devices can be used to realize high-speed, colorless, and cost-effective access network transmitters either as arrays or discrete elements, and they can find several application areas in the next generation of high-speed networks such as 5G fronthauling, high-speed PONs and data centers.

5.2. Perspectives

The results presented in this thesis are based on continuous improvement and mastering of device design, fabrication, and characterization by III-V Lab in parallel with optical telecom evolutions over the years, and technical discussions with Télécom Paris. The performances of the devices can be further improved in the future by optimizing the building blocks both separately and as integrated circuits. For example, the input/output coupling efficiency can be improved by using narrower tapers, leveraging the SI-BH waveguide technology. Moreover, in addition to the optimized cladding layer used in the current devices, the insertion loss of the SSC can be further reduced by using a higher bandgap material in the waveguide section so that it becomes transparent to wavelengths in the working region of the EAM section in a PIC, although this requires an extra epitaxy step (i.e., 3 epitaxy steps for an REAM-SOA-SSC PIC).

Apart from minimizing the SSC and input/output coupling losses, the output power can be maximized by integrating longer SOAs, with optimized QW layers for high saturation output power so as to achieve linear operation of the SOA. Thermal performance of the SOA can be

improved by either increasing the bandgap discontinuity or using aluminum-based material system (e.g., GaInAlAs/InP QWs) or even a combination of GaInAlAs/GaInAsP MQW structures in order to obtain large barrier offsets, which then provides strong electron confinement.

Similarly, the E/O bandwidth of an EAM can be improved by shortening its length, which results in a lower modulator capacitance. The reduction in extinction ratio when shortening the EAM length can be compensated by increasing the number of QW layers, but it has to be done sensibly to minimize the required driving voltage. Therefore, there is a tradeoff between the number of QW layers, modulation strength, E/O bandwidth and reverse bias voltage of an EAM.

On the other hand, high-power EAMs can be realized by using aluminum-based material system such as GaInAlAs/InP MQWs since it offers a lower valence band offset compared to GaInAsP, enabling photogenerated heavy-holes escape at a relatedly faster rate. But it is also important to consider the type of integration technique (e.g., selective area growth) to be used with GaInAlAs since aluminum is susceptible to surface oxidation, which makes not compatible with butt-joint integration technology. Finally, polarization-independent components can be realized by using tensile strained QWs or a combination of compressive and tensile strained wells and barriers.

In order to take full advantage of the low-cost nature of reflective EAM-SOAs, we recommend parallel integration of the components to realize a multi-channel transmitter (e.g., at OLT side) in a WDM-PON system while discrete devices can also be used at the remote office (e.g., at the ONU side). Moreover, we recommend testing the devices for bidirectional transmission over a single wavelength by erasing the downlink information through SOA gain saturation, which can have a significant impact on the overall system cost as it allows using the available wavelength channels more efficiently. Furthermore, in order to analyze the high-speed performances of the devices and see the achievable transmission distance, we recommend performing transmission experiments at bit rates ≥50 Gb/s using the REAM-SOA PICs based on shorter EAMs (80-μm long EAM in the C-band and 100-μm long EAM in the O-band). Finally, to study the effects of transmission impairments (e.g., crosstalk and nonlinear effects) on the transmission performances of reflective devices, we also recommend testing the devices in a multi-channel (WDM) transmission system.

List of Abbreviations

AR	Anti-reflection
ARoF	Analog radio-over-fiber
ASE	Amplified spontaneous emission
AWG	Arbitrary waveform generator
AWG	Arrayed waveguide grating
BER	Bit error rate
BH	Buried heterostructure
BRS	Buried rib stripe
CB	Conduction band
CBO	Conduction band offset
CoC	Chip-on-carrier
C-RAN	Centralized radio access network
CW	Continuous wave
CMOS	Complementary metal-oxide-semiconductor
DER	Dynamic extinction ratio
DML	Directly modulated laser
DRoF	Digital radio-over-fiber
DS	Downstream
DU	Digital unit
DUT	device under test
DWDM	Dense wavelength division multiplexing
E/O	Electro-optic
EAM	Electroabsorption modulator
EDFA	Erbium doped fiber amplifier
EML	Externally modulated laser
ER	Extinction ratio
EVM	Error vector magnitude
FiWi	Fiber-wireless
FM	Frequency modulation
FSR	Free spectral range
HF	High frequency
HH	Heavy hole
HR	High-reflection
HSP	High-speed passive optical network
ICP	Inductively coupled plasma
IF	Intermediate frequency
IFoF	Intermediate-frequency-over-fiber
IM	Intensity modulation
IM/DD	Intensity modulation / direction detection
ISI	Intersymbol interference
ITU	International telecommunication union
LH	Light hole
LO	Local oscillator
MQW	Multiple quantum well
MZ	Mach-Zehnder

NF	Noise figure
NG-PON2	Next-generation passive optical network 2
NRZ	Non-return-to-zero
ODN	Optical distribution network
O/E	Optoelectronic
OER	Outer extinction ratio
OLT	Optical line terminal
ONU	Optical network unit
OOK	On-off keying
OTF	Optical tunable filter
PD	Photodiode
PDK	Process design kit
PIC	Photonic integrated circuit
PM	Phase modulation
PON	Passive optical network
QCSE	Quantum confined Stark effect
QW	Quantum well
REAM	Reflective electroabsorption modulator
RF	Radio frequency
RIN	Relative intensity noise
RSOA	Reflective semiconductor optical amplifier
RTT	Round trip time
RU	Radio unit
RW	Ridge waveguide
SAG	Selective area growth
SCH	Separate confinement heterostructure
SEM	Scanning electron microscope
SI-BH	Semi-insulating buried heterostructure
SI-InP	Semi-insulating indium phosphide
SMF	Single-mode fiber
SNR	Signal-to-noise ratio
SO	Spin-orbit split-off
SOA	Semiconductor optical amplifier
SSC	Spot-size converter
SSE	Source spontaneous emission
TDCEQ	Transmitter and dispersion eye closure for PAM-4
TDM	Time division multiplexing
TE	Transverse electric
TEC	Thermoelectric controller
TM	Transverse magnetic
TWDM	Time and wavelength division multiplexing
UD-WDM	Ultra-dense wavelength division multiplexing
US	Upstream
VB	Valence band
VBO	Valence band offset
VNA	Vector network analyzer
VOA	Variable optical attenuator
WDM	Wavelength division multiplexing
WNE	When not enabled

References

[1]. T. Pfeiffer, "Next generation mobile fronthaul and midhaul architectures," in *IEEE/OSA Journal of Optical Communications and Networking*, vol. 7, no. 11, pp. B38-B45, 1 November 2015.

[2]. P. Chanclou *et al*., "How does passive optical network tackle radio access network evolution?," in *IEEE/OSA Journal of Optical Communications and Networking*, vol. 9, no. 11, pp. 1030-1040, Nov. 2017.

[3]. C. Lim *et al*., "Evolution of Radio-Over-Fiber Technology," in *Journal of Lightwave Technology*, vol. 37, no. 6, pp. 1647-1656, 15 March15, 2019.

[4]. "Common Public Radio Interface: eCPRI Interface Specification v2.0 (2019)," available online at: http://www.cpri.info/downloads/eCPRI_v_2.0_2019_05_10c.pdf.

[5]. K. Miyamoto, *et al*., "Performance evaluation of ethernet-based mobile fronthaul and wireless comp in split-PHY processing," in IEEE/OSA Journal of Optical Communications and Networking, vol. 9, no. 1, pp. A46-A54, Jan. 2017.

[6]. "5G White Paper," available online at: https://www.ngmn.org/work-programme/5g-white-paper.html.

[7]. "IMT Vision – Framework and overall objectives of the future development of IMT for 2020 and beyond," Recommendation ITU-R M.2083-0, 2015.

[8]. "40-Gigabit-capable passive optical networks 2 (NG-PON2): Physical media dependent (PMD) layer specification," ITU-T Recommendations G.989.2 (2014).

[9]. E. Ruggeri *et al*., "A 5G Fiber Wireless 4Gb/s WDM Fronthaul for Flexible 360° Coverage in V-Band massive MIMO Small Cells," in *Journal of Lightwave Technology*, vol. 39, no. 4, pp. 1081-1088, 15 Feb.15, 2021.

[10]. "5G wireless fronthaul requirements in a passive optical network context," ITU-T Recommendation, G.Sup66, Sept. 2019.

[11]. J. S. Vardakas *et al*., "Towards high capacity and low latency backhauling in 5G: The 5G STEP-FWD vision," 2017 19th *International Conference on Transparent Optical Networks* (*ICTON*), Girona, 2017, pp. 1-4

[12]. C. Knittle, "IEEE 50 Gb/s EPON (50G-EPON)," 2020 *Optical Fiber Communications Conference and Exhibition (OFC)*, San Diego, CA, USA, 2020, pp. 1-3.

[13]. D. Zhang, D. Liu, X. Wu, and D. Nesset, "Progress of ITU-T higher speed passive optical network (50G-PON) standardization," in *IEEE/OSA J. Opt. Common. Netw.*, vol. 12, no. 10, pp. D99-D108, Oct. 2020.

[14]. R. Bonk *et al*., "The underestimated challenges of burst-mode WDM transmission in TWDM-PON," *Optical Fiber Technology*, vol. 26, part A, 2015, pp. 59-70.

[15]. H. Debrégeas *et al*., "TWDM-PON Burst Mode Lasers With Reduced Thermal Frequency Shift," in *Journal of Lightwave Technology*, vol. 36, no. 1, pp. 128-134, 1 Jan.1, 2018.

[16]. H. Schmuck *et al*., "Evaluation of Heater Implementations for Wavelength Drift Mitigation in Directly Modulated Lasers Under Burst Mode Operation," 2018 *European Conference on Optical Communication* (*ECOC*), Rome, 2018, pp. 1-3.

[17]. F. Koyama and K. Iga, "Frequency chirping in external modulators," in *Journal of Lightwave Technology*, vol. 6, no. 1, pp. 87-93, Jan. 1988.

[18]. H. Venghaus and N. Grote (Eds.), "Fibre Optic Communication - Key Devices," 2nd ed., Springer 2017.

[19]. H. Debregeas and K. Mekhazni, "Laser Assemblies," *European Patent Application*, EP3675295A1, Jul. 02, 2020. Available online at: https://data.epo.org/publication-server/rest/v1.0/publication-dates/20200701/patents/EP3675295NWA1/document.pdf.

[20]. K. Taguchi *et al*., "Reverse Bias Voltage Controlled Burst-Mode Booster SOA in λ-Tunable ONU Transmitter for High-Split-Number TWDM-PON," *J. Opt. Commun. Netw*. 10, 431-439 (2018).

[21]. W. Kobayashi *et al*., "50-Gb/s Direct Modulation of a 1.3-μm InGaAlAs-Based DFB Laser With a Ridge Waveguide Structure," in *IEEE Journal of Selected Topics in Quantum Electronics*, vol. 19, no. 4, pp. 1500908-1500908, July-Aug. 2013.

[22]. S. Yamaoka *et al*., "Directly modulated membrane lasers with 108 GHz bandwidth on a high-thermal-conductivity silicon carbide substrate," *Nat. Photonics*, 15, 28−35 (2021).

[23]. J. Kim *et al*., "800 Gb/s (80 × 10 Gb/s) capacity WDM-PON based on ASE injection seeding," Opt. Express 22, 10359-10365 (2014).

[24]. Q. Hu *et al*., "25-Gb/s ASE-seeded WDM PON," 21st *OptoElectronics and Communications Conference (OECC) held jointly with 2016 International Conference on Photonics in Switching (PS)*, Niigata, Japan, 2016, pp. 1-3.

[25]. D. Smith *et al*., "Colourless 10Gb/s reflective SOA-EAM with low polarization sensitivity for long-reach DWDM-PON networks," *35th European Conference on Optical Communication*, Vienna, Austria, 2009, pp. 1-2.

[26]. D.-H. Lee *et al*., "Design and performance of 10-Gb/s L-band REAM-SOA for OLT Transmitter in next generation access networks," *Opt. Express* 23, 2339-2346 (2015).

[27]. A. Naughton *et al*., "Demonstration of multi-channel 80 Gbit/s integrated transmitter and receiver for wavelength-division multiplexing passive optical network and fronthauling applications," *Electronics Letters*, Vol. 52, No. 8, pp. 637−639, Apr. 2016.

[28]. K. Lawniczuk *et al*., "40-Gb/s Colorless Reflective Amplified Modulator," in *IEEE Photonics Technology Letters*, vol. 25, no. 4, pp. 341-343, Feb.15, 2013.

[29]. X. Zhou and N. Deng, "A 25-Gb/s 20-km wavelength reused WDM system for mobile fronthaul applications," 2015 *European Conference on Optical Communication (ECOC)*, Valencia, Spain, 2015, pp. 1-3.

[30]. R. Vaernewyck *et al*., "113Gb/s (10 x 11.3Gb/s) ultra-low power EAM driver array," *Opt. Express* 21, 256-262 (2013).

[31]. J. Kim *et al*., "400 Gb/s (40 × 10 Gb/s) ASE Injection Seeded WDM-PON based on SOA-REAM," in *Optical Fiber Communication Conference/National Fiber Optic Engineers Conference 2013*, OSA Technical Digest (online) (Optical Society of America, 2013), paper OW4D.4.

[32]. Atra K. *et al*., "25 Gb/s Colorless Transmitter Based on Reflective Electroabsorption Modulator for Ultra-Dense WDM-PON Application," in Auer M.E., Tsiatsos T. (eds) *Internet of Things, Infrastructures and Mobile Applications. IMCL 2019. Advances in Intelligent Systems and Computing*, vol 1192. Springer, Cham.

[33]. K. Atra *et al*., "Reflective Electroabsorption Modulators for Beyond 25 Gb/s Colorless Transmissions," [accepted: *IEEE Journal of Lightwave Technology*, JLT2021].

[34]. K. Atra *et al*., "O-Band Reflective Electroabsorption Modulator for 50 Gb/s NRZ and PAM4 Colorless Transmission," 2020 *Optical Fiber Communications Conference and Exhibition (OFC)*, San Diego, CA, USA, 2020, pp. 1-3.

[35]. K. Atra *et al*., "An InP Reflective SOA-EAM for 10 Gb/s Colorless Multi-IFoF/mmWave Fiber-Wireless Uplink in 5G Networks," [accepted: *Conference on Lasers and Electro-Optics*, CLEO2021].

[36]. Q. T. Nguyen *et al*., "Multi-functional R-EAM-SOA for 10-Gb/s WDM access," 2011 *Optical Fiber Communication Conference and Exposition and the National Fiber Optic Engineers Conference*, Los Angeles, CA, USA, 2011, pp. 1-3.

[37]. H. Takesue and T. Sugie, "Wavelength channel data rewrite using saturated SOA modulator for WDM networks with centralized light sources," in *Journal of Lightwave Technology*, vol. 21, no. 11, pp. 2546-2556, Nov. 2003.

[38]. Wooram Lee *et al*., "Bidirectional WDM-PON based on gain-saturated reflective semiconductor optical amplifiers," in *IEEE Photonics Technology Letters*, vol. 17, no. 11, pp. 2460-2462, Nov. 2005.

[39]. L.A. Coldren, S.W. Corzine, and M.L. Mašanović, "Diode Lasers and Photonic Integrated Circuits", 2nd Ed., © 2012 John Wiey & Sons, Inc.

[40]. S. Chuang, "Physics of Photonic Devices," 2nd Ed., © John Wiley & Sons, Inc. 2009.

[41]. I. Saïdi, S. Ben Radhia, and K. Boujdaria, "Band structures of GaAs, InAs, and InP: A 34 k p model," *Journal of Applied Physics* 104, 023706 (2008).

[42]. I. Vurgaftman, J.R. Meyer, L.R. Ram-Mohan, "Band parameters for III−V compound semiconductors and their alloys," *Journal of Applied Physics* **89**, 5815 (2001).

[43]. N.K. Dutta and Q. Wang, "Semiconductor Optical Amplifiers," © 2006 World Scientific Publishing Co. Pte. Ltd.

[44]. S. Adachi, "Material parameters of In1−xGaxAsyP1−y and related binaries," *J. Appl. Phys*. 53, 8775 (1982).

[45]. M. Krijn, "Heterojunction band offsets and effective masses in Ill-V quaternary alloys," *Semicond. Sci. Technol*. **6** (1991) 27−31.

[46]. R.L. Moon, G.A. Antypasj, and L.W. James, "Bandgap and lattice constant of GaInAsP as a function of alloy composition," *Journal of Electronic Materials*, voL 3, No. 3, 1974.

[47]. S. Birner, "How to treat Quaternaries in nextnano," available online at: https://www.nextnano.de/nextnano3/input_parser/database/docu/Quaternaries.pdf.

[48]. S. Birner, "Modeling of semiconductor nanostructures and semiconductor-electroyte interfaces," PhD Thesis 2011, ISBN 978-3-941650-35-0. Available online at: https://www.nextnano.com/downloads/publications/PhD_thesis_Stefan_Birner_TUM_2011_WSIBook.pdf.

[49]. *nextnano* − Software for semiconductor nanodevices: https://www.nextnano.de/customer/tutorials.php

[50]. O. Madelung, "Semiconductors-Group IV Elements and III-V Compounds," in *Data in Science and Technology*, R. Poerschke, Editor in Chief, Springer-Verlag, Berlin, 1991.

[51]. A. Maho, "Sources appliquées aux cavités auto-alimentées pour les nouveaux réseaux d'accès multiplexés en longueur d'onde," Réseaux et télécommunications [cs.NI]. Institut National des Télécommunications, 2017.

[52]. A. Verdier, "Modélisation, conception, fabrication, caractérisation et valorisation d'amplificateurs optiques à semiconducteur de très large bande spectrale," PhD thesis, INSA/Université de Toulouse and III-V Lab, 2018.

[53]. H. C. Casey Jr. and P. L. Carter, "Variation of intervalence band absorption with hole concentration in p-type InP," *Appl. Phys. Lett*. 44, 82 (1984).

[54]. P. Harrison and A. Valavanis, "Quantum Wells, Wires and Dots: Theoretical and Computational Physics of Semiconductor Nanostructures," 4th Ed., © 2016 John Wiley & Sons, Ltd.

[55]. R. Sahara, K. Morito, and H. Soda, "Engineering of barrier band structure for electroabsorption MQW modulators," *Electron. Lett*., vol. 30, no. 9, pp. 698−699, 1994.

[56]. S. Kasap and P. Capper, "Handbook of Electronic and Photonic Materials," 2nd Ed., © Springer International Publishing AG 2017.

[57]. A. Chen and E.J. Murphy, "Broadband Optical Modulators," © 2012 by Taylor & Francis Group, LLC.

[58]. A.M. Fox *et al*., "Quantum well carrier sweep out: relation to electroabsorption and exciton saturation," in *IEEE Journal of Quantum Electronics*, vol. 27, no. 10, pp. 2281-2295, Oct. 1991.

[59]. X. Dai *et al*., "Versatile Externally Modulated Lasers Technology for Multiple Telecommunication Applications," in *IEEE Journal of Selected Topics in Quantum Electronics*, vol. 27, no. 3, pp. 1-12, May-June 2021.

[60]. Y. Matsui *et al*., "Enhanced modulation bandwidth for strain-compensated InGaAlAs-InGaAsP MQW lasers," in *IEEE Journal of Quantum Electronics*, vol. 34, no. 10, pp. 1970-1978, Oct. 1998.

[61]. M. Fox, "Optical Properties of Solids," 2nd Ed., © Oxford University Press 2010.

[62]. G. Bastard, "Wave mechanics applied to semiconductor heterostructures," © EDP Sciences 1992.

[63]. D.A.B. Miller, "Optical physics of quantum wells," in *Quantum Dynamics of Simple Systems, Instit. Phys*., pp. 239-266, 1996.

[64]. M. Connelly, "Semiconductor Optical Amplifiers", Springer 2002.

[65]. E P O'Reilly, "Valence band engineering in strained-layer structures," 1989 *Semicond. Sci. Technol*. **4** 121.

[66]. S. Chelles *et al*., "On the design of polarization-insensitive optoelectronic devices," 1995 *Semicond. Sci. Technol*. **10** 105.

[67]. P. Voisin, "Bandgap engineering of electro-optical modulators and switches," *Semicond. Sci. Technol*. **11** (1996) 1601−1607.

[68]. F. Devaux *et al*., "Full polarization insensitivity of a 20 Gb/s strained-MQW electroabsorption modulator," in *IEEE Photonics Technology Letters*, vol. 6, no. 10, pp. 1203-1206, Oct. 1994.

[69]. K. Wakita *et al*., "Polarization-independent electroabsorption modulators using strain-compensated InGaAs-InAlAs MQW structures," in *IEEE Photonics Technology Letters*, vol. 7, no. 12, pp. 1418-1420, Dec. 1995.

[70]. FIMMWAVE by Photon Design, Available online at: https://www.photond.com/products/fimmwave.htm.

[71]. S.B. Youssef, "Optical properties of Zn-doped InP single crystals, Physica A: Statistical Mechanics and its Applications, Volume 235, Issues 3−4, 1997, Pages 334-344.

[72]. D.A.B. Miller *et al*., "Band-Edge Electroabsorption in Quantum Well Structures: The Quantum-Confined Stark Effect," *Phys. Rev. Lett*., vol. 53, No. 22, pp. 2173-2176, 1984.

[73]. D.A.B. Miller, *et al*., "Electric field dependence of optical absorption near the band gap of quantum-well structures," *Phys. Rev*. B **32**, 1043.

[74]. Y.P. Varshni, "Temperature dependence of the energy gap in semiconductors," *Physica*, Vol. 34, Issue 1, 1967, pp. 149-154.

[75]. G. Agrawal and N. Dutta, "Semiconductor Lasers," Springer 993.

[76]. H. Takesue and T. Sugie, "Wavelength channel data rewrite using saturated SOA modulator for WDM networks with centralized light sources," in *Journal of Lightwave Technology*, vol. 21, no. 11, pp. 2546-2556, Nov. 2003.

[77]. D.M. Baney, P. Gallion, and R.S. Tucker, "Theory and Measurement Techniques for the Noise Figure of Optical Amplifiers," *Optical Fiber Technology*, Volume , Issue 2, 2 , Pages 22-154.

[78]. T. Briant *et al*., "Accurate determination of the noise figure of polarization-dependent optical amplifiers: theory and experiment," in *IEEE Journal of Lightwave Technology*, vol. 24, no. 3, pp. 1499-1503, March 2006.

[79]. M. Smit *et al*., "An introduction to InP-based generic integration technology," 2014 *Semicond. Sci. Technol*. 29 083001.

[80]. H. Debrégeas and C. Kazmierski, "Challenges and advances of photonic integrated circuits," *Comptes Rendus Physique*, Vol. 9, Issues 9−10, 2008, pp. 1055-1066.

[81]. H. Debrégeas et al., "Components for High Speed 5G Access," 2018 *Optical Fiber Communications Conference and Exposition* (OFC), San Diego, CA, 2018, pp. 1-3.

[82]. T. Sizer *et al*., "Measurement of carrier escape rates, exciton saturation intensity, and saturation density in electrically biased multiple-quantum-well modulators," in *IEEE Journal of Quantum Electronics*, vol. 30, no. 2, pp. 399-407, Feb. 1994.

[83]. https://www.mentor.com/products/ic_nanometer_design/custom-ic-design/photonics.

[84]. https://nazca-design.org/.

[85]. M. J. O'Mahony, "Semiconductor laser optical amplifiers for use in future fiber systems," in IEEE *Journal of Lightwave Technology*, vol. 6, no. 4, pp. 531-544, April 1988.

[86]. N. Olsson, "Lightwave systems with optical amplifiers," in *Journal of Lightwave Technology*, vol. 7, no. 7, pp. 1071-1082, July 1989.

[87]. D. Marcuse, "Reflection loss of laser mode from tilted end mirror," in IEEE *Journal of Lightwave Technology*, vol. 7, no. 2, pp. 336-339, Feb. 1989.

[88]. D. Marcuse, "Tilt, offset, and end-separation loss of lowest-order slab waveguide mode," in IEEE *Journal of Lightwave Technology*, vol. 4, no. 11, pp. 1647-1650, Nov. 1986.

[89]. F. Vogelbacher *et al*., "Analysis of silicon nitride partial Euler waveguide bends," *Opt. Express* 27, 31394-31406 (2019).

[90]. H. Haus, "Waves and Fields in Optoelectronics," Prentice-Hall series in solid state physical electronics, 1984.

[91]. S. Zhang, "Traveling-wave Electroabsorption Modulators," Ph.D. thesis, University of California, Santa Barbara, 1999.

[92]. M.E. Chin and W.S.C. Chang, "Theoretical design optimization of multiple-quantum-well electroabsorption waveguide modulators," in IEEE *Journal of Quantum Electronics*, vol. 29, no. 9, pp. 2476-2488, Sept. 1993.

[93]. "Multichannel DWDM applications with single-channel optical interfaces," ITU-T Recommendation G.698.1.

[94]. J.S. Wey, “The Outlook for PON Standardization: A Tutorial,” in *Journal of Lightwave Technology*, vol. 38, no. 1, pp. 31-42, 1 Jan.1, 2020.

[95]. M. Trajkovic *et al*., “Impedance Matching for High-Speed InP Integrated Electro-Absorption Modulators,” 2018 IEEE *Photonics Conference* (IPC), Reston, VA, 2018, pp. 1-2.

[96]. F Devaux *et al*., “Electroabsorption modulators for high-bit-rate optical communications: a comparison of strained InGaAs/InAIAs and InGaAsP/InGaAsP MQW” *Semicond. Sci. Technol*. Vol. 10, Nov. 7, 1995, pp. 887-901.

[97]. R. Saunders, J.P. King, and I. Hardcastle, “Wideband chirp measurement technique for high bit rate sources,” *Electronics Letters*, vol. 30, no. 16, pp. 1336-1338, 4 Aug. 1994.

[98]. C. Henry, “Theory of the linewidth of semiconductor lasers,” in IEEE *Journal of Quantum Electronics*, vol. 18, no. 2, pp. 259-264, Feb. 1982.

[99]. Y. Kim *et al*., “Chirp characteristics of 10-Gb/s electroabsorption modulator integrated DFB lasers,” in IEEE *Journal of Quantum Electronics*, vol. 36, no. 8, pp. 900-908, Aug. 2000.

[100]. J.-G. Provost et al., “Measuring the Chirp and the Linewidth Enhancement Factor of Optoelectronic Devices with a Mach−Zehnder Interferometer,” IEEE *Photon. J.*, vol. 3, no. 3, pp. 476 - 488, June 2011.

[101]. B.K. Saravanan, “Frequency Chirping Properties of Electroabsorption Modulators Integrated with Laser Diodes,” PhD dissertation, Ulm University, 2006.

[102]. T. Watanabe *et al*., “Transmission performance of chirp-controlled signal by using semiconductor optical amplifier,” in IEEE *Journal of Lightwave Technology*, vol. 18, no. 8, pp. 1069-1077, Aug. 2000.

[103]. F. Devaux, Y. Sorel and J.F. Kerdiles, “Simple measurement of fiber dispersion and of chirp parameter of intensity modulated light emitter,” in IEEE *Journal of Lightwave Technology*, vol. 11, no. 12, pp. 1937-1940, Dec. 1993.

[104]. F. Dorgeuille and F. Devaux, “On the transmission performances and the chirp parameter of a multiple-quantum-well electroabsorption modulator,” in IEEE *J. Quantum Electron*., vol. 30, no. 11, pp. 2565-2572, Nov. 1994.

[105]. V. Nodjiadjim *et al*., “0.7-um InP DHBT Technology With 400-GHz fT and fMAX and 4.5-V BVCE0 for High Speed and High Frequency Integrated Circuits,” in *IEEE Journal of the Electron Devices Society*, vol. 7, pp. 748-752, 2019.

[106]. J. King, D. Leyba and G. D. LeCheminant, “TDECQ (transmitter dispersion eye closure quaternary) replaces historic eye-mask and TDP test for 400 Gb/s PAM4 optical transmitters,” 2017 *Optical Fiber Communications Conference and Exhibition* (OFC), Los Angeles, CA, 2017, pp. 1-3.

[107]. “IEEE Standard for Ethernet Amendment 9: Physical Layer Specifications and Management Parameters for 25 Gb/s and 50 Gb/s Passive Optical Networks,” in IEEE Std 802.3ca-2020 , vol., no., pp.1-267, 3 July 2020.

[108]. R. Sleigh and S. Reinhold, “How to overcome test challenges in 400G/PAM-4 designs,” © Keysight. Available online at: https://www.keysight.com/upload/cmc_upload/All/PAM-4_January2017_Final.pdf.

[109]. 3GPP, ETSI TS 138 104 V15.3.0 (2018-10).

Curriculum Vitae

23/10/1988	Born in Wolkite, Ethiopia
04/2018 − 03/2021	PhD, Electronic and Optoelectronic Engineering, Télécom Paris, Institut polytechnique de Paris in collaboration with III-V Lab, Palaiseau (France)
10/2015 − 10/2016	MSc, Master of Science in Photonic Networks Engineering (Erasmus Mundus MAPNET), Aston University, Birmingham (United Kingdom)
09/2014 − 09/2015	MSc, Master on Photonic Networks Engineering (Erasmus Mundus MAPNET), Scuola Superiore Sant'Anna, Pisa (Italy)
09/2005 − 07/2009	BSc, Bachelor of Science in Electrical Engineering, Hawassa University, Hawassa (Ethiopia)
03/2016 − 09/2016	Master Thesis Student, IHP Microelectronics in collaboration with Technische Universität Berlin, Frankfurt (Oder) (Germany)
12/2009 − 09/2014 05/2017 − 03/2018	RAN Rollout Technician, Ethio telecom, Adama (Ethiopia)

List of Publications

K. Atra *et al*., “Reflective Electroabsorption Modulators for Beyond 25 Gb/s Colorless Transmissions,” in *Journal of Lightwave Technology*, vol. 39, no. 15, pp. 5035-5041, Aug.1, 2021.

K. Atra *et al*., “An InP Reflective SOA-EAM for 10 Gb/s Colorless Multi-IFoF/mmWave Fiber-Wireless Uplink in 5G Networks,” 2021 *Conference on Lasers and Electro-Optics* (CLEO), May 12, 2021.

K. Atra *et al*., “Reflective Electroabsorption Modulator for 50 Gb/s Colorless Transmission,” in *Enabling 6G Mobile Networks*, Chapter 8, Section 8.4 © Springer 2021.

K. Atra *et al*., “O-Band Reflective Electroabsorption Modulator for 50 Gb/s NRZ and PAM-4 Colorless Transmission,” 2020 *Optical Fiber Communications Conference and Exhibition* (OFC), San Diego, CA, USA, 2020, pp. 1-3.

K. Atra *et al*., “25 Gb/s Colorless Transmitter Based on Reflective Electroabsorption Modulator for Ultra-dense WDM-PON Application,” In: Auer M.E., Tsiatsos T. (eds) *Internet of Things, Infrastructures and Mobile Applications* (IMCL-2019). *Advances in Intelligent Systems and Computing*, vol 1192, pp. 1089-1100. Springer, Cham.

Acknowledgments

It has been an interesting period to conduct my research work at III-V Lab, and this work would not have been a success without the support and contributions of my colleagues at III-V Lab. I also gratefully acknowledge the financial support from the European Union via the Horizon2020 5GSTEP-FWD ITN project under Grant Agreement Number 722429.

My sincere thanks to Héléne Debregeas and Mohand Achouche for giving me the opportunity to join the research team at III-V Lab and trusting me to handle this project. I am grateful for Héléne's support during the first six months of my study. She was approachable and encouraging while fostering my independence as a researcher.

It was unfortunate to learn Héléne's departure from III-V Lab, but luckily, Giancarlo Cerulo was there to take over the industrial supervisory role. I am grateful for Giancarlo's availability for discussions of any type throughout this period and for his consistent encouragement to push the limits. His valuable and constructive comments helped me shape my work and build on my technical as well as soft skills. His continued support on the theoretical and experimental analysis of semiconductor devices is something that truly helped me to go deeper into the device physics and to achieve results that are not straightforward to be obtained. His careful reading and critical review of my publications and then this thesis helped me improve my manuscript significantly.

I am also grateful for my thesis director, Didier Erasme, for his support since the beginning of my research work. His familiarity with the evolution of technological standards helped me shape my work and focus on meeting the requirements of emerging passive optical network technologies. His knowledge of semiconductor devices at both component and system levels was immensely helpful. Despite his departure from Télécom Paris, I am grateful for his availability for discussions whenever needed and for his continued support during this period.

Fortunately, Cédric Ware was also there to support me as an academic co-supervisor during Didier's departure. Cédric's critical comments and encouragement to take initiatives in managing my project helped me not only on the technical aspect but also to be able to foresee possible outcomes of my work and manage my project effectively. I sincerely thank both Didier and Cédric for carefully reading this thesis and providing their valuable and constructive feedbacks.

I gratefully acknowledge the contribution of Jean-Guy Provost in building the experimental setups used to obtain most of the results presented in this thesis as well as in our publications. The discussions I had with Jean-Guy helped me to do experiments knowing the expected outcomes, and better interpret and refine the results afterwards.

Several people contributed to this project, and I would like to extend my appreciation and thank Karim Mekhazni for mounting the components I studied in this thesis and for his friendly responses in every request I made. I also thank Harry Gariah for providing the lensed fibers used for characterizing our components and replacing them swiftly whenever they are damaged, Fabrice Blache for measuring the small-signal frequency response of one of our components, Filip George for his support and contribution to the 50 Gb/s transmission results we obtained, Francois Duport for his support in far-field measurements, and Franck Malecot for his critical review of our publications, and for his continued support and encouragement.

I also acknowledge the support of the WinPhoS group at Aristotle University of Thessaloniki in Greece and thank the team for hosting me during my secondment. I would like to thank Eugenio Ruggeri for his support and collaboration during the experiments we performed together, specifically in performing the analog radio-over-fiber transmission. I also thank Amalia Miliou and Chris Vagionas for their support during my secondment.

I am grateful for the support and encouragements I received from friends, former classmates, and my siblings. I would also like to thank the jury members for their willingness to examine the PhD thesis, the times they spent to carefully read this manuscript, and their invaluable feedbacks.

Finally, I sincerely thank my family for their love, constant support, and inspiration. I hope my sister Bethlehem (Asnakech), who I lost during my PhD studies, looks down and be proud of what I have achieved as a person and as a brother.

Kebede Tesema Atra

(ከበደ ተሰማ አጥራ)

Palaiseau, 2021

ECOLE DOCTORALE

Titre : Conception d'un réseau optique passif ultra-dense pour prendre en charge un grand nombre d'utilisateurs finaux

Mots clés : Électroabsorption, Transmetteur incolore, Réfléchissant, 5G Fronthaul, Chirp

Résumé : Dans cette thèse, nous étudions des modulateurs à électroabsorption (EAM) en réflexion, intégrés de manière monolithique sur InP avec des amplificateurs optiques à semiconducteurs (SOA), pour réaliser des transmetteurs indépendants de la longueur d'onde (achromatiques). Ces composants sont conçus pour des applications dans les réseaux d'accès, qui nécessitent un déploiement dense de transmetteurs-récepteurs optiques à faible coût. Les composants sont basés sur des zones actives à multi-puits quantiques GaInAsP/InP (MQW) et ont été fabriqués par un technologie à guides d'onde enterrés (semi-insulating buried heterostructure, SIBH). Une approche d'intégration longitudinale type 'bout-à-bout' (butt-joint) a été adoptée pour combiner les zones actives MQW des différentes fonctions de bases (building blocks, BBs) sur une même puce. Nous analysons des circuits, basés sur plusieurs combinaisons des BBs, avec trois longueurs de modulateur différentes (80, 100 et 150 µm). Nous effectuons une analyse complète des performances statiques et dynamiques des composants réalisés. Pour les SOA, nous obtenons un gain >17 dB, avec un facteur de bruit d'environ 4 dB. Pour les EAM, nous atteignons une bande passante de modulation >33 GHz et un taux d'extinction dynamique jusqu'à 15 dB. Les EAM présentent un chirp nul, pour des tensions de polarisation inverse dans la plage comprise entre −1,2 V et −1,5 V, en fonction de la longueur d'onde de fonctionnement. Pour les composants fonctionnants dans la bande C, nous démontrons des transmissions achromatiques à 25 Gb/s, sur une plage spectrale de 15 nm, jusqu'à 16 km, en utilisant le format de modulation non-return-to-zero (NRZ). Avec les composants fonctionnant dans la bande O, nous montrons des transmissions jusqu'à 50 Gb/s NRZ, ainsi que des transmissions PAM-4 sans égalisation. Enfin, nous effectuons une transmission multicanal bande V/IFoF de 10 Gb/s, atteignant une amplitude de vecteur d'erreur <11%.

Title: Design of Ultra Dense Passive Optical Network to Support High Number of End Users

Keywords: Electroabsorption, Colorless Transmitter, Reflective, 5G Fronthaul, Chirp

Abstract: In this thesis, we study reflective electroabsorption modulators (EAMs) monolithically integrated with semiconductor optical amplifiers (SOAs) to realize wavelength-independent (colorless) transmitters for low-cost access network applications that require dense deployment of optical transceivers. The devices are based on GaInAsP/InP multiple quantum-wells (MQWs), leveraging semi-insulating buried heterostructure (SI-BH) waveguide and butt-joint integration technologies. We analyze different design tradeoffs by considering three modulator lengths (80, 100 and 150 µm). After fabrication, we perform a complete performance analysis of our components in both static and dynamic modes. We obtain >17 dB SOA gain with a noise figure of about 4 dB. For the EAM, we achieve >33 GHz modulation bandwidth and up to 15 dB dynamic extinction ratio. The EAMs exhibit zero-chirp for reverse bias voltages in the range between −1.2 V and −1.5 V, depending on the operating wavelength. For C-band components, we demonstrate up to 16 km colorless transmission, over 15 nm, at 25 Gb/s using non-return-to-zero (NRZ) modulation format. With components working in the O-band, we perform up to 50 Gb/s NRZ as well as PAM-4 transmissions without equalization. Finally, we perform a 10 Gb/s multi-channel V-band/IFoF transmission, achieving <11% error vector magnitude.

Institut Polytechnique de Paris
91120 Palaiseau, France